

# **Design and Implementation of Enablers in Materials Acceleration Platforms for Battery Research**

Fuzhan Rahmanian

Vollständiger Abdruck der von der TUM School of Natural Sciences der Technischen Universität München zur Erlangung einer  
Doktorin der Ingenieurwissenschaften (Dr.-Ing.)  
genehmigten Dissertation.

Vorsitz: Hon.-Prof. Dr. Richard W. Fischer

Prüfende der Dissertation:

1. Prof. Dr.-Ing. Helge Stein
2. Prof. Dr. Jennifer Rupp
3. Assoc. Prof. Dr. Ivano Eligio Castelli

Die Dissertation wurde am 14.05.2024 bei der Technischen Universität München eingereicht und durch die TUM School of Natural Sciences am 31.05.2024 angenommen.



TECHNICAL UNIVERSITY OF  
MUNICH

TUM SCHOOL OF NATURAL SCIENCES

**Design and Implementation of  
Enablers in Materials Acceleration  
Platforms for Battery Research**

**Design und Implementierung von  
Verbesserungselementen in  
Materialbeschleunigungsplattformen  
für die Batterieforschung**

**Fuzhan Rahmanian**





"The ever accelerating progress of technology and changes in the mode of human life give the appearance of approaching some essential singularity in the history of the race beyond which human affairs, as we know them, could not continue."

John von Neumann, 1958



## Acknowledgments

Looking back on the incipit of my PhD journey in early 2020, the world felt markedly different. It was a time before the global disarray brought by the pandemic, before new conflicts broke out in Europe, and before technology surged to prominence with artificial intelligence. The day that I entered the empty laboratory, I could not have imagined what the next four years had in store for me, and I can confidently say that this time was equally challenging, arduous, educational, insightful, and eventful on both a personal and academic level. The conclusion of this project represents a significant personal achievement for two reasons: firstly, this PhD was undertaken in a field detached from my undergraduate and graduate experiences, and secondly, because of all the parallel knowledge I could gain to pursue this degree. This experience has proven to me that steadfast dedication and sacrifice in pursuit of one's convictions can lead to extraordinary outcomes.

All this would not have been possible without the support of the figure who has most profoundly impacted my academic life now and in the past years, Prof. Dr. Helge Stein. To him, I extend my deepest gratitude. As his first student to complete the journey to a doctorate, I sincerely hope that his experience as a mentor was as enriching as his guidance has been fruitful for me. If so, I am confident that future students privileged to work under his supervision will significantly contribute to research and the broader scientific community. For me, his guidance and our close collaboration from day one stretched over all possible aspects of research, from laboratory planning to grant applications, conferences, and even a shift in Institution. His creative approaches to problem-solving have always fascinated me and changed my mindset on tackling research challenges from various perspectives, a type of creativity that nowadays the era of research demands. I am further thankful for his constant availability; be it Sunday, midnight, or a holiday, he always responded promptly and guided me through all the situations. I want to remark and highlight how Prof. Stein has always supported my admittedly ambitious "wants" and "wishes", permitting me to pursue a parallel Master's degree and also complete a successful internship at BASF, opportunities that would not have been possible without his support. He constantly encouraged me to engage in different areas, offering fresh perspectives

at every turn. Truly, he stands as a guiding figure in my life, imparting numerous invaluable lessons. As I advance in my career, I am eager to apply these lessons and exemplify the ideals he has instilled in me.

My journey of successes and challenges that I have faced could never have been conducted without the wholehearted and daily effort -words fall short when expressing my deepest gratitude- of my fiancé Luca Zangari. Despite the constant fatigue and demanding workloads, he never wavered, providing love and support through countless night shifts, forfeited vacations, and endless words of encouragement. He always urged me to pursue my dreams and helped me to achieve them, supporting me through additional courses, pursuing a different degree, relocating to a new city, and much more. Even as we lived among unopened boxes in our new apartment in the past months, he never stopped supporting my aspirations. In all these years, he always placed my needs above his own and has selflessly encouraged me to aim for the best, often forgetting himself in the process. I can never thank him enough; this would not have been possible without him. He filled every moment of this journey with joy, from gathering the math books I adored, cooking my favorite dishes, decorating our walls with my degrees, composing beautiful music, driving me to work daily, and staying by my side during all the late nights. I could write a book to the detail with everything he has done for me over these years. I cherish every moment and feel blessed every day to have him in my life.

I also want to express my gratitude to someone who is no longer here and will never witness this moment: my grandmother, whom I lost last year, along with both of my grandfathers. She encouraged me to seek a better life here in Germany, taught me to be an independent woman, and rejoiced in every achievement of my life. She often said, 'I can't wait until you finish your degree, so I can raise my hands and say we did it.' Although her sentence made me laugh since I was the one doing the work, her response was always touching: 'Your success makes me happy and fulfilled.' We may never celebrate this moment together, but I will close my eyes, raise my hands for her, and say, 'We did it', just as she wished. I extend my heartfelt gratitude to my family—my parents and my supportive younger brother, who always seeks to share and celebrate each milestone with me. From my earliest days, their sacrifices, and efforts have always been focused on providing me with a well-rounded education, from music to mathematics. Their enduring support and dedication have been the keystone of my journey, leading to this moment, where they are here in Munich to witness its end. Similarly, my parents- and grandparents-in-law have been a source of encouragement and support throughout this journey. Starting this path was not a decision I made alone; my father encouraged me toward it, teaching me the values of lifelong learning, continual self-education, and the importance of disseminating knowledge.

I would like to further express my deepest gratitude to several people in my profes-

sional career who have taught me valuable lessons. It starts with Prof. Dr. Othmar Marti, who always motivated me and kept me excited about my work. I fondly remember our discussions about optics and cameras at the Physics Colloquium. He supported my decision to change my path toward fulfilling my potential, and he is indeed one of the most significant role models of my life. I want to name also Prof. Dr. Ute Kaiser, who has supported me on various levels. As a paragon of independence and profound knowledge, she is highly esteemed within the scientific community. I am deeply honored to have such an exemplary role model and mentor in my life. Prof. Dr. Neumann, who has dedicated immense effort to educating students; his numerous emails, meetings, and detailed explanations have greatly facilitated my learning and teaching skills. I am also grateful to Dr. George Baryannis, my supervisor and advisor, during my AI master's degree in Huddersfield. His dedication to late-night tutoring for distance learners and his thorough guidance through the courses provided me with a strong background in logic and logical programming. My time during this master's program was filled with joy, surrounded by highly motivated people in a friendly environment, all made possible through his coordination. For the time during my internship at BASF, I want to sincerely appreciate Dr. Hergen Schultze, who made me experience true and authentic leadership. His commitment to sustainability and his inspiring way of guiding others are qualities I admire and strive to incorporate into my future career. I am thankful for the time and the positive and friendly atmosphere I experienced in his group. My gratitude extends further to Dr. Robert Lee for his supportive supervision during the internship. He was always available to listen, guide me through various topics, and showed me immense support for our collaborative publication. I am grateful to him and Dr. Dominic Linzner for all the insights into problem-solving. Collaborating with such brilliant minds in mathematics was truly a privilege, and I cherish the rich learning experiences we shared.

I am grateful to all my colleagues who have supported me at various stages of my work. Special thanks go to Stefan Fuchs, who helped make our automated system work despite the many challenges we faced; even though the system failed thousands of times over several years, we finally succeeded. I would also like to thank the POLiS-cluster of Excellence, and in particular Dr. Christian Punckt, for their continued support in pursuing this path and working tirelessly to fund this project. My gratitude extends to all the collaborators and colleagues in the BIG-MAP project. This journey has been shaped by the lessons I've learned from others, the growth I've experienced, and the contributions that brought this work to fruition. I am sincerely thankful to everyone who made this path a reality for me.



# Abstract

The conventional development of advanced materials for high-performance batteries is a decade-long journey. A considerable amount of capital and effort is required to sustain the trial-and-error approaches from discovery to commercialization. Herein, it is essential to accelerate the identification of promising materials in the domain of energy storage and conversion, requiring agile and disruptive research methods to significantly shorten the development life-cycle and spur innovation. The integration of indispensable tools such as machine learning, data science, and high-throughput experimentation is increasingly recognized for its capacity to generate insights and optimize battery performance, thus accelerating research paradigms. State-of-the-art Materials Acceleration Platforms (MAPs) leverage these advancements to deploy intelligent automated workflows, minimize researcher intervention, and maximize autonomous laboratory operations.

This thesis aims to engineer tools for MAPs applicable in autonomous electrochemical experimentation and predictive analysis to enhance battery informatics. The study involves various stages of laboratory device integration, hardware interfacing, deployment of custom-designed software, and automatic testing. It unites rigorous electrochemical data analysis and data management systems and leverages deep learning, machine learning, and active learning algorithms to orchestrate AI-accelerated experiments for optimization tasks at an unprecedented rate. The objective is to reduce the time required to extract fundamental knowledge compared to traditional approaches and ensure high-throughput experimentation with reliability, reproducibility, and multi-fidelity. Ultimately, this research contributes to the advancement of battery technology and marks a significant leap toward the realization of self-driving laboratories.





# Kurzfassung

Der herkömmliche Entwicklungsprozess fortschrittlicher Materialien für Hochleistungsbatterien ist ein jahrzehntelanger Prozess. Für die Aufrechterhaltung des serendipitären Ansatzes von der Entdeckung bis zur Kommerzialisierung ist eine beträchtliche Menge an Arbeit und Kapital erforderlich. Daher ist es von entscheidender Bedeutung, die Identifizierung vielversprechender Materialien für die Energiespeicherung und -umwandlung zu beschleunigen, was agile und disruptive Forschungsmethoden erfordert, um den Entwicklungszyklus wesentlich zu verkürzen und Innovationen voranzutreiben. Die Integration von unverzichtbaren Werkzeugen wie maschinelles Lernen, Datenwissenschaft und Hochdurchsatz-Experimente wird zunehmend für ihre Fähigkeiten genutzt, Erkenntnisse zu generieren und die Batterieleistung zu optimieren, wodurch Forschungsparadigmen beschleunigt werden. Hochmoderne Materialbeschleunigungsplattformen (MAPs) verwenden diese Fortschritte, um intelligente automatisierte Arbeitsabläufe einzusetzen, die Notwendigkeit für das Eingreifen der Forscher zu minimieren und den autonomen Laborbetrieb zu maximieren.

Ziel dieser Arbeit ist die Entwicklung von Werkzeugen für MAPs für autonome elektrochemische Experimente und prädiktive Analysen zur Verbesserung der Batterieinformatik. Die Studie umfasst verschiedene Phasen der Integration von Laborgeräten, Hardware-Schnittstellen, den Einsatz von maßgeschneiderter Software und automatischen Tests. Sie vereint rigorose elektrochemische Datenanalyse sowie Datenverwaltungssysteme und nutzt Deep Learning, maschinelles Lernen und aktive Lernalgorithmen, um KI-beschleunigte Experimente für Optimierungsaufgaben mit noch nie dagewesener Schnelligkeit zu orchestrieren. Ziel ist es, den Zeitaufwand für die Gewinnung grundlegender Erkenntnisse im Vergleich zu herkömmlichen Ansätzen zu reduzieren und Experimente mit hohem Durchsatz, hoher Zuverlässigkeit, Reproduzierbarkeit und Vielseitigkeit zu ermöglichen. Letztlich trägt diese Forschung zur Weiterentwicklung der Batterietechnologie bei und markiert einen bedeutenden Schritt in Richtung der Realisierung selbstfahrender Labore.



# List of Publications

## First Authorship Publications

### Peer Reviewed

[1] **Fuzhan Rahmanian**, Robert M. Lee, Dominik Linzner, Kathrin Michel, Leon Merker, Balazs B. Berkes, Leah Nuss, Helge S. Stein.  
Attention towards chemistry agnostic and explainable battery lifetime prediction, *Nature - npj computational materials*, **10**, 100 (2024),  
<https://doi.org/10.1038/s41524-024-01286-7>

[2] **Fuzhan Rahmanian**, Stefan Fuchs, Bojing Zhang, Maximilian Fichtner, Helge S. Stein.  
Autonomous millimeter scale high throughput battery research system (Auto-MISCHBARES), *RSC - Digital Discovery*, (2024),  
<https://doi.org/10.1039/D3DD00257H>

[3] **Fuzhan Rahmanian**, Monika Vogler, Christian Wölke, Peng Yan, Stefan Fuchs, Martin Winter, Isidora Cekic-Laskovic & Helge Sören Stein.  
Conductivity experiments for electrolyte formulations and their automated analysis. *Nature - Scientific Data*, **10**, 43 (2023),  
<https://doi.org/10.1038/s41597-023-01936-3>

[4] **Fuzhan Rahmanian**, Monika Vogler, Christian Wölke, Peng Yan, Martin Winter, Isidora Cekic-Laskovic, Helge S. Stein.  
One-Shot Active Learning for Globally Optimal Battery Electrolyte Conductivity. *Batteries & Supercaps*, **5**, 10, e202200228 (2022),  
<https://doi.org/10.1002/batt.202200228>

[5] **Fuzhan Rahmanian**, Jackson Flowers, Dan Guevarra, Matthias Richter, Maximilian Fichtner, Phillip Donnelly, John M. Gregoire, Helge S. Stein.  
Enabling Modular Autonomous Feedback-Loops in Materials Science through Hierarchical Experimental Laboratory Automation and Orchestration, *Advanced Materials Interfaces*, **9**, 8, 2101987 (2022),  
<https://doi.org/10.1002/admi.202101987>

## Co-Authorship Publications

### Peer Reviewed

[6] Bojing Zhang, Leon Merker, Monika Vogler, **Fuzhan Rahmanian**, Helge Sören Stein

Apples to apples: shift from mass ratio to additive molecules per electrode area to optimize Li-ion batteries, *RSC - Digital Discovery*, (2024)

<https://doi.org/10.1039/D4DD00002A>

[7] Katarina Cicvarić, Leon Merker, Bojing Zhang, **Fuzhan Rahmanian**, Miran Gaberšček, Helge Sören Stein

Fast formation of anode-free Li-metal batteries by pulsed current, *RSC - Physical Chemistry Chemical Physics*, (2024)

<https://doi.org/10.1039/D4CP00775A>

[8] Helge S. Stein, Alexey Sanin, **Fuzhan Rahmanian**, Bojing Zhang, Monika Vogler, Jackson K. Flowers, Leon Fischer, Stefan Fuchs, Nirmal Choudhary, Lisa Schroeder. From materials discovery to system optimization by integrating combinatorial electrochemistry and data science, *Current Opinion in Electrochemistry*, **35**, 101053, (2022)

<https://doi.org/10.1016/j.coelec.2022.101053>

[9] Sven Daboss, **Fuzhan Rahmanian**, Helge S. Stein, Christine Kranz.

The potential of scanning electrochemical probe microscopy and scanning droplet cells in battery research, *Electrochemical Science Advances*, **2**, 4, e2100122, (2021)

<https://doi.org/10.1002/elsa.202100122>

[10] Anass Benayad, Diddo Diddens, Andreas Heuer, Anand Narayanan Krishnamoorthy, Moumita Maiti, Frédéric Le Cras, Maxime Legallais, **Fuzhan Rahmanian**, Yuyoung Shin, Helge Stein, Martin Winter, Christian Wölke, Peng Yan, Isidora Cekic-Laskovic.

High-Throughput Experimentation and Computational Freeway Lanes for Accelerated Battery Electrolyte and Interface Development Research, *Advanced Energy Materials*, **12**, 17, 2102678, (2021)

<https://doi.org/10.1002/aenm.202102678>

---

[11] Prof. Ivano E. Castelli, Dr. Daniel J. Arismendi-Arrieta, Prof. Arghya Bhowmik, Dr. Isidora Cekic-Laskovic, Dr. Simon Clark, Prof. Robert Dominko, Dr. Eibar Flores, Jackson Flowers, Karina Ulvskov Frederiksen, Dr. Jesper Friis, Dr. Alexis Grimaud, Dr. Karin Vels Hansen, Prof. Laurence J. Hardwick, Prof. Kersti Hermansson, Dr. Lukas Königer, Dr. Hanne Lauritzen, Dr. Frédéric Le Cras, Dr. Hongjiao Li, Dr. Sandrine Lyonnard, Dr. Henning Lorrman, Prof. Nicola Marzari, Prof. Leszek Niedzicki, Dr. Giovanni, **Fuzhan Rahmanian**, Prof. Helge Stein, Dr. Martin Uhrin, Prof. Wolfgang Wenzel, Prof. Martin Winter, Dr. Christian Wölke, Prof. Tejs Vegge. Data Management Plans: the Importance of Data Management in the BIG-MAP Project, *Batteries & Supercaps*, **4**, 12, 1803-1812, (2021)  
<https://doi.org/10.1002/batt.202100117>



# Conference & Scientific Contributions

[1] **Fuzhan Rahmanian**

Workflows and orchestration in Self Driving Laboratories, Machine Learning@INT workshop, Artificial Intelligence for Materials Science, Department of Informatics, Karlsruhe Institute of Technology (KIT), Karlsruhe, 13 February 2024. Oral Presentation

[2] **Fuzhan Rahmanian**

Elements for Materials Accelerations Platforms, BIG-MAP EUnified Battery Data Space Workshop *BIG-MAP - European Union's Horizon 2020*, Grindelwald, Switzerland, 29-31 January 2024. Oral Presentation

[3] **Fuzhan Rahmanian**

Design and Implementation of a Material Acceleration Platform for Enhanced Battery Performance, BIG-MAP Project Meeting *BIG-MAP - European Union's Horizon 2020*, Brussels, Belgium, 25. October 2023. Oral presentation.

[4] **Fuzhan Rahmanian**, Stefan Fuchs, Maximilian Fichtner, Helge S. Stein.

Autonomous millimeter scale high throughput battery research system. E-MRS 2023 SPRING MEETING, *European Materials Research Society*, Exhibition & Convention Center, Strabourg, France, 29. May 2023. Oral presentation.

[5] **Fuzhan Rahmanian**, Stefan Fuchs, Maximilian Fichtner, Helge S. Stein.

Auto-MISCHBARES. 16th International conference on materials chemistry (MC16), *Royal Society of Chemistry*, University College Dublin, Ireland, 03. July 2023. Oral presentation.

[6] **Fuzhan Rahmanian**

AI Accelerated Asynchronous Experimentation for Battery Materials Discovery, 2021 MRS Fall Meeting & Exhibit *Materials Research Society (MRS)*, Boston, USA, 30. November 2021. Oral presentation.

[7] **Fuzhan Rahmanian**, Helge S. Stein

How can machine learning and autonomy accelerate chemistry?, Chemical Science Symposium *Royal Society of Chemistry*, Online, Germany, 29. September 2020. Poster presentation.





# Awards Recieved

## **Awards granted in the scope of this doctoral thesis:**

### **[1] BIG-MAP PhD AWARD,**

FUZHAN RAHMANIAN (KIT) is awarded the BIG-MAP PhD award for her exceptional contribution to the enhancement of the scientific objectives of BIG-MAP and for taking a leading role in establishing a collaborative environment and mindset between the project partners.

BIG-MAP Project-Meeting, 24. & 25. October 2023, SOLOVAY, Brussels, Belgium.

## **Awards granted beyond the scope of this doctoral thesis:**

### **[2] The Chancellor's Prize,**

FUZHAN RAHMANIAN has been awarded *The Chancellor's Prize* for outstanding achievement by a postgraduate student

University of Huddersfield, 30. March 2022, Huddersfield, United Kingdom.

### **[3] The Departmental Prize for the Best Overall Performance on Postgraduate study in the Computer Science Department,**

Awarded to Fuzhan Rahmanian - Artificial Intelligence Distance Learning

University of Huddersfield, School of Computing and Engineering, October 2021, Huddersfield, United Kingdom.

### **[4] Departmental Prize for the Best Postgraduate Project in the Computer Science Department,**

Awarded to Fuzhan Rahmanian - Artificial Intelligence Distance Learning

University of Huddersfield, School of Computing and Engineering, October 2021, Huddersfield, United Kingdom.



# Contents

<b>Acknowledgments</b>	<b>v</b>
<b>Abstract</b>	<b>ix</b>
<b>Kurzfassung</b>	<b>xi</b>
<b>List of Publications</b>	<b>xiii</b>
<b>Conference &amp; Scientific Contributions</b>	<b>xvii</b>
<b>Awards Recieved</b>	<b>xix</b>
<b>1. Introduction</b>	<b>1</b>
1.1. A Phenomenological Perspective . . . . .	2
1.2. Digital Transformation . . . . .	3
1.2.1. Beyond Linear Exploration . . . . .	4
1.2.2. Chemoentric Era of Inverse Design . . . . .	4
1.2.3. Material Genome Initiative & Beyond . . . . .	5
1.2.4. Closing the Experimental Loop . . . . .	7
1.2.5. Intelligent Acceleration Platforms . . . . .	8
1.2.6. The spawning of MAPs . . . . .	9
1.2.7. From Optimization to Discovery . . . . .	10
1.3. Holistic Strategies for Multilayered Batteries . . . . .	11
1.3.1. The path of MAPs for Materials Screening . . . . .	12
1.3.2. The Iceberg Illusion of Interfaces . . . . .	13
1.3.3. Temporal Narratives in System Analytics . . . . .	14
1.4. Digital Movements in Smart MAPs . . . . .	15
1.5. Europe’s Solution to Energy Storage . . . . .	16
1.5.1. Blueprinting the Energy MAP . . . . .	17
1.6. Perspectives on a Singularity . . . . .	19
<b>2. Aim and Objectives</b>	<b>23</b>
<b>3. Research Design and Methodology</b>	<b>27</b>
3.1. Software & Informatics Tools . . . . .	27
3.1.1. Concurrent Programming . . . . .	27
3.1.2. Web-Server Communication . . . . .	31
3.1.3. Research Data management . . . . .	33

3.2. Statistics, ML, and DL tools . . . . .	37
3.2.1. Active Learning . . . . .	38
3.2.2. Uncertainty Quantification . . . . .	40
3.2.3. Sequence Modeling . . . . .	43
3.3. Electrochemical methods . . . . .	51
3.3.1. Battery Fundamentals . . . . .	52
3.3.2. Electrochemical Impedance Spectroscopy . . . . .	55
3.3.3. Cyclic Voltammetry . . . . .	57
<b>4. Results and Publications</b>	<b>61</b>
4.1. Enabling Modular Autonomous Feedback-Loops in Materials Science through Hierarchical Experimental Laboratory Automation and Orchestration . . . . .	62
4.1.1. Publication Details . . . . .	62
4.1.2. Manuscript . . . . .	65
4.1.3. Supporting Information . . . . .	73
4.2. Conductivity experiments for electrolyte formulations and their automated analysis . . . . .	78
4.2.1. Publication Details . . . . .	78
4.2.2. Individual Contribution . . . . .	80
4.2.3. Manuscript . . . . .	81
4.3. One-Shot Active Learning for Globally Optimal Battery Electrolyte Conductivity . . . . .	92
4.3.1. Publication Details . . . . .	92
4.3.2. Manuscript . . . . .	95
4.3.3. Supporting Information . . . . .	104
4.4. Attention towards chemistry agnostic and explainable battery lifetime prediction . . . . .	111
4.4.1. Publication Details . . . . .	111
4.4.2. Manuscript . . . . .	114
4.4.3. Supporting Information . . . . .	130
4.5. Autonomous millimeter scale high throughput battery research system	157
4.5.1. Publication Details . . . . .	157
4.5.2. Manuscript . . . . .	160
4.5.3. Supporting Information . . . . .	174
<b>5. Conclusion and Outlook</b>	<b>187</b>
5.1. In aid of digital intelligence . . . . .	187
5.2. Perspectives on scalable efforts . . . . .	190
5.3. Ethics for the present and the future . . . . .	190

---

<b>A. Appendix</b>	<b>193</b>
A.1. Licenses and Reprint permissions . . . . .	193
<b>List of Figures</b>	<b>199</b>
<b>Abbreviations</b>	<b>209</b>
<b>Bibliography</b>	<b>215</b>



*“The only constant is change,  
and the rate of change is increasing”*  
— Peter Diamandis

# 1. Introduction

## Why is the race for better batteries a race against time and data scarcity?

Material discovery and design approaches resemble a polymorph puzzle that changes shape once put together<sup>1</sup>. Conventionally, scientists assembled these puzzle pieces by investing a disproportionate amount of time and capital in empirical methods<sup>2</sup>. Especially in battery research, the vast and complex chemical space<sup>3, 4</sup> requires a depth of analysis exacerbated by the lengthy process of brute-force strategies<sup>5</sup>. This further amplifies complexity in the high-dimensional design spaces where the optimization of electrolytes, electrodes along with their physical and mechanical properties<sup>6, 7</sup> result in a matrix of outcomes that urge for exploration and systematic exploitation<sup>8, 9</sup>.

The path to optimal battery materials involves a series of iterative processes, each requiring precision and a profound understanding of physiochemical parameters<sup>10</sup>. The optimization steps concern not only the composition of materials but also include the design of electrodes and electrolytes<sup>11</sup>, the development of efficient cycling protocols, and the assessment of battery interfaces<sup>12</sup> stability, such as solid electrolyte interphase (SEI) and cathode electrolyte interphase (CEI). These processes directly affect a battery’s lifetime and performance, and it is essential to understand the extent of their impact<sup>13</sup>. Thus, the final puzzle piece is lifespan prediction, where the lengthy cycling procedures introduce latency in performance feedback<sup>14</sup>. Early-cycle data prediction could enhance development progress and manufacturing processes. These multifaceted challenges necessitate a paradigm shift in battery research<sup>15</sup>. Conventional methods, while foundational, require transformation to address these complex challenges<sup>16</sup>. Modern research strategies<sup>17</sup>, such as the implementation Materials Acceleration Platforms (MAPs)<sup>18, 19</sup>, are indispensable for discovery<sup>20</sup> and development of the next-generation battery systems<sup>21</sup> for energy storage and conversion applications<sup>10</sup>.



## 1.1. A Phenomenological Perspective

According to Kuhn<sup>22</sup>, scientific progression unfolds not through mere linear accumulation of knowledge but through a series of transformative shifts in science's fundamental concepts and methodologies. In line with this perspective is the emergence of initiatives such as MAPs, which are emblematic of a broader scientific evolution over the past and current centuries. Developments were brought forward by breakthroughs in digital technologies<sup>23</sup> along with the evolution of material sciences, which has experienced several paradigmatic transformations, each building upon its forerunners. The inception of modern scientific understanding began with empirical science of the 17th century, characterized by rigorous observation and experimentation. This phase signified a shift from insightful premises to a reliance on empirical evidence<sup>24</sup>. In the late 1870s, Edison's exhaustive exploration of over 1600 materials for the optimal lightbulb was a precursor to High-Throughput Experimentation (HTE) design, where the systematic variation of experimental parameters in a vast search space established essential techniques for observing material properties<sup>25</sup>. Further examples of primitive HTEs were involved just a few decades later in discoveries that massively impacted society's standard of living. Alwin Mittasch at BASF in 1909, through an iterative approach for optimizing the catalyst, allowing for industry-scale ammonia synthesis, which is still a crucial element for agricultural fertilization<sup>26</sup>.

It was soon apparent that even a high degree of acceleration cannot justify a mindless screening procedure. HTE is most effective when the experimental endeavor is minimized while the information retained is maximized. The mindful application of Design of Experiments (DoE) is required to reach efficacy<sup>26</sup>, and it involves the systematic design of a search space grid with predefined steps for each parameter to explore their performance impact. The expansion of phenomenological approaches continued throughout the 1950s; it sought to explain nature through increasingly complex scientific laws and principles based on mathematics, significantly impacting domains such as physics, chemistry, and biology<sup>22, 27</sup>.

## 1.2. Digital Transformation

The omnipresence of computers today, along with the leaps in power and efficiency achieved by silicon-based transistor chips, can make it challenging to imagine that the formal foundations for these advancements were laid a mere 70 years ago by researchers<sup>28</sup> such as Alan Turing, who formalized theoretical computer sciences as a discipline<sup>29</sup>. Gordon Moore's 1965 observation, which accurately predicted the exponential growth in computing power<sup>30</sup>, marked the evolution from Z3, the first programmable floating-point machine by Konrad Zuse<sup>31</sup>, to *Frontier*, today's most powerful supercomputer. In parallel, the term 'Artificial Intelligence (AI)' was proposed by John McCarthy at Dartmouth in 1956; the first AAAI was held at Stanford in 1980, and AI experienced its boom in that decade. In 1997, IBM's Deep Blue beat Garry Kasparov at chess<sup>32</sup>, and today, Large Language Models (LLMs) are conquering multiple domains of society<sup>33</sup>. Against this backdrop, it was not long until the society and scientific community started to benefit<sup>34</sup>. Material sciences soon integrated its ideas into this digital transformation<sup>35</sup>.

In 1970, Joseph J. Hanak<sup>36</sup> contributed significantly to the field of materials research by introducing 'multiple-sample concepts' with high-throughput techniques for processing and testing new low-temperature superconductors that created gradient libraries of multiple compositional properties while being limited by the computational possibilities of his time. His work on combinatorial principles was progressively acknowledged in the 1990s when it was applied in biochemistry and pharmaceutical studies at UC Berkley<sup>37</sup>. Combinatorial Materials Sciences (CMS) was officially started in 1995 by Xiang et al. with their effort to unravel the physiochemical properties of solid-state materials<sup>38</sup>. From 1997, industrial interests from companies such as Symyx Technologies could publish a material library for 25000 inorganic compounds, establishing the state-of-the-art for HTE at the time<sup>39</sup>. Despite skepticism, Xiang and Takeuchi<sup>1</sup> were able to capture the importance of advances in tools and experimental techniques, reflecting them into the systematic execution of multiple experiments and codified CMS in 2003; together with HTE, the creation of extensive material libraries was rapidly increasing and added scientific value by inferring knowledge<sup>40</sup> from the correlations between composition, structure, and properties in reduced time<sup>1</sup>.

### 1.2.1. Beyond Linear Exploration

As outlined by Maier et al.<sup>26</sup> in 2007, there was a need for software and computational tools for the analysis of large datasets and pattern identification<sup>41</sup>. The development of highly parallelized computational architectures in hardware<sup>42</sup>, such as Central Processing Units (CPUs) and Graphics Processing Units (GPUs), has accelerated the efficiency of training algorithms including Artificial Neural Networks (ANNs) and genetic algorithms (GAs)<sup>26</sup> and enabled more complex statistical modeling capable of learning intricate patterns in data<sup>43, 42</sup>. The convergence of advancement in computer science, alongside AI technologies<sup>44, 45</sup>, has unlocked new potential in material discovery<sup>24, 46, 47</sup> bringing the discipline on the verge of the next Kuhnian paradigm shift<sup>22</sup>. Now, the pursuit of material knowledge is no longer linear but multidimensional, driven by data<sup>48</sup>, computation, and an innovative spirit that seeks to redefine the possible<sup>45, 49</sup>.

### 1.2.2. Chemoemtric Era of Inverse Design

The physical properties of a wide range of synthesized materials are still to be explored, despite the greater availability of a library of materials derived from HTE<sup>50</sup>. Obstacles in the path between serendipitous and intentional discovery limit their potential to uncover materials in a plausible chemical neighborhood that can be derived from a minimal configurational change<sup>51, 52</sup>; in a conventional direct approach, the three dimensions of atomic fingerprint, composition, and structure (ACS) are taken as input for the exploration of material properties  $P(ACS)$ , which are not pursued a priori. An approach to material design where the targeted properties of a given ACS are the goal and not the outcome is what characterizes the inverse design philosophy<sup>53</sup> (Figure 1.1). Early approaches to inverse design were mathematical; for instance, the inversion of the Schrödinger equation to find the potential energy for desired eigenvalues has been a long-standing topic in the literature<sup>54</sup>. Analytic solutions provided by inversions of equations might prove impractical due to mathematical constraints, the inherent complexity of material systems, and the necessity for scalable solutions<sup>55</sup>. Modern applications of inverse design rely on data-driven techniques to offer a feasible alternative<sup>48</sup>. Herein, this 'form follows function' conceptualization manipulates datasets from deliberate discovery to uncover relationships between

properties, functionalities, and molecular structures<sup>53</sup>. Ideally, a tool for inverse physicochemical design would be both efficient in sampling the chemical space and optimizing property gradients to output accessible compounds<sup>40, 52</sup>. This can be achieved by capturing the probability distribution of nonlinear correlated properties and structures, a task where deep generative models are particularly adept. Through the use of complex sampling, generative models can create latent representations of a chemical space<sup>56</sup>. This allows optimizers to efficiently map inputs to targets, utilizing backpropagation to navigate local min-max traps and rapidly calculate gradient information relative to design variables<sup>50</sup>. The outcome is enhanced exploration and guided optimization<sup>5</sup>, efficient at handling multi-objective design and complexities from high-dimensionality of microstructure space<sup>57</sup>. Common generative models applied for inverse design in material science are variational autoencoder (VAE)<sup>40</sup>, Generative Adversarial Networks (GANs)<sup>58</sup>, reinforcement learning (RL)<sup>59, 60</sup>, and Recurrent Neural Network (RNN)<sup>61</sup> in applications such as the prediction of crystal structures for inorganic materials or the molecular representation of redox flow batteries<sup>48</sup>. Inverse design has shown promise in overcoming major roadblocks in laboratory experimentation by exploring unknown and counterintuitive compounds often required for technological applications<sup>56</sup>.

### 1.2.3. Material Genome Initiative & Beyond

From 1990, data-intensive scientific endeavors, in combination with computing power and experimental data, unlocked genetic mysteries with The Human Genome Project (HGP)<sup>62</sup>, which was completed in 2003<sup>63</sup> with the sequencing and mapping of the entire base pairs of human DNA<sup>64</sup>. Its modalities inspired material scientists to apply similar principles to their research through the integration of data sharing, HTE, and modeling<sup>65</sup>. Ceder initiated the Materials Genomics project at MIT<sup>66</sup>, utilizing advanced data mining to seek optimal materials for lithium-based batteries for electric personal mobility. Concurrently, Curtarolo at Duke University developed the Materials Genomics Center to enhance the study of metal alloy research with the introduction of Automatic-FLOW (AFLOW)<sup>67, 68</sup>, an automated system capable of predicting new crystal structures. A crucial milestone for modern material science was reached in 2011 with the launch of the Material Genome Initiative (MGI)<sup>69</sup>. President Barack Obama set the goal to double the speed and lower the cost in

the discovery, development, and deployment of advanced materials, cementing the intentions of the United States<sup>70</sup> with hundreds of millions of dollars in funding and with the words "We can do it faster"<sup>71</sup>. Since then, The Materials Projects<sup>66</sup> as the core data repository of MGI, as well as other databases such as Open Quantum Materials Database (OQMD)<sup>72</sup>, are being utilized as interactive multichannel exploration tools for data-driven approaches and data-informed prototyping<sup>42</sup>.

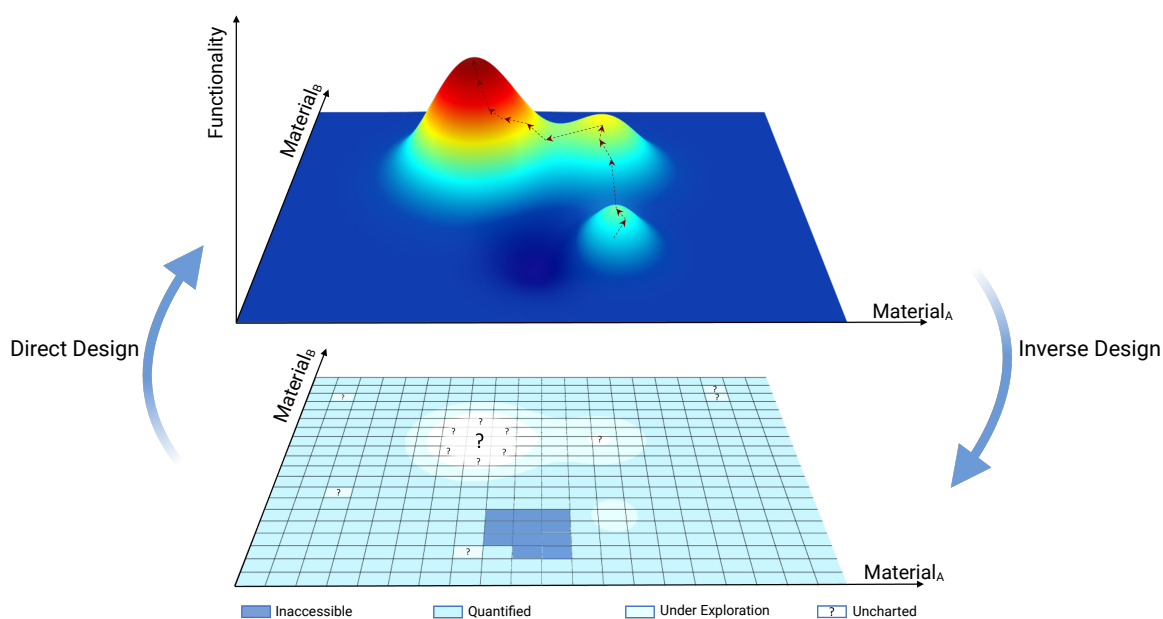


**Figure 1.1.:** Comparative overview of material design strategies, namely direct and inverse approaches. In the direct approach, experiments include the entire range of possible combinations of materials A and B through HTE or manual experimentation. This process segregates regions based on a prior search into physically infeasible areas (inaccessible) and previously explored (quantified) regions, while also identifying unmeasured (under exploration) and unknown (uncharted) ones. Here, the combinations of each material with their known ACS, are explored for a potential functionality  $P(ACS)$ . In contrast, the inverse strategy reverses the sequence by estimating the target functionality,  $P(ACS)$ , and guides the search toward optimal ACS combinations in fewer steps. This approach is illustrated in a contour plot, where the estimated functionality is derived from the quantified ACS data from the lower grid space, and the measurements are directed to compounds with predicted maximized functionality<sup>53</sup>. Such a strategy enables a more efficient, targeted exploration and can accelerate the discovery of novel materials.

### 1.2.4. Closing the Experimental Loop

The success of projects such as MGI has validated the proposition of faster materials discovery<sup>23</sup>. CMS<sup>1</sup>, high-throughput characterization<sup>73, 74</sup>, and robust inverse design<sup>53, 40</sup> are all integral components of a "closed-loop" setup capable of maximizing the potential of data resources and exploiting their intrinsic prior knowledge<sup>75, 76</sup>. An ideal closed-loop design involves an iterative process that integrates a continuous feedback mechanism, connecting several stages from material conception to experimental execution, testing and characterization<sup>77</sup>, which allows identifying the most promising material designs, reducing experimental trials and the time gaps between each step in the discovery chain<sup>50, 44</sup>. The development of AI technology has enabled closed-loop systems to acquire self-optimization capabilities, incorporating informed decision-making and automated feedback<sup>75, 78</sup>. In this context, Active Learning (AL) algorithms guided high-throughput experimental workflows through heuristic exploration and exploitation within the search space<sup>9</sup>. These algorithms enabled predictions of figure-of-merit (FOM) based on an in-depth analysis and data extraction, benchmarking experimental learning-based approaches<sup>40</sup>. Nevertheless, the insight creation was limited to sufficient interoperability and data integration. Tools, machines, and control mechanisms were often isolated and did not rely on effective ways of communications<sup>32</sup>. Addressing this challenge, Application Programming Interface (API) emerged as a natural fit, capable of enhancing the interactions between various segments of scientific research processes<sup>79, 46</sup>. For instance, large data projects such as AFLOWLib in 2014 relied on API<sup>80</sup> communication to allow retrieval of datasets through interchangeable and customizable queries that are accessible and human-readable. APIs are now prominent in modern decentralized data handling; their journey from simple command-line tools to the interface of service access architecture, on-premise and cloud, follows the progression of the connectivity protocol for big-data<sup>24</sup>. They ensure coherent communication using the same digital language across various components of an ecosystem. In 2018, the convergence of digitalization efforts and novel experimental designs led to the evolution of closed-loop discovery and its related terminology into MAPs<sup>18</sup>, a strategic rebranding in materials science<sup>46</sup>, with benefits specifically in electrochemical energy storage<sup>10</sup>.

### 1.2.5. Intelligent Acceleration Platforms

MAPs are not merely an extension of the closed-loop systems, but a more sophisticated embodiment of it<sup>18</sup>. Besides all the features of HTEs, MAPs incorporate a higher degree of automation<sup>81</sup>, autonomy<sup>82</sup> and instrumental abstraction to accelerate the discovery and optimization of materials<sup>17, 83</sup>. MAPs elevate HTE<sup>84, 73</sup> with modular robotic platforms<sup>85</sup>, machine learning (ML),<sup>45, 86</sup> and statistical knowledge<sup>87, 88</sup>. Inherent to this functionality are web interfaces and unified data infrastructures, which enhance the interoperability and data collection at all stages from preparation to characterization<sup>83</sup>. This ensures detailed lineage and provenance for data<sup>89</sup> and enables real-time, systematic analysis and modeling across diverse experiments<sup>90</sup> (Figure 1.2). The modular nature of MAPs offers profound insights into physico-chemical parameters<sup>91</sup> in less time compared to drudgerous Edisonian approaches, minimizes human error, and maximizes productivity, promoting device reusability across a multitude of instruments and laboratories<sup>92, 93</sup>.

Autonomous Research System (ARES) in 2016 designed to optimize the synthesis of carbon nanotubes (CNTs), is considered to be the first HTE labeled as MAPs. This autonomous system allowed control over the growth processes of these nanotubes in a six-dimensional parameter space. By leveraging GAs and random forest (RF) for AL, ARES efficiently performed up to 100 experiments daily, surpassing manual methods. After completing 534 experiments, this system achieved its targeted growth rates with minimal expert intervention, highlighting a milestone in automated, learning-based approaches for material synthesis<sup>94</sup>. This was followed by another platform in 2018: Chemputer. It shifted towards automated, machine-driven experimentation and integrated a Chemical Assembly (ChASM), as a unique scripting language, to a robotic system to automate organic material synthesis, enhancing safety and reproducibility of chemical processes<sup>95</sup>.



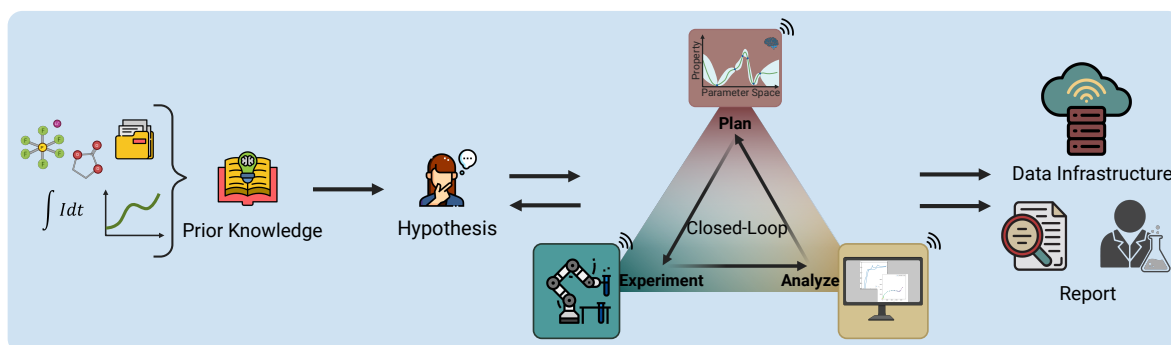


**Figure 1.2.:** Schematic representation of MAPs. The process begins by collecting prior knowledge, such as empirical data, literature reviews, and statistical analyses of previous experiments. This information is then used by the scientist to formulate a hypothesis for a research question. Following this step, the MAPs carry out an iterative high-throughput experiment using a closed-loop feedback mechanism that integrates the robotic experimentation platform, real-time analysis, and AI/ML-driven algorithms to optimize experimental parameters and plan the subsequent run. This iterative process is orchestrated by web interfaces that communicate between devices and servers at every stage to accelerate data transfer. Every phase, from setup and preparation to characterization, is stored in a unified data repository and is documented in reports that adhere to Findable, Accessible, Interoperable, and Reusable (FAIR) data principles.

### 1.2.6. The spawning of MAPs

In 2018, the development of AL algorithms for multi-objective optimization challenges in MAPs was evidenced by the introduction of frameworks such as Chimera<sup>96</sup> and Phoenix<sup>97</sup> that utilized Bayesian Optimization (BO) with minimal requisite of prior knowledge. Phoenix, distinctively, leveraged kernel density estimation to efficiently identify the global optimal condition<sup>98</sup>, beneficial in resource-limited environments. Additionally, it significantly enhanced uncertainty estimation capability through a practical exploration and exploitation<sup>9</sup> of decision spaces. Subsequently, beginning in 2019, a growth in MAPs development has been observed that resulted in an escalating number of related initiatives worldwide. This growth began with ChemOS<sup>99, 100</sup>, which exhibited advanced infrastructure software with its modular design-enabled orchestrating and scheduling of experimental procedures through a central workflow manager. This allowed for coeval feedback from past experiments into future planning and was supported by its flexible data storage and transfer capabilities<sup>101</sup>. ChemOS<sup>102, 100</sup>, primarily utilized Phoenix<sup>98</sup> and later incorporated Chimera<sup>96</sup> and Gryffin<sup>103</sup> for user-specific parameter prioritization and incorporation of categorical descriptors, alongside with Golem<sup>104</sup> and Gemini<sup>105</sup> respectively for



handling input uncertainties<sup>106</sup> and enhancing multifidelity to reduce biases. Its integration with a chatbot, utilizing Natural Languages Processing (NLP), provided an intuitive user-centric interface. The hardware-agnostic nature of the platform further enabled easy extension and broad applications, supporting cross-disciplinary research fields and remote control<sup>102</sup>. These features exemplified the characteristics of the Experiment-as-a-Service (EaaS) model<sup>107, 108</sup> and in 2020, the platforms Ada<sup>109</sup> and Langner<sup>110</sup> adapted ChemOS into their operations. Ada, designed to optimize thin film materials, demonstrated significant acceleration by completing 35-sample experimental campaigns in less than 30 hours<sup>109</sup>. The Langner platform, on the other hand, was applied in the organic photovoltaics, effectively fabricating up to 6048 films per day. Its use of Phoenix for multidimensional space exploration allowed for identifying competitive photostable blends in just 15 iterations<sup>110</sup>.

The open-source, AI-integrated software package Experiment Specification, Capture and Laboratory Automation Technology (ESCALATE)<sup>111</sup>, simplified and abstracted data pipelining for MAPs initiatives. This ontological platform streamlined data management from collection to experiment creation and was suitable for ML applications<sup>88</sup>. In 2020, the user-friendly Robot-Accelerated Perovskite Investigation and Discovery (RAPID) platform<sup>112</sup>, in conjunction with ESCALATE, further accelerated discovery in the perovskite field, achieving over a 5-fold increase in research efficiency. Materials Acceleration Operation System (MAOS)<sup>91</sup> initiated a new perspective on user-centric approach<sup>19</sup> in MAPs, integrating virtual reality (VR) with collaborative robots for autonomous material synthesis and quality assurance through a RL schema. Here, the training involved VR-based remote laboratory simulation by administrators, translating recorded operations into real-world robotic commands. Post-training, MAOS employed cloud-based data storage and an AI-planner to autonomously analyze and optimize high-throughput data<sup>90</sup>.

### 1.2.7. From Optimization to Discovery

The progressive integration of the BO algorithm within MAPs<sup>113</sup> significantly catalyzed discovery rates from 2020<sup>57, 114</sup> onwards. Bayesian experimental autonomous researcher (BEAR)<sup>115</sup> exemplified this with its high multifidelity capability in au-

onomously optimizing the geometric parameters to enhance material toughness in additive components. This workflow reduced experimental trials by 60-fold and enabled benchmarking in only 12 hours. This was a substantial improvement over the month-long duration typically required by traditional grid-search methods. Concurrently, closed-loop, autonomous system for materials exploration and optimization (CAMEO)<sup>116</sup> integrated phase map blueprints as prior data for real-time AI-driven guidance for exploitation of composition-structure relationships. The platform discovered novel compositions with competitive physical properties, achieving a 10-fold iteration reduction with only 19 experiments. Using a batched Bayesian algorithm, the Mobile Robotics Chemist<sup>117</sup> identified novel photocatalysts six times more active than existing formulations by conducting 688 experiments in eight days. This demonstrated a 1000-fold and 10-fold acceleration compared to manual and semi-automated workflows. These developments, among others, continued to enhance the evolution of MAPs, further accelerating material discoveries in numerous domains<sup>108, 118, 119, 120</sup>.

### 1.3. Holistic Strategies for Multilayered Batteries

Digitalization efforts in battery material research, particularly for Lithium-ion batteries (LiBs), are progressing towards more innovative and more sustainable manufacturing<sup>121, 10</sup>. This progression is characterized by enhanced automation and interconnectivity in the production chain, aiming for seamless integration from raw materials to fully assembled battery cells<sup>122</sup>. In this development, building a digital workflow for rechargeable systems with high energy and power density, particularly within MAPs, involves an intertwined array of challenges<sup>123, 124</sup>. The advances, which were slightly impeded relative to other materials' discovery efforts, need to extend across the material composition, interfaces, and systems<sup>125, 126</sup>. Addressing the multifaceted nature of batteries requires a multimodal approach in HTE settings<sup>127</sup>. This approach is essential to achieve Pareto-optimal cell chemistry, a demanding task<sup>128, 129</sup>, involving a systematic balance of multiple performance attributes which include electrochemical stability, safety considerations, and scalability<sup>20</sup>. As such, these complexities make the research and manufacturing processes arduous, yet essential for practical evaluation of the overall performance<sup>130</sup>. The difficulties, intensified by the diverse

material properties and environmental factors<sup>10</sup>, set the goal to not only develop high-performance batteries but also to ensure that solutions are sustainable<sup>121, 131</sup> and socially unobjectionable<sup>129, 132</sup>.

### 1.3.1. The path of MAPs for Materials Screening

Progress in energy storage solutions (ESS), particularly in HTE for battery material screening, experienced a notable growth<sup>13, 131</sup>, starting from late 2014. A notable contribution was the introduction of a hierarchical computation method that, to a significant extent, evaluated the stability of various electrolyte properties, including redox potential and structural characteristics<sup>133</sup>. This was a precursor to the Electrolyte Genome Project<sup>134</sup> in 2015, an open-source initiative that utilized big data and computational techniques to deepen the physicochemical understanding of battery electrolytes on a multiscale level. By 2016, the project had significantly contributed to techno-economic model development for redox flow battery electrolytes while pursuing cost minimization of material design<sup>135</sup>. Despite progression in these computational platforms for optimizing battery materials, the complexities intrinsic to experimental workflows have carried over into a selected number of initiatives within MAPs<sup>136</sup>. Beginning in 2019, an automated test-stand<sup>137</sup> was introduced to rapidly optimize binary search spaces for aqueous electrolyte solutions, utilizing real-time high-throughput data acquisition and a ML-assisted algorithms. This system discovered novel electrolytes by completing hundreds of tests in less than a day. It achieved high precision, registering a deviation of 0.5 mS/cm in conductivity measurements and a minimal 0.02 V shift in stability windows. Follow-up studies by Dave et al.<sup>138</sup> enhanced this server-based robotic platform with Dragonfly<sup>139</sup>, a BO-guided algorithm, with four acquisition functions, starting from a five-sample random strategy. The system could test and analyze 140 mixed-anion sodium electrolyte formulations in under 40 hours and identify compounds with superior electrochemical stability. This platform was further expanded to Clio<sup>140</sup>, which was tailored for evaluating non-aqueous electrolytes in LiBs. Clio showcased increased efficiency, achieving six-fold acceleration in its testing process. Within two days, it examined 42 distinct formulations for optimization of three solvents and a single Li-ion salt, which led to the discovery of six benchmarks for fast-charging electrolytes.

In recent years, the high-throughput approaches in combinatorial synthesis and characterization were further advanced by miniaturization<sup>92</sup>, significantly reducing material usage and enabling rapid assembly in electrochemical experimentation. An example is given by the Scanning Droplet Cell (SDC), a tool<sup>140</sup> initially applied in electrocatalysis<sup>141, 142, 143</sup> that has been expanded to battery-oriented studies<sup>144, 16</sup>. A roadblock that requires sophisticated engineering and design persists in maintaining consistent droplet formation and ensuring compatibility with commonly used carbonate and fluorinated salt formulations<sup>145</sup> in non-aqueous batteries<sup>146, 144</sup>. By leveraging technologies such as 3D printing, this downsampling approach can replace the need for full-scale instruments, thus lowering expenses and mitigating material scarcity<sup>147</sup>.

### 1.3.2. The Iceberg Illusion of Interfaces

In battery interfaces, the impact of electrolytes extends from charge transfer to the formation of interphases such as SEI and CEI<sup>125, 148</sup>, which are critical factors in defining quality, reliability, and life (QRL) of batteries<sup>149, 150</sup>. A comprehensive understanding of their underlying mechanisms necessitates advanced analytical methods<sup>20</sup>. Algorithms such as GANs<sup>151</sup> in 2014 catered to this requirement and enhanced the capabilities of generative models<sup>152</sup> and strengthened their reliability and interpretability by integrating uncertainty estimation<sup>153, 154</sup>. The *in silico* progression has been instrumental in generating electrochemically stable interfaces<sup>155, 55</sup> by combining physical insights with computation models<sup>5</sup> and unraveling their complexities through advanced image analysis<sup>156</sup> and spectroscopic techniques<sup>50</sup>. However, the fidelity of insight gained from Deep Learning (DL) is contingent on the availability of extensive datasets, which introduced its challenges in battery interface research<sup>157</sup>. At the experimental level, evaluating these interfaces encounters further hurdles, augmented by diverse experimental conditions and the necessity for multiple measurement devices<sup>10</sup>. Such evaluation requires exhaustive preparation, stringent safety guidelines, and comprehensive electrochemical analysis such as Electrochemical Impedance Spectroscopy (EIS)<sup>149</sup>. The impact of these interfaces is not limited to the initial battery cycles; additionally, it extends throughout the entire lifespan, directly correlating with their aging process and impacting their State of Health (SoH)<sup>14</sup>. This intricate dynamic represents a "Grand Challenge", as outlined by Bhowmik<sup>5</sup>. Despite

considerable efforts<sup>125, 158, 159</sup>, a gap remains in developing MAPs that cohesively connect interfaces to the broader battery systems<sup>157, 160</sup>. Such platforms, which integrate extensive databases, operando characterization, and multimodal approaches, are essential in advancing this area of research<sup>5, 129</sup>.

### 1.3.3. Temporal Narratives in System Analytics

In battery testing at the system level, the prolonged evaluation cycles add a temporal dimension<sup>161</sup> that intensifies the challenges for accurate health prognostics inferred by battery management systems (BMS)<sup>162</sup>. Although there have been advances in the integration of data-driven modeling with closed-loop optimization<sup>163</sup>, progress towards complete autonomy in MAPs remains gradual<sup>10</sup>, mainly due to the nonlinear relationship between battery capacity and both cyclic and calendar aging profiles<sup>162</sup>. Thus, there is a necessity to engineer a unified methodology to formulate accurate prediction and timely measure and analyze degradation behavior, ensuring long-term, unmanned operations<sup>164, 165</sup>. The data-centric approach of the study by Severson et al.<sup>14</sup> in 2019 utilized a feature-based model, i.e., elastic net, from data of the first 100 cycles of 124 commercial LiBs cells, to accurately predict their lifetime trajectory. Additionally, by implementing regularized logistic regression, they were able to classify cell longevity based on discharge measurements from only the initial five cycles. This work was carried onto a closed-loop optimization (CLO) workflow<sup>163</sup> in 2020, where it was combined with a BO-guided approach to identify optimal fast-charging protocols from 224 candidates. Compared to traditional procedures with random protocol selection as a baseline, the test time of this system was decreased from 7700 to only 500 battery-hours during an experimental time of 16 days, resulting in a substantial reduction in resources needed<sup>163</sup>.

Reliability of advancement in statistical forecasting, coupled with the role of uncertainty quantification<sup>166</sup>, has become indispensable<sup>167</sup>. A prime example was the development of an autoregressive ensemble RNN designed for predicting battery degradation trajectories considering both aleatoric and epistemic uncertainties<sup>168</sup>. The model utilized a comprehensive set of six features per training cycle and implemented saliency analysis, which formalized the importance of input features upon measurement and their impact on output prediction<sup>168</sup>. Among data-driven

strategies, DL pipelines have increasingly been recognized<sup>169</sup> for their capability in uncovering insights directly from raw data<sup>170, 171</sup> and eliminating the necessity of feature engineering<sup>162</sup>. For instance, Fan et al.<sup>172</sup> combined Gated Recurrent Units (GRU) with Convolutional Neural Network (CNN) to enhance the fidelity of SoH estimation. This integration enabled the extraction of temporal-spatial dependencies from direct measurement parameters of current, voltage, and temperature.

Despite significant advancements, a fundamental challenge remains when considering the explainability of DL architectural designs<sup>57</sup>. Attention mechanisms<sup>173</sup>, initially developed in NLP applications for enhancing sequence-to-sequence models<sup>174</sup>, are a promising solution<sup>175</sup>. They strengthen the capability of DL models to manage temporal dependencies and complex data patterns, providing human experts with reliable and interpretable analysis<sup>176, 177</sup>. Crucially, the success of generalization across DL models for accurate prediction hinges on the availability of extensive amounts of data<sup>178</sup>. This prerogative prevents overfitting and bias to establish explainable, in-depth research insights for battery design studies<sup>5</sup>. However, the absence of homogenous data<sup>157</sup> is the missing piece that, to date, represents the main obstacle in the development of MAPs for real-time, online monitoring of battery health prognostics<sup>10</sup>.

## 1.4. Digital Movements in Smart MAPs

To implement a modular and versatile MAPs capable of covering all dimensions of batteries, it is essential to address several distinct layers of complexities<sup>179, 180</sup>. At the software level, a predominant facet is developing an API-centric framework adaptable beyond individual instruments and single laboratory needs<sup>102, 46</sup>. This involves addressing the complexities of software dependencies<sup>99</sup> as current robust autonomous workflows are primarily constrained by laboratory middleware, which will become increasingly cumbersome with the broadening scope of experimental platforms. In addition, the incompatibility of commercial softwares<sup>181</sup> with the open-source, version-controlled development restricts adaptability and community engagement, essential for the promotion of automated orchestration<sup>182, 183</sup>.

The path to digitalization in modular automation design for battery platforms can be furthered through a versatile analysis server. Its fidelity can be demonstrated in a range of complex analysis capabilities<sup>88</sup>, from electrochemical tests to advanced imaging and characterization methods<sup>184</sup>, while adaptability is manifested in the capacity of processing various file formats<sup>89</sup>. The server's ability to generate comprehensive reports and provide advanced visualization further enhances the dynamic modularity within the system<sup>185</sup>. Another milestone is the deployment of a robust Data Management System (DMS) for cataloging the extensive data generated by laboratory automation and understanding its flow across various projects<sup>186</sup>. Adherence to FAIR<sup>187</sup> principles in data lineage is crucial to ensure traceability from data acquisition, processing, and associated metadata, essential to accurate data interpretation at any level<sup>89</sup>. In conjunction with an advanced data analysis server, this architecture will enable frictionless real-time integration between experimental data and modelling<sup>188</sup>. Herein, leveraging AI-driven algorithms hinges on augmenting system transparency and trust through enhanced explainability<sup>102</sup>, which will enable models to achieve a level of proficiency in data interpretation comparable to that of expert analysis<sup>189</sup>. Expanding upon this premise, DL models for non-convex optimization in high-dimensional parameter spaces amplify the explainability through multi-task learning approaches<sup>162</sup>. This collective learning philosophy enables the exploitation of complex property correlations and accounts for experimental uncertainty, resulting in more informed decision-making<sup>190</sup>. Addressing these complexities in MAPs will enhance the system's reliability, reproducibility, and autonomy through insightful knowledge extraction<sup>78, 191</sup> and remains a point of contention in this field of study<sup>15</sup>.

## 1.5. Europe's Solution to Energy Storage

In order to solve the current disjunctions in global battery research, Europe, with its Battery 2030+<sup>192</sup> initiative, is gaining strategic autonomy by reliably accelerating the pace of discovery in joining their domains<sup>20</sup>. Acceleration is being achieved with the development of applications as part of the broader efforts to integrate experimental and computational research through advanced data analytics and ML algorithms, autonomous robotics with standardization and ontology-guided data management at its core<sup>129</sup>.



Battery 2030+ made the development of tools and methods for understanding the spatiotemporal evolution of interfaces and interphases in batteries across multiple chemistries possible with the European Materials Modelling Ontology (EMMO)<sup>193</sup>. It was developed under the auspices of the European Materials Modelling Council (EMMC)<sup>194</sup> as an ontology designed to facilitate interdisciplinary communication, and it has become a key enabler of the Battery 2030+ project, functioning as its designated knowledge space<sup>195, 186</sup>. The creation of this unified language benefitted a variety of projects in this initiative and contributed considerably to lowering its Technology Readiness Level (TRL)<sup>15</sup> allowing endeavors such as Battery Interface Genome – Materials Acceleration Platform (BIG-MAP)<sup>196</sup> and Battery interface ontology (BattINFO)<sup>197, 198</sup> to achieve scientific maturity with clarity in development stages, effective risk management and fluid exchange between involved parties<sup>136</sup>.

### 1.5.1. Blueprinting the Energy MAP

Initiatives such as BIG-MAP have successfully addressed the subsequent layer of complexity by incorporating efficacious AI techniques that necessitate the integration and implementation of extensive datasets and data management plans (DMPs)<sup>191, 195</sup>. To that end, interface calculation data is stored and shared to combat the current scarcity in the battery research community. Partners involved in the BIG-MAP project collaborated to interlink experimental and predictive data<sup>200, 191</sup> within the unified ontological infrastructure<sup>198</sup> (Figure 1.3), with explainability as one of the main features.

BIG-MAP is a game-changing project consistent with the FAIR data principles<sup>187</sup> developed by a network of European experts and research institutions and represents the largest collaborative platform of its kind. It includes remarkable tools for data integration and management, analysis, laboratory notebooks, simulations, and predictive modeling; examples<sup>199</sup> include Aurora, a platform for automated robotics developed on the AiiDA<sup>201</sup> python platform, PRISMA<sup>202</sup>, a robust application for high throughput spectrum analysis, and an app to model SEI formation with AL<sup>203</sup>. To date, a total of 30 apps are supported on the BIG-MAP registry<sup>199</sup>. The initiative's manifesto delineates a holistic, closed-loop strategy, ensuring a comprehensive



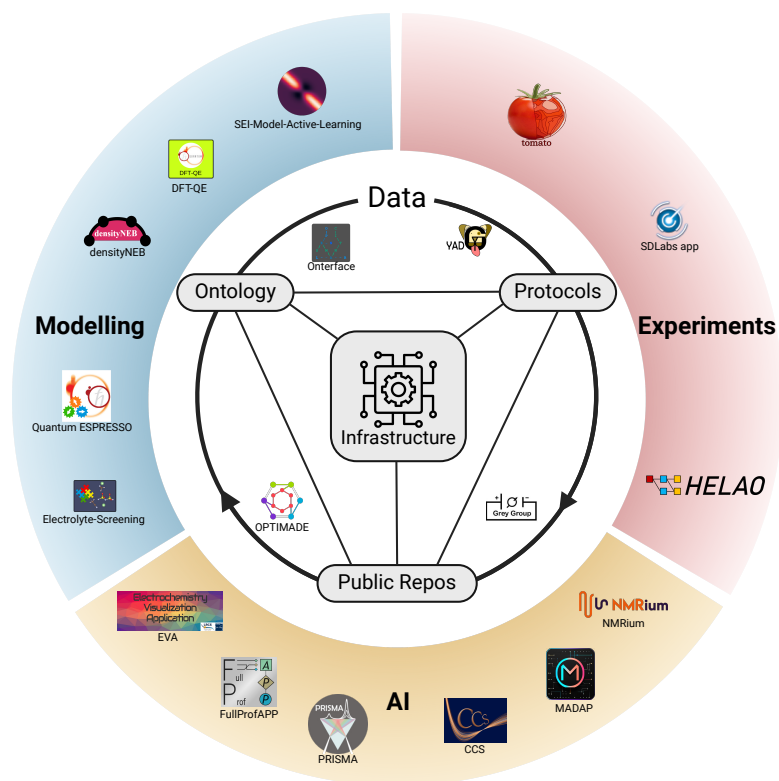


**Figure 1.3.:** An overview of the data and information flow across various domains in the BIG-MAP project<sup>196</sup>. It showcases the integration of experimental workflows, computational tools, and data-driven strategies within a unified and shared data infrastructure. Herein, standardized protocols and ontologies, together with public repositories, ensure data exchange and interoperability across theoretical, experimental, and AI-driven domains. The commitment to FAIR principles<sup>187</sup> is further reinforced by the open-source publication of data in the cloud and the collection of tools and developed software within the BIG-MAP registry<sup>199</sup> to allow for efficient collaboration among project partners. Applications such as SD-Labs, HELAO, and tomato for experimental design and laboratory automation are curated, along with computational resources such as the SEI Modeler and Quantum Espresso. Other applications, including PRISMA and EVA, are designed for spectral characterization and electrochemical analysis. The BIG-MAP project is a collaborative platform that aims to unravel the complexities of batteries from materials development to end-use applications to ultimately accelerate and advance the frontiers of energy storage technology.

understanding of the complete battery value chain, from basic materials to end-use applications, emphasizing the crucial role of interfaces for enhanced performance and longevity with the consideration of commercialization challenges<sup>15</sup>. The project aligns with European sustainability goals and is positioning our continent at the forefront of energy storage technology and contributing to the global transition towards a cleaner energy future.

Looking ahead, the scientific roadmap for future battery design and material discovery must involve accelerating existing and future platforms, refining, cataloging, and sharing interface mapping and enhancing smart functionalities of sensing and self-healing. The research attention should additionally be focused on addressing critical non-chemical aspects such as reproducibility in manufacturing and recyclability<sup>10</sup> for ecological footprint. The race against data scarcity and time, therefore, is evident, especially considering that talent and knowledge transfer between domains is not instantaneous. However, by virtue of Battery 2030+ and other initiatives worldwide, the transfer is already in motion.

## 1.6. Perspectives on a Singularity

In recent years, the democratization and cost reduction in robotics<sup>214</sup>, coupled with the spread of programming skills in scientific fields, reduced computing costs, and the accessible implementation of ML frameworks, have significantly impacted the materials science communities. This is evident in the development of widespread MAPs, or as they are recently known, SDLs<sup>102, 209</sup>. With the application of AI, automation, and the increase in computational power, SDLs are set to accelerate scientific discovery<sup>189, 190</sup>. Notable recent progress includes A-Lab, built on Google's DeepMind, which conducted closed-loop experimentation with AL for 17 days, achieving a 71% success rate<sup>211</sup>. Additionally, BayBE, an engine developed by the Merck Group in collaboration with the University of Toronto, enhances experimental design and optimizes industrial applications. Recently released as open source, BayBE demonstrates the transition from theoretical frameworks to practical, autonomous experimentation<sup>212, 213</sup>. Industrial interest confirms that knowledge-driven experimentation with mere autonomy is no longer the goal, and global collaboration will become the standard going forward<sup>179</sup>. Generative AI<sup>215</sup> and LLMs<sup>33, 216</sup> represent a further step in self-optimization, enabling unsupervised decision-making processes in future SDLs iterations<sup>49</sup>. This increasing autonomy promises significant advances in new-material synthesis for sustainability, carbon neutrality, and especially the development of safe, scalable, earth-abundant materials for batteries. However, it raises important questions about governance, security, and broader societal impacts<sup>217</sup>. All

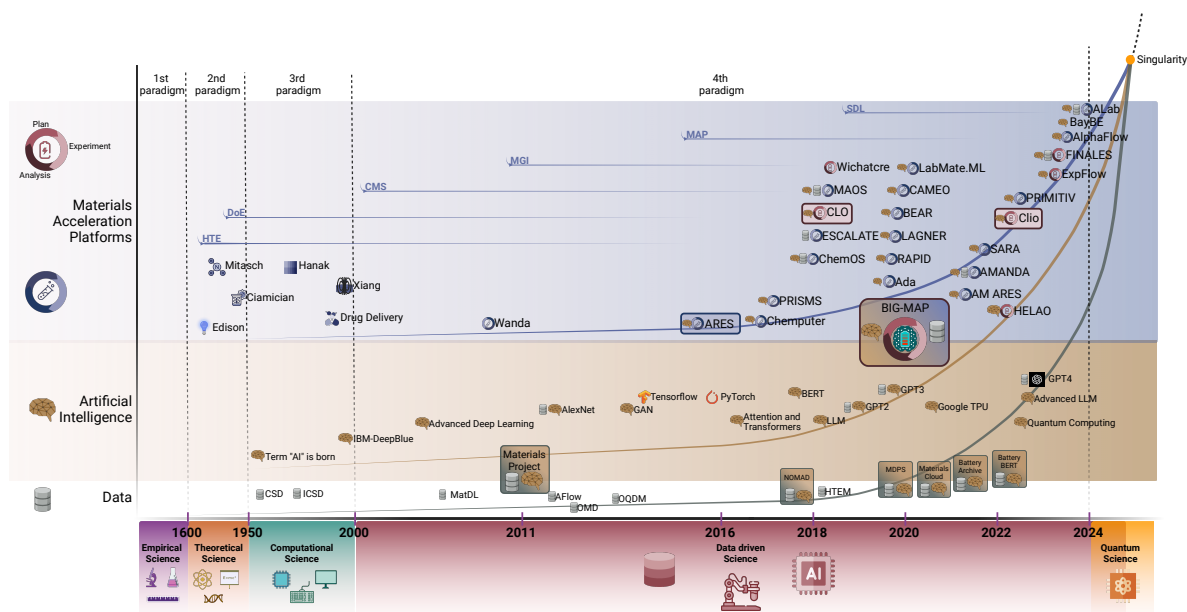


**Figure 1.4.:** Tracing the trajectory of chronological scientific innovation, this figure encapsulates the evolution of data repositories, AI technology, and MAPs through four paradigm shifts, including empirical, theoretical, computational, and data-driven science<sup>24</sup>. It illustrates the progression from Edison’s methodical materials experiments in 1870s, which established the basis for HTE<sup>25</sup>, to the introduction of systematic DoE approaches in the early 20th century<sup>26</sup>. Initial databases such as the Cambridge Structural Database (CSD)<sup>204</sup> and the Inorganic Crystal Structure Database (ICSD)<sup>205</sup> laid the groundwork for the integration of materials science into the digital age after the emergence of the term AI in 1956<sup>32</sup>. Advancements in CMS<sup>1</sup> were initiated by Hanak’s gradient libraries in the 1970<sup>36</sup> and Xiang’s optimization of solid-state material in 1995<sup>38</sup>. These, among other efforts, resulted in MGI, which aimed to reduce development time and cost<sup>69, 71</sup> of experimentation. The Materials Project<sup>66</sup> and OQMD<sup>72</sup> were among the core outcomes of this initiative. The evolution of additional repositories, such as AFLOW<sup>67, 68</sup> along with technological advances, led to the coining of the term MAPs in 2018<sup>18</sup>. Among these platforms, ARES stands out as one of the inaugural MAPs<sup>94</sup>. Others, such as ChemOS<sup>102, 100</sup> and ESCALATE<sup>111</sup>, contribute to orchestration and data management. In parallel, the AI leaps forward with advanced models such as GANs and libraries like TensorFlow and PyTorch<sup>24, 27</sup>. This further accelerates the development of repositories such as Novel Materials Discovery (NOMAD)<sup>206, 207</sup>, and Material’s Cloud<sup>186</sup>. All these progressions led to the growth of MAPs, including RAPID<sup>112</sup>, Ada<sup>109</sup>, and Autonomous Materials and Device Application Platform (AMANDA)<sup>108</sup>, among others. In the battery-related studies, the figure highlights platforms such as CLO<sup>163</sup>, Clio<sup>140</sup>, and ExpFlow<sup>208</sup>. In this research domain, the BIG-MAP<sup>196, 10</sup> project is the largest European collaborative platform that aims to advance material studies for the next generation of batteries. These endeavors are presented as introductions to the present era, where the term MAPs has evolved into Self-Driving Laboratories (SDLs)<sup>102, 209</sup>. Recent advancements in AI such as AlphaFlow<sup>210</sup>, A-Lab<sup>211</sup>, and Bayesian Back End (BayBE)<sup>212, 213</sup> represent an additional step towards a potential scientific singularity, an event where AI-enabled materials discovery may exceed human capabilities and trigger a transformative shift of explorative power.

markers point to an upcoming paradigm shift in scientific discovery, and soon, the community will have to face a "Materials Singularity" (Figure 1.4), a moment where the rapid integration of AI and SDLs will potentially lead to breakthroughs at a speed and complexity beyond human capability.



*“The goal is to turn data into information,  
and information into insight.”*

— Carly Fiorina

## 2. Aim and Objectives

This thesis addresses the challenges of designing a modular automation platform for battery research. It seeks to answer the question: "Can the integration of AI technology and informatics tools accelerate insights in battery-related studies?" To answer the query, this thesis explores the potential of an orchestration system for distributed research instruments. It examines various building blocks for conducting experiments and integrating data from diverse sources to transform raw inputs into valuable insights. Thus, the aim is to engineer reliable tools and a platform to accelerate advancements in battery informatics.

The primary objective of this project is to design a SDC for non-aqueous systems, emblematic of the behavior of a half-cell at a millimeter scale and capable of on-demand electrolyte formulation<sup>146</sup>. Following the development of hardware components, the secondary objective is to plan and implement a Python-based software interface for laboratory instruments to maximize device reusability through a modular web framework and to establish an architecture that enhances the scalability and robustness of device operations (Sec. 4.1).

An additional essential element is the development of a modular Python package for comprehensive data analysis tailored to various electrochemical tests. The program supports a diverse range of files and data formats, incorporates FAIR principles, and enables effective data lineage tracking and visualization. Its architecture underlines extendibility for additional functionalities and ensures compatibility for both standalone use and integration within various software environments (Sec. 4.2). The design and development of a relational data infrastructure is another fundamental component to ensure the integrity and accessibility of research data<sup>191</sup>. Therefore, a locally hosted PostgreSQL is engineered for efficient data storage and management, from user details to metadata and instrument outputs (Sec. 4.5).

Various AI tools tailored for specific insights are developed at different stages during

this project. This includes the design of an ML pipeline to demonstrate the utility of one-shot AL in data-scarce scenarios, utilizing a polynomial regression model with uncertainty estimation. It showcases the prediction of conductivity optima at various temperature ranges for non-aqueous electrolyte formulations (Sec. 4.3). Beyond the scope of this thesis, another objective is to implement and develop a DL pipeline and a modular Python package for multitask learning, targeting forecasts of battery lifetime and degradation parameters. Integration of uncertainty quantification and attention mechanisms enhances the design's reliability and interpretability and demonstrates generalization across battery types and testing protocols (Sec. 4.4).

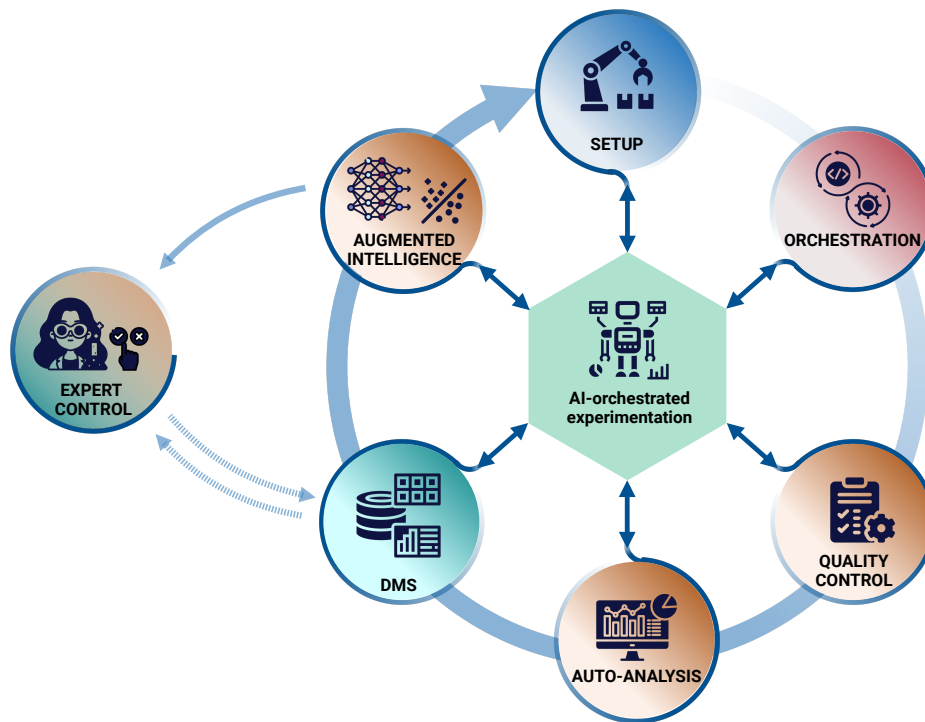


**Figure 2.1.:** Design of enablers and tools for a reliable materials acceleration platform for battery-related studies engineered for the fulfillment of this thesis' objectives and achieved through the integration of various building blocks. These include the development of hardware components for the experimental setup (SDC), the design of an asynchronous Python-based web interface for orchestrating sequential or parallel experiments for orchestration (HELAO), the implementation of a real-time quality control mechanism, the development of a data analysis package (MADAP), the design of a FAIR-based data management system, a user-friendly interface, and two AI-based frameworks. In particular, an ML pipeline for active learning applications and a DL pipeline for predicting high-dimensional scenarios such as battery lifetime (ARCANA). Together, these tools contribute to an advanced intelligent acceleration platform (Auto-MISCHBARES).

The next milestone focuses on developing an asynchronous server-based orchestration framework to automate experiment scheduling and execution, enabling both sequential and parallel experimentation through a user-defined experiment list sketched via a web interface (Sec. 4.1). Additionally, the project includes designing a real-time quality control system to proactively identify and address potential failures and ensure experimental reliability (Sec. 4.5). The final objective is to further utilize ML tools, particularly AL, to conceptualize an intelligent acceleration platform, showcasing the search optimization of the Schwefel function's global minimum, which demonstrates the framework's robustness and transformative role of AI technologies (Sec. 4.1). Overall, this thesis prepares the ground for scientists to utilize the platform and its tools, that promise acceleration and enhancement of scientific discovery and indicate their potential for broader research applications<sup>16</sup>.





*“We can’t solve problems by using the same kind of thinking we used when we created them.”*

— Albert Einstein

## 3. Research Design and Methodology

The present chapter outlines this thesis’s primary interdisciplinary tools and concepts, spanning from computer science and informatics to Artificial Intelligence technologies and electrochemical methods. The subsequent chapter (Chap. 4) will present detailed discussions of these techniques and accelerators for experimental workflow, particularly in the Methods and Supplementary sections of each featured publication and scientific study provided as addenda to this work.

### 3.1. Software & Informatics Tools

This section focuses on three main subjects required for developing software for laboratory automation platforms. Initially, it introduces types of concurrent programming, namely multiprocessing, multithreading, and asynchronous execution. These techniques enable instruments to be called simultaneously, allow parallel testing, and support the execution of multiple sequences of events asynchronously. Additionally, the discourse covers the communication methods for software development, including FastAPI for handling multiple requests and WebSocket for enabling a real-time interactive platform for the user during experiments. The methods discussed in these two subsections are complemented by additional explanations presented in Section 4.1 and 4.5. The last subsection pertains to the integration of the Research Data Management (RDM) lifecycle as a requirement of any research software. Detailed elaboration and practical implementations are provided in Sections 4.1, 4.2, 4.4, and 4.5.

#### 3.1.1. Concurrent Programming

Today’s computing hardware is becoming more efficient and powerful. However, it is still a limited resource that must be carefully allocated among many workloads during any given processing cycle. Therefore, parallelization and concurrency are

indispensable tools for modern software development and hardware architecture design. In computer science and engineering, concurrency improves software efficiency by strategically executing task sequences through the orchestration of multiple operations in overlapping intervals, focusing on logical coordination and resource optimization without necessitating simultaneous execution. The core of this strategy involves precise decision-making on "what to execute and when to execute it", ensuring task prioritization and timely execution. This is especially useful in scenarios where tasks have varying degrees of interdependency and require efficient synchronization. The allocation of tasks switches at a high frequency, and concurrency can create the illusion of simultaneity. A special form of concurrency is parallelism. It refers to the execution of multiple tasks or segments of a single task across single or multiple processor architectures at the same time that are logically or physically partitioned<sup>218</sup>. The definition of these computational concepts is outlined in Figure 3.1. Concurrency can be achieved through three types of switching decisions; multiprocessing, multithreading, and asynchronous processing.

### **Multiprocessing**

Multiprocessing enables the concurrent execution of independent tasks using multiple processes across different CPU cores. This approach is ideal for CPU-bound and compute-intensive applications, as each process operates in its own memory space, and tasks are assured of being executed independently without frequent interprocess communication.<sup>219</sup>

### **Multithreading**

Multithreading allows multiple threads to run parallel within a unified process context, enabling the same memory reference. This facilitates efficient communication and data sharing among threads, making it advantageous for Input/Output (I/O)-bound tasks, which are operations that wait for external events, such as file reads or network responses, while allowing other threads to proceed during idle periods<sup>220</sup>. However, the shared memory model requires careful management to prevent concurrency issues such as data races, a condition where two or more threads simultaneously read or write to the same memory space. Deadlock and starvation are two common challenges in multithreaded programming. Deadlock occurs when

threads are mutually blocked, each waiting for resources held by the other to be available, leading to a standstill. During starvation, threads with lower priority are perpetually denied access due to higher-priority threads being given precedence. All these pitfalls can be avoided with a thread-safe software design to ensure error-free inter-thread communication. Recent Python versions offer adaptable solutions for both CPU and I/O bound tasks, with built-in packages to handle concurrency, threading, and subprocess-management<sup>221</sup>.

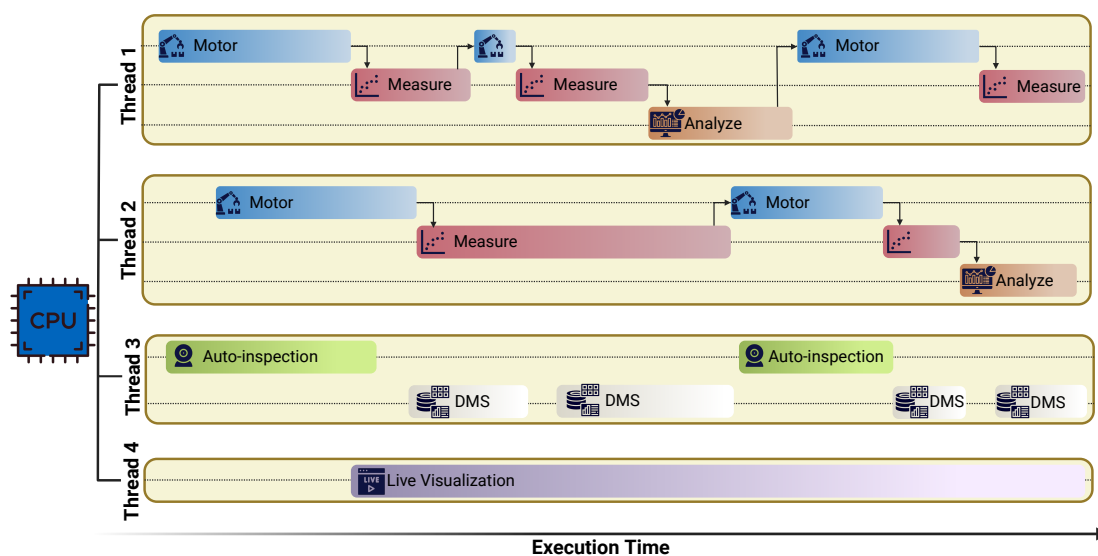


**Figure 3.1.:** Schematic representation of concurrent multithreading system, where the non-blocking execution of tasks is achieved through parallelism across multiple CPU cores and concurrency within threads. Here, each horizontal lane represents a single thread running in parallel with others. Threads 1 and 2 illustrate the concurrent execution of a sequence of experimental tasks in separate setups. Thread 3 manages real-time auto-inspection and dynamic data management tasks, and Thread 4 maintains a live visualization throughout the operation. This depiction exemplifies the two different types of executions applicable in the design of laboratory automation frameworks.

### Asynchronous frameworks

Asynchronous processing represents another concurrency mechanism where tasks are initiated and executed independently. It allows a system to execute multiple operations simultaneously without waiting for one task to complete prior to starting the next. Due to its non-blocking operational framework, the architectural design is effective in I/O-bound contexts, such as handling multiple web server requests via API calls. This approach improves the efficiency of the system and minimizes the

latency<sup>219</sup>.

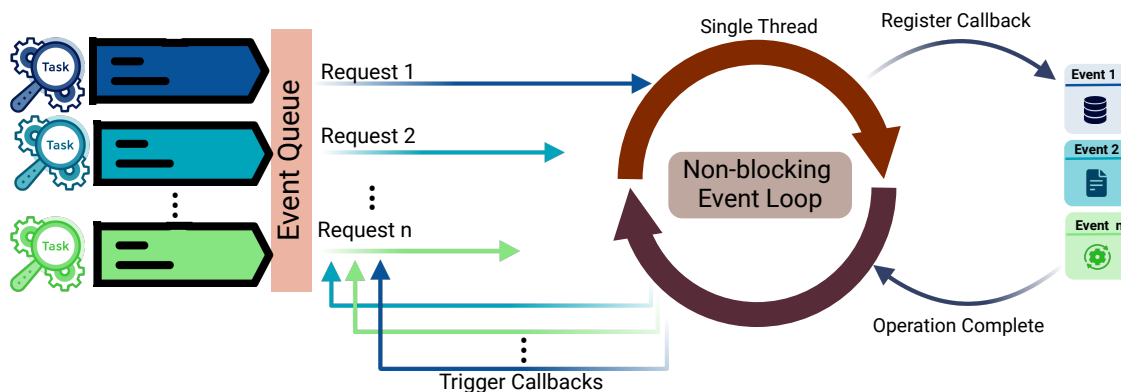


**Figure 3.2.:** An asynchronous event-driven execution framework, where multiple tasks submit requests to an event queue. A single-threaded, non-blocking event loop processes these requests and orchestrates the execution flow by scheduling and delegating events in the queue and registering callbacks without awaiting operation completion. Once operations are finished, the registered callbacks will be triggered, and the event loop will continue to process new requests. Completed responses are asynchronously returned to the tasks.

In Python, the `asyncio` library enables this behavior through coroutines, tasks, and the event loop to implement cooperative multitasking within an event-driven framework. Coroutines are functions defined with the `async def` syntax that allows execution to be paused and resumed at `await` expressions, ensuring non-blocking operation. Tasks are coroutine wrappers that are scheduled in a queue and orchestrated by the event loop, a mechanism that serves as a central coordinator and manages the nonlinear flow of tasks. Here, coroutines can be executed concurrently on a single thread, pausing at an `await` expression and resuming execution when the awaited operation is complete (Figure 3.2). This execution model, supported by context switching, enables the development of scalable and responsive applications without the complexity of threading designs or the performance limitations associated with Global Interpreter Lock (GIL), which restricts the concurrent execution of multiple native threads. Asynchronous operations bypass this constraint without direct interference from the GIL. The standard API architecture promotes non-blocking information flow, allowing clients to make multiple requests simultaneously and receive instant responses while requests are being processed in the background<sup>222</sup>. This type of processing is most useful for laboratory automation software and long-running experiments.

### 3.1.2. Web-Server Communication

Online interaction between different instruments and controlling devices in a laboratory is a key component in the development of automation in experimental settings and is best designed using modern communication tools. In this regard, RESTful APIs and Websockets have reached maturity in web-based frameworks and are applicable for asynchronous tasks and live data transmission, respectively.

#### FastAPI

Representational State Transfer (REST) is a protocol that facilitates interoperability and data exchange between microservices or systems, enabling access and communication through a unified set of stateless operations. A robust web framework for building RESTful APIs in Python 3.7+, FastAPI<sup>223</sup>, uses standard Python type hints to support the development process. Communication is facilitated through endpoints, which are specific URLs where clients can request data or perform actions. These interactions are managed by Python functions annotated with FastAPI decorators for POST, GET, PUT, and DELETE HTTP-Methods, aligned with Create, Read, Update, Delete (CRUD) operations. GET queries are used to get data without altering the server state, which makes them idempotent to read operations. On the other hand, POST queries are used to submit data to a server for processing, creation, or modification<sup>224</sup>.

Each request can have several components, including path parameters, query parameters, headers, and content bodies. Path parameters are defined in URLs to locate resources, while the query parameters, represented as a string appended to URLs after a '?' sign, filter the data to be retrieved. Headers provide meta-information about the request or response, and the request body transmits data in bytes to process. A model class can be implemented using Pydantic<sup>225</sup> to handle request bodies. This module inherits from BaseModel and is necessary for data type validation and structure. It enforces schema and reduces errors while maintaining type safety and data integrity through Python type annotations.<sup>226</sup> (Figure 3.3). The responses from the endpoints are versatile and support a variety of types, such as JSON, HTML, and custom formats. Status codes indicate the outcome of requests between the client and server, ranging from successful operations (2xx codes) to client errors (4xx codes) and server errors (5xx codes).

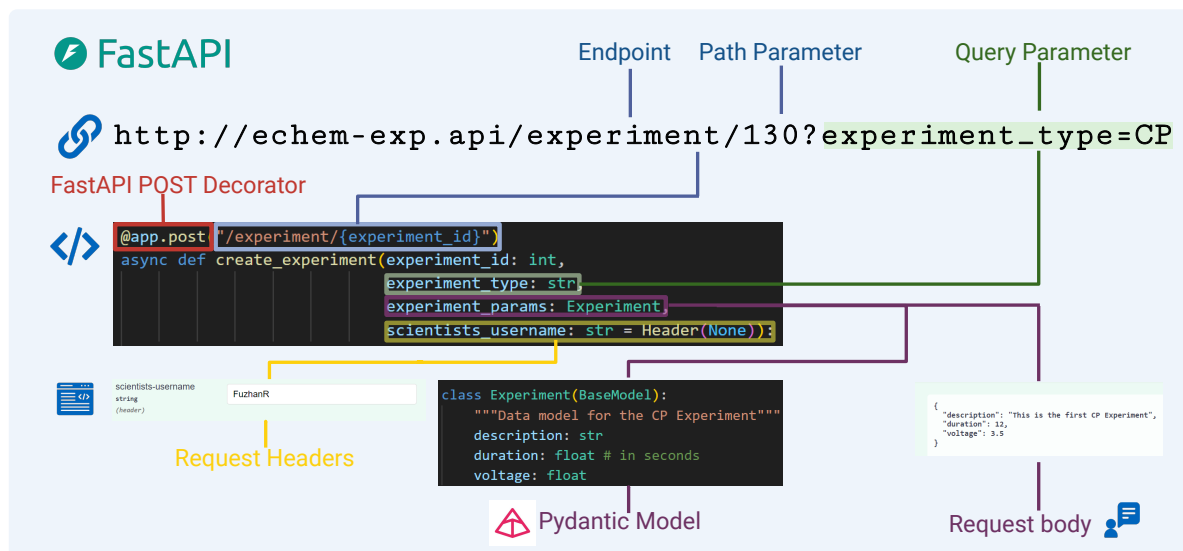


**Figure 3.3.:** Illustration of the API communication process and endpoint configuration in the FastAPI framework, showcased at an exemplary function, which contains the components of an API request and its corresponding validation mechanism. The provided code snippet shows a FastAPI POST decorator that defines an asynchronous endpoint. This request includes `experiment_id` as the path parameter for unique experiment identification and the query parameter `experiment_type`. Additionally, this example illustrates the request header, `scientists_username`, implemented for tracking and authentication. The `Experiment` class, which inherits from the `BaseModel` module of the Pydantic package, defines the schema of the request body, with attributes such as `description`, `duration`, and `voltage`. This is used to validate the type of the incoming request.

FastAPI's architecture inherits from Starlette, a basic routing and middleware tool with expanded security attributes such as sessions cookies, leverages Uvicorn, a lightweight and scalable server, and uses Asynchronous Server Gateway Interface (ASGI) to create an asynchronous framework suitable for high-performance web services. This combination makes FastAPI suitable for real-time applications and non-blocking I/O tasks, as it can handle high volumes of concurrent requests and asynchronous operations.<sup>224</sup> To simplify API exploration, FastAPI's design also includes automatic documentation generation through Swagger User Interface (UI) and ReDoc. To promote error-free codebase and improved maintainability, FastAPI supports integration with Pytest, a Python testing framework that encourages test-driven development (TDD) practices for code robustness and reliability<sup>218</sup>.

## Websockets

WebSockets is another protocol for web server communication that maintains a persistent, two-way communication channel between the server and the client through a single connection. This protocol enables instantaneous data transmission and reception, which is essential for applications requiring timely updates, such as real-time experiment monitoring<sup>227</sup>. Unlike the traditional request-response model, where each new data piece necessitates a separate HTTP request and potentially introduces latency and inefficiency, WebSockets keep the channel open after the initial handshake by upgrading an existing HTTP connection. Herein, this bidirectional communication allows data to be transmitted between the server and client in real-time, enabling dynamic updates without the need for continuous polling or reloading<sup>228</sup>. This enhances data-driven decision-making processes by creating a more interactive user experience.

In designing a lab automation framework, integrating Websockets for real-time functionalities, such as live visualization of measurements, alongside structured APIs for more conventional request-response tasks (e.g., FastAPI) ensures a responsive, scalable, and maintainable workflow<sup>17, 229</sup>.

### 3.1.3. Research Data management

Data veracity, reproducibility, repurposeability, and trustworthiness are validated by RDM throughout the entire lifecycle of scientific research<sup>10, 230</sup>. A RDM framework, outlined in Figure 3.4, allows for effective data utilization from the collection phase during experimental design to the final stages of data preservation<sup>89</sup>. Trust in data integrity is essential for reproducibility, a core tenant of scientific inquiry, where high-quality data generated from experimental workflows is both traceable and manageable through solid stewardship plans<sup>231</sup>. Crucially, experimental data and associated digital assets that are subject to long-term management retain their value and remain accessible for future scientific endeavors<sup>232</sup>. The challenges presented by the 5Vs, namely volume, variety, velocity, veracity, and value, hinge on the implementation of reliable RDM strategies that cover all research outputs, such as experiments, source codes, algorithms, and software packages, to maintain their



usability and integrity over time<sup>233</sup>. A proactive data management plan is essential for all stakeholders involved in the data-driven material science research lifecycle to comply with current analytical and regulatory requirements<sup>200</sup>.

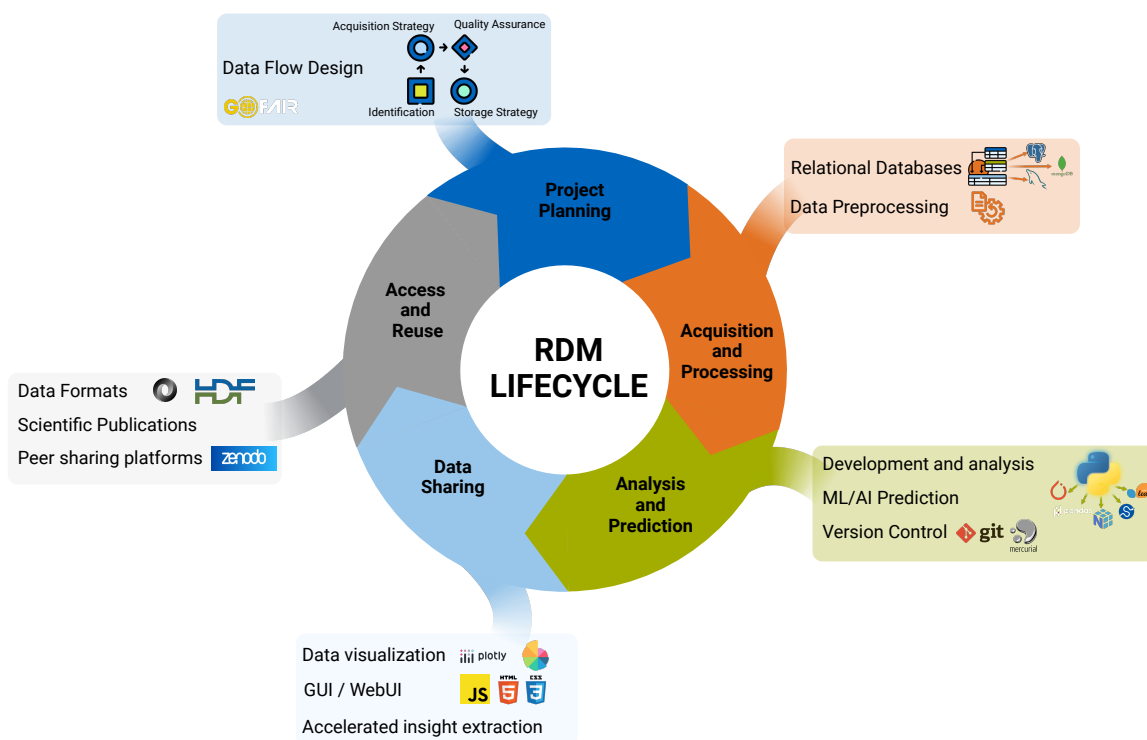


**Figure 3.4.:** Overview of RDM lifecycle. This diagram illustrates the sequential phases of RDM, beginning with Project Planning, where strategies for data management and compliance with FAIR principles<sup>187</sup> are established. It progresses through Data Acquisition and Preprocessing to create and structure the planned databases and assure data quality. The next phase continues with the Analysis and Prediction, where AI, ML, and statistical algorithms are applied, and code developments are supported by version control systems. In the following phase, data sharing is achieved through visualization tools such as Matplotlib and Plotly<sup>234</sup> and results are shared via interactive web UIs or graphical user interface (GUI)s. The cycle is completed with the Access and Reuse of data across local storage or cloud-based repositories such as Zenodo<sup>235</sup> to facilitate its extended use and impact.

## Project Planning

The RDM lifecycle begins with the planning phase, which includes the design of a data flow and represents a blueprint in alignment with the FAIR principles<sup>187</sup>. The process initiates with the identification of data sources and the assessment of data acquisition strategies under consideration of the diversity of methods and

instruments used in its generation. It outlines the curation process steps, including quality assurance and validation to maintain data integrity and compliance with ethical standards<sup>236</sup>. This planning phase also involves determining storage solutions and formats based on the nature of the data and the requirements of potential future users<sup>237</sup>. Additionally, the integration of metadata standards provides a structured description of data, including its provenance and characteristics, and makes datasets shareable and publishable<sup>191</sup>.

### Acquisition and Processing

The data acquisition phase of RDM requires the instantiation of the planned databases for data storage and relies on principles that maintain the integrity and accuracy of the collected data<sup>195</sup>. Relational databases are characterized by a structured schema that defines data types and relationships. They support data manipulation and retrieval, as well as robust query handling and operational reliability in compliance with the atomicity, consistency, isolation, and durability (ACID) principle<sup>238</sup>. Additionally, normalization eliminates data redundancy and dependency constraints within these databases<sup>239</sup>. Herein, The First Normal Form (1NF) ensures that entries are atomic and single-valued. The Second Normal Form (2NF) removes partial dependencies and assesses the dependency of non-key attributes only on the primary keys, and the Third Normal Form (3NF) further reduces transitive and indirect dependencies ( $\{A \rightarrow B, B \rightarrow C\} \models A \rightarrow C$ ). These forms simplify data management and allow for precise definitions of table creation and their inherited relationships, data updates, and insertions<sup>240</sup>. The implementation of Universally Unique Identifiers (UUIDs) additionally prevents duplicate data entries and enables data lineage tracking across different systems. These actions can be managed using a relational database management system (RDBMS), available in commercial and open-source versions, such as PostgreSQL<sup>241</sup>.

Alongside data acquisition, data preprocessing is indispensable for the quality and informativeness of data, making it valuable for analytical purposes and ensuring its long-term usability. By removing inaccuracies, redundancies, and heterogeneity, this process restructures raw data into a coherent unit and avoids data quality and consistency issues. This prepares data for ML modeling applications, supports model

performance, and facilitates the extraction of meaningful insights. Data preprocessing connects the collection of raw data to its practical use to strengthen the robustness and reliability of research findings<sup>242</sup>.

### **Analysis and Prediction**

The following phase of RDM involves analyzing data and may include the application of AI and ML techniques for prediction objectives. Analytical frameworks tailored to unique experimental applications can be developed and maintained using software that facilitates low-level control through high-level language constructs. Here, version control systems, such as git, can be used to monitor the changes made by each contributor at any given time to promote accountability at all stages of research<sup>232</sup>. The modularity and scalability of the codebase benefit from the use of modern software design patterns applicable to object-oriented and functional scenarios<sup>243</sup>. Documentation and detailed logging of every action is necessary for maximum transparency and traceability. These measures enable accurate analysis and prediction to generate actionable knowledge<sup>232</sup>.

### **Data Sharing**

The data sharing phase maximizes the extraction of information, permitting diverse interpretations from multiple stakeholders<sup>83</sup>. It allows for data exchanges while granting confidentiality for sensitive information through approaches such as federated learning<sup>244</sup>. Intelligent visualization of both raw and processed data using libraries in common programming languages such as R and Python contribute to the distribution of derived knowledge through web-based UI or GUI<sup>195</sup>. Web UI development commonly utilizes standard frontend languages such as HTML, CSS, and JavaScript, with API communication through, for instance, Python Flask<sup>245</sup> for backend connectivity. On the other hand, for GUIs, libraries such as PySimpleGui<sup>246</sup> provide intuitive and user-friendly interfaces to construct interactive widgets and applications for local execution. This approach to data sharing promotes transparency and accelerates insight extraction, benefiting both small teams and large-scale consortia in collaborative research environments<sup>247</sup>.

## Access and Reuse

The last stage of the RDM lifecycle focuses on techniques for data storage, publication, and subsequent reuse, guided by the FAIR principles, to elevate the preservation and utility of digital assets<sup>236</sup>. Various data formats are available to store complex experimental structures along with their metadata. For example, the JSON format, with its nested architecture, can improve the findability and interoperability of datasets<sup>89, 248</sup>. The HDF5 format is intended for intensive I/O processing and storage, while simpler structures can be written to CSV files. Relational databases also serve as scalable storage solutions, especially considering the already tabular design that adheres to the schema defined during the planning phase. Independence from local hardware is offered by cloud-based repositories such as Zenodo<sup>235</sup> and Figshare<sup>249</sup> that provide secure and configurable access to datasets while maintaining data integrity and compliance with confidentiality requirements. Publishing data on academic platforms increases its visibility within the scientific community and simplifies the peer review process. Positioning data within digital libraries and archives ensures data accessibility across diverse scientific domains and enhances its repurposeability<sup>250</sup>. This maximizes the potential impact on future scientific discoveries by allowing datasets to be adapted and reused in varying study settings, thus increasing the immediate and long-term value of research projects<sup>195</sup>. Such a scalable infrastructure is designed to support the dynamic requirements of expanding projects, promotes sustainable data management practices that align with broader research objectives, and embodies a commitment to openness, interoperability, and the advancement of knowledge across disciplines<sup>251</sup>.

## 3.2. Statistics, ML, and DL tools

This section addresses methods and algorithms from statistics, ML and DL techniques. In 3.2.1 the discussion verges on AL algorithm in the context of laboratory automation and distributed instrumentation, focusing on how experimental optimization can be achieved. Complementary details are provided in Section 4.1, which reports on the development of hierarchical autonomous laboratory automation and orchestration (HELAO) software. Section 3.2.2 outlines the uncertainty quantification method, applied in evaluating a model's performance using polynomial regression, that

is described in Section 4.3. Lastly, in segment 3.2.3, an introduction to sequence modeling for time series applications is presented. The specifics of this modeling approach, along with the main blocks in the design and engineering of an explainable and regularized deep model, are further elaborated in Section 4.4. This has led to the development of the `arcana-batt` Python package for multi-output prediction of parameters to estimate battery lifetime. Additional statistical methods are described in Section 4.2 and 4.5 and include coverage of peak detection methods, motion detection algorithms, and other techniques used to implement the data analysis package and develop reliable software components for sequential experimentation that comprise the autonomous millimeter scale high-throughput battery research system (Auto-MISCHBARES) framework.

### 3.2.1. Active Learning

Accelerated science, as envisioned by early-stage autonomous feedback loops<sup>76</sup> for chemistry and materials science<sup>83, 5</sup>, seeks to deliver improved and promising materials through efficient chemical space exploration. These workflows are based on the principle of AL algorithm, which includes a feedback loop<sup>252, 253</sup> in planning subsequent experiments from previous ones, and thus aim to integrate experiment, analysis, and data management<sup>17, 99</sup>. Relying on the reproducibility characteristic of high-throughput materials science, the goal is to reduce the amount of required experiments while maximizing knowledge gain and experimental robustness<sup>17</sup>.

After defining the quantities of interest, the AL cycle begins with the random selection of an initial experiment from the exploration space, guided by a predefined DoE approach.<sup>254</sup> This experiment is then executed automatically based on the specified configurations. Following the automated measurement and real-time analysis, the experiment's merit is evaluated, and a learning function is used to determine the parameters' values for the next experiment. The ML model instantiates this function to forecast the FOM for prospective experiments in the exploration area<sup>9</sup>. Figure 3.5 illustrates the application of a RF regressor as a predictive model, which reduces the variance. Mathematically, this is expressed as  $Var[y] = \frac{\sigma^2}{n}$ , where  $\sigma^2$  is the variance of the model predictions, and  $n$  represents the number of decision tree estimators. Here, the regressor improves the reliability of its predictions by averaging the outputs of

multiple decision tree estimators. Additionally, during training, the model selects a random subset of features for each decision tree split to prevent overfitting and increase out-of-sample prediction accuracy<sup>255</sup>. This technique allows the model to consider different aspects of the data by using an ensemble of trees, which provides diverse insights for its predictions and enhances its generalizability. Furthermore, its capability for parallel training reduces computational costs and decreases training time, which is desirable for a model that requires real-time updates and predictions<sup>256</sup>.

The regressor model is retrained with the updated dataset and is then evaluated across all non-sampled measurements within the defined space to obtain the predictions of the FOM ( $\mu$ ) and its associated uncertainty ( $\sigma$ ). To improve the model's performance and experimental outcomes, the autonomous feedback loop incorporates model predictions and uncertainty measures. Due to the error-prone environments<sup>9</sup> in which the underlying measurement instruments operate, there is often a false sense of data precision<sup>18</sup>, and uncertainties are predominately attributed to the model itself and are known as epistemic uncertainty<sup>257</sup>. Given these challenges, in the next procedural step of the AL algorithm, the acquisition function quantifies the expected utility or informativeness of unlabeled data points, i.e. potential experiments, to decide the subsequent measurement. The choice of the acquisition function may vary depending on the research objectives. In the provided example in Figure 3.5, this function, described by Rohr et al.<sup>9</sup>, determines the coordinates that maximize the quantity in the upper confidence bound. The formula for the acquisition function is defined as

$$\lambda \cdot \mu + (1 - \lambda) \cdot \sigma_{\text{preds}} \quad (3.1)$$

where  $\lambda$  parameter, ranging between 0 and 1, adjusts the balance between exploiting areas where the model predicts high values ( $\mu$ ) and exploring areas where the model is uncertain. Here, this is indicated as  $\sigma_{\text{preds}}$ , representing the standard deviation of predictions across all decision tree estimators in the ensemble and highlighting the areas of potential information gain<sup>257</sup>. This acquisition function provides a flexible and versatile mechanism to prioritize either exploration or exploitation depending on the objective. Thus, the experimental parameters that achieved the highest value of the acquisition function are opted as the next experimental configuration; if mul-

tiple points share the maximum value, one is selected at random. The suggested experiment is then tested, and the resulting data and outcomes are added to the existing dataset. The model will then be updated for the next cycle. This iterative process of observing data, updating models, and selecting experiments continues to systematically explore and exploit the search space to discover optimal solutions or deepen understanding of the modeled phenomenon<sup>116, 254</sup>.

Rohr et al.<sup>9</sup> additionally introduced a comprehensive set of metrics to evaluate the effectiveness of the AL approach. Among them,  $^{all}ALM$  measures the proportion of all “good” materials identified within the top percentile of the FOM for a given iteration cycle. This approach enables a systematic comparison to a baseline method, which involves random selection at each iteration. The authors defined two metrics for this comparison. The enhancement factor is measured as,

$$\frac{^{all}ALM_{ML\_guided\_process}}{^{all}ALM_{random\_sampling}} \quad (3.2)$$

which quantifies the improvement in  $^{all}ALM$  metrics by integrating a predictive model to guide experimental iterations over random sampling within a fixed experimental budget. The second comparison metric is an acceleration factor that indicates the reduction in the number of samples or experiments required to reach the same level of  $^{all}ALM$ :

$$^{all}ALM_{ML\_guided\_process} = ^{all}ALM_{random\_sampling} = y \quad (3.3)$$

The factor is expressed as the ratio of cycles required in AL compared to a random sampling baseline to reach this level. These metrics demonstrate the capability of the AL approach in making intelligent and informed decisions and identifying high-potential materials with fewer experiments compared to the conventional high-throughput methods.

### 3.2.2. Uncertainty Quantification

Uncertainty quantification is crucial for assessing the reliability of predictions made by ML algorithms, especially when using decision mechanisms such as AL. Among the

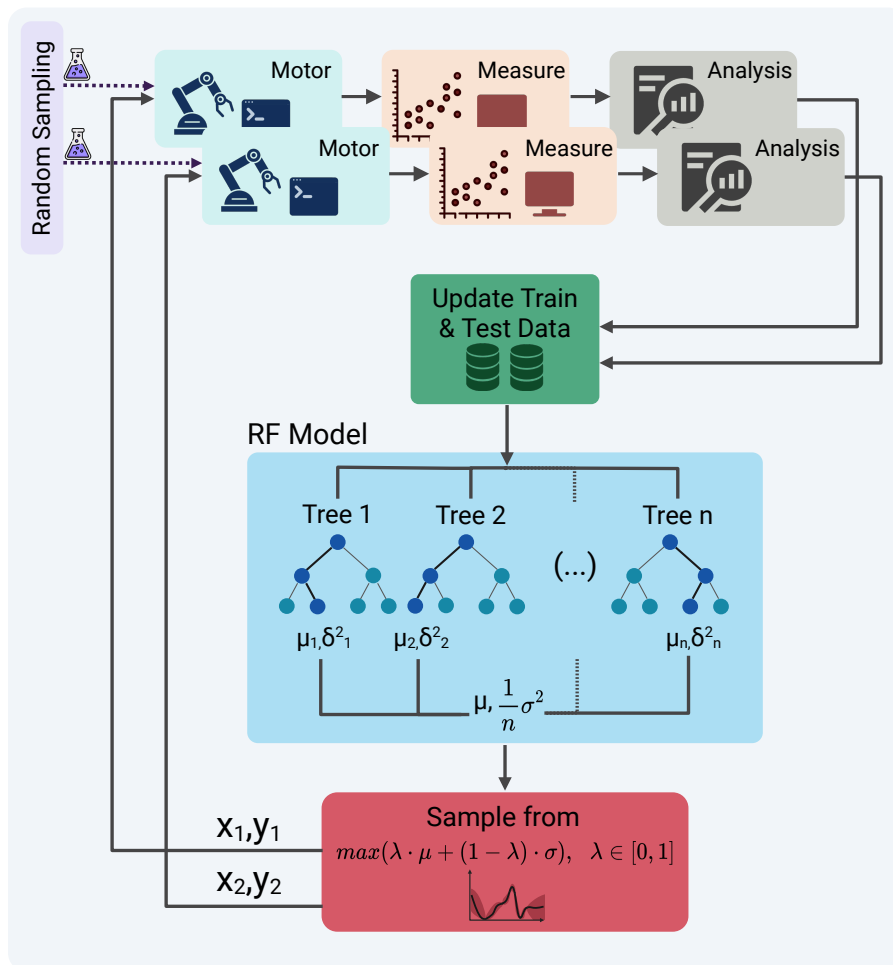


**Figure 3.5.:** A feedback loop for high-throughput experimentation. The schematic illustrates a closed-loop system, initiating with a randomly selected trial from a predefined list of experiments. The automated sequential process includes testing, measurement, and data analysis to derive the experiment’s FOM that is then incorporated into an AL framework; here, the data of the completed experiment is added to the training dataset and is simultaneously removed from the testing queue. The selected ML model, represented here by a RF regressor, is retrained with the updated dataset and proceeds to predict the FOM for the remaining unsampled trials, accompanied by an estimated mean ( $\mu$ ) and standard deviation ( $\sigma$ ). Following this prediction, an acquisition function, represented here by an upper confidence bound heuristic, is applied to acquire these predictions to target areas of the greatest model uncertainty. This function balances between explorative and exploitative strategies via a tunable parameter,  $\lambda$ . The experiment that maximizes the acquisition function’s criteria is thus selected for the subsequent execution, with its parameters sent to the devices. This iterative feedback loop perpetuates until a predefined experimental budget is reached or the optimal solution within the search space is empirically determined.



various strategies for this quantification, conformal prediction is a proven approach to measuring prediction certainty<sup>258</sup>. This statistical method is versatile as it can be used under the assumption of data exchangeability, where the data is independent and identically distributed (i.i.d.), without the need to determine the underlying joint data distribution,  $P_{X,Y}$ <sup>259</sup>. Given i.i.d., training data is

$$(X_i, Y_i) \in \mathbb{R}^d \times \mathbb{R}, i = 1, 2, \dots, n$$

and considering

$$Y = \mu(X) + \epsilon, \quad (3.4)$$

where  $\mu$  represents the target estimator function and  $\epsilon$  refers to the noise, the objective is to estimate a prediction interval  $\hat{C}_{n,\alpha}$  for a new observation,  $X_{n+1}$ , that approximates the true target value,  $Y_{n+1}$ , with a probability of at least  $1 - \alpha$ . Here,  $\alpha$  represents a pre-defined error rate and sets the significance level for the proportion of future data points that are expected to be outside the predicted interval defined as

$$P\{Y_{n+1} \in \hat{C}_{n,\alpha}(X_{n+1})\} \geq 1 - \alpha. \quad (3.5)$$

One approach to constructing this interval is the jackknife+ method, a variant of conformal prediction techniques. This method considers the variability of model predictions through leave-one-out (LOO) cross-validation, along with calibration and conformity scores. Herein, for each instance in the training set, the model is trained on all other instances to predict the excluded one. The conformity score is then calculated as the LOO residuals, which measures the agreement between the expected and actual values for each left-out instance. The jackknife+ method can be extended to k-fold cross-validation, where one fold is left out at a time. This expands the method's applicability to larger datasets or computationally intensive models. Mathematically, the conformity score for the  $i$ -th data point is commonly defined as the absolute error between these two values<sup>259</sup> and is expressed as

$$S_i = |Y_i - \hat{\mu}_{-i}(X_i)|, \quad (3.6)$$

where  $\hat{\mu}_{-i}$  is the prediction model trained without the  $i$ -th data point. To calibrate the prediction interval, empirical quantiles of the conformity scores are used to estimate its bounds and establish a threshold for prediction error within a desired confidence interval. This leads to the formulation of the prediction interval around the new observation  $X_{n+1}$ , guided by the  $1-\alpha$  quantile of the conformity score, as follows<sup>260, 259</sup>:

$$\hat{C}_{n,\alpha}^{\text{jackknife}^+}(X_{n+1}) = [\hat{q}_{n,\alpha}^- \{ \hat{\mu}_{-i}(X_{n+1}) - S_i \}, \hat{q}_{n,\alpha}^+ \{ \hat{\mu}_{-i}(X_{n+1}) + S_i \}]. \quad (3.7)$$

Here,  $\hat{q}_{n,\alpha}^-$  and  $\hat{q}_{n,\alpha}^+$  correspond to the lower and upper quantiles and are calculated from the leave-one-out conformity scores (Figure 3.6). This method, which can be implemented using MAPIE Python library<sup>261</sup>, accounts for the variability in the regression function and promotes stable and reliable uncertainty quantification results for practical applicability<sup>262</sup>.

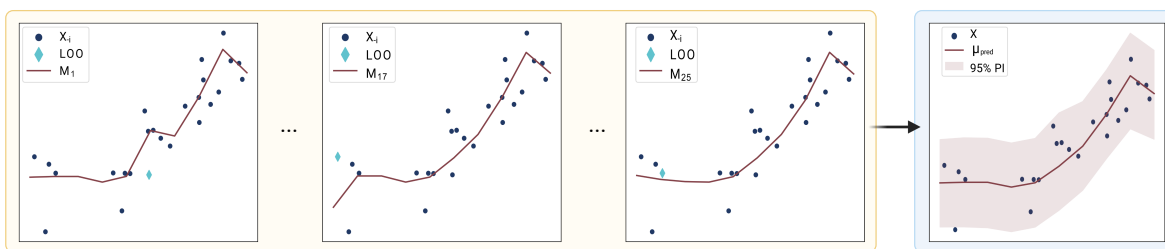


**Figure 3.6.:** Estimation of prediction interval using the jackknife+ method. The series of panels enclosed in the yellow frame represents the model evaluations ( $M_1, \dots, M_{17}, \dots, M_{25}, \dots$ ), with each model trained on subsets of the data excluding one observation ( $X_{-i}$ ) in successive LOO iterations to calculate the corresponding conformity score from the residual error. The process loops across the entire training dataset. The rightmost panel combines all these evaluations, utilizing the empirical quantiles of the conformity scores to establish the prediction interval for new observations, depicted as a shaded area. This provides a reliable measure of uncertainty for future predictions.

### 3.2.3. Sequence Modeling

This section describes some fundamental building blocks utilized in the design and development of a highly regularized attention-based sequence-to-sequence (Seq-to-Seq) architecture, thoroughly elaborated in Section 4.4. The following paragraphs explore RNNs, particularly the long short term memory (LSTM) model, which is used as part of the Seq-to-Seq model for the structuring of the encoder and decoder.

The regularization techniques for optimizing the learning process along with further advanced approaches, such as attention mechanisms and customized implementations of methods, including the quantile loss function, rigorous early stopping, teacher forcing for Seq-to-Seq flow, and transfer learning, are provided in detail in Section 4.4.

### Recurrent Neural Network

To model the sequential data in applications such as time series prediction, RNNs architecture are designed. These networks are an extension of feed-forward neural networks (FFNNs) and incorporate a looped architecture with feedback connections, enabling the network to maintain historical information. This architectural design captures the temporal dependencies through an internal memory state ( $h$ ), which is updated at each step with newly received input data alongside all information from previous states. This dynamic creates a recursive dependency and preserves the continuity across the input sequence<sup>263</sup> and can be mathematically expressed as:

$$h^{(t)} = f(h^{(t-1)}; x^{(t)}; \theta), \quad (3.8)$$

where  $h^{(t)}$  and  $x^{(t)}$  represent the hidden state and the input at time  $t$ , and  $\theta$  refers to the trainable parameters. The function  $f$ , integrates the previous state and the current input to produce the new state.

Similar to other neural networks, the RNN architecture is defined by its layers and activation functions. Each layer within a RNN contains a set of parameters, namely weights and biases, which are optimized during training. This network shares the same weights across all time steps, and biases provide further adjustments to the neuron's activation potential. Activation functions introduce element-wise non-linearity into a layer during the learning process, enabling the network to understand the dynamics of complex sequential data patterns and maintain the dimension of each layer. These functions must be monotonic and differentiable, as neural networks utilize gradient-based learning to optimize their trainable parameters. Commonly implemented activation functions in RNN are shown in Figure 3.7.

The sigmoid function (Equation 3.9) transforms the input values ( $x$ ) into a probability

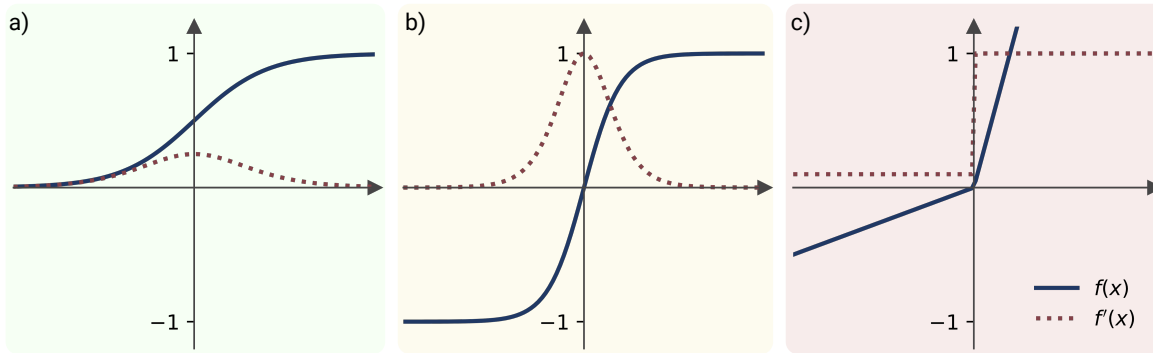


**Figure 3.7.:** The schematic illustration of common neural network activation functions and their derivatives. a) represents the sigmoid activation function, which maps input to values between 0 and 1, and its derivative, which is maximal at the function’s inflection point, indicating maximum input sensitivity. b) depicts the hyperbolic tangent (tanh) function, which produces outputs ranging from  $-1$  to  $1$ , with its derivative reaching its highest absolute value at the origin. c) presents the leaky rectified linear unit (Leaky ReLU) activation function, which prevents gradient vanishing during backpropagation for negative inputs by allowing a small and non-zero gradient. The derivative of this function maintains a constant positive slope for negative inputs and a slope of one for positive ones.

output within the interval  $(0,1)$ . It saturates extreme values, negative or positive, preventing abrupt changes in the outputs and moderating the magnitude of the changes. This function is expressed as

$$\sigma(x) = \frac{1}{1 + e^{(-x)}}. \quad (3.9)$$

The tanh (Equation 3.10) is a frequently used function in recurrent architectures, scaling the input values to the range between  $(-1, 1)$ . This function is known for leading to faster and more stable convergence compared to the sigmoid function and is defined as

$$\tanh(x) = \frac{e^x - e^{-x}}{e^x + e^{-x}}. \quad (3.10)$$

A Leaky ReLU is defined in Equation 3.11, where  $\alpha$  is a small, positive slope. This function mitigates non-active gradients when  $x < 0$ , allowing the gradient flow for inactive states and facilitating ongoing learning during training. It is expressed as follows:

$$\text{LeakyReLU}(x) = \max(\alpha x, x). \quad (3.11)$$

Figure 3.8 depicts the basic RNN and its unfolded structure, which comprises a single recurrent layer. This unfolding process converts the recurrent structure into an expanded computational graph, where each node represents the network at a specific time. During the forward propagation phase of computation, the network processes the input sequentially. It updates its hidden states at each step with

$$a^{(t)} = Ux^{(t)} + Wh^{(t-1)} + b, \quad (3.12)$$

$$h^{(t)} = \tanh(a^{(t)}). \quad (3.13)$$

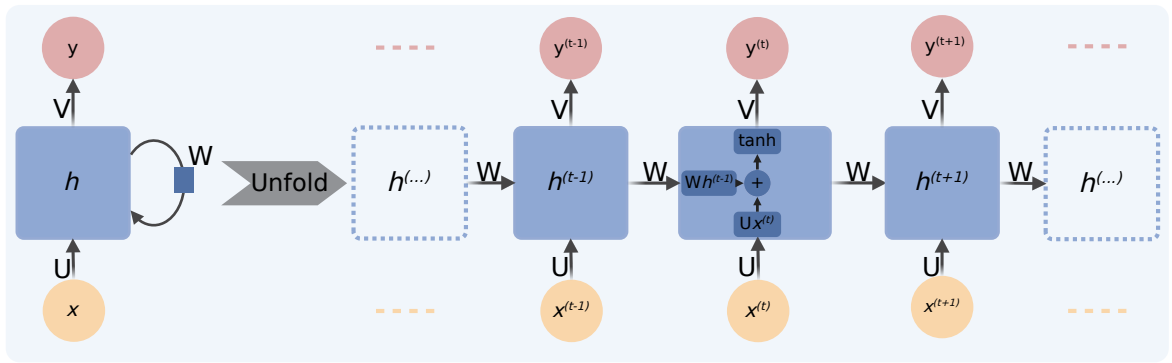


**Figure 3.8.:** Schematic of an RNN. The circuit diagram on the left illustrates the compact cyclic architecture of an RNN in which the hidden state  $h$ , is recurrently updated based on the current input ( $x$ ) and the previous states. This update process is parameterized by weight matrices  $U$  and  $W$ , for input-to-hidden and hidden-to-hidden connections, respectively. The graph on the right side depicts the unfolded RNN across multiple time steps, detailing the processing of input sequences. At each time step  $t$ , the hidden state is updated by applying a  $\tanh$  activation function to the weighted sum of the input  $x^{(t)}$  and the previous hidden state  $h^{(t-1)}$ . The output  $y^{(t)}$  at this time step is then calculated from the hidden state through another transformation involving the weight matrix  $V$ , which connects this state to the output. This unfolded computational graph demonstrates how RNN captures temporal dependencies within sequences.

The input-to-hidden, hidden-to-hidden transformations are described by the weighted matrices  $U$  and  $W$  respectively and the bias vector is represented by  $b$ . The hidden state at time  $t$ ,  $h^{(t)}$ , is calculated using the activation function  $\tanh$ . Finally, the output for time  $t$ ,  $\hat{y}^t$ , is determined by computing

$$\hat{y}^t = Vh^{(t)} + c \quad (3.14)$$

with  $V$  and  $c$  being the hidden-to-output weight matrix and the output bias vector, respectively. During the training phase, the RNN adjusts its parameters to minimize the loss function, which typically measures the difference between the actual target and the predicted output. This optimization is obtained through backward propagation through time (BPTT), where gradients of the loss function are computed and propagated through the network. With mean square error (MSE)

$$L = \frac{1}{2} \sum_{t=1}^T \|\hat{y}^{(t)} - y^{(t)}\|^2 \quad (3.15)$$

considered as the loss function, the gradient with respect to (w.r.t.) different parameters can be calculated as follows :

$$\delta^{(t)} = \frac{\partial L}{\partial y^{(t)}} = \hat{y}^{(t)} - y^{(t)}, \quad (3.16)$$

where  $\delta^{(t)}$  represents the error, which is the derivative of the loss function ( $L$ ) w.r.t. the output at time  $t$  obtained using the chain rule. The loss gradient w.r.t. the hidden states ( $h^{(t)}$ ) can be derived as:

$$\frac{\partial L}{\partial h^{(t)}} = \frac{\partial L}{\partial y^{(t)}} \cdot \frac{\partial y^{(t)}}{\partial h^{(t)}} = \delta^{(t)} \cdot V, \quad (3.17)$$

which illustrates how alterations in the hidden state at time  $t$  will impact the output  $t$  and, consequently, the loss. However, in this recurrent setup, errors in prediction at a subsequent time step ( $t+1$ ) also influence the gradients at an earlier stage. Mathematically the impact is expressed as

$$\frac{\partial L}{\partial h^{(t)} \text{ from } h^{t+1}} = \frac{\partial L}{\partial h^{(t+1)}} \cdot \frac{\partial h^{(t+1)}}{\partial a^{(t+1)}} \cdot \frac{\partial a^{t+1}}{\partial h^{(t)}} = \frac{\partial L}{\partial h^{(t+1)}} \cdot (1 - (h^{(t+1)})^2) \cdot W. \quad (3.18)$$

By combining the two terms in Equations 3.17 and 3.18, the gradient ( $\nabla_{h^{(t)}} L$ ) can be expressed as:

$$\nabla_{h^{(t)}} L = \nabla_{h^{(t+1)}} L \cdot (1 - (h^{(t+1)})^2) \cdot W + \delta^{(t)} \cdot V. \quad (3.19)$$

The loss gradient w.r.t. the output bias ( $c$ ), denoted as  $\nabla_c L$ , is the sum of the direct gradient impacts from the output layer across all time steps:

$$\nabla_c L = \sum_{t=1}^T \frac{\partial L}{\partial y^{(t)}} = \sum_{t=1}^T \delta^{(t)}. \quad (3.20)$$

The loss gradient relative to output weights ( $V$ ) captures the error at each output step influenced by the respective hidden state and is given by:

$$\nabla_V L = \sum_{t=1}^T \frac{\partial L}{\partial y^{(t)}} \cdot h^{(t)} = \sum_{t=1}^T \delta^{(t)} \cdot h^{(t)}. \quad (3.21)$$

Two gradients, one w.r.t. hidden bias and one w.r.t. to hidden-to-hidden weights ( $W$ ), are calculated in relation to the hidden layer parameters which capture the temporal dependencies:

$$\nabla_b L = \sum_{t=1}^T \frac{\partial L}{\partial y^{(t)}} \cdot \frac{\partial y^{(t)}}{\partial h^{(t)}} \cdot \frac{\partial h^{(t)}}{\partial a^{(t)}} = \sum_{t=1}^T \delta^{(t)} V \odot (1 - (h^{(t)})^2) \quad (3.22)$$

$$\nabla_W L = \sum_{t=1}^T \delta^{(t)} V \odot (1 - (h^{(t)})^2) \cdot h^{(t-1)}. \quad (3.23)$$

Lastly, the gradient w.r.t. input-to-hidden weights ( $U$ ) considers the impact of each input at respective time steps:

$$\nabla_U L = \sum_{t=1}^T \delta^{(t)} V \odot (1 - (h^{(t)})^2) \cdot x^t. \quad (3.24)$$

The RNN, however, is constricted in learning long-term dependencies due to exploding or vanishing gradient problems, as illustrated by the recursive nature of the gradients (Equation 3.19). This can result in slow convergence or instability in the training process<sup>264</sup>. One advanced architecture introduced by Hochreiter et al.<sup>265</sup> was the LSTM network, which can mitigate this drawback and maintain a more constant error flow through time steps.

## Long Short-Term Memory

LSTM networks enable improved gradient flow for capturing long-duration dependencies within the network through an internal recurrence mechanism known as the cell state ( $s$ ). This unit functions as a linear self-loop, without weights and biases, maintaining long-term memory without inducing gradient issues<sup>263, 265</sup>. It operates in parallel with the external recurrence mechanism, which includes hidden units and shares the same weight parameters for managing short-term memory. The interaction between these two recurrences is modulated by gating units<sup>266</sup>. An LSTM consists of three gates, namely the forget, input, and output gates (Figure 3.9).

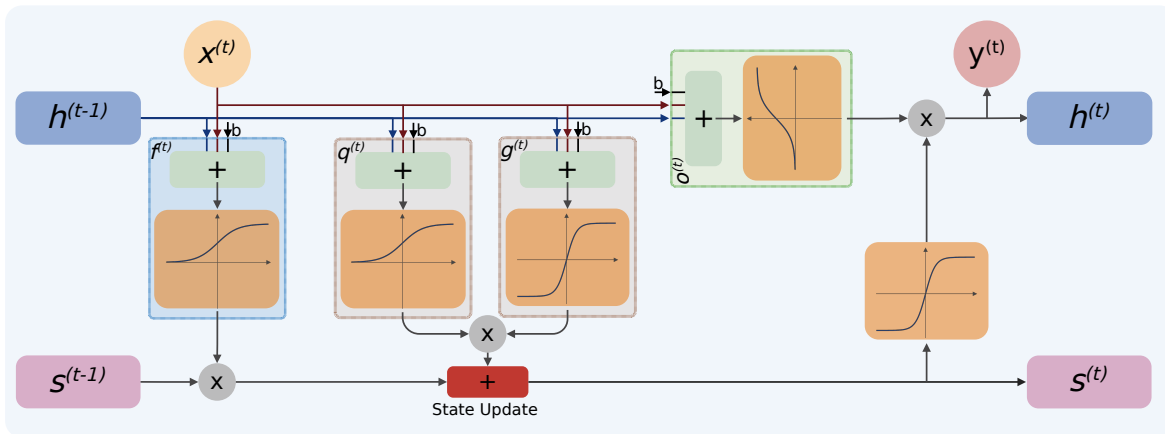


**Figure 3.9.:** Schematic representation of an LSTM unit during the  $t$ -th time step. This structure illustrates the information flow from the input vector ( $x^{(t)}$ ), the previous hidden state ( $h^{(t-1)}$ ), and the cell state ( $s^{(t-1)}$ ) through various gates: the forget  $f^{(t)}$ , input  $g^{(t)}q^{(t)}$ , and output gate  $o^{(t)}$ . Each gate executes a pointwise operation that combines  $x^{(t)}$ ,  $h^{(t-1)}$ , and their corresponding weights with their bias, subsequently passing through a non-linear activation function. The forget gate calculates the amount of short-term information remembered from  $h^{(t-1)}$  in the long-term memory  $s^{(t-1)}$  while ignoring the rest. The input gate consists of two sections that decide both the quantity of short-term information to be acquired and its proportion to be stored in the long-term memory. The combination of these two gates results in a state update, which is the new long-term memory,  $s^{(t)}$ . Lastly, the information from the output gate is multiplied by the transformed updated cell state, resulting in a new hidden state,  $h^{(t)}$ .

The forget gate  $f_i^{(t)}$  for cell  $i$  at time step  $t$ , utilizes conditional self-loop weights to determine the proportion of long-term memory to retain. This decision is informed by incorporating the current input vector  $x_j^{(t)}$  and the previous hidden state  $h_j^{(t-1)}$  and processing them through a sigmoid activation function. The gate's output is



represented by the following equation:

$$f_i^{(t)} = \sigma \left( \sum_j U_{i,j}^f x_j^{(t)} + \sum_j W_{i,j}^f h_j^{(t-1)} + b_i^f \right), \quad (3.25)$$

where  $U^f$  and  $W^f$  represent the forget gate weights for the input and the recurrent state, respectively, and  $b^f$  indicates the bias. The input gate subsequently determines the amount of short-term memory that should be considered for potential long-term memory. This process calculates the portion of new data for updating the state using a sigmoid activation function ( $q_i^{(t)}$ ):

$$q_i^{(t)} = \sigma \left( \sum_j U_{i,j}^q x_j^{(t)} + \sum_j W_{i,j}^q h_j^{(t-1)} + b_i^q \right). \quad (3.26)$$

It then produces the candidate state values by processing short-term memory, input, and their weights through a tanh activation function, given by  $g_i^{(t)}$ .

$$g_i^{(t)} = \tanh \left( \sum_j U_{i,j}^g x_j^{(t)} + \sum_j W_{i,j}^g h_j^{(t-1)} + b_i^g \right). \quad (3.27)$$

The total quantity of learned information can be calculated by multiplying the  $q_i^{(t)}$  and  $g_i^{(t)}$  values. The cell state  $s_i^{(t)}$  is then updated by a combination of the forget gate's output, which modulates the remembered old memory, and the input gate's output, which adds new memory:

$$s_i^{(t)} = f_i^{(t)} s_i^{(t-1)} + g_i^{(t)} q_i^{(t)}. \quad (3.28)$$

Lastly, the output gate  $o_i^{(t)}$  determines what proportions of the cell state should influence the output hidden state  $h_i^{(t)}$ . This is achieved by transforming the updated cell state through a tanh function and then scaling this output with a sigmoid gate. The potential short-term memory to be remembered in the updated hidden state is:

$$o_i^{(t)} = \sigma \left( \sum_j U_{i,j}^o x_j^{(t)} + \sum_j W_{i,j}^o h_j^{(t-1)} + b_i^o \right), \quad (3.29)$$

$$h_i^{(t)} = \tanh(s_i^{(t)})o_i^{(t)}. \quad (3.30)$$

Various advanced implementations can further enhance the capability of LSTM networks to learn long-term dependencies and stabilize training. For instance, skip connections introduce a delay mechanism into the network by providing more temporal context through access to earlier states<sup>267</sup>. Regularization techniques such as dropout can be implemented to prevent, among others, overfitting issues and ensure robust performance on unseen data<sup>268</sup>. This method randomly removes a subset of the network's unit at each training step. Beyond these approaches, the integration of attention mechanisms, allows for the dynamic selection of relevant features<sup>269</sup>. Other strategies, such as teacher forcing<sup>263</sup> and multitasking learning, promote greater generalization<sup>270</sup>. Optimizing the training procedure can also benefit from implementing a learning rate scheduler to increase the convergence rate by adaptively adjusting the learning rate during the training phase<sup>271</sup>, as well as other regularization techniques as, for example, early stopping<sup>272</sup>. A detailed discussion of all these strategies is provided in Section 4.4.

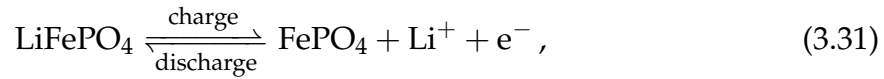
### 3.3. Electrochemical methods

The following section introduces the electrochemical principles behind the design and development of the two software packages used to analyze and model the data presented in this dissertation, namely *arcana-batt* and *madap*. It begins by outlining the working principles of batteries, which guide the extraction of parameters from cycling data to model their lifetime using DL models, as described extensively in Section 4.4. The section continues by providing an overview of the basics of electrochemical tests such as EIS and cyclic voltammetry (CV). These principles support the design of the electrochemical data analysis package, Modular and Autonomous Data Analysis Platform (MADAP), which utilizes statistical tools to derive electrochemical values. Complementary details on this analysis package can be found in Sections 4.2 and 4.5.

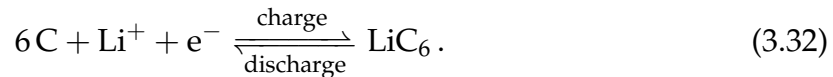
### 3.3.1. Battery Fundamentals

Lithium-ion batteries (LIBs) structure comprises four principal components, namely negative and positive electrodes, electrolytes, and a separator<sup>273</sup>. Although a diverse range of materials can be utilized for each component, this discussion focuses on lithium iron phosphate (LFP) batteries since its half-cell configuration is used to showcase the functionality of the presented reliable lab automation software packages (Section 4.5). The cathode of the selected battery is made from LFP with a theoretical capacity and energy density of  $\approx 170 \text{ mAhg}^{-1}$  and  $\approx 550 \text{ Whkg}^{-1}$ , respectively<sup>274</sup>. The cathode is coated on an aluminum current collector sheet, which resists corrosion through passivation from electrolyte interactions<sup>275</sup>. The anode is composed of graphite ( $\text{C}_6$ ) with a high theoretical capacity of  $\approx 370 \text{ mAhg}^{-1}$ , which supports the reversible intercalation of lithium ions during charging and discharging cycles<sup>276</sup>. This electrode uses a copper collector for its high conductivity and electrochemical stability. The electrolyte typically contains lithium hexafluorophosphate ( $\text{LiPF}_6$ ) salt, essential for charge transfer and high ionic conductivity, and is dissolved in a mixture of solvents, such as ethylene carbonate (EC) and propylene carbonate (PC). These components in rechargeable LIBs operate based on the “rocking chair” model<sup>275</sup>. In terms of electrochemistry, this involves a series of redox reactions characterized by the movement of lithium ions, which intercalate into one electrode during charging and deintercalate during discharging. In the charging process, lithium ions migrate from the LFP cathode, pass through the electrolyte, and are intercalated into the graphite anode, which is accompanied by a reduction reaction in which the lithium ions accept electrons from the external circuit to form lithiated graphite (Figure 3.10). This charging process increases the cell voltage ( $E_{\text{cell}} = E_{\text{cathode}} - E_{\text{anode}}$ ) due to changes in the chemical potentials of the electrodes. Additionally, a rise in internal resistance can be observed that is caused by degradation or structural change in the electrode materials and the buildup of concentration gradients, impacting the charging efficiency and thermal behaviors. To accommodate these changes, the charging system adjusts the voltage to maintain a constant charging current and to compensate for the increased resistance<sup>277</sup>. During discharge, the process reverses; lithium ions deintercalate from the anode through an oxidation reaction, releasing stored electrical energy<sup>273</sup>. The cathodic reaction, involving the intercalation and

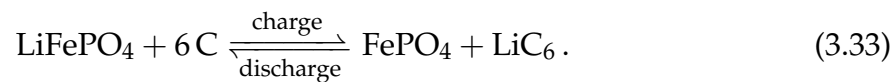
deintercalation mechanisms of lithium ions, can be described as



and the anodic reaction can be expressed as:



Within the electrochemical stability window, the overall reversible reaction, where no decomposition of components occurs, is given by:



This equation illustrates the closed-loop transfer of ions and electrons during these redox reactions, describing the functionality of batteries in storing and releasing energy<sup>278</sup>. The actual amount of electric charge delivered at the rated voltage during each discharge cycle is represented as the discharge capacity ( $Q_{dis}$ ) of a cell and is measured in ampere-hours (Ah). This is empirically determined by integrating the discharge current ( $I_{dis}$ ) over the period  $t$  and mathematically expressed as:

$$Q_{discharge} = \int_0^{\Delta t} I_{dis}(t) dt. \quad (3.34)$$

The charge capacity is calculated analogously. Additionally, the C-rate is a metric that quantifies the rate of discharge or charge of a battery relative to its maximum capacity ( $Q_{nominal}$ ), given in units of  $\text{h}^{-1}$ . This capacity, which differs from the theoretical capacity, represents the usable charge capacity under specified operational conditions and varies with different C-rates due to practical inefficiencies such as increased resistance that lowers the discharge capacity at higher rates. Thus, the C-rate parameter helps to evaluate battery performance. Elevated C-rates can accelerate the degradation of battery components, impacting the balance between operational demands and longevity<sup>277</sup>; it is formulated as:

$$\text{C-rate} = \frac{I}{Q_{nominal}}. \quad (3.35)$$

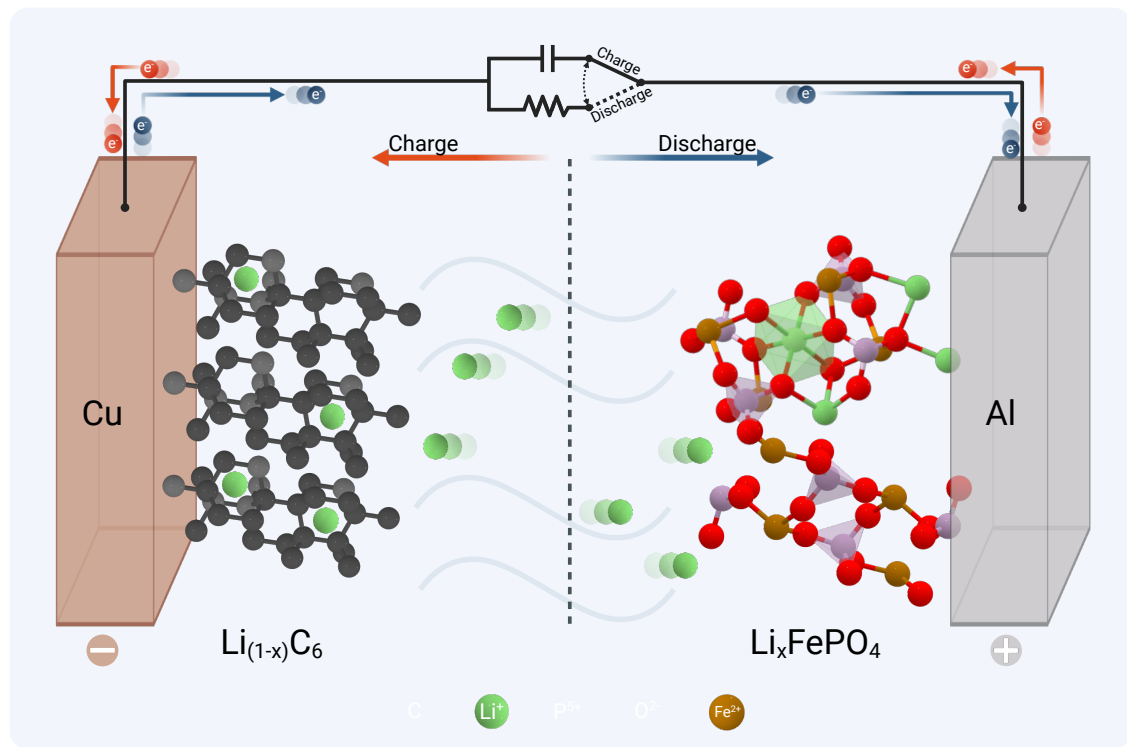


**Figure 3.10.:** The electrochemical process of a rechargeable Li-ion battery during charging and discharging cycles is illustrated by the "rocking chair" model. The anode consists of a graphite-based composite on a copper current collector, and the cathode comprises LFP on an aluminum foil. The direction of electron and lithium-ion flow is indicated by the orange and blue arrows for charge and discharge. Lithium ions are transferred during charging from the cathode to the anode across the electrolyte and intercalate into the graphite layers. This is accompanied by the flow of electrons through the external circuit, resulting in a reduction reaction within the anode to balance the charge. Reversely, the discharge process involves the deintercalation of lithium ions from the graphite layers at the anode, whereby they flow back through the electrolyte and towards the cathode, with electrons traveling through the external circuit to the aluminum sheet, thus delivering electric energy. Crystal structures of LFP, FePO<sub>4</sub>, and graphite were obtained from the Materials Project<sup>66</sup>.

To evaluate the reversibility of the battery's electrochemical processes, it is essential to consider its charge retention capability during cycling. This can be quantified by coulombic efficiency (CE), which is defined as:

$$CE(\%) = \frac{Q_{dis}}{Q_{ch}} \cdot 100. \quad (3.36)$$

This parameter quantifies the percentage of charge that can be recovered from the battery relative to the amount stored during the charging process. A higher CE sug-

gests minimal cycling energy losses and good battery health<sup>277</sup>. The battery's overall condition throughout its lifecycle is defined by its SoH, which is a measurement of the current capacity relative to the initial capacity.

$$SoH = \frac{Q_{current}}{Q_{initial}} \cdot 100. \quad (3.37)$$

A reduction in the SoH is indicative of a diminished practical discharge capacity, which is to be attributed to the deterioration of the electrode material and the depletion of active lithium<sup>279, 14</sup>.

### 3.3.2. Electrochemical Impedance Spectroscopy

EIS denotes a non-destructive analytical technique that applies a sinusoidal potential or a current to a system and measures the resulting sinusoidal electrical response in terms of current or potential<sup>280</sup>. This method enables the linearization of the current-voltage relationship under potentiostatic or galvanostatic conditions. Here, time is associated to angular frequency ( $\omega$ ), and their relation is described by the equation

$$\omega = 2\pi T^{-1} = 2\pi f, \quad (3.38)$$

where  $T$  (s) represents the oscillation period, and  $f$  (Hz) is the frequency. To analyze the system's response, the input signal and its corresponding output in the time domain, which are characterized by a phase shift ( $\phi = \phi_{response} - \phi_{input}$ ), are converted into the frequency domain, using Fourier transform<sup>281</sup>. In this context, impedance ( $Z$ ) is a measure of a system's resistance to the flow of electrical energy across a range of frequencies. Mathematically, this parameter is represented as the complex ratio of voltage to current, extending Ohm's law to include alternating current circuits, and is given by

$$Z(\omega) = \frac{V(\omega)}{I(\omega)} e^{i\phi} = |Z| e^{i\phi}, \quad (3.39)$$

where  $\phi$  ( $^\circ$ ) represents the phase difference and  $|Z|$  ( $\Omega$ ) is the magnitude of the impedance. These parameters, as functions of frequency, are graphically depicted in

a Bode plot, which illustrates the frequency response characteristics of the system. In accordance with Euler’s formula, the impedance can be decomposed into real and imaginary components:

$$Z(\omega) = |Z|\cos(\phi) + i \cdot |Z|\sin(\phi) = \text{Re}(Z) + i \cdot \text{Im}(Z) . \quad (3.40)$$

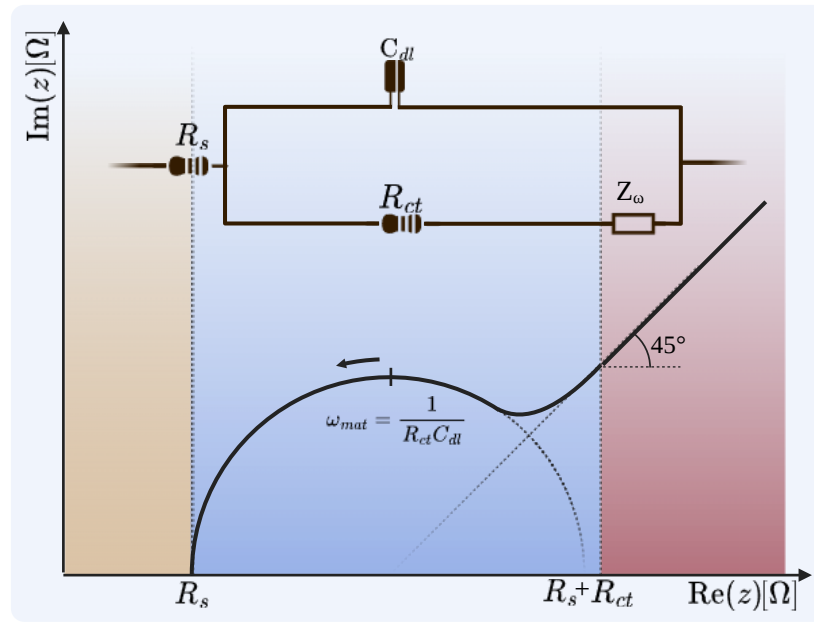


**Figure 3.11.:** Schematic representation of Nyquist plot illustrating the impedance characteristics of a Randles equivalent circuit model (ECM) over a wide range of frequencies. The circuit elements consist of the solution resistance  $R_s$ , which is positioned at the highest frequency and intercepts on the real axis, representing the ionic transport resistance of the electrolyte. The charge transfer resistance,  $R_{ct}$ , is indicative of the kinetic barriers at the electrode-electrolyte interface, and the capacitance,  $C_{dl}$ , is representative of the accumulated charge in the electrode’s double layer. All these charge transfer-controlled features can be observed in the semicircle in the Nyquist plot. The total impedance at low-frequency intercept on the real axis is the sum of  $R_s$  and  $R_{ct}$ . The line at a  $45^\circ$  angle is indicative of a Warburg impedance  $Z_w$ , which models the mass transfer limitations, such as the diffusion of lithium ions in the electrolyte. It is important to note that in non-ideal systems, variations in electrolyte properties and electrode surface conditions result in deviations from ideal capacitive behavior. These deviations can be modeled by a constant phase element, which alters the representation of the Nyquist plot from ideal behavior<sup>281</sup>.

This formulation allows the representation of impedance in a Cartesian coordinate system, as illustrated by a Nyquist plot. This plot deconvolutes various electrochemical phenomena at characteristic frequencies, thereby providing insights into the

kinetics and stability of the system<sup>281</sup>. Here, each phenomenon can be modeled by different elements in an ECM. For instance, a typical ECM known as a Randles circuit incorporates resistors ( $R_s$  and  $R_{ct}$ ), capacitors ( $C_{dl}$ ), and Warburg impedance ( $Z_W$ ) elements. These represent the solution resistance, charge-transfer resistance, and double-layer capacitance and account for lithium-ion diffusion<sup>282</sup> (Figure 3.11). The fitting of the Nyquist plot to the ECM enables the extrapolation of qualitative and quantitative insights into the underlying electrochemical processes. This thesis does not present an experimental application of the aforementioned test, but rather its principles are discussed for the sake of completeness. However, the technique is incorporated into the data analysis package, MADAP, where the ECM is fitted using an “Impedance” Python package<sup>283</sup> that leverages non-linear least squares fit from SciPy module<sup>284</sup>.

### 3.3.3. Cyclic Voltammetry

CV is a versatile electrochemical technique used to study the kinetic aspects of electrochemical reactions. In CV, a controlled, linearly varying potential is applied to an electrode to monitor the resulting currents and to capture the dynamics of electrochemical reactions, including electron transfer rates, species intercalation at the electrode surface, and their diffusion within the electrochemical cell. This method uses a potential-scan mechanism, in which the electrode potential is swept back and forth, resulting in a voltammogram that depicts the system’s diffusion-driven flux and redox behavior. The scan rate determines the speed of the forward and backward sweeps; elevated scan rates result in increased current and reduced diffusion, which has profound effects on the shape of the voltammogram. The current response to the applied potential is modeled by the Butler-Volmer equation, which accounts for the overpotential required to drive the reaction at the desired rate by overcoming energy barriers and dynamic concentration gradients that develop during potential sweeps. The gradients lead to non-steady-state conditions where diffusion limitations cause deviations from the inherently exponential behavior predicted by the Butler-Volmer equation, resulting in peak-shaped features in the voltammogram<sup>285</sup> (Figure 3.12). Mathematically, this relationship is illustrated by the equation

$$i = i_0 \left( e^{\frac{\alpha_a n F}{RT} (E - E_{eq})} - e^{-\frac{\alpha_c n F}{RT} (E - E_{eq})} \right), \quad (3.41)$$



where  $i_0$  ( $\text{A}/\text{m}^2$ ) refers to the exchange current density,  $\alpha$  represents the charge transfer coefficient,  $F$  ( $\text{Cmol}^{-1}$ ) is the Faraday constant,  $R$  ( $\text{JK}^{-1}\text{mol}^{-1}$ ) stands for the gas constant,  $T$  (K) is the temperature, and  $E_{eq}$  (V) is the standard electrode potential at equilibrium. This equation considers both the applied voltage and the electrode's chemical environment, quantifying the impact of the electric field on the electrochemical reaction rate at the electrode interface<sup>285</sup>.

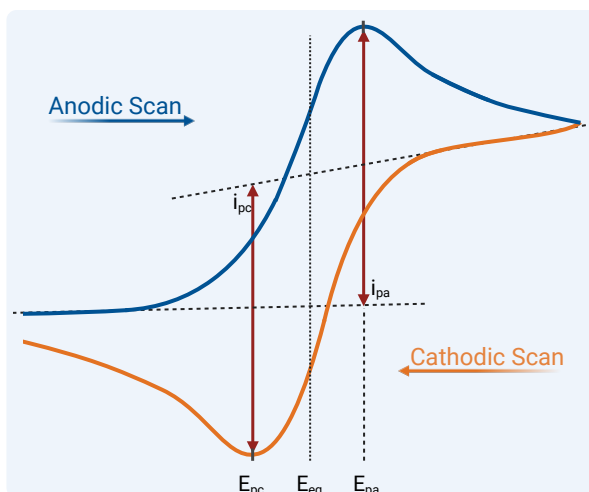


**Figure 3.12.:** Schematic presentation of a voltammogram obtained from a CV test. The graph illustrates a curve obtained during a potential sweep, including anodic and cathodic scans, that recorded the current responses. In the forward pass, an oxidation reaction occurs, followed by the double layer's charging and an anodic peak ( $E_{pa}$ ,  $I_{pa}$ ). During the backward scan, the oxidized species are reduced, resulting in a cathodic peak ( $E_{pc}$ ,  $I_{pc}$ ). The peaks provide further insights into the reversibility of the electrochemical system.

During each scan in CV, the electrode undergoes two processes; the first is the Faradaic process, which involves electron transfer through oxidation and reduction reactions, and the second is the non-Faradaic process, which includes capacitive effects due to the charging of the electrical double layer that occurs without electron transfer between species. During the cathodic sweep, as the potential is scanned negatively, the electrode predominantly exhibits Faradaic behavior with reduction reactions. As the potential becomes increasingly negative, the surface concentration of the reactants decreases, causing the current to rise due to higher reduction rates until the reactants are nearly depleted. Here, the current reaches a maximum, representing a cathodic peak. Following this peak, the current decreases as the diffusion layer

thickens, gradually impeding further mass transport of reactants to the electrode surface. When the sweep direction is reversed to anodic, oxidation reactions begin, and the current rises to reach an anodic peak and then begins to decrease<sup>286</sup> (Figure 3.12). For reversible electrochemical reactions, the voltammogram shows Nernst behavior, illustrating the adjustment of the electrode potential to changes in the concentration of the electroactive species. This relationship is described by the Nernst equation

$$E = E_{eq} + \frac{RT}{nF} \ln \frac{[Ox]}{[Red]}, \quad (3.42)$$

where  $n$  is the number of electrons transferred, and  $[Ox]$  and  $[Red]$  are the concentrations of the oxidized and reduced forms of the species, respectively. According to this principle, the peak currents for anodic and cathodic reactions are identical ( $i_{pa} = i_{pc}$ ), and the peak-to-peak separation ( $\Delta E_p = E_{pa} - E_{pc}$ ) is ideally approximate 59 mV at 25 °C per electron transferred, to maintain equilibrium conditions. Additionally, for these reversible reactions, the diffusion coefficient as  $D$  ( $\text{cm}^2\text{s}^{-1}$ ), which measures the rate at which species diffuse towards the electrode, can be calculated from the peak current using the Randles–Sevcik equation at 25 °C as

$$i = 2.69 \times 10^5 n^{1.5} AC(D\nu)^{0.5}, \quad (3.43)$$

where  $A$  ( $\text{cm}^2$ ) is the electrode area,  $C$  ( $\text{mol}/\text{cm}^3$ ) is the reactive species concentration, and  $\nu$  ( $\text{Vs}^{-1}$ ) is the scan rate. Each cycle of the voltammogram describes the electrochemical characteristics at varying potentials and provides insight into the kinetic properties of the system<sup>285</sup>.



*“Artificial Intelligence is the new electricity.”*

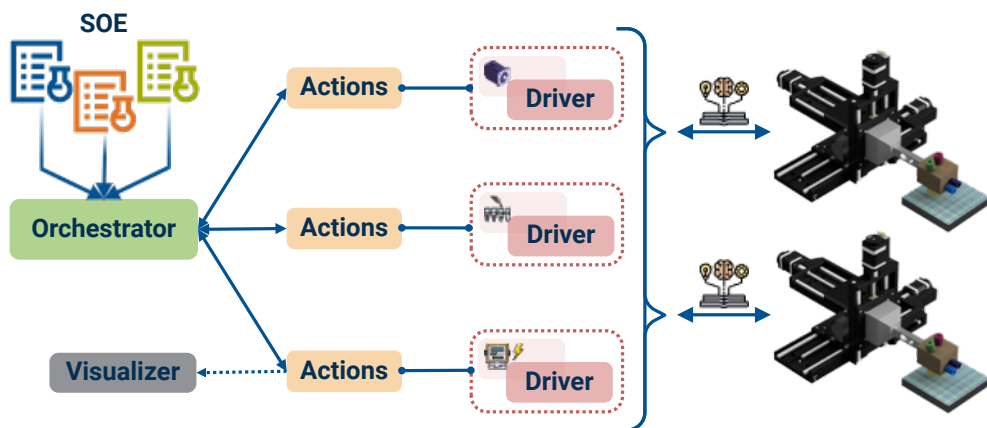
— Andrew Ng

## 4. Results and Publications


This chapter provides an overview of the main articles published in peer-reviewed journals that pertain to and extend beyond the scope of this dissertation. It begins with the demonstration of a hierarchical orchestration platform for autonomous feedback-loop systems, which is detailed in Section 4.1. The data management methods applied in this study and the SDC setup utilized to showcase the framework are presented in co-authored publications by Castelli et al.<sup>191</sup> and Dobass et al.<sup>146</sup>, respectively. Section 4.2 outlines the specifications for designing and developing data analysis software that adheres to FAIR principles. A summary of data-driven methods is presented in a co-authored paper by Benayad et al.<sup>13</sup>. Subsequently, two applications using AI tools will then be discussed. These include the implementation of one-shot active learning in Section 4.3, and the design and implementation of an explainable deep learning framework delineated in Section 4.4. Eventually, Section 4.5 demonstrates the integration of developed AI and computational tools into a reliable and robust acceleration platform that leverages data analysis, data management, and statistical and machine learning algorithms. Additionally, a perspective on the potential for data science integration into material workflows to accelerate materials discovery is provided in a co-authored paper by Stein et al.<sup>16</sup>. Each of the five core peer-reviewed publications highlights the published code repositories and the developed software. A summary of the main article content, individual contributions, the main manuscript, and additional information are also provided.

## 4.1. Enabling Modular Autonomous Feedback-Loops in Materials Science through Hierarchical Experimental Laboratory Automation and Orchestration

### 4.1.1. Publication Details




---

<b>Title:</b>	"Enabling Modular Autonomous Feedback-Loops in Materials Science through Hierarchical Experimental Laboratory Automation and Orchestration"
<b>Journal:</b>	<i>Advanced Materials Interfaces</i> * 2022
<b>Publisher:</b>	Wiley-VCH GmbH
<b>Authors:</b>	<b>Rahmanian, Fuzhan</b> and Flowers, Jackson and Guevarra, Don and Richter, Matthias and Fichtner, Maximilian and Donnely, Phillip and Gregoire, John M. and Stein, Helge Sören
<b>Status:</b>	Published: 6. January 2022
<b>DOI:</b>	<a href="https://doi.org/10.1002/admi.202101987">https://doi.org/10.1002/admi.202101987</a>
<b>Developed Software:</b>	 <a href="https://github.com/helgestein/helao-pub">https://github.com/helgestein/helao-pub</a>

---

\* For reprint permission refer to Section A.1

## Publication Content

The necessity for MAPs is rooted in the need for rapid gain of insights and optimization of materials for their properties of interest. This demands an integrated approach of experimental procedures, characterization, analysis, and machine learning for autonomous planning. Herein, the HELAO framework has been developed with these challenges in mind as a first-of-its-kind solution and has been designed to be versatile, modular, and lightweight to support maximal reusability in orchestrating distributed research instruments across software and hardware. The HELAO architecture is built on a hierarchical structure from low-level drivers to high-level orchestrator, which enhances the scalability of experimental setups and is positioned to ease the incorporation of new functionalities or devices. The developed drivers cover a variety of laboratory devices from manufacturers such as Metrohm, Lang, CAT, Mecademic, and others. These intercompatible drivers can operate independently as required. The driver servers enable communication between devices, while the action servers host higher-level functions that depend on specific instrument configurations, thereby allowing for user customization. At the highest level, the orchestrator manages lists of experiments and coordinates long-running experimental sequences with multiple measurements. HELAO interfaces with a FastAPI web framework to support various synchronous and asynchronous operations, backed by Pydantic type validation. All measurements are displayed through an interactive live visualizer, and all experimental sequences are executed through a scripting tool, which minimizes the need for user-specific programming. This platform's scalability and ease of integration enable it to support inter-laboratory workflows and to operate across different workstations.

HELAO framework adheres to FAIR data principles, thereby contributing to the integrity and accessibility of scientific data by allowing reproducibility of all experimental steps, configurations, metadata, and results through tracking. This system is not limited to experimental execution but also supports simulations. Another notable feature of HELAO is its active learning server integration, which is capable of autonomously planning subsequent experiments and optimizing research outcomes by updating and learning from ongoing results. The framework's ability to parallelize operations further accelerates research. The functionality of this framework is demonstrated in the simulation of determining the local maxima of the Schwefel function.

Here, parallel autonomous experimentation is conducted across two identical setups sharing a common learner and optimizer. Through AL, HELAO achieved a doubling of speed compared to traditional autonomous sequential experimentation.

### **Individual Contributions**

In the development of HELAO, **Fuzhan Rahmanian** contributed substantially to the implementation of essential drivers for the SDC setup suitable for electrochemical applications and designed and integrated the active learning server into the workflow to optimize the parameters autonomously and plan successive experiments. H.S. and J.G. conceived the scaffolding for HELAO and its underlying software structure. **F.R.**, J.F., D.G., M.R., and P.D. developed additional drivers, servers, and actions and conducted experiments to test the framework. J.F. was responsible for designing the orchestrator and integrating the action server of the instruments into it. **F.R.** and J.F. designed and implemented scripts for multiple sequential and parallel experimentation with a distributed thread workload. **F.R.**, J.F. and H.S. wrote the main manuscript, and all authors reviewed the work for publication.

## 4.1.2. Manuscript

## RESEARCH ARTICLE

 Check for updates

**ADVANCED  
MATERIALS  
INTERFACES**  
www.advmatinterfaces.de

## Enabling Modular Autonomous Feedback-Loops in Materials Science through Hierarchical Experimental Laboratory Automation and Orchestration

Fuzhan Rahmanian, Jackson Flowers, Dan Guevarra, Matthias Richter, Maximilian Fichtner, Phillip Donnelly, John M. Gregoire,\* and Helge S. Stein\*

Materials acceleration platforms (MAPs) operate on the paradigm of integrating combinatorial synthesis, high-throughput characterization, automatic analysis, and machine learning. Within a MAP, one or multiple autonomous feedback loops may aim to optimize materials for certain functional properties or to generate new insights. The scope of a given experiment campaign is defined by the range of experiment and analysis actions that are integrated into the experiment framework. Herein, the authors present a method for integrating many actions within a hierarchical experimental laboratory automation and orchestration (HELAO) framework. They demonstrate the capability of orchestrating distributed research instruments that can incorporate data from experiments, simulations, and databases. HELAO interfaces laboratory hardware and software distributed across several computers and operating systems for executing experiments, data analysis, provenance tracking, and autonomous planning. Parallelization is an effective approach for accelerating knowledge generation provided that multiple instruments can be effectively coordinated, which the authors demonstrate with parallel electrochemistry experiments orchestrated by HELAO. Efficient implementation of autonomous research strategies requires device sharing, asynchronous multithreading, and full integration of data management in experimental orchestration, which to the best of the authors' knowledge, is demonstrated for the first time herein.

enabled the emergent paradigm of conducting research in materials acceleration platforms (MAP)<sup>[5,6]</sup>. Within these MAPs different research tasks are accelerated and integrated to efficiently address the ever increasing complexity of materials optimization through targeted materials synthesis, processing, analysis, and insight generation.<sup>[7]</sup>


Demonstrations of autonomous workflows to date,<sup>[8–11]</sup> have been based on a single instrument in a single laboratory.<sup>[12]</sup> This limited purview of the autonomous experimentation is rooted in the laboratory middleware in which orchestration of the laboratory hardware occurs within a single computer-instrument pairing.<sup>[11]</sup> Some notable examples include ChemOS,<sup>[12]</sup> which in principle is capable of distributing work across different machines through the ROS<sup>[13]</sup> backend. This inarguably powerful software does however impose complex software dependencies that grow with increased purview of the experimental platform. While commercial software such as LabView by National

### 1. Introduction

Ever increasing performance demands necessitate the acceleration of materials science and chemistry.<sup>[1,2]</sup> Progress within the Materials Genome Initiative,<sup>[3]</sup> advances in high-throughput experimentation,<sup>[4]</sup> and proliferation of machine learning have

Instruments can facilitate programming for instrument automation, it does not meet the needs of the MAP community due to its incompatibility with the open-source development of version-controlled software. In instances where there is no (official) application programming interface (API) for a device, or an instrument's software driver must continually evolve with

F. Rahmanian, J. Flowers, M. Fichtner, H. S. Stein  
Helmholtz Institute Ulm (HIU)  
Helmholtzstr. 11, 89081 Ulm, Germany  
E-mail: helge.stein@kit.edu

 The ORCID identification number(s) for the author(s) of this article can be found under <https://doi.org/10.1002/admi.202101987>.

© 2022 The Authors. Advanced Materials Interfaces published by Wiley-VCH GmbH. This is an open access article under the terms of the Creative Commons Attribution-NonCommercial License, which permits use, distribution and reproduction in any medium, provided the original work is properly cited and is not used for commercial purposes.

<sup>[†]</sup>Present address: Carleton College, Northfield, MA, USA

DOI: 10.1002/admi.202101987

F. Rahmanian, J. Flowers, H. S. Stein  
Karlsruhe Institute of Technology (KIT)  
Institute of Physical Chemistry (IPC)  
Fritz-Haber-Weg 2, 76131 Karlsruhe, Germany  
D. Guevarra, M. Richter, P. Donnelly,<sup>[†]</sup> J. M. Gregoire  
Division of Engineering and Applied Science and  
Liquid Sunlight Alliance (LiSA)  
California Institute of Technology (Caltech)  
Pasadena, CA 91125, USA  
E-mail: gregoire@caltech.edu  
M. Fichtner  
Karlsruhe Institute of Technology (KIT)  
Institute of Nanotechnology (INT)  
P.O. Box 3640, D-76021 Karlsruhe, Germany



hardware advancements, ROS and LabView can incur substantial overhead in software management.

Modular software design facilitates community sharing of techniques across sub-fields. For example, organic chemistry uses tailored languages,<sup>[14]</sup> to express research tasks in a human and computer readable format.<sup>[15,16]</sup> Sharing of experimental control techniques across such domains requires a high level of modularity in conjunction with the data management-informed design of the experimental control framework.

In addition to the necessity of being able to orchestrate a multitude of laboratory instruments, there is a critical need to be able to trace back all undertaken steps that lead to the acquisition of data or synthesis of a material,<sup>[14,17]</sup> beyond FAIR<sup>[18]</sup> guidelines. Experiment provenance management is critical for enabling reproduction of an experiment.<sup>[19]</sup> Such reproductions or more general sharing of experiment protocols can be enabling of the computer automation of laboratory devices via drivers that provide an abstraction layer between the central software and hardware. If these criteria are met, autonomous inter-laboratory workflows<sup>[7]</sup> can be deployed and motivate the discretization of an experimental provenance into its elementary instrumental actions. We therefore view the levels of experiment abstraction to be hierarchical in nature.

The hierarchical laboratory automation and orchestration framework was built with the goals of being able to integrate any laboratory device for which a software driver is available or can be written, and to enable any configuration of the devices including serial and parallel experimentation, sharing of equipment across multiple instruments, and orchestration of multiple measurements in multiple laboratories. To facilitate continued adoption of active learning in experiment workflows,

the framework is designed for facile switching between human and machine-based experiment selection. The framework adopts a data management wherein all gathered data and all instructions are stored in a "FAIR" way, giving the instruction data the same level of attention as the resulting measurement data. For these requirements to be met, we seek a software framework for communicating with devices hosted or operated on different computers (i.e., some instruments are mutually exclusive to be connected on a PC due to driver constraints). We seek to be platform independent and minimize additional requirements such as extensive software dependencies.

In the present work we describe the hierarchical experimental laboratory automation and orchestration (HELAO) framework to address the needs of next-generation experiments. At a high level, the modularity of HELAO is built upon a widely used web framework called fastAPI<sup>[20]</sup> as shown in **Figure 1**. The main design idea is to represent every device of an instrument as a (asynchronous) web server (Figure 1, right side). Basic functions of devices are exposed to and bundled by actions, which themselves are again web servers. Only these actions are called by an orchestrator executing experiments on one or multiple instruments (Figure 1, left side). For future proofness, HELAO was developed in python 3.8+ with type hinting and pydantic type validation. The modular design allows for the integration of arbitrary devices, including those operated through OPC-UA.<sup>[21]</sup>

The design guidelines and protocols necessary to orchestrate instrumentation in the laboratory are outlined in the following sections, together with a detailed description of the individual constituents. We demonstrate the orchestration of an active learning run on two instruments and deposited the resulting

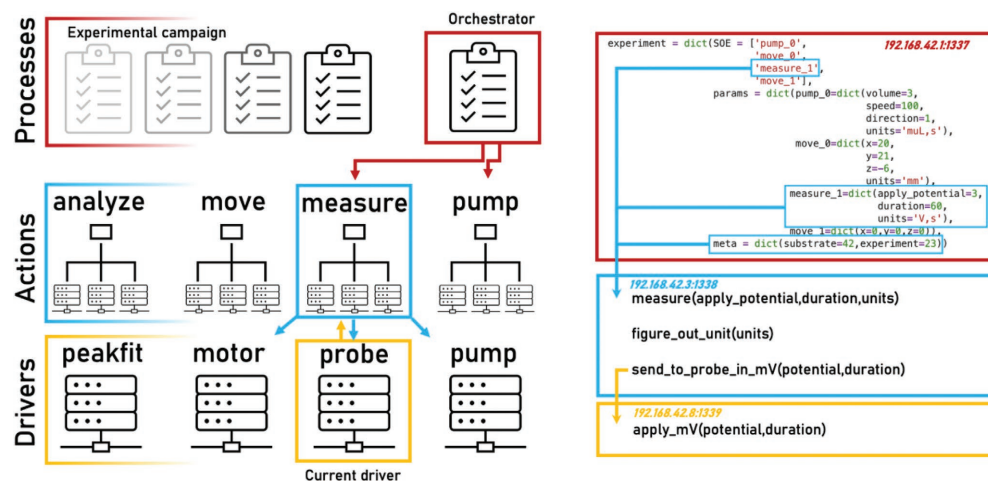


**Figure 1.** A schematic representation of HELAO where experiments are executed by sequentially calling actions which are high level wrappers for lower level driver instructions. Communication goes hierarchically down from the orchestrator level to actions, which may however communicate among each other, to the lowest level of drivers which can only communicate with actions. The orchestrator, actions, and drivers are all exposing python class functions through a web interface allowing for highly modular and distributed hosting of each item. Experiments are encoded as python dictionaries (a data type) containing a sequence of events (SOE) that outlines in which the actions are to be executed. Many experiments form a process. All actions require parameters and metadata that are all echoed back.

data including all instructions and the code at [github.com/helgestein/helao-pub](https://github.com/helgestein/helao-pub).

## 2. Results

### 2.1. Implementation of Hardware Drivers

The aim of HELAO is to be a universal laboratory automation framework, democratizing accelerated experimental research workflows. To this end, the two laboratories at the California Institute of Technology (Caltech) and Karlsruhe Institute of Technology (KIT) started to implement major hardware components amenable for automatization. In Table 1, all currently implemented hardware drivers are listed. During development of these drivers, it became apparent that there exist two major types of drivers based on whether their function calls are natively blocking or non-blocking. Those with non-blocking operations typically accept an instruction, execute it, and require the user to ask if the current operation is finished.

A special class of devices is auxiliary (aux) devices. These are broadly defined as software “devices” used, for example, for data analysis, regression, and prediction. These aux drivers could in principle be written for any python interfaceable software or hardware which is necessary for a special experiment, for example, background inference algorithms<sup>[22]</sup> or special machine learning models.<sup>[23]</sup>

With the devices available at the time of writing this manuscript, highly complex instruments have and are being built, whose detailed descriptions will be the subject of future work. As an initial example of the scope of the present HELAO implementations, the operated instruments are comprised of the devices shown in Table 1 that include four scanning droplet cells (SDCs) at Karlsruhe Institute of Technology (KIT) (each consisting of lang, autolab, pump, force, aux, kadi), one SDC at Caltech (galil,

gamry), a coupled Raman and FTIR spectrometer (owis, ocean, arcoptix, aux, kadi), a battery cycler (arbin, aux), and a coin cell assembly system (mecademic, rail, arbin, arduino, aux).

### 2.2. Hardware-in-the-Loop Active Learning

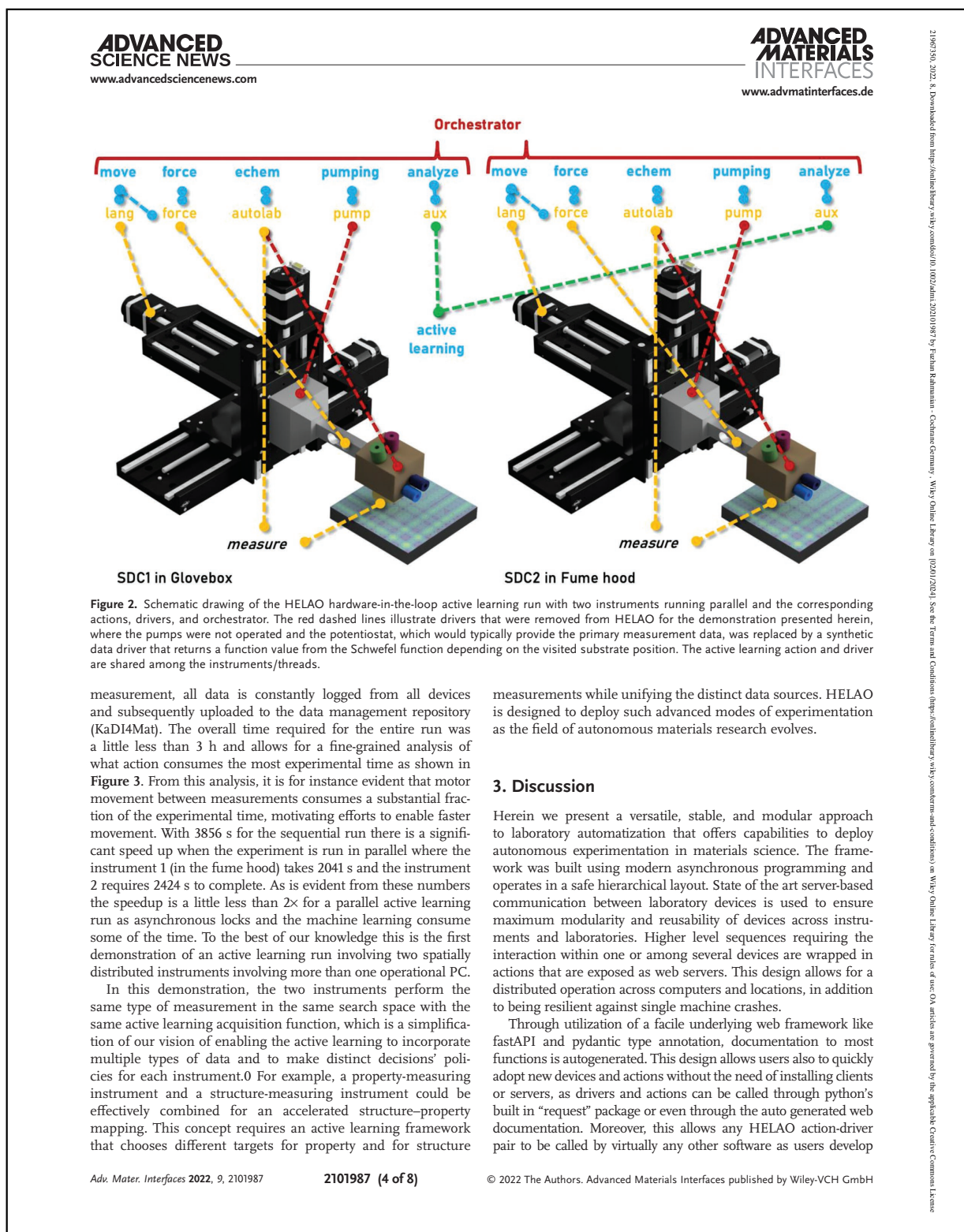
A hardware-in-the-loop demonstration run of HELAO is shown in Figure 2. The instrument is copied two times where one setup was run in a fume hood and another one was run in a glove box. The two instruments share a common learner and optimizer, which are controlled along with both instruments by a single orchestrator. An example video of a parallel active learning run can be found in the Supporting Information. To demonstrate the operation and identification of a known global maximum, the potentiostat driver in each instrument was replaced by a synthetic data generator. This synthetic driver returns a scaled Schwefel function<sup>[24]</sup> depending on the position where the SDC touches down on a substrate, providing the source data with which the active learning server identifies the next target substrate position 3.

The active learning run is stopped once a threshold value (top percentile) is found. Actions in this run consist of, for example, “move to waste”, “remove the droplet”, “move to sample offset”, “move to the defined point”, “move down to substrate”, “get output value”, “predict the next best position using active learning algorithm.” The hdf5 file generated during this run was recorded on 05.10.2021 and has been uploaded to KaDI4Mat upon completion of the session under the records 20287 and 20280. Public release of the dataset<sup>[25]</sup> with the <https://doi.org/10.6084/m9.figshare.16798177.v1> had been triggered on 09.10.2021. The hdf5 file for this run may also be found in the Supporting Information.

One experiment takes ≈108 s. Depending on the number of datapoints the learning step requires more time. During the

**Table 1.** Currently implemented devices in the laboratories at KIT and Caltech. Instruments built from this include scanning droplet cells, high-throughput spectrometers, and a battery assembly robot. The extreme modularity allows us to mix and match any of these devices by simply defining a sequence of events, that is, to build an integrated SDC and spectrometer or a sample exchange robot without code changes to HELAO. For each device we note the communication protocol and the physical quantity being controlled and/or measurement. We also note whether the instrument is “natively blocking” meaning that the device is unable to process new commands until the currently running command is finished.

Device name	Type	Communication	Measures/Controls	Manufacturer	Natively blocking
lang	Motion	.net API	Position	Lang GmbH	No
galil	Motion, IO	TCP/IP	Position	Galil Motion Control Inc.	No
owis	Motion	Serial commands	Position	Owis GmbH	No
mecademic	Motion	Python TCP/IP API	Position, state	Mecademic Ltd.	no
rail	Motion	TCP/IP	Position	Jenny Science AG	No
autolab	Potentiostat	.net API	Electrochemistry	Methrohm Autolab B.V.	Yes
gamry	Potentiostat	.dll for serial communication	Electrochemistry	Gamry Instruments Inc.	Yes
arbin	Potentiostat	autohotkey	Electrochemistry	Arbin Inc.	No
pump	Pumping	Serial commands	n.a.	CAT engineering GmbH	No
arcoptix	Spectroscopy	.dll api	IR spectra	arcoptix S.A.	Yes
ocean	Spectroscopy Raman	Python package	Raman spectra	ocean insights GmbH	Yes
force	force sensing	Serial commands	Force	ME Meßsysteme GmbH	n/a
arduino	Relays, I/O	Python package	n.a.	arduino	No
kadi	Data management	Python package	n.a.	KIT	Yes
aux	Machine learning and analysis	Python package	n.a.	n.a.	Yes



*Adv. Mater. Interfaces* 2022, 9, 2101987

**2101987 (4 of 8)**

© 2022 The Authors. Advanced Materials Interfaces published by Wiley-VCH GmbH

21067350, 2022, 8, Downloaded from https://onlinelibrary.wiley.com/doi/10.1002/admi.202101987 by Fudan University, Cochrane Germany, Wiley Online Library on [02/01/2024]. See the Terms and Conditions (https://onlinelibrary.wiley.com/terms-and-conditions) on Wiley Online Library for rules of use; OA articles are governed by the applicable Creative Commons License

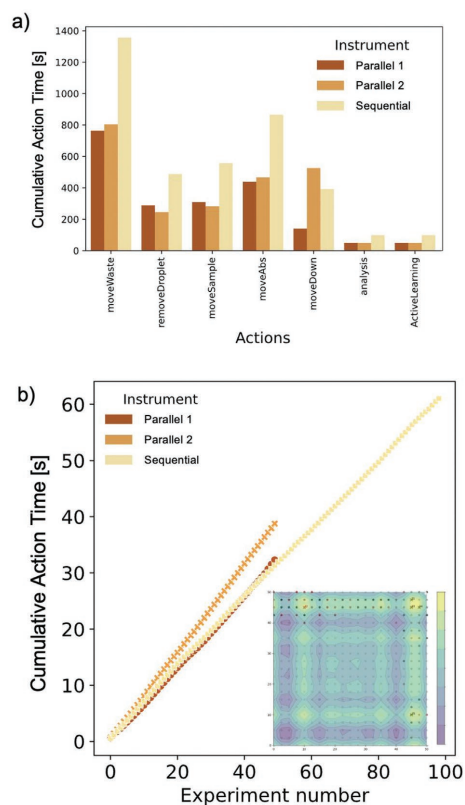


**Figure 3.** a) Time spent at each action for a sequential and a parallel run with two instruments; b) total time spent per run. The time spent does not form a perfectly straight line as some actions need different time (i.e., movements are shorter or longer). The inset shows the parallel run and highlights visited points in black and red depending on whether they were visited by instrument 1 or 2. The sequence of events for each measurement is typically the order shown in the horizontal axis of (a).

orchestrators to employ complementary modes of research. If users wish to deploy active learning to a device that does not accept standard web requests like OPC-UA (often encountered in industrial settings) fastAPI compatible wrappers can be built.

This high degree of modularity and interoperability is only possible through a very lightweight design that puts relatively few restrictions on the user compared to middleware like ROS or ChemOS. Other competing softwares and frameworks are ARES OS that is currently only demonstrated to operate on a single computer instrument pairing. Another mature and great alternative to the lightweight implementation of HELAO is the bluesky project.<sup>[26]</sup> Bluesky works with similar hardware abstraction ideas like HELAO, but puts significantly more constraints on a user and is, in our view, more built around streamlining the research process as a whole. However, orchestrating multiple instruments

in parallel has not been demonstrated by any other laboratory automation framework. These parallelization efforts will be increasingly impactful with development of optimizers that incorporate uncertainty and multiple optimization strategies.<sup>[27]</sup>

The framework is built with the goal of being fully FAIR compliant and allows users to rerun an experiment without much or any overhead. We view this degree of data management to be FAIR+. By logging every possible parameter along the entire research process, it is possible to extract utilization figures, find bugs, and determine bottlenecks in high-throughput experimentation. Direct interfacing with data management software has been demonstrated, to the best of our knowledge, for the first time in an autonomous research environment. All data gathered during the active learning sessions has been automatically uploaded upon the completion of the session and is publicly available at figshare<sup>[25]</sup> and from the Supporting Information of this manuscript. Within the university network all recorded data is made publicly available by default without an embargo period as a statement to encourage more data sharing. HELAO is demonstrated to be stable and versatile and is published under the LGPL license at <https://github.com/helgestein/helao-dev>. Stand-alone example configurations with reference driver implementations and a how-to guide of writing custom drivers are available alongside documentation thereof as part of the public code repository.

The parallel active learning run with hardware-in-the loop of HELAO demonstrates for the first time that two (and technically unlimited more) spatially separated instruments in a materials science laboratory are capable of collaboratively optimizing together for faster discovery. Contributions and collaborations with and by the community to expand the hardware support for HELAO is therefore warmly welcome. Future efforts will aim to bridge HELAO with methods from theoretical materials' science to build modular physics-informed instrumentation and autonomous feedback loops connecting laboratories.

#### 4. Experimental Section

**Design Guidelines and Protocols:** From the bottom-up hardware perspective, a research instrument is an assembly of devices. A device is a piece of laboratory equipment, defined as the largest "thing" that has a dedicated communication stream, that is, a multi-channel potentiostat, or a motor control board.

Devices are typically shipped with a driver that enables access to some or all its functions, that is, measuring a current. From the top-down perspective, a user or operator wishes to perform a series of experiments, which are each a list of actionable events defined as "actions" in HELAO. The actions are to be executed in a particular order with predefined or variable parameters and/or designed on-the-fly via a decision policy. In this latter case, evaluation of the decision policy can be viewed as a particular type of action whose execution impacts future actions. The instructions for an experimental campaign are given to an orchestrator, which governs their sequential execution from a queue. Each action is materialized by the drivers, thereby completing the top-to-bottom instrument framework. Everything that happens to or on that instrument originates within the orchestrator.

In order for the ensemble of devices to operate in concert as a single instrument, it is convenient to assemble the various elements listed above into a single software framework. Hierarchically from bottom to top, each device driver (internally communicating through, for example, serial, TCP/IP commands, or a dynamic link library) is exposed through

a `uvicorn`<sup>[28]</sup> web server through `fastAPI`. Construction of actionable functions ("actions") are constructed from the API calls exposed by the drivers, where each action may involve multiple API calls.

An example of an action to pump a mixture of three fluids would therefore be "initiated" by the orchestrator calling the respective action. This action then calls the pump driver server. Internally the driver server is sequentially called by the mixture action as the hardware requires us to first initialize each pump channel, prime the pumps, and only then turn the pumps on. The orchestrator will receive a nested reply from the action that entails all information exchanged, down to the lowest level, that is, initialization, priming, execution.

A rigorous commitment to data management is foundational to this framework's implementation. Requests to the driver and action servers track all functions called, as well as all (echoed) input parameters and outputs of those functions. The orchestrator tracks additional metadata, such as the time at which an action was performed or the point on a substrate at which an experiment was conducted, in addition to accepting arbitrary custom metadata. All of these are then automatically saved (redundantly), in the native file format (if applicable), and in an `hdf5` file together with the parameters and metadata. Methods for depositing the `hdf5` file into institutional repositories like `KaDI4Mat`<sup>[29]</sup> or `MEAD`<sup>[19]</sup> repositories are automatically executed after each session. From `KaDI4Mat`<sup>[29]</sup> experimental data can be accessed internally but also be shared with the community through materials cloud or to inform simulations through `AIDA`<sup>[30,31]</sup>.

Due to each element of the authors' software framework being a server, a very high degree of modularity is achieved. This allows, for instance, a single instance of a device to fulfill requests from multiple action servers sequentially. This type of resource sharing requires the actions to be programmed to ingest calls from multiple orchestrators, for example by notifying the orchestrators of the un/availability of each action. A more straightforward implementation of resource sharing is for a single orchestrator to govern multiple instruments with a shared piece of equipment, which they demonstrate herein. More generally, this design allows for distributed hosting of devices on different machines, potentially dispersed around the globe.

**Drivers and Driver Servers:** Any (autonomous) experimental workflow consists of smaller organizational units, that is, a `SDC`<sup>[32]</sup> instrument consists of several hardware devices such as motors, a force sensor, pumps, and a potentiostat. In addition, there are software devices such as data analysis and experimental design. All of these devices need to be able to receive commands, perform the instruction, and reply with measurement data or a status and echo back the input parameters. With respect to the orchestrator, interaction with an analysis or active learning module is equivalent to that of a hardware device, motivating virtual and physical devices to be implemented in the same manner.

**Driver Server Design:** Drivers provide the lowest-level interaction with devices based on the elementary communication commands for the respective device, for example, connect, disconnect, query the device status, or read data. Some drivers are therefore more complex than others, as some devices offer direct python APIs whilst others require development of python wrappers or source code. Positively notable examples are for instance python drivers offered by Mecademic or Palmsens offering well-documented software development kits (SDKs). Each device is paired to a dedicated driver server. Calling driver functions can only be done through the web-based API by sending web requests, enabling software modularity that mimics hardware modularity wherein devices can be reconfigured into new instruments.

**Driver Parameters:** Drivers accept parameters, which are validated through pydantic data types that inherit from the pydantic's `BaseModel`. This automatically annotated and type-hinted validation scheme allows users to assess how a request should be formatted in order to receive a desired device behavior. Additionally, the pydantic validation scheme ensures proper data handling, easing data management downstream. Traceability and ease in debugging are ensured by each driver server echoing all provided input parameters alongside the output data. For this purpose, the return object from any server including drivers is a python dictionary (an unsorted data type containing key value pairs) containing

two keys for the input parameters and output data. The parameter key is described by its name, the value(s), and optionally a physical unit. The data key contains data, which contains the data acquired or derived from the device. These python dictionaries play a signal role between different organizational units, for example calling the pump requires specification of volume, speed, and direction. The response from the pump (a device acting but not measuring) is the entire serial string communication response (potentially containing valuable error messages) from the pump as output. The units returned for pumping are for instance speed in microliters per minute, total volume in microliters, and a binary flag for forward versus backward pumping direction.

**Actions and Action Servers Design:** Hierarchically above drivers, actions wrap one or many driver functions such that the action function has a name and parameters that are meaningful for the deployment of the device(s) in a particular type of experiment. This provides an abstraction layer where two action functions can be programmed in different labs using different devices/drivers, enabling shared higher-level code that calls the action functions. Similar to driver servers, actions also expose their functionalities as servers and again are not limited to a single instrument. Communication with multiple device drivers is intended for when knowing what multiple devices are needed to realize a single physical action, such as motor actuation with feedback from a force sensor. To manage shared driver/device-level resources, direct communication between drivers is forbidden, requiring any such message passing to occur via the action server.

**Action Parameters:** Similar to driver servers, the return statement of an action server is a python dictionary containing the parameters and data. The output from an action can be customized for the specific use case, but is generally the aggregate return statements received from all driver server calls downstream. After execution of the relevant action function, the return statements of the called actions will be received by the orchestrator as the highest level of this hierarchy.

A major advantage of driver/action distinction is the possibility of multiple operating computers sharing one device. Any failures on a higher level (i.e., computer crash and/or program failure of the deployed visualizer or orchestrator) do not affect the operation of an instrument.

This design also facilitates the resolution of hardware conflicts and smart instrument communication, since some simultaneously-executing actions could logically cause a contradiction. Therefore, a driver blocks further execution until the current request has been fulfilled. For instance, when the force sensor is measuring the amount of applied force as an action, this action server will block execution of subsequent actions until the current action is finished, which is implemented by awaiting (an asynchronous function call) the response from the force sensor driver. After the awaited response is received, the next action will be called. This locked execution of sequential instructions allows for a safe operation without the need of a state machine. An alternative implementation would require a state machine on the highest level, thus violating the design principle that dictates little to no changes upon addition of new hardware.

**Orchestrator/Local and External Database:** The highest level in the framework is the orchestrator, which sends out instructions to actions from a list of experiments to be performed, where the orchestrator also holds the sequence of actions and the respective parameters needed to perform each experiment. The orchestrator server accepts experiments through an API function called `addExperiment`, which adds an experiment to a list that is executed in the first-in-first-out order. Upon exhaustion of experiments from the process, the orchestrator remains online and awaits the next experiment(s). In total, initializing a HELAO session involves launching  $n + m + 1$  servers, where  $n$  is the number of devices in the system and  $m$  is the number of action servers. In the standard configuration, each driver is controlled by its own action server ( $m = n$ ). Alternatively, an action server may govern multiple devices or a driver may be directly incorporated into an action server ( $m < n$ ). Based on an instrument-specific configuration file, a launch script governs the initialization of each server. If two copies of an instrument exist, they require unique configuration files with unique IP addresses, such that deploying HELAO for a cloned instrument can be achieved by updating the IP addresses in a copy of the configuration file.



**Defining a Process:** The main purpose of the orchestrator is the execution of a list of (dynamically editable) experiments from the process as well as data management. For defining a sequential experiment involving multiple devices, experiments need to be specified by a sequence of what actions are to be executed in a particular order with all necessary parameters. An instrument is factually defined by the devices called in a sequence of events. An experiment is defined by a python dictionary containing two dictionary keys: the Sequence of Events (SOE) key, which contains an ordered list outlining the exact order in which actions are to be executed and the "params" key containing all necessary parameters for any of the actions outlined in the SOE. As actions may be called multiple times they are numbered sequentially in the SOE. Calling an action through the orchestrator requires four parts: the name of the action, the desired function, a number which indicates the  $n$ -th time that we call that specific action within a SOE and the thread number (e.g., "motor/moveAbs-3:1" for calling the third absolute movement of a motor belonging to thread 1). Thread numbers are important for deploying active learning across multiple instruments. Two or more instruments/threads run independent of each other until some action requires input from all threads or a SOE is finished.

The parameters for actions are stored under the "MoveAbs-3" key in the parameter dictionary and contains the specific values for running that particular action (i.e.,  $dx = 2$  mm,  $dy = 3$  mm,  $dz = 0$  mm).

**Defining a Session:** To start and end a session lasting for one or more experiments the first and last actions to be called are the "start" and "finish" actions, natively implemented within the orchestrator (i.e., not as servers), hence being called native actions. The data acquired within a session is locally stored in a single hdf5 file that is then uploaded to KaDI4Mat upon calling the "finish" action. Storing data locally and uploading it at the end of a session has been shown to be significantly faster and avoids reliance on the speed or availability of the master database, which may not be directly controlled by the lab running the experiments. An illustrative example for this design choice is when we measured a series of Raman spectra and performed the upload after taking each spectrum. Whilst each spectrum only took a second to measure, the upload time was comparable, forcing instrument down time that was remedied by asynchronous data uploading.

**Data Analysis and Machine Learning Servers:** A goal of HELAO is to enable active learning accelerated experiments across a wide range of laboratory instruments. Active learning does however require automatic data analysis and machine learning based suggestion of the next best subsequent experiment.

These two functionalities are implemented as servers in HELAO. On a high level, active learning within the HELAO framework is simply the alteration of parameters of an action by some suggestion of an algorithm. The parameter to be changed in a subsequent experiment is referred to as the "target". The algorithm needs to have access to all (analyzed) data to suggest the target. This "source" data needs to be well posed for the machine learning algorithm, which typically requires analysis of the raw data. The automated data analysis in HELAO is again a server-action. A unique aspect of an analysis server is its required access to raw data, which is implemented by using pointers to the location in the orchestrator memory of where relevant data (the source data) is stored. Likewise, the server dedicated to machine learning for active learning needs to be pointed to the input and output values of the analyzed data. Inside the active learning action, the datasets are aggregated on-the-fly from the orchestrator temporary storage (what is later the hdf5 file being uploaded). A target can be specified from a list of candidates or be freely decided by the algorithm, depending on the chosen optimizer, and upon receiving the target the orchestrator updates and runs the pending measurement action.

These functionalities allow for autonomous operation where the user only has to define the budget of active learning runs, pointers to the input and output values, and the choice of optimizer and the estimator.

The active learning server can be equipped with a broad range of optimizers and regression algorithms. Also, several acquisition functions have been implemented including expected improvement (EI) and probability of improvement (POI). We envision the possibility

for incorporating different fidelity sources by adaption of optimizers that can handle different fidelities, which is an active area of machine learning research where advancements can be readily incorporated into HELAO.

As some ML algorithms require significant computational resources within a thread and some actions are data-transfer intensive, servers may become unresponsive. To solve this issue, the most computationally expensive tasks like machine learning can be wrapped inside a celery<sup>[3]</sup> server. Celery is a server-based framework capable of distributing high workloads across compute clusters. We empirically observed this necessity for long running active learning runs with a high degree of freedom.

**Visualizer:** On the same hierarchical level of the orchestrator is the visualizer, which can be viewed as a "read only" orchestrator that has global access and does not store data. This server can display the live data of, for example, electrochemical test measurements or Raman spectroscopy to assess data quality during a run.

## Supporting Information

Supporting Information is available from the Wiley Online Library or from the author.

## Acknowledgements

This work contributes to the research performed at CELEST (Center for Electrochemical Energy Storage Ulm-Karlsruhe) and was partly funded by the Deutsche Forschungsgemeinschaft (DFG, German Research Foundation) under Germany's Excellence Strategy – EXC 2154 – Project number 390874152. This project has also received funding from the European Union's Horizon 2020 research and innovation program under grant agreement No 957189. Design of software architecture at Caltech was supported by the Liquid Sunlight Alliance, which is supported by the U.S. Department of Energy (DOE), Office of Science, Office of Basic Energy Sciences (BES), Fuels from Sunlight Hub under Award Number DE-SC0021266. The authors would like to thank Ephraim Schoof for developing the KaDI4Mat API and helping in the initial interfacing with data management. They would like to thank KIT IAM for hosting KaDI4Mat.

Open access funding enabled and organized by Projekt DEAL.

## Conflict of Interest

The authors declare no conflict of interest.

## Author Contributions

H.S.S. and J.M.G. conceived the idea and designed the first software layout. H.S.S. developed the first drivers and server-based communication protocols. F.R., J.F., D.G., M.R., and P.D. implemented drivers, wrote actions, and conducted the experiments. F.R. implemented drivers pertaining to SDC and deployed machine learning algorithms to HELAO. J.F. integrated these contributions into the orchestrator. All authors reviewed the manuscript.

## Data Availability Statement

The data that support the findings of this study are openly available in [figshare] at [https://doi.org/10.6084/m9.figshare.16798177.v1], reference number [16798177].

## Keywords

laboratory automation, materials acceleration, high-throughput experimentation, data management

Received: October 12, 2021

Revised: November 21, 2021

Published online: January 6, 2022

- [1] K. Alberi, M. B. Nardelli, A. Zakutayev, L. Mitas, S. Curtarolo, A. Jain, M. Fornari, N. Marzari, I. Takeuchi, M. L. Green, M. Kanatzidis, M. F. Toney, S. Butenko, B. Meredig, S. Lany, U. Kattner, A. Davydov, E. S. Toberer, V. Stevanovic, A. Walsh, N.-G. Park, A. Aspuru-Guzik, D. P. Tabor, J. Nelson, J. Murphy, A. Setlur, J. Gregoire, H. Li, R. Xiao, A. Ludwig, et al., *J. Phys. Appl. Phys.* **2019**, *52*, 013001.
- [2] J.-P. Correa-Baena, K. Hippalgaonkar, J. van Duren, S. Jaffer, V. R. Chandrasekhar, V. Stevanovic, C. Wadia, S. Guha, T. Buonassisi, *Joule* **2018**, *2*, 1410.
- [3] M. L. Green, C. L. Choi, J. R. Hatrick-Simpers, A. M. Joshi, I. Takeuchi, S. C. Barron, E. Campo, T. Chiang, S. Empedocles, J. M. Gregoire, A. G. Kusne, J. Martin, A. Mehta, K. Persson, Z. Trautt, J. Van Duren, A. Zakutayev, *Appl. Phys. Rev.* **2017**, *4*, 011105.
- [4] E. J. Amis, X. D. Xiang, J. C. Zhao, *MRS Bull.* **2002**, *27*, 295.
- [5] Materials Acceleration Platform—Accelerating Advanced Energy Materials Discovery by Integrating High-Throughput Methods with Artificial Intelligence. 109, <http://mission-innovation.net/wp-content/uploads/2018/01/Mission-Innovation-IC6-Report-Materials-Acceleration-Platform-Jan-2018.pdf>.
- [6] M. Aykol, J. S. Hummelshøj, A. Anapolosky, K. Aoyagi, M. Z. Bazant, T. Bligaard, R. D. Braatz, S. Broderick, D. Cogswell, J. Dagdelen, W. Drisdell, E. Garcia, K. Garikipati, V. Gavini, W. E. Gent, L. Giordano, C. P. Gomes, R. Gomez-Bombarelli, C. B. Gopal, J. M. Gregoire, J. C. Grossman, P. Herring, L. Hung, T. F. Jaramillo, L. King, H.-K. Kwon, R. Maekawa, A. M. Minor, J. H. Montoya, T. Mueller, et al., *Matter* **2019**, *1*, 1433.
- [7] H. S. Stein, J. M. Gregoire, *Chem. Sci.* **2019**, *10*, 9640.
- [8] K. F. Jensen, C. W. Coley, N. S. Eyke, *Angew. Chem., Int. Ed.* **2020**, *59*, 22858.
- [9] C. W. Coley, N. S. Eyke, K. F. Jensen, *Angew. Chem., Int. Ed.* **2020**, *59*, 23414.
- [10] T. Dimitrov, C. Kreisbeck, J. S. Becker, A. Aspuru-Guzik, S. K. Saikin, *ACS Appl. Mater. Interfaces* **2019**, *11*, 24825.
- [11] P. Nikolaev, D. Hooper, F. Webber, R. Rao, K. Decker, M. Krein, J. Poleski, R. Barto, B. Maruyama, *npj Comput. Mater.* **2016**, *2*, 16031.
- [12] L. M. Roch, F. Häse, C. Kreisbeck, T. Tamayo-Mendoza, L. P. E. Yunker, J. E. Hein, A. Aspuru-Guzik, *Sci. Rob.* **2018**, *3*, eaat5559.
- [13] M. Quigley, B. Gerkey, K. Conley, J. Faust, T. Foote, J. Leibs, E. Berger, R. Wheeler, A. Ng, *Proc. of the IEEE Intl. Conf. on Robotics and Automation (ICRA), Workshop on Open Source Robotics*, Kobe, Japan, May **2009**.
- [14] I. M. Pendleton, G. Cattabriga, Z. Li, M. A. Najeeb, S. A. Friedler, A. J. Norquist, E. M. Chan, J. Schrier, *MRS Commun.* **2019**, *9*, 846.
- [15] P. S. Gromski, J. M. Granda, L. Cronin, *Trends Chem.* **2020**, *2*, 4.
- [16] P. S. Gromski, A. B. Henson, J. M. Granda, L. Cronin, *Nat. Rev. Chem.* **2019**, *1*, 119.
- [17] I. E. Castelli, D. J. Arismendi-Arrieta, A. Bhowmik, I. Cekic-Laskovic, S. Clark, R. Dominko, E. Flores, J. Flowers, K. U. Frederiksen, J. Friis, A. Grimaud, K. V. Hansen, L. J. Hardwick, K. Hermansson, L. Königer, H. Lauritzen, F. L. Cras, H. Li, S. Lyonnard, H. Lorrmann, N. Marzari, L. Niedzicki, G. Pizzi, F. Rahmanian, H. Stein, M. Uhrin, W. Wenzel, M. Winter, C. Wölke, T. Vegge, *arXiv:2106.01616 [cond-mat.mtrl-sci]* **2021**.
- [18] M. D. Wilkinson, M. Dumontier, I. J. Aalbersberg, G. Appleton, M. Axton, A. Baak, N. Blomberg, J.-W. Boiten, L. B. da Silva Santos, P. E. Bourne, J. Bouwman, A. J. Brookes, T. Clark, M. Crosas, I. Dillo, O. Dumon, S. Edmunds, C. T. Evelo, R. Finkers, A. Gonzalez-Beltran, A. J. G. Gray, P. Groth, C. Goble, J. S. Grethe, J. Heringa, P. A. C. 't Hoen, R. Hoof, T. Kuhn, R. Kok, J. Kok, et al., *Sci. Data* **2016**, *3*, 160018.
- [19] E. Soedarmadji, H. S. Stein, S. K. Suram, D. Guevarra, J. M. Gregoire, *npj Comput. Mater.* **2019**, *5*, 79.
- [20] FastAPI, <https://fastapi.tiangolo.com/#license> (accessed: June 2021).
- [21] Home Page, <https://opcfoundation.org/> (accessed: June 2021).
- [22] S. E. Ament, H. S. Stein, D. Guevarra, L. Zhou, J. A. Haber, D. A. Boyd, M. Umehara, J. M. Gregoire, C. P. Gomes, *npj Comput. Mater.* **2019**, *5*, 77.
- [23] B. Rohr, H. S. Stein, D. Guevarra, Y. Wang, J. A. Haber, M. Aykol, S. K. Suram, J. M. Gregoire, *Chem. Sci.* **2020**, *11*, 2696.
- [24] F. Häse, M. Aldeghi, R. J. Hickman, L. M. Roch, M. Christensen, E. Liles, J. E. Hein, A. Aspuru-Guzik, *arXiv:2010.04153 [stat.ML]* **2020**.
- [25] HDF5 Files, <https://figshare.com/s/1578223bbf5d4de605af>
- [26] D. Allan, T. Caswell, S. Campbell, M. Rikitin, *Synchrotron Radiat. News* **2019**, *32*, 19.
- [27] M. Aldeghi, F. Häse, R. J. Hickman, I. Tamlyn, A. Aspuru-Guzik, *arXiv:2103.03716 [math.OA]* **2021**.
- [28] The Uvicorn Project, <https://www.uvicorn.org/>
- [29] N. Brandt, L. Griem, C. Herrmann, E. Schoof, G. Tosato, Y. Zhao, P. Zschumme, M. Selzer, *Data Sci. J.* **2021**, *20*, 8.
- [30] L. Talirz, S. Kumbhar, E. Passaro, A. V. Yakutovich, V. Granata, F. Gargiulo, M. Borelli, M. Uhrin, S. P. Huber, S. Zoupanos, C. S. Adorf, C. W. Andersen, O. Schütt, C. A. Pignedoli, D. Passerone, J. VandeVondele, T. C. Schulthess, B. Smit, G. Pizzi, N. M. Marzari, *Sci. Data* **2020**, *7*, 299.
- [31] G. Pizzi, A. Cepellotti, R. Sabatini, N. Marzari, B. Kozinsky, *Comput. Mater. Sci.* **2016**, *111*, 218.
- [32] The Potential of Scanning Electrochemical Probe Microscopy and Scanning Droplet Cells In Battery Research - Daboss - Electrochemical Science Advances - Wiley Online Library <https://chemistry-europe.onlinelibrary.wiley.com/doi/full/10.1002/elsa.202100122> (accessed: October 2021).
- [33] The Celery Project, <https://celeryproject.org/> (accessed: October 2021).

### 4.1.3. Supporting Information

**ADVANCED  
MATERIALS**  
INTERFACES

#### Supporting Information

for *Adv. Mater. Interfaces*, DOI: 10.1002/admi.202101987

Enabling Modular Autonomous Feedback-Loops in  
Materials Science through Hierarchical Experimental  
Laboratory Automation and Orchestration

*Fuzhan Rahmanian, Jackson Flowers, Dan Guevarra,  
Matthias Richter, Maximilian Fichtner, Phillip Donnely,  
John M. Gregoire,\* and Helge S. Stein\**



## Enabling modular autonomous feedback-loops in materials science through hierarchical experimental laboratory automation and orchestration

Fuzhan Rahmanian<sup>1,2</sup>, Jackson Flowers<sup>1,2</sup>, Dan Guevarra<sup>4</sup>, Matthias Richter<sup>4</sup>, Maximilian Fichtner<sup>1,3</sup>, John M. Gregoire<sup>4,\*</sup>, Helge S. Stein<sup>1,2,\*</sup>

<sup>1</sup> Helmholtz Institute Ulm (HIU), Helmholtzstr. 11, 89081 Ulm, Germany

<sup>2</sup> Karlsruhe Institute of Technology (KIT), Institute of Physical Chemistry (IPC), Fritz-Haber-Weg 2, 76131 Karlsruhe, Germany

<sup>3</sup> Karlsruhe Institute of Technology (KIT), Institute of Nanotechnology (INT), P.O. Box 3640, D-76021 Karlsruhe, Germany

<sup>4</sup> Division of Engineering and Applied Science, and Liquid Sunlight Alliance (LiSA), California Institute of Technology (Caltech), Pasadena, California, USA

Address correspondence to: [helge.stein@kit.edu](mailto:helge.stein@kit.edu), [gregoire@caltech.edu](mailto:gregoire@caltech.edu)

In this section, we are going to demonstrate the steps required for running a process by our proposed HELAO framework. The experiment in question will be maximization of a scaled Schwefel function, virtually sampled by moving a pair of motorized probes in parallel to different (x,y) positions on the function. In the proposed demo, two devices and two auxiliary servers including lang motor, force sensor, analyze and active learning respectively are required to be instantiated.

As described in the main section of the paper, we operate the orchestrator by sending it lists of actions to perform, called “experiments”. Generally, one experiment will comprise all the actions we need to perform to complete a measurement at a single point on a substrate, but this formalism is not strict, and can easily be adapted for experiments which do not use substrates at all. While plans are to build a more user-friendly graphical interface in the near future, we currently construct these experiments directly as python dictionaries. An experiment dictionary has three keys: “soe” (sequence of experiments), which contains a list of all the actions to be performed in the experiment in order, “params”, which contains a dictionary which has the actions to be performed as keys and dictionaries of their parameters as values under those keys, and “meta”, which accepts a dictionary of arbitrary metadata.

Below, the first experiment dictionary in our parallel active learning demonstration process is given as an example of this structure. As can be seen under the “soe” key of this dictionary, each action name has three components: the name of the server performing the action (with an optional colon and integer to distinguish between multiple instances of the same server), these instances are separated by a “/” from the name of the action, which is optionally separated by an “\_” from an indexing integer. The latter distinguishes between multiple actions of the same type in a single experiment, or between the actions of multiple experiments in a process.

This particular experiment begins with “orchestrator/start”, which, as described in the paper, primes the orchestrator to begin collecting data. It is then followed by several motor movements such as “lang:2/moveWaste\_0”, which would normally be necessary to handle pumped liquids in our electrochemistry experiments, but are merely ornamental in this demo representation. After these, “lang:2/moveAbs\_0” moves to an arbitrary sample point (dx0, dy0) taken from the defined search space which is required for initializing the process. “lang:2/moveDown\_0” uses feedback from the force sensor to safely move the probe into contact with the substrate, as we would in an actual electrochemical experiment, and “measure:2/schwefelFunction\_0” takes the value of the Schwefel function at this point. “analysis/dummy\_0” performs a placeholder analysis.

Looking under the “params” key, we have a dictionary of parameters for each of our actions. Most of these are relatively straightforward, but there is some value in explaining the parameter structure for “dummy\_0”. Active learning normally requires analyzing our data as it is acquired. Data analysis functions in our active learning routines must be able to operate on data as it is collected. From the structure of our action return statements, we are able to predict under what headings each data value will be stored within our hdf5 files. The parameters of this analysis function are partial addresses to these values within the hdf5 file.

```
add_process(dict(soe=['orchestrator/start', 'lang:2/moveWaste_0', 'lang:2/RemoveDroplet_0',
'lang:2/moveSample_0', 'lang:2/moveAbs_0', 'lang:2/moveDown_0', 'measure:2/schwefelFunction_0', 'analysis/dummy_0'],
    params={'start': {'collectionkey': 'al_parallel'},
            'moveWaste_0': {'x': 0, 'y': 0, 'z': 0},
            'RemoveDroplet_0': {'x': 0, 'y': 0, 'z': 0},
            'moveSample_0': {'x': 0, 'y': 0, 'z': 0},
            'moveAbs_0': {'dx': dx0, 'dy': dy0, 'dz': dz},
            'moveDown_0': {'dz': 0.12, 'steps': 4, 'maxForce': 1.4, 'threshold': 0.13},
            'schwefelFunction_0': {'x': dx0, 'y': dy0},
            'dummy_0': {'x_address': 'experiment_0:0/schwefelFunction_0/data/parameters/x',
                       'y_address': 'experiment_0:0/schwefelFunction_0/data/parameters/y',
                       'schwefel_address': 'experiment_0:0/schwefelFunction_0/data/data/key_y'}},
    meta=dict()))
```

We often use a “for” loop to define a large number of experiments and, consequently, send those experiments all at once to the orchestrator, to be performed one at a time. Shown below is one such for loop, generating the list of experiments which follows the initial experiment described just above. The “soe” here is identical to the initial experiment, with an additional two actions, “ml/activeLearningParallel” and “orchestrator/modify”, at the start of each experiment. “activeLearningParallel” takes in data from the dummy analysis of the previous experiment, by the same means that the analysis server itself takes in data from the results of other actions, and then stores the data in an active memory, sends that data to

a model, and suggests a new point  $(x_2, y_2)$  at which the Schwefel function should be sampled. The active memory of the “ml” action server is central to how we enable multi-threading, as multiple experiment threads in the orchestrator can each access a single “ml” server, and thus can give data to and take suggestions from the same model. The “modify” action is coded directly into the orchestrator, and is uniquely able to modify the action parameters of an in-progress experiment from values within the previous experimental results. It takes as inputs a set of addresses within the relevant hdf5 file, and pointers to values within the current “params” dictionary. Any value that will be changed by this function must be initialized to “?”, as can be seen in the parameters for “moveAbs” and “schwefelFunction” below.

```
n = 100
for i in range(n):
    add_process(dict(soe=[f'ml/activeLearningParallel_{i}', f'orchestrator/modify_{i}',
                        f'lang:2/moveWaste_{i+1}', f'lang:2/RemoveDroplet_{i+1}',
                        f'lang:2/moveSample_{i+1}', f'lang:2/moveAbs_{i+1}',
                        f'lang:2/moveDown_{i+1}', f'measure:2/schwefelFunction_{i+1}',
                        f'analysis/dummy_{i+1}'],
                    params={f'activeLearningParallel_{i}':{'name': 'sdc_2', 'num': int(i+1),
                    'query': query, 'address':f'experiment_{i}:0/dummy_{i}/data/data'},
                    f'modify_{i}':{'addresses':
                    [f'experiment_{i+1}:0/activeLearningParallel_{i}/data/data/next_x',
                    f'experiment_{i+1}:0/activeLearningParallel_{i}/data/data/next_y',
                    f'experiment_{i+1}:0/activeLearningParallel_{i}/data/data/next_x',
                    f'experiment_{i+1}:0/activeLearningParallel_{i}/data/data/next_y'],
                    'pointers':[f'schwefelFunction_{i+1}/x',f'schwefelFunction_{i+1}/y',
                    f'moveAbs_{i+1}/dx', f'moveAbs_{i+1}/dy']},
                    f'moveWaste_{i+1}':{'x': 0, 'y':0, 'z':0},
                    f'RemoveDroplet_{i+1}': {'x':0, 'y':0, 'z':0},
                    f'moveSample_{i+1}': {'x':0, 'y':0, 'z':0},
                    f'moveAbs_{i+1}': {'dx':'?', 'dy':'?', 'dz':dz},
                    f'moveDown_{i+1}': {'dz':0.12, 'steps':4, 'maxForce':1.4, 'threshold':
                    0.13},
                    f'schwefelFunction_{i+1}':{'x':'?', 'y':'?'},
                    f'dummy_{i+1}':
                    {'x_address':f'experiment_{i+1}:0/schwefelFunction_{i+1}/data/parameters/x',
                    'y_address':f'experiment_{i+1}:0/schwefelFunction_{i+1}/data/parameters/y',
                    'schwefel_address':f'experiment_{i+1}:0/schwefelFunction_{i+1}/data/data/key_y'}},
                    meta=dict()))

    add_process(dict(soe=[f'orchestrator/finish'], params={'finish': None}, meta={}))
```

Finally, as shown in the function “add\_process”, we use the python package “requests” to send each experiment to be performed to the orchestrator, through the parameters of the orchestrator’s “addExperiment” function, as defined by fastAPI. The “thread” parameter of this function is also visible. While normally experiments are performed in the order in which they are received, it is possible to run multiple such sequences in parallel by assigning different thread values to different experiments. In our parallel active learning experiment, each instrument was run on a different thread, and they communicated only by contributing data to the same model within the memory of the active learning server.

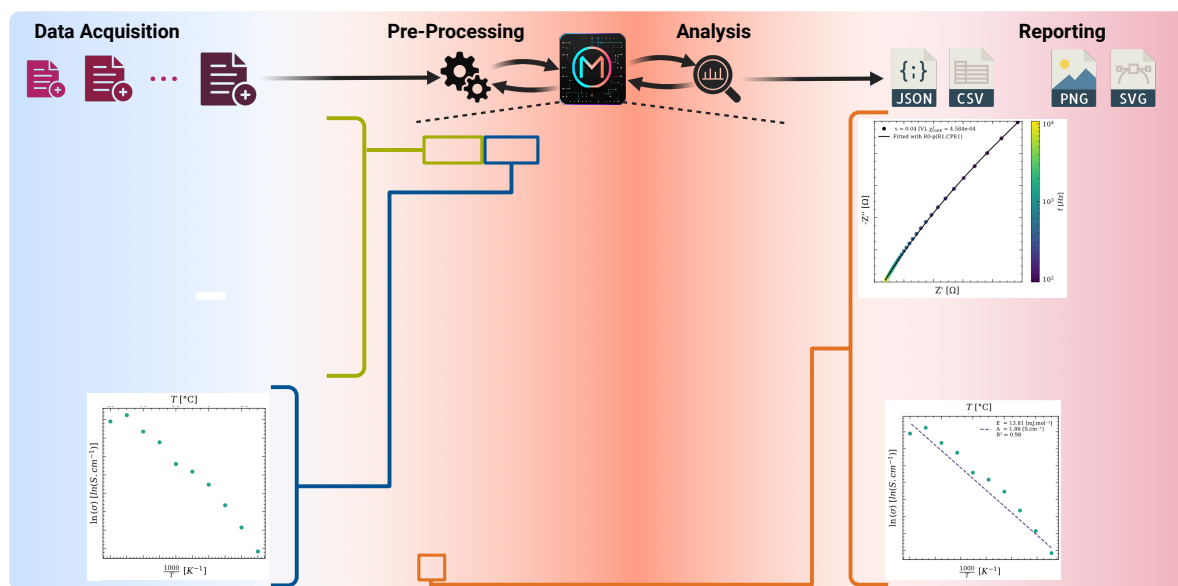
```
def add_process(sequence, thread=0):
    server = 'orchestrator'
    action = 'addExperiment'
    params = dict(experiment=json.dumps(sequence), thread=thread)
```

```
requests.post("http://{}:{}_{}".format(
    config['servers']['orchestrator']['host'], 13380, server, action), params=params).json()
```


We have included a demo of the process we have just exemplified above in action. In this video\*, we demonstrate how such a parallel run appears to the user. Two anaconda terminals can be observed in the left column, which correspond to two devices. Once an action is performed, its fastAPI server sends a message to the terminal hosting that server and the subsequent action will be then executed. Note that the lower terminal is substantially more crowded than the upper terminal, as it is hosting the orchestrator, analysis, and machine learning servers in addition to an instrument. In the middle of the frame, an acquisition function taken from the active learning function at every step is depicted. Based on the maximum of the acquisition function, the next subsequent experiment can be selected. Lastly, in the right column, video feeds of the two SDCs are displayed. The operated SDCs are located in the Glovebox (later for battery application ) and in our fume hood (for other inorganic experimentations)

## 4.2. Conductivity experiments for electrolyte formulations and their automated analysis

### 4.2.1. Publication Details




---

<b>Title:</b>	"Conductivity experiments for electrolyte formulations and their automated analysis"
<b>Journal:</b>	<i>scientific data - Nature*</i> 2023
<b>Publisher:</b>	Springer Nature
<b>Authors:</b>	<b>Rahmanian, Fuzhan</b> and Vogler, Monika and Wölke, Christian and Peng, Yan and Winter, Martin and Cekic-Laskovic, Isidora and Stein, Helge Sören
<b>Status:</b>	Published: 19. January 2023
<b>DOI:</b>	<a href="https://doi.org/10.1038/s41597-023-01936-3">https://doi.org/10.1038/s41597-023-01936-3</a>
<b>Developed Software:</b>	 <a href="https://github.com/fuzhanrahmanian/MADAP">https://github.com/fuzhanrahmanian/MADAP</a>

---

\* For reprint permission refer to Section A.1

## Publication Content

The integrity of prior knowledge and the quality of experimental data are essential when applying ML algorithms. However, the data quality is often compromised by experimental noise, which requires manual evaluation by researchers to analyze and extract relevant parameters. This underscores the importance of data analysis in the design of laboratory automation framework. Herein, MADAP, a versatile Python-based toolkit, has been designed and developed to support a range of electrochemical analyses. The package generates real-time publication-quality plots and structured reports that include raw and processed data, model parameters, output values, and their respective uncertainties. It ensures complete data provenance tracking, following FAIR principles for reproducibility and transparency of research findings. MADAP is accessible through three interfaces: a command-line interface (CLI), a GUI designed with PySimpleGUI<sup>246</sup>, and a Python library, installable with `pip install madap`, which can be integrated into automated experimental setups. This modularity allows researchers to select the optimal approach for the specific requirements.

The package's structured approach to the analysis process, from data input to report generation, includes data acquisition that supports various file formats, pre-processing that is responsible for data cleaning, and detailed analysis that is inherited from abstract classes for consistency and expandability. MADAP includes a range of analytical tools for EIS, Arrhenius, and voltammetry methods, the latter of which is detailed in a subsequent publication (Section 4.5). Here, EIS partially utilizes the impedance Python library<sup>283</sup> to fit data to user-defined equivalent circuits and evaluate the linearity and stability of the system. In the absence of a predefined circuit, MADAP iteratively searches for the optimal fit using a series of built-in equivalent circuit models and optimizes its parameter values through a remeasuring strategy alongside root mean squared error (RMSE) score. Visualization includes Nyquist and Bode plots, along with real and imaginary residuals to evaluate the potential for overfitting. The Arrhenius class uses linear regression of the `scikit-learn` library for the fit to derive parameters such as activation energy. The quality of the fit is evaluated via MSE and  $R^2$  metrics. Detailed documentation for each module is available at <https://fuzhanrahmanian.github.io/MADAP/> and was autogenerated through sphinx. In a practical application, MADAP was tested on electrolyte formu-

lation data from the Helmholtz Institute Münster, which involved measuring ionic conductivity across various compositions under different temperatures, with a total of 5040 individual measurements. The results produced by MADAP were found to be consistent with those obtained from manual analyses by the institute. This demonstrates the efficacy and reliability of MADAP in data-driven settings, providing insights and offering acceleration to researchers.

#### 4.2.2. Individual Contribution

During the development of MADAP, **Fuzhan Rahmanian** designed the UML and the corresponding structure for the implementation of EIS and Arrhenius analysis classes. **F.R.** developed on GitHub and deployed the Python package on PyPI that included a CLI and a GUI with the corresponding formatting of the plotting. **F.R.** curated the sphinx documentation and the GitHub repository. **F.R.** designed the import and export mechanism for reporting, the data cleaning steps, and the logging functionality of the framework. **F.R.** wrote the script for the .exe creation. M.V. and **F.R.** created the data frame structure for the raw and processed data. C.W. and P.Y. performed the experiment to create the raw data. **F.R.** and M.V. wrote the manuscript, and all authors reviewed it before publication.

## 4.2.3. Manuscript

[www.nature.com/scientificdata](https://www.nature.com/scientificdata)

# scientific **data**

[Check for updates](#)

OPEN

DATA DESCRIPTOR

## Conductivity experiments for electrolyte formulations and their automated analysis

**Fuzhan Rahmanian**<sup>1,2</sup>, **Monika Vogler**<sup>1,2</sup>, **Christian Wölke**<sup>3</sup>, **Peng Yan**<sup>3</sup>, **Stefan Fuchs**<sup>1,2</sup>, **Martin Winter**<sup>3,4</sup>, **Isidora Cekic-Laskovic**<sup>3</sup> & **Helge Sören Stein**<sup>1,2</sup>✉

Electrolytes are considered crucial for the performance of batteries, and therefore indispensable for future energy storage research. This paper presents data that describes the effect of the electrolyte composition on the ionic conductivity. In particular, the data focuses on electrolytes composed of ethylene carbonate (EC), propylene carbonate (PC), ethyl methyl carbonate (EMC), and lithium hexafluorophosphate (LiPF<sub>6</sub>). The mass ratio of EC to PC was varied, while keeping the mass ratio of (EC + PC) and EMC at fixed values of 3:7 and 1:1. The conducting salt concentration was also varied during the study. Conductivity data was obtained from electrochemical impedance spectroscopy (EIS) measurements at various temperatures. Based on the thus obtained temperature series, the activation energy for ionic conduction was determined during the analysis. The data is presented here in a machine-readable format and includes a Python package for analyzing temperature series of electrolyte conductivity according to the Arrhenius equation and EIS data. The data may be useful e.g. for the training of machine learning models or for reference prior to experiments.

### Background & Summary

Electrolytes are crucial for the performance of batteries<sup>1</sup> since they enable shuttling of the ions, provide electrical isolation of the electrodes and have a defining influence on the formation and stability of the solid electrolyte interface (SEI)<sup>2</sup> and the cathode electrolyte interface (CEI)<sup>2-4</sup>. Achieving high performance electrolytes, typically requires the presence of various components like organic solvents, co-solvents, functional additives and conducting salts<sup>5</sup>. The concentration of each component and the ratio between the components have a strong impact on the conductivity of the electrolyte<sup>6-8</sup>. Ding *et al.* showed in several studies<sup>6-9</sup>, that the composition of the electrolyte, especially the PC content, affects the viscosity and glass transition temperature of the electrolyte. The amount of PC also hinders crystallization of EC<sup>6,10</sup>. This allows for the formulation of electrolytes with improved performance at low temperatures<sup>10,11</sup>.

The dataset<sup>12</sup> presented herein provides a comprehensive basis for future optimization studies, as it contains a wide variation of formulations and temperatures, including the raw data. Furthermore, it can help to gain deeper insights regarding composition-property-performance relationships. Fractions of this dataset served as the basis for several machine learning models published elsewhere<sup>11,13,14</sup>. The automated high-throughput experimentation system<sup>13</sup> available at the Helmholtz Institute Münster is used to formulate a variety of electrolyte solutions based on EC, EMC, PC and LiPF<sub>6</sub>. Ratios of (PC + EC):EMC of 3:7 and 1:1 are covered in the dataset<sup>12</sup>. The concentration of the conducting salt varies between 0.2 mol kg<sup>-1</sup> and 2.1 mol kg<sup>-1</sup>, while the ratio of EC:PC ranges from 0.0 to 9.2.

The robotic system<sup>13</sup> used for the acquisition of the data is able to dispense liquid and solid components into aluminium or polymer vials with high accuracy. Each formulation is identified by a batch number and measurements are identified by a unique ID stored and reported on the vial through a QR code. After sample-preparation, the automated setup performs the targeted measurement. Subsequently, the system returns a JSON formatted file for each formulation, which allows for downstream processing. Here, we present the data<sup>12</sup> as a CSV file to summarize the results received from 504 individual JSON files. Manual analysis of the

<sup>1</sup>Helmholtz Institute Ulm, Applied Electrochemistry, Helmholtzstr. 11, 89081, Ulm, Germany. <sup>2</sup>Karlsruhe Institute of Technology, Institute of Physical Chemistry, Fritz-Haber-Weg 2, 76131, Karlsruhe, Germany. <sup>3</sup>Helmholtz Institute Münster (IEK-12), Forschungszentrum Jülich GmbH, Corrensstraße 46, 48149, Münster, Germany. <sup>4</sup>MEET Battery Research Center, University of Münster, Corrensstraße 46, 48149, Münster, Germany. ✉e-mail: [helge.stein@kit.edu](mailto:helge.stein@kit.edu)

SCIENTIFIC DATA | (2023) 10:43 | <https://doi.org/10.1038/s41597-023-01936-3>1



www.nature.com/scientificdata/

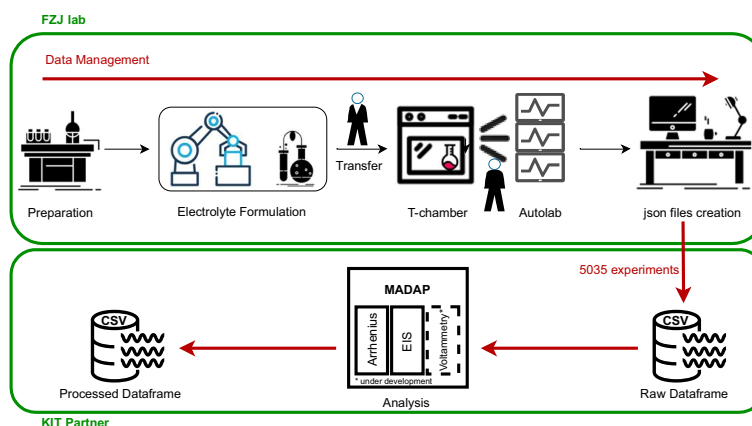


**Fig. 1** The overall workflow representation from experimentation to data generation in Helmholtz-Institute Münster and data analysis in Karlsruhe Institute of Technology (KIT) and its partners.

raw data is time intensive, which is why we have developed an automated Python-based data analysis package called Modular and Autonomous Data Analysis Platform (*MADAP*)<sup>15</sup> with a command line interface (CLI) and a graphical user interface (GUI) that can process the aggregated CSV. This package is generalized and can be used on a variety of datasets as described below. The overall workflow of generating and analyzing data is shown in Fig. 1. All input parameters are tracked and saved in the output obtained from *MADAP*<sup>15</sup> to allow full data provenance tracking<sup>16,17</sup> of not just the experimental but also the data analysis steps in the research workflow<sup>18</sup>.

The dataset<sup>12</sup> can be used to train machine learning models in order to predict promising electrolyte formulations to reach an optimum conductivity, as demonstrated by Rahmanian *et al.*<sup>11</sup>. Further, the research community may find the data useful in the design of their own experiments and in decisions concerning the use of hardware, software and human resources. The use of this dataset together with analysis tools like *MADAP*<sup>15</sup> as a base for further lithium-ion battery research, enables the generation of further insights such as the activation energy of the ion conduction process. It is even possible to add other analysis procedures to *MADAP*<sup>15</sup> to further expand the automation it provides.

### Methods

**High throughput experimentation (HTE) system.** The robotic HTE system<sup>13</sup>, used to acquire the data<sup>12</sup> presented here, is designed for high-throughput operation in a nitrogen atmosphere. The setup designed for the formulation of electrolyte solutions is able to prepare 96 formulations in 8 h by gravimetric dosing of solid and liquid materials into polymer or aluminium vials. Up to 10 mL of electrolyte can be formulated within one vial. The setup also provides functionalities to close the vials, mix, and heat their content using a heated shaker plate. Further, EIS measurements are performed automatically. To track the samples, each vial is automatically labelled using a QR code representing information like the date of preparation, an ID for the electrolyte mixture and information regarding the chemicals used. In preparation for EIS measurements, a volume of 750  $\mu$ L of the electrolyte is automatically filled into single-use Eppendorf<sup>®</sup> Safe-Lock Tubes with a capacity of 2 mL. The use of single-use equipment avoids cross contamination in this step of the process. Subsequently, electrodes are automatically immersed into the sample. These electrodes are designed to generate reproducible results independent of the shape of the vial or the depth of immersion<sup>19</sup>. For the measurement, the samples are arranged in groups of eight samples per rack, three of which are mounted on one larger rack. Four of these combined racks can be connected to the *Metrohm Autolab* potentiostat, which is used for the measurements<sup>13</sup>.

**EIS measurement.** After the assembly of the racks, they are manually transferred to a *Memmert TTC256* temperature chamber for EIS measurements. The connection of the cells to the *Metrohm Autolab* potentiostat is also done by the operator. The temperature chamber is programmed such, to cover the temperature ranges between  $-30$  °C and  $60$  °C in steps of  $10$  °C. Subsequent to an equilibration period of 2 h for each temperature, the EIS measurements are automatically performed with an applied AC voltage of 40 mV and frequencies between 20 kHz to 50 Hz. A multiplexer distributes the output of twelve channels to eight outputs each. Hence, 96 channels are available to connect to each of the 96 cells on a rack<sup>13</sup>. Each experiment is repeated several times to provide up to 8 sets of values to the dataset. Repetitions can be identified and distinguished based on the running number in the experimentID.

**Data management in the experimental setup.** The data recording during the experimental workflow is handled by a laboratory information management system. It records identifiers for the starting materials, test

www.nature.com/scientificdata/

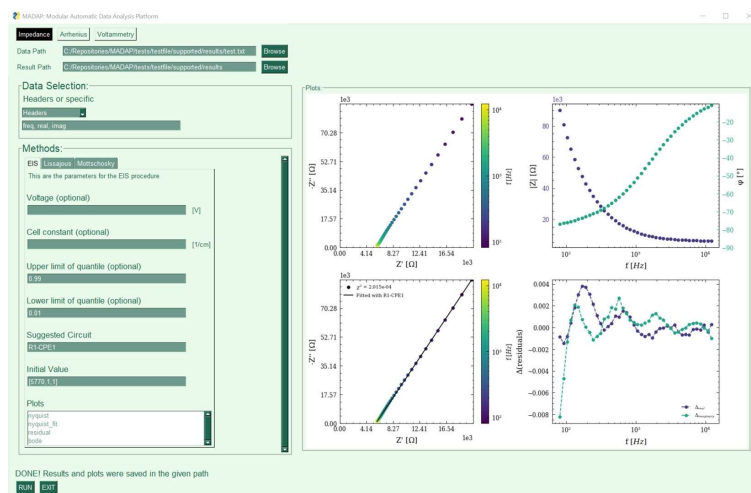


**Fig. 2** A showcase of the Graphical User Interface diagram of MADAP<sup>15</sup>.

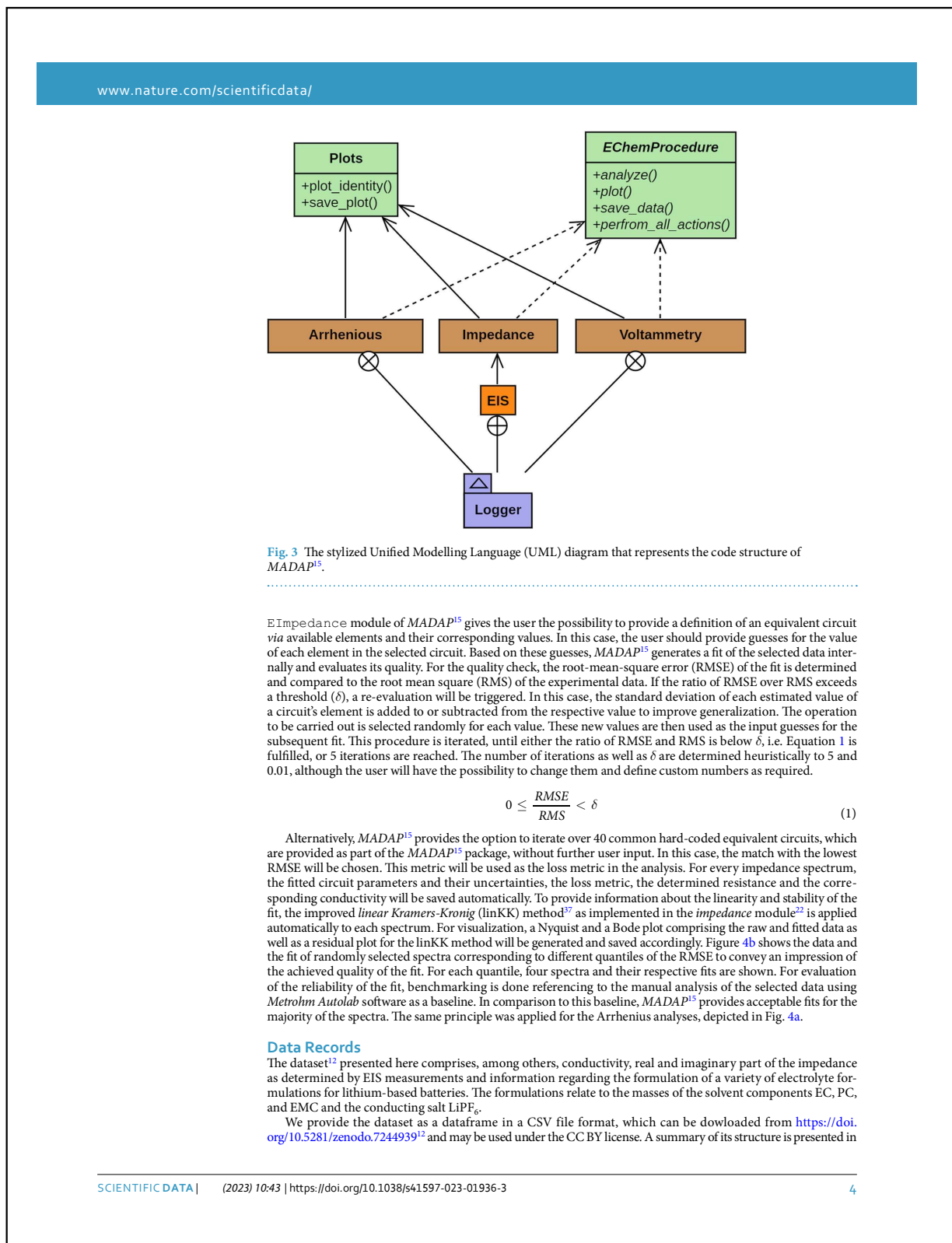
protocols and relevant experimental parameters. Furthermore, the system is able to merge these data with meta-data comprising further details about the electrolytes used in a measurement. After conclusion of a measurement, the collected data including the metadata is saved to a JSON file, which can be used for analysis.

**Analysis Software (MADAP).** For the data analysis, a variety of tools are present and available, e.g. ZView<sup>20</sup>, pyEIS<sup>21</sup>, impedance<sup>22</sup>, Aftermath<sup>23</sup> and Origin<sup>24</sup>. We decided to bundle some of these tools into a compact, modular software package called MADAP<sup>15</sup>, thoroughly documented using sphinx<sup>25</sup>. This analysis tool provides all the necessary means to perform electrochemical data analysis based on experimental datasets, while providing full data provenance tracking, and plot publication quality results. It can perform a variety of automated electrochemical analyses, including EIS, linear and cyclic voltammetry and the analysis of temperature series according to the Arrhenius equation. In this paper, we focus on Arrhenius analysis and EIS measurements. MADAP<sup>15</sup> is deployed in Python3 and is publicly accessible as a GitHub repository (<https://github.com/fuzhanrahmanian/MADAP>)<sup>15</sup>, a pip installable package (`pip install madap`), and an executable (<https://github.com/fuzhanrahmanian/MADAP/releases/tag/v1.0.0>) with a graphical user interface (GUI) created with PySimpleGui<sup>26,27</sup>, as shown in Fig. 2. The accessibility of MADAP<sup>15</sup>, by means of a CLI as well as a GUI, provides the broader scientific community with a variety of entry points for the data analysis. The generic nature of the procedure assures that the package can be expanded with further analysis methods without impacting the existing methodologies. Further, this enables its integration into autonomous research workflows<sup>28–30</sup>. The basic workflow of an analysis using MADAP<sup>15</sup> comprises the three steps of data acquisition, pre-processing and the analysis itself. In the former, the user can import different data types (.txt, .json, .hdf5 or .h5, .xml, .pkl and .csv) and select the data to be analyzed based on ranges of indices for rows and columns or by specifying column labels. The pre-processing step can detect outliers based on given upper and lower limits of the relevant quantile using the *Quantile-based flooring and capping* algorithm<sup>31</sup>. The user may choose to specify custom limits or use the default values implemented in MADAP<sup>15</sup>. In version 1.0, the default values are chosen as 0.01 for the lower and 0.99 for the upper limit. Afterwards, the user can choose what type of analysis shall be performed, i.e. voltammetry, EIS or Arrhenius.

Figure 3 depicts the code structure used in MADAP<sup>15</sup>. In the beginning of each analysis, all the procedures instantiate an abstract class called `EChemProcedure`, which enforces the presence of methods called `analyze`, `plot`, `save data` and `perform all actions`. All procedures additionally inherit from the common `Plots` class, which equips them with the common plotting functionalities, providing outputs with scientific format<sup>32</sup>. The complete procedure is continuously logged to review potential errors.

The linear fit required for the Arrhenius type analysis<sup>33</sup> is implemented in MADAP<sup>15</sup> using the functionalities for linear regression provided in the *scikit-learn* package<sup>34</sup>. The activation energy and the pre-exponential factor are derived from this fit. The regression loss, which is chosen as a quality metric, is calculated using the mean square error (MSE). Finally, plots and data files for the raw and fitted data as well as the model's parameters are automatically generated and saved in a designated location in accordance to the FAIR (Findability, Accessibility, Interoperability, and Reusability) data principle<sup>35</sup>.

EIS analysis and fitting are performed by a partial adoption of the *impedance* package provided by Matthew D. et al.<sup>22</sup>. In this package, the model uses a non-linear square fit as supplied by the *SciPy*<sup>36</sup> package. The



www.nature.com/scientificdata/

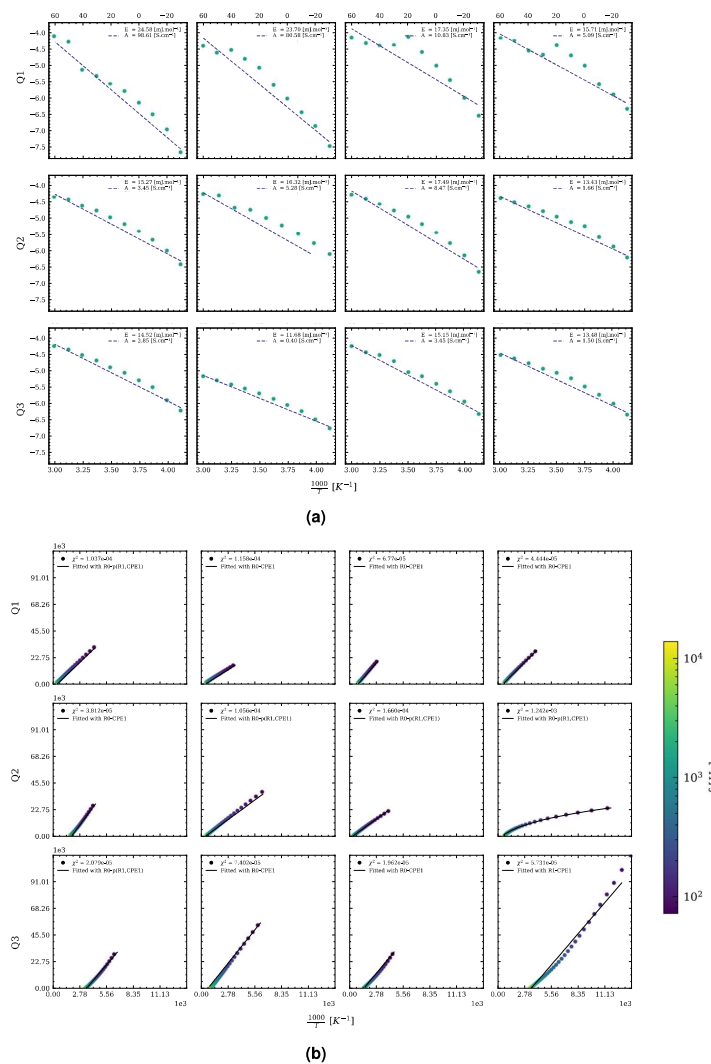


**Fig. 4** Fits randomly selected from Q1, Q2, Q3 based on the (a)  $R^2$  score of the Arrhenius fit and (b) RMSE of the eis fit determined by MADAP<sup>15</sup> for 5035 electrolyte measurements with a frequency range between 50 and 20k.

Table 1. This table also shows the data type, the range of values covered for each quantity, the number of unique values and the physical unit. In this section, we elucidate more on the data and the interrelations within the dataframe. The robotic system operated at the Helmholtz Institute Münster outputs the raw data in JSON format. Although, this format is machine-readable, we decided to provide the data in CSV format, which can easily be read into the user's script as a table, e.g. using the Pandas<sup>38</sup> library available for Python. Each line in the dataframe represents all the data available for a single measurement. Parameters, which are shared by several experiments, are repeated in each line, where they are applicable. In the following, we will elucidate more on each column of the dataframe.

[www.nature.com/scientificdata/](http://www.nature.com/scientificdata/)

Column name	Description	Data type	Range	Unique entries	Unit
experimentID	A unique identifier for each experiment coding an operator, the date of the experiment and the batch of the electrolyte used.	string	not applicable	504	—
temperature	The temperature at which the measurement was conducted	float	(−30, 60)	10	°C
frequency	A series of frequency values selected for the electrochemical impedance spectroscopy	Str[List[float]]	(50, 20000)	1	Hz
real_impedance	A series of the real part of the impedance measured by means of the electrochemical impedance spectroscopy	Str[List[float]]	(−390106, 114305526)	5035	Ω
imaginary_impedance	A series of the imaginary part of the impedance measured by means of the electrochemical impedance spectroscopy	Str[List[float]]	(−371850382, 103)	5035	Ω
cell_constant_standard_deviation	A tuple comprising the cell constant and its standard deviation determined from five measurements using a 0.01 M KCl (aq) standard solution at 20 °C with a 2 h equilibration period between measurements	Str[Tuple[float]]	(3.815, 4.720); (0.000, 0.178)	339	cm <sup>−1</sup>
PC	The mass of propylene carbonate (PC) used for electrolyte formulation	float	(0.273, 5.306)	105	g
EC	The mass of ethylene carbonate (EC) used for electrolyte formulation	float	(0.000, 4.320)	99	g
EMC	The mass of ethyl methyl carbonate (EMC) used for electrolyte formulation	float	(5.293, 9.457)	105	g
LiPF <sub>6</sub>	The mass of lithium hexafluorophosphate (LiPF <sub>6</sub> ) used for electrolyte formulation	float	(0.301, 4.093)	100	g
metadata	Further metadata regarding the electrolyte solution arranged in a dictionary with the keys experimentDate, experimentType, formatVersion, channel, electrolyteAmount, suspectedMeasurementError, PC, EC, EMC, and LiPF <sub>6</sub>	Str[Dict[str]]	not applicable	504	—
phase_shift	The phase shift as obtained from EIS analysis as implemented in MADAP	Str[List[float]]	(0.131, 89.882)	5035	°
EIS_conductivity	The conductivity as obtained from EIS analysis performed using MADAP	float	(0.000, 0.019)	5035	S cm <sup>−1</sup>
EIS_fittedParameters	The values and corresponding uncertainties of the elements in the equivalent circuit as determined using MADAP	Str[List[tuple]]	not applicable	5035	—
EIS_RMSE	The RMSE of the fit obtained by applying the equivalent circuit determined using MADAP in the real and imaginary dimension	float	(4.363, 28560.795)	5035	—
EIS_numberRCelements	The required number of RC elements in the equivalent circuit required to reproduce the EIS spectrum determined using the linKK method as implemented in the <i>impedance</i> package <sup>23</sup>	float	(5, 11)	7	—
EIS_fitEvaluation	A numeric value indicating the quality of the fit. A value close to unity indicates a good fit.	float	(0.576, 0.850)	5035	—
EIS_resistance	The ionic charge transfer resistance as obtained from EIS analysis as implemented in MADAP	float	(241.781, 25564.121)	5035	Ω
EIS_chiSquare	A statistical measure for the goodness of the fit as obtained from the linKK method as implemented in the <i>impedance</i> package <sup>23</sup>	float	(0.000, 0.322)	5035	—
EIS_circuit	The equivalent circuit for the EIS spectrum as obtained from the linKK method as implemented in the <i>impedance</i> package <sup>23</sup>	string	not applicable	8	—
EIS_impedance	A list of impedance values obtained from the fit generated during the EIS analysis performed using MADAP	Str[List[complex]]	not applicable	5035	Ω
EIS_residualReal	The real part of the residuals of the fit as determined using the linKK method as implemented in the <i>impedance</i> package <sup>23</sup>	Str[List[float]]	(−0.118, 0.170)	5035	Ω
EIS_residualImaginary	The imaginary part of the residuals of the fit as determined using the linKK method as implemented in the <i>impedance</i> package <sup>23</sup>	Str[List[float]]	(−0.118, 0.170)	5035	Ω
Arrhenius_activationEnergy	The activation energy obtained from the analysis according to the Arrhenius equation using MADAP	float	(9.427, 30.413)	504	kJ mol <sup>−1</sup>
Arrhenius_preExponential	The pre-exponential factor obtained from the analysis according to the Arrhenius equation using MADAP	float	(0.109, 962.145)	504	—
Arrhenius_R2	The R <sup>2</sup> score corresponding to the linear fit obtained in the analysis according to the Arrhenius equation using MADAP	float	(0.186, 0.999)	504	—
Arrhenius_MSE	The mean square error for the linear fit determined during the analysis according to the Arrhenius equation using MADAP	float	(0.000, 0.703)	504	—
Arrhenius_InConductivity	A list of lnσ obtained from the linear fit according to the Arrhenius equation determined by MADAP	float	(−8.175, −3.713)	5035	ln(S cm <sup>−1</sup> )

**Table 1.** This table describes the data comprised in the dataset presented herein.

**experimentID.** This column provides a unique identifier for each experiment, which enables traceability of the data. It codes the operator, the date of the experiment, the label of the electrolyte and a running number differentiating the repeats. The format of the experimentID is: [operator]\_[date of the experiment]\_[label of the electrolyte]\_[running number].

www.nature.com/scientificdata/

**temperature.** The temperature, at which each measurement was performed, is reported in this column. Each row corresponds to a measurement at one temperature. The values range from  $-30^{\circ}\text{C}$  to  $60^{\circ}\text{C}$ . For five formulations, the measurement at  $-30^{\circ}\text{C}$  is not reported in the dataset.

**frequency.** This column reports a string, which comprises a list of the frequencies used in the EIS measurements. The frequencies are reported in units of Hz and cover a range from 20 kHz to 50 Hz.

**real\_impedance.** Values for the real part of the impedance,  $Z'$ , in the unit  $\Omega$  are given in this column in the form of a string of a list of floats. The values in this column for all measurements range from  $-3.901 \times 10^5 \Omega$  to  $11.430 \times 10^7 \Omega$ . The negative values result from artefacts in the measurements.

**imaginary\_impedance.** The imaginary part of the impedance,  $Z''$ , is presented in this column. The values are given in  $\Omega$  and range from  $-37.185 \times 10^7 \Omega$  to  $103.002 \Omega$ . The positive values result from artefacts in the measurements.

**cell\_constant\_standard\_deviation.** The cell constant and the respective standard deviation values are reported in  $\text{cm}^{-1}$  and determined from five reference measurements using 0.01 M KCl (aq) standard solution at a temperature of  $20^{\circ}\text{C}$ <sup>13</sup>. In the dataset, they are reported in a common column as a tuple, in which the first value corresponds to the cell constant and the second value reports the standard deviation. The values for the cell constant range from 3.815 to 4.720, while the standard deviations span a range from 0.000 to 0.178.

**PC.** This column reports the mass of PC in g used during the preparation of the electrolyte formulation. The values are given as floats and range from 0.273 g to 5.306 g.

**EC.** The mass of EC used during the preparation of the electrolyte formulation is reported in this column. The values are given as floats in units of g and are spanning a range from 0.000 g to 4.320 g.

**EMC.** In this column, we report the mass of EMC used for the preparation of the electrolyte formulation. The values are given in g and comprise values between 0.480 g and 9.457 g.

**LiPF<sub>6</sub>.** This column presents the mass in g of LiPF<sub>6</sub> comprised in the formulations. The values reach from 0.301 g to 4.093 g.

**metadata.** In this column, additional information is reported, which cannot be reasonably presented in tabular form. The metadata are presented as a string of a dictionary. It reports the date and type of the experiment using the keys *experimentDate* and *experimentType*, respectively. Further, the version of the JSON format is associated with the key *formatVersion*. The number of the channel running the experiment, the amount of electrolyte used in the respective measurement, and the suspected measurement error are correlated with the keys *channel*, *electrolyteAmount*, and *suspectedMeasurementError*, respectively. The keys *PC*, *EC*, *EMC*, and *LiPF<sub>6</sub>* are linked to further information regarding the respective electrolyte component which is represented in dictionary format. The keys *Batch-No*, *CAS-No*, and *comment* present the respective information as a string. The date of delivery and the date of opening of the container are given as strings in the format MM/YY and can be accessed using the keys *dateOfDelivery* and *dateOfOpening*. The molar mass of the substance is reported as a float with the key *molarMass*, while its unit is given as a string using the key *molarMassUnit*. The *name* key is associated with a string stating the long name of the chemical. The purity of the material is found using the key *purity*, while the SMILES string is given with the key *SMILES*. Both of these quantities are reported as strings. The amount of the respective substance used in the formulation is accessed with the key *substanceAmount*, while the respective unit is found using the key *substanceAmountUnit*. Finally, the *supplier* key returns the supplier, from which the material was obtained.

Moreover, the dataframe also contains data resulting from the analysis of the experimental data using the MADAP<sup>15</sup> Python package. The MADAP<sup>15</sup> analysis workflow is performed on a Lenovo Workstation with an AMD Ryzen Threadripper PRO 3975WX processor at 3500 MHz with 32 cores and 64 Logical Processors. The workstation is equipped with 128 GB of RAM and an RTX A6000 GPU running with Microsoft Windows 10 Pro. The single core performance of the CPU turned out to be a bottleneck during operation, since the used libraries are not optimized for multicore processing or GPU training. Hence, MADAP<sup>15</sup> was configured to use all 32 cores for multithreaded operation for this scenario. In the following, we elucidate more on the analyzed results contained in the dataframe by going through the column names associated with analyzed data.

**phase\_shift.** This column reports the phase shift ( $\phi$ ) or phase angle as obtained from the EIS analysis implemented in the MADAP<sup>15</sup> package according to Eq. 2:

$$\phi = \arctan \left| \frac{Z''}{Z'} \right|. \quad (2)$$

The data is given as a string of a list with values ranging from 0.131 to 89.882 given in  $^{\circ}$ .

**EIS\_conductivity.** The ionic conductivity obtained as the quotient of the cell constant and the resistance determined from the EIS analysis implemented in MADAP<sup>15</sup> is reported in this column. The conductivity is given in units of  $\text{S cm}^{-1}$  and the values range from  $0.000 \text{ S cm}^{-1}$  to  $0.019 \text{ S cm}^{-1}$ .

www.nature.com/scientificdata/

**EIS\_fittedParameters.** In this column, we report the determined values of the circuit's elements as well as their uncertainties as obtained from the analysis. These parameters are represented as a string of a list of tuples. The first element of each tuple illustrates the value of the respective element, and the second value shows the standard deviation error obtained from the output of the *impedance* package<sup>22</sup>. The order of the tuples corresponds to the order of a given circuit's elements as presented in column *EIS\_circuit*.

**EIS\_RMSE.** This column reports the RMSE of the fit in the real and the imaginary dimension as obtained from EIS analysis. The values are given as floats.

**EIS\_numberRCelements.** An optimal number of RC elements in an equivalent circuit determined using the linKK method can be verified by a metric, which subtracts the ratio between the sums of negative and positive resistor values from unity. The symbolic representation of this metric is conventionally chosen to be  $\mu$  and its values are reported as floats in our dataframe. The number of RC elements considered as optimal is the one, which results in a value of  $\mu$  below 0.85<sup>37</sup>.

**EIS\_fitEvaluation.** This column reports a numeric value providing means to estimate the degree of over- or under-fitting. The values range from 0.576 to 0.850 and are reported as floats. The upper limit is fixed at 0.850 to avoid overfitting, as described by Schönleber *et al.*<sup>37</sup>.

**EIS\_resistance.** From the EIS analysis, the resistance of the electrolyte towards ionic charge transfer is obtained. The values resulting from the analysis are reported in this column in units of  $\Omega$ . A range from 241.781  $\Omega$  to  $25.564 \times 10^3 \Omega$  is spanned by the data.

**EIS\_chiSquare.** This statistical value determines the goodness of the fit derived from the linKK method and is calculated as the sum of squares of the real and imaginary residual error. The  $\chi^2$  values are reported as floats.

**EIS\_circuit.** The manual or auto-selected circuit used to fit the EIS data of the concerned measurement is reported in this column. In the representation, serial connections are displayed as *element<sub>1</sub>-element<sub>2</sub>*, while *p(element<sub>1</sub>, element<sub>2</sub>)* indicates a parallel electric connection. The elements in the circuit are represented by *R* for resistance and *C* for capacity. A constant phase element is indicated by *CPE* and a Warburg element is represented as *W*. An additional list of elements, which may be used by the user, can be found in the *impedance* package<sup>22</sup>. In this column, the fitted circuit for each conductivity experiment is represented by a string.

**EIS\_impedance.** This column represents a list of impedance values obtained from the fitted model with frequency as input and the measured impedance as output. The data is reported as a string of a list.

**EIS\_residualReal.** The residual errors of the real impedance obtained from the linKK method can be seen in this column. They are given as a string of a list.

**EIS\_residualImaginary.** In this column, the residual error derived from the linKK method for imaginary impedance as a consistency factor is reported as a string of a list.

**Arrhenius\_activationEnergy.** For calculating the activation energy from the conductivity experiment, a linear fit between the inverse temperatures in 1000/K and the natural logarithm of conductivities is applied. The activation energy can be calculated with the Arrhenius equation and is reported as a float in this column with the unit  $\text{mJ mol}^{-1}$ .

**Arrhenius\_preExponential.** The pre-exponential factor obtained from the linear fit according to the Arrhenius equation is reported in this column. The values of this factor are given as a float with the unit  $\text{Scm}^{-1}$ .

**Arrhenius\_R2.** In this column, the  $R^2$  score of the linear fit is shown as a unitless float.

**Arrhenius\_MSE.** In this column, we report the mean square error of the linear fit as a unitless float.

**Arrhenius\_InConductivity.** A list of the natural logarithmic conductivities obtained from the linear fit is reported in this column as a string of a list of floating point numbers.

All the relevant data concerning the raw data, fitting parameters and results of the analysis are saved in the presented dataset. The data is therefore fully traceable and reusable. This is compliant with the FAIR<sup>35</sup> data standard. The workflow is schematized in Fig. 5.

The column named *Data Type* in Table 1 shows the data type obtained after reading the dataframe from the CSV file using Pandas<sup>38</sup> *read\_csv* method. The user should note the information provided in the column *Description* to see the structure of the string. For example, the real part of the impedance is read as a string type variable. However, it actually represents a list of floats and should be cast to this data type.

#### Technical Validation

The reliability of the experimental data is validated by repeating each measurement several times. Invalid data is not stored in the dataset<sup>12</sup> reported here. Each measurement is examined by an expert in the field to ensure high quality of the data.

www.nature.com/scientificdata/

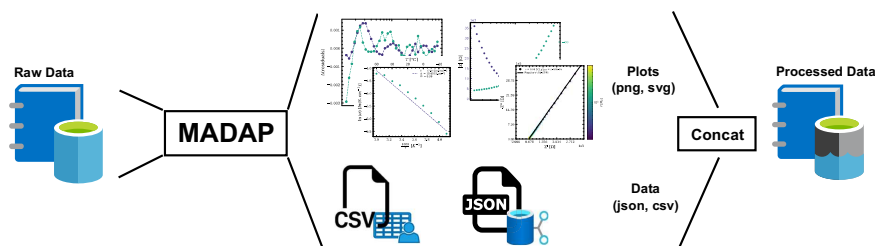


Fig. 5 Schematic representation of the given dataframe consisting of raw and processed data.

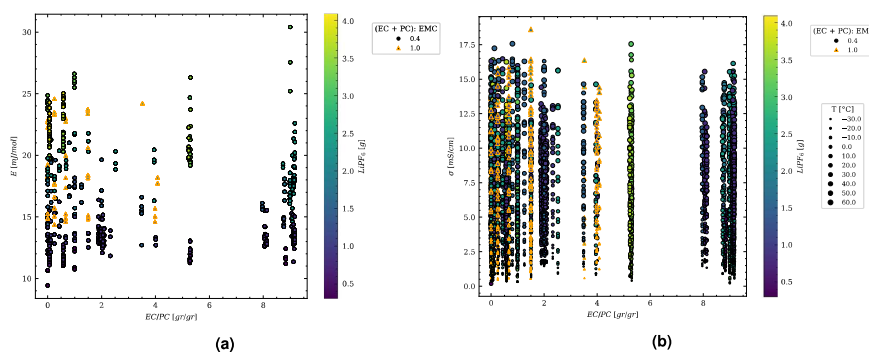


Fig. 6 Results from the analysis according to the Arrhenius equation. (a) represents the activation energies for two (EC + PC):EMC ratios of 0.4 and 1, derived by *MADAP15* using a linear regression fit, (b) shows the conductivity value for the mentioned ratios at 10 discrete temperatures between  $-30.0$  °C and  $60.0$  °C obtained from the analysis performed by *MADAP15* using non-linear least square fit of SciPy<sup>36</sup> module. For a part of this fit, the impedance module<sup>22</sup> has been utilized.

The data obtained from the analysis is verified using an appropriate metric for each analysis. For the Arrhenius type analysis, the quality of the fit is quantified by the mean squared error (MSE).

The impedance data reported in this work is pre-processed for analysis by excluding negative impedance values and outliers to enable a reliable analysis. The linKK method is used to verify the linearity of the spectrum and also reports the goodness of the fit by the statistical  $\chi^2$  value corresponding to the residual errors of the impedance data. Consequently, the resulting fit of the equivalent circuit is verified by means of the RMSE. This workflow returns the parameters corresponding to the equivalent circuit as presented in the section Data Records.

For visualization, we generated quantiles based on  $R^2$  and RMSE for all the fits performed during the analyses. Figure 4 shows the results of four randomly selected analyses taken from each quantile to provide an overview of the distribution of the fitting quality. In Fig. 4a, fits corresponding to quantiles based on  $R^2$  are shown, while Fig. 4b presents fits for quantiles based on RMSE. The first row in each subfigure gives an impression of the lowest fit quality, while the best fits are shown in the last row of the subfigures. Additionally, the conductivity and the activation energy calculated by *MADAP15* are depicted in Fig. 6.

### Usage Notes

It is recommended to apply the *MADAP15* package to use, extend or adapt the provided data analysis. For performing analysis using the *MADAP15* package, a specific range of rows and columns of the dataframe can be selected. For example, to reproduce one of the result of this article for Arrhenius analysis, the published dataset was selected as input for the *MADAP15* GUI and the row indices from 3967 to 3977 and column 2 for temperatures and column 13 for electrolyte conductivity selected for the evaluation. Both plotting types were chosen, and the RUN button was pressed. Further results can be derived similarly.

Note that, in case a definition of the formulation in terms of molar fractions is desired, the amounts of substances for each component of the electrolyte as reported in the dictionary given in the column labelled metadata can be used.



www.nature.com/scientificdata/

#### Code availability

The code of the *MADAP*<sup>15</sup> package is publicly available on <https://github.com/fuzhanrahmanian/MADAP> and the documentation can be found in <https://fuzhanrahmanian.github.io/MADAP/>. A stand-alone windows executable can be downloaded from the GitHub repository as well. Furthermore, *MADAP*<sup>15</sup> can be installed by running `pip install madap`.

The analysis results presented in this article are generated using *MADAP*<sup>15</sup> version 1.0. Contributions are welcome, but should follow the common guidelines for group software development, which can be found in the CONTRIBUTION section of the *MADAP*<sup>15</sup> the repository. The code is developed for the Python version 3.9 and above and should use the following packages and versions: `attrs >= 21.4.0`, `matplotlib >= 3.5.3`<sup>39</sup>, `numpy >= 1.22.4`<sup>40</sup>, `pandas >= 1.4.2`<sup>38</sup>, `pytest >= 7.1.2`, `scikit_learn >= 1.1.2`, and `impedance >= 1.4.1`<sup>22</sup>. For running the GUI, *PySimpleGUI* >= 4.60.3<sup>36</sup> is required additionally.

Received: 31 October 2022; Accepted: 3 January 2023;

Published online: 19 January 2023

#### References

- Verma, P., Maire, P. & Novák, P. A review of the features and analyses of the solid electrolyte interphase in Li-ion batteries. *Electrochim. Acta* **55**, 6332–6341, <https://doi.org/10.1016/j.electacta.2010.05.072> (2010).
- Peled, E. & Menkin, S. SEI: Past, Present and Future. *J. Electrochem. Soc.* **164**, A1703–A1719, <https://doi.org/10.1149/2.1441707jes> (2017).
- Qian, Y. *et al.* Influence of electrolyte additives on the cathode electrolyte interphase (CEI) formation on  $\text{LiNi}_{1/3}\text{Mn}_{1/3}\text{Co}_{1/3}\text{O}_2$  in half cells with Li metal counter electrode. *J. Power Sources* **329**, 31–40, <https://doi.org/10.1016/j.jpowsour.2016.08.023> (2016).
- Gauthier, M. *et al.* Electrode–Electrolyte Interface in Li-Ion Batteries: Current Understanding and New Insights. *J. Phys. Chem. Lett.* **6**, 4653–4672, <https://doi.org/10.1021/acs.jpcclett.5b01727> (2015).
- Zhao, W. *et al.* Recent advances in the research of functional electrolyte additives for lithium-ion batteries. *Curr. Opin. Electrochem.* **6**, 84–91, <https://doi.org/10.1016/j.coelec.2017.10.012> (2017).
- Ding, M., Li, Q., Li, X., Xu, W. & Xu, K. Effects of Solvent Composition on Liquid Range, Glass Transition, and Conductivity of Electrolytes of a (Li, Cs)  $\text{PF}_6$  Salt in EC-PC-EMC Solvents. *J. Phys. Chem. C* **121**, 11178–11183, <https://doi.org/10.1021/acs.jpcc.7b03306> (2017).
- Ding, M. *et al.* Change of Conductivity with Salt Content, Solvent Composition, and Temperature for Electrolytes of  $\text{LiPF}_6$  in Ethylene Carbonate–Ethyl Methyl Carbonate. *J. Electrochem. Soc.* **148**, A1196, <https://doi.org/10.1149/1.1403730> (2001).
- Ding, M. S. & Jow, T. R. Conductivity and Viscosity of PC-DEC and PC-EC solutions of  $\text{LiPF}_6$ . *J. Electrochem. Soc.* **150**, A620, <https://doi.org/10.1149/1.1566019> (2003).
- Ding, M. S. Liquid Phase Boundaries, Dielectric Constant, and Viscosity of pc-dec and pc-ec Binary Carbonates. *J. Electrochem. Soc.* **150**, A455–A462, <https://doi.org/10.1149/1.1557968> (2003).
- Hubble, D. *et al.* Liquid electrolyte development for low-temperature lithium-ion batteries. *Energy Environ. Sci.* **15**, 550–578, <https://doi.org/10.1039/D1EE01789F> (2022).
- Rahmanian, F. *et al.* One-shot active learning for globally optimal battery electrolyte conductivity. *Batteries & Supercaps* **5**, <https://doi.org/10.1002/batt.202200228> (2022).
- Rahmanian, F. *et al.* Dataset of 5035 conductivity experiments for lithium-ion battery electrolyte formulations at various temperatures. *Zenodo* <https://doi.org/10.5281/zenodo.7244939> (2022).
- Narayanan Krishnamoorthy, A. *et al.* Data-Driven Analysis of High-Throughput Experiments on Liquid Battery Electrolyte Formulations: Unraveling the Impact of Composition on Conductivity. *Chemistry-Methods* **2**, <https://doi.org/10.1002/cmtd.202200008> (2022).
- Flores, E. *et al.* Learning the laws of lithium-ion transport in electrolytes using symbolic regression. *Digital Discovery* **1**, 440–447, <https://doi.org/10.1039/D2DD00027J> (2022).
- Rahmanian, F. Modular and autonomous data analysis platform. *Zenodo* <https://doi.org/10.5281/zenodo.7374383> (2022).
- Soedarmadji, E., Stein, H. S., Suram, S. K., Guevarra, D. & Gregoire, J. M. Tracking materials science data lineage to manage millions of materials experiments and analyses. *npj Comput. Mater.* **5**, 1–9, <https://doi.org/10.1038/s41524-019-0216-x> (2019).
- Castelli, I. E. *et al.* Data Management Plans: The Importance of Data Management in the BIG-MAP Project. *Batteries Supercaps* **4**, 1803–1812, <https://doi.org/10.1002/batt.202100117> (2021).
- Stein, H. S. *et al.* From materials discovery to system optimization by integrating combinatorial electrochemistry and data science. *Curr. Opin. Electrochem.* **35**, 101053, <https://doi.org/10.1016/j.coelec.2022.101053> (2022).
- Wiemhöfer, H.-D., Grünebaum, M. & Hiller, M. M. Micro electrode liquid measurement cell. *WIPO Utility Patent No. WO 2014/139494 A1* (2014).
- AMETEK Inc. Zview. *Scientific Instruments* <https://www.ameteksi.com/products/software/zview-software-en> (2019).
- Knudsen, K. B. Pyeis: A Python-Based Electrochemical Impedance Spectroscopy Analyzer and Simulator. *ECS Meet. Abstr. MA2019-01*, 1937, <https://doi.org/10.1149/MA2019-01/39/1937> (2019).
- Murbach, M. D., Gerwe, B., Dawson-Elli, N. & Lok-kun, T. impedance.py: A Python package for electrochemical impedance analysis. *J. Open. Source Softw.* **5**, 2349, <https://doi.org/10.21105/joss.02349> (2020).
- Spinner, N. AfterMath EIS Data Import Procedure. *Pine Research Instrumentation* <https://pineresearch.com/shop/kb/software/software-help-and-support/using-aftermath/aftermath-import-procedure> (2016).
- Deschenes, L. A. & Bout, D. A. V. Origin 6.0: Scientific Data Analysis and Graphing Software Origin Lab Corporation (formerly Microcal Software, Inc.). web site: [www.originlab.com](http://www.originlab.com). commercial price: 595.academicprice: 446. *J. Am. Chem. Soc.* **122**, 9567–9568, <https://doi.org/10.1021/ja004761d> (2000).
- Sphinx Development Team. Sphinx 4.0.0+ documentation. *Sphinx* <https://www.sphinx-doc.org/en/master/> (2020).
- Podrżaj, P. & Walker, N. Proceedings of the 8th International Conference on Informatics and Applications ICIA2019, Japan, 2019 (2019).
- PySimpleGUI. PySimpleGUI: Python GUIs for humans. *PySimpleGUI* <https://www.pysimplegui.org/> (2018).
- Rahmanian, F. *et al.* Enabling modular autonomous feedback-loops in materials science through hierarchical experimental laboratory automation and orchestration. *Adv. Mater. Interfaces* **9**, 2101987, <https://doi.org/10.1002/admi.202101987> (2022).
- Pizzi, G., Cepellotti, A., Sabatini, R., Marzari, N. & Kozinsky, B. AiiDA: automated interactive infrastructure and database for computational science. *Computational Mater. Sci.* **111**, 218–230, <https://doi.org/10.1016/j.commatsci.2015.09.013> (2016).
- Allan, D., Caswell, T., Campbell, S. & Rakitin, M. Bluesky's ahead: A multi-facility collaboration for an *la Carte* software project for data acquisition and management. *Synchrotron Radiat. N.* **32**, 19–22, <https://doi.org/10.1080/08940886.2019.1608121> (2019).
- Dekking, F. M., Kraaikamp, C., Lopenhaa, H. P. & Meester, L. E. A *Modern Introduction to Probability and Statistics: Understanding why and how*, vol. 488 (Springer, 2005).
- Garrett, J. D. & Peng, H. SciencePlots (v1. 0.6). *Zenodo* <https://doi.org/10.5281/zenodo.4106650> (2020).

www.nature.com/scientificdata/

33. Laidler, K. J. The development of the arrhenius equation. *J. Chem. Educ.* **61**, 494–498, <https://doi.org/10.1021/ed061p494> (1984).
34. Pedregosa, F. et al. Scikit-learn: Machine learning in Python. *J. Mach. Learn. Res.* **12**, 2825–2830, <https://doi.org/10.5555/1953048.2078195> (2011).
35. Wilkinson, M. D. et al. The FAIR guiding Principles for scientific data management and stewardship. *Sci. Data* **3**, 1–9, <https://doi.org/10.1038/sdata.2016.18> (2016).
36. Virtanen, P. et al. SciPy 1.0: fundamental algorithms for scientific computing in python. *Nat. Methods* **17**, 261–272, <https://doi.org/10.1038/s41592-019-0686-2> (2020).
37. Schönleber, M., Klotz, D. & Ivers-Tiffé, E. A Method for Improving the Robustness of linear Kramers-Kronig Validity Tests. *Electrochim. Acta* **131**, 20–27, <https://doi.org/10.1016/j.electacta.2014.01.034> (2014).
38. W McKinney. Data Structures for Statistical Computing in Python. In S., van der Walt & J., Millman (eds.) *Proceedings of the 9th Python in Science Conference*, 56–61, <https://doi.org/10.25080/Majora-92bf1922-00a> (2010).
39. Hunter, J. D. Matplotlib: A 2d graphics environment. *Comput. Sci. Eng.* **9**, 90–95, <https://doi.org/10.1109/MCSE.2007.55> (2007).
40. Harris, C. R. et al. Array programming with NumPy. *Nature* **585**, 357–362, <https://doi.org/10.1038/s41586-020-2649-2> (2020).

### Acknowledgements

This work contributes to the research performed at CELEST (Center for Electrochemical Energy Storage Ulm-Karlsruhe) and was funded by the German Research Foundation (DFG) under Project ID 390874152 (POLiS Cluster of Excellence). This project received funding from the European Union's Horizon 2020 research and innovation programme under grant agreement No 957189.

### Author contributions

C.W. and P.Y. conducted the experiments and created the JSON files containing the raw data, E.R. designed the data analysis platform including the GUI and created the pip package for the conducted experiments and analyzed the results. M.V. & E.R. created the data frame containing raw and processed data. All authors reviewed the manuscript.

### Funding

Open Access funding enabled and organized by Projekt DEAL.

### Competing interests

The authors declare no competing interests.

### Additional information

**Correspondence** and requests for materials should be addressed to H.S.S.

**Reprints and permissions information** is available at [www.nature.com/reprints](http://www.nature.com/reprints).

**Publisher's note** Springer Nature remains neutral with regard to jurisdictional claims in published maps and institutional affiliations.

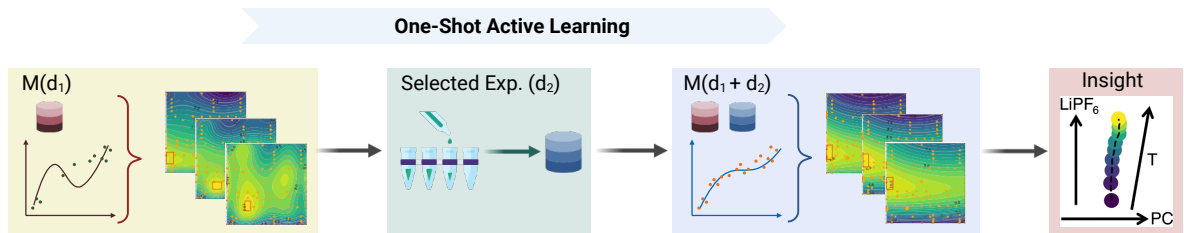


**Open Access** This article is licensed under a Creative Commons Attribution 4.0 International License, which permits use, sharing, adaptation, distribution and reproduction in any medium or format, as long as you give appropriate credit to the original author(s) and the source, provide a link to the Creative Commons license, and indicate if changes were made. The images or other third party material in this article are included in the article's Creative Commons license, unless indicated otherwise in a credit line to the material. If material is not included in the article's Creative Commons license and your intended use is not permitted by statutory regulation or exceeds the permitted use, you will need to obtain permission directly from the copyright holder. To view a copy of this license, visit <http://creativecommons.org/licenses/by/4.0/>.


© The Author(s) 2023

## 4.3. One-Shot Active Learning for Globally Optimal Battery Electrolyte Conductivity

### 4.3.1. Publication Details




---

<b>Title:</b>	"One-Shot Active Learning for Globally Optimal Battery Electrolyte Conductivity"
<b>Journal:</b>	<i>Batteries &amp; Supercaps</i> * 2022
<b>Publisher:</b>	Wiley
<b>Authors:</b>	<b>Rahmanian, Fuzhan</b> and Vogler, Monika and Chrisitan, Wölke and Yan, Peng and Winter, Martin and Cekic-Laskovic, Isidora and Stein, Helge Sören
<b>Status:</b>	Accepted: 23. August 2022
<b>DOI:</b>	<a href="https://doi.org/10.1002/batt.202200228">https://doi.org/10.1002/batt.202200228</a>
<b>Developed Software:</b>	 <a href="https://github.com/BIG-MAP/electrolyte_optimization_one_shot_active_learning">https://github.com/BIG-MAP/electrolyte_optimization_one_shot_active_learning</a>

---

\* For reprint permission refer to Section A.1

## Publication Content

Autonomous experimental workflows with feedback loops typically begin with a random experiment. Subsequent experimental parameters are then iteratively selected using a learning algorithm and an optimizer to enhance model performance. This process expands prior knowledge at every step to unravel parameter interdependencies. A challenge that often the model encounters is the scarcity of data, which can lead to overfitting or inefficient learning. The incorporation of existing datasets as prior knowledge into the workflow can accelerate insight acquisition and optimize experimental parameters, thus deepening the understanding of physicochemical interrelationships. Herein, this study introduces an active learning pipeline within a human-in-the-loop framework, utilizing a dataset from the Helmholtz Institute of Münster (HIM) as its prior knowledge. The dataset consists of 80 electrolyte formulations of LiBs, with conductivity measured across temperatures ranging from  $-30\text{ }^{\circ}\text{C}$  to  $60\text{ }^{\circ}\text{C}$  in  $10\text{ }^{\circ}\text{C}$  increments. The study defined a search space of  $10^4$  potential formulations and aimed to identify those with optimal ionic conductivity at all defined temperatures using an interpretable model. This approach involved the implementation of regularized polynomial regression with hyperparameter optimization and uncertainty estimation.

Following training and validation, the model predicted ionic conductivity for untested formulations at each temperature. In a fully exploitative setting, the top 10 formulations demonstrating the highest conductivity for each temperature were selected, and through random sampling, 24 formulations from temperatures  $-30\text{ }^{\circ}\text{C}$ ,  $20\text{ }^{\circ}\text{C}$ , and  $60\text{ }^{\circ}\text{C}$  were experimentally tested by the collaborator at HIM. The initial test findings aligned with the model predictions at lower temperatures, although discrepancies were observed at higher temperatures. The model was retrained following one-shot experimental testing and the inclusion of additional data, which constituted 30% more than the initial dataset. This retraining improved prediction accuracy, reduced uncertainty, and aligned better with the existing literature. For interpretability, the coefficients of the optimized third-degree polynomial model were recorded to capture the trends of solvent and conducting salt across varying temperatures. Additionally, the conductivity gradient relative to formulation variations was calculated, which enabled the derivation of the maximal allowable error in formulations. This study

highlights the importance of prior knowledge in increasing model trustworthiness, optimizing experimental design, and accelerating material discovery.

### **Individual Contribution**

During the efforts for the publications of this study, **Fuzhan Rahmanian** performed the data cleaning from the delivered HIM dataset. **F.R.** designed the data ingestion pipeline, developed the model, implemented the uncertainty estimation with MAPIE, and oversaw the training procedure. **F.R.** performed the analysis, plotted the results, and curated the code and GitHub repository. **F.R.** drafted the manuscript. M.V. validated the results with existing values in the literature and supported the finalization of the manuscript. C.W. and P.Y. conducted the experimental measurements in both the initial and second experimentation run. All the authors reviewed the manuscript.

## 4.3.2. Manuscript



Batteries &amp; Supercaps

Research Article  
doi.org/10.1002/batt.202200228

www.batteries-supercaps.org

## One-Shot Active Learning for Globally Optimal Battery Electrolyte Conductivity\*\*

Fuzhan Rahmanian,<sup>[a, b]</sup> Monika Vogler,<sup>[a, b]</sup> Christian Wölke,<sup>[c]</sup> Peng Yan,<sup>[c]</sup> Martin Winter,<sup>[c, d, e]</sup> Isidora Cekic-Laskovic,<sup>[c]</sup> and Helge S. Stein<sup>\*,[a, b]</sup>

Non-aqueous aprotic battery electrolytes need to perform well over a wide range of temperatures in practical applications. Herein we present a one-shot active learning study to find all conductivity optima, confidence bounds, and relating formulation trends in the temperature range from  $-30^{\circ}\text{C}$  to  $60^{\circ}\text{C}$ . This optimization is enabled by a high-throughput formulation and characterization setup guided by one-shot active learning utilizing robust and heavily regularized polynomial regression.

Whilst there is an initially good agreement for intermediate and low temperatures, there is a need for the active learning step to improve the model for high temperatures. Optimized electrolyte formulations likely correspond to the highest physically possible conductivities within this formulation system when compared to literature data. A thorough error propagation analysis yields a fidelity assessment of conductivity measurements and electrolyte formulation.

### Introduction

High-conductivity electrolytes in secondary batteries are of paramount importance for ensuring high performance and reliability of each battery cell chemistry.<sup>[1]</sup> In specialty applications such as aerospace or stationary storage in remote locations, bespoke electrolytes are however necessary.<sup>[2]</sup> High or low temperatures make the electrolyte a limiting performance factor,<sup>[1–4]</sup> e.g., in electric vehicles which suffer from relatively narrow optimal temperature windows of  $15^{\circ}\text{C}$  to  $35^{\circ}\text{C}$ .<sup>[1]</sup> Many studies<sup>[3–5]</sup> have thus been conducted to evaluate lithium-ion battery (LIB) electrolytes at low temperatures in respect to their conductivity. There exists only a limited number of electrolyte studies that consider wide temperature ranges<sup>[6–9]</sup> as recently reviewed by Lin et al.<sup>[10]</sup> Emblematic are the studies of Smart et al.<sup>[6]</sup> and Fan et al.<sup>[7]</sup> that both evaluate a limited

number of formulations between  $-60^{\circ}\text{C}$  to  $20^{\circ}\text{C}$  and  $-125^{\circ}\text{C}$  to  $70^{\circ}\text{C}$ , respectively. The studies by Dave et al.<sup>[11,12]</sup> consider a wide range of electrolyte formulations but within a narrow range of temperatures. Utilizing an existing dataset<sup>[13,14]</sup> spanning a wide range of formulations and temperatures, we aim to perform as few as possible additional experiments to discover formulations with maximum conductivity for a wide range of temperatures. This is performed in a workflow called one-shot active learning. This means that a machine learning algorithm is used to suggest the most promising subsequent experiment for improving the outcome and model. Besides aiming to discover optimal electrolyte formulations for a range of temperatures, we also seek to evaluate whether there exists a globally optimal electrolyte. Although, conductivity optima can be predicted from the existing dataset using a machine learning model, we believe that more physically meaningful predictions can be obtained upon re-training of the model from one-shot active learning suggestions. From the post shot model, we then seek to deduce insights on the effects of different parameters on the conductivity values, which could not be generated solely based on the initially available dataset.

Compared to previous deployments of machine learning<sup>[15]</sup> in the field of battery electrolyte optimization,<sup>[11]</sup> we investigate whether an improvement in conductivity may already be achieved through a single iteration cycle. This approach is mostly analogous to the workflow of Attia et al.<sup>[16]</sup> for fast charging protocol optimization, as herein we are using a high-throughput electrolyte formulation robot and a machine learning based optimizer, that were not integrated and in fact run at two different locations asynchronously. This enabled us to deploy active learning without requiring the experimental equipment to have a direct interface to our active learning infrastructure, potentially allowing a greater adoption of this research paradigm.<sup>[17,18]</sup> This one-shot active learning study aims to find optimally conducting electrolyte formulations at temperatures ranging between  $-30^{\circ}\text{C}$  and  $60^{\circ}\text{C}$  with as few

[a] F. Rahmanian, M. Vogler, Prof. Dr. H. S. Stein  
Helmholtz Institute Ulm, Applied Electrochemistry, Helmholtzstr. 11, 89081 Ulm, Germany  
E-mail: helge.stein@kit.edu

[b] F. Rahmanian, M. Vogler, Prof. Dr. H. S. Stein  
Karlsruhe Institute of Technology, Institute of Physical Chemistry, Fritz-Haber-Weg 2, 76131 Karlsruhe, Germany

[c] Dr. C. Wölke, P. Yan, Prof. Dr. M. Winter, Dr. I. Cekic-Laskovic  
Helmholtz-Institute Münster (IEK-12), Forschungszentrum Jülich GmbH, Corrensstraße 46, 48149 Münster, Germany

[d] Prof. Dr. M. Winter  
MEET Battery Research Center, University of Münster, Corrensstraße 46, 48149 Münster, Germany

[e] Prof. Dr. M. Winter  
Helmholtz-Institute Münster (IEK-12), Forschungszentrum Jülich GmbH, Corrensstraße 46, 48149 Münster, Germany

[\*\*] A previous version of this manuscript has been deposited on a preprint server (<https://doi.org/10.26434/chemrxiv-2022-1z8gn>).

Supporting information for this article is available on the WWW under <https://doi.org/10.1002/batt.202200228>

© 2022 The Authors. Batteries & Supercaps published by Wiley-VCH GmbH. This is an open access article under the terms of the Creative Commons Attribution License, which permits use, distribution and reproduction in any medium, provided the original work is properly cited.

extra measurements as necessary. Opposed to applying machine learning algorithms to conclude from existing datasets, active learning<sup>[18,19]</sup> is integrated in the data acquisition process with the idea of improving the model through intelligent suggestion of additional measurements. Usually, optimization loops in materials science<sup>[12,20]</sup> are run over several iterations, the approach herein, however, aims to only perform a single iteration to achieve an improvement in conductivity and potentially reduction in uncertainty. The existing dataset of lithium hexafluorophosphate (LiPF<sub>6</sub>) in ethylene carbonate (EC), ethyl methyl carbonate (EMC) and propylene carbonate (PC) was totaling 80 electrolyte formulations with measured conductivities at  $-30$  to  $60$  °C.<sup>[13,14]</sup> The suggestion of new formulations was fully exploitative,<sup>[20]</sup> i.e., requested formulations were selected solely based on their predicted conductivity at a respective temperature with complete neglect of model uncertainty. Active learning in fully exploitative mode has been shown to significantly increase the so-called “enhancement factor” by Rohr et al.<sup>[20]</sup> The enhancement factor describes the increase in probability of finding an optimum given a fixed budget of experiments. There are other research modes<sup>[20]</sup> not explored in this study. However, a recent study by Flores et al.<sup>[13]</sup> focused on the “understanding driven” research mode. Their symbolic regression approach<sup>[13]</sup> works well for high temperatures but fails for highly concentrated liquid electrolytes at low temperatures, indicating a change in the physicochemical behavior. Organizationally, this study is the human-in-the-loop version of the fully autonomous active learning study presented by Rahmanian et al.<sup>[21]</sup>

## Results and Discussion

### Pre-shot model training

The dataset DS1 used herein is the same underlying the study presented by Flores et al.<sup>[13]</sup> using the formulation and characterization setup reported by Krishnamoorthy et al.<sup>[14]</sup> The herein presented one-shot active learning approach is model free, meaning that we do not utilize any physics or chemistry knowledge except correct pose of the input (formulation) and output (conductivity) and a compartmentalization of the problem by temperature.

The global trends of electrolyte conductivity, captured by our model M1, are shown in Figure 1, which illustrates the conductivity ( $\sigma$ ) over  $r_{\text{LiPF}_6}$  and  $r_{\text{PC}}$  at  $-30$  °C,  $-10$  °C,  $20$  °C, and  $60$  °C (additional temperatures see S2). For all considered temperatures the  $R^2$  score is approximately 0.73–0.80, which indicates a good fit. However, the degree of the polynomial used for the fit is higher for the high temperatures compared to low temperatures. The orange datapoints in Figure 1 indicate the formulations covered by dataset DS1.

Overall, conductivity is strongly correlated with temperature as expected from Debye-Hückel-Onsager (DHO) theory,<sup>[13,22]</sup> however this theory is only valid for dilute solutions. Consequently, we observe low conductivity for  $r_{\text{LiPF}_6} > 0.8$  or  $r_{\text{LiPF}_6} < 0.1$ . In general, we observe the maximum conductivity

shifting towards higher conducting salt concentrations at higher temperatures as it was reported by Landesfeind et al.<sup>[23]</sup> and Ding et al.<sup>[24,25]</sup> for various electrolyte formulations. The lowest overall measured conductivity is  $194 \text{ mS cm}^{-1}$  at  $-30$  °C. Conductivity is showing a generally less pronounced dependence on  $r_{\text{PC}}$  than on  $r_{\text{LiPF}_6}$ . This observation correlates with the concentration-conductivity relationship that is primarily dependent on conducting salt concentration.<sup>[25]</sup>

Going from low to high temperatures, the system seems to allow for higher  $r_{\text{PC}}$  and  $r_{\text{LiPF}_6}$  while yielding a high conductivity which is in good agreement with established theory.<sup>[25,26]</sup> The model M1 also seems to prefer little presence of PC at low temperatures for higher conductivity.<sup>[25,26]</sup> Our finding is in good agreement with Ding et al.<sup>[26]</sup> who report, similar trends with temperature.<sup>[27]</sup> They discuss the higher EC and PC contents by an increase in the dielectric constant and consequently higher conductivity.<sup>[27,28]</sup> At  $20$  °C, a narrow global optimum at relatively high  $r_{\text{PC}} \approx 0.35$  is observed. The plot of the conductivity corresponding to  $60$  °C shows a very small region with high conductivity around  $r_{\text{PC}} \approx 0.35$  and  $r_{\text{LiPF}_6} \approx 0.38$ , and additionally a maximum at  $r_{\text{PC}} \approx 0.3$  and very high  $r_{\text{LiPF}_6} \approx 1.2$ . All but the  $-10$  °C optima exist near unsampled formulations. Based on the prediction of the trained model M1, 10 samples with highest predicted conductivity for each temperature were selected and reported to the experimentalists. The requested and considered formulations can be found in the [https://github.com/BIG-MAP/electrolyte\\_optimization\\_one\\_shot\\_active\\_learning](https://github.com/BIG-MAP/electrolyte_optimization_one_shot_active_learning) repository.

### One-shot predictions and measurements

Utilizing the above results obtained from M1 (see Figure 1), we predict 10 top percentile formulations at every temperature, resulting in a total of 100 electrolyte formulations. These formulations were communicated to the experimentalists omitting the predicted conductivity. The experimentalists randomly selected 24 formulations from these 100 suggestions. These selected formulations correspond to optimization temperatures of  $-30$  °C,  $20$  °C and  $60$  °C. Conductivity measurements were conducted for the selected formulations covering all the temperatures between  $-30$  °C and  $60$  °C in steps of  $10$  °C analogously to the generation of the dataset DS1. The data obtained from the measurement of these 24 formulations constitute dataset DS2. Figure 2 compares the M1 predicted vs. measured conductivities for the 24 newly measured formulations. There is a small deviation between the requested and measured formulations due to slight imperfections in the formulation process. Hence, Figure 2 shows the conductivity prediction at the actually formulated composition. Inaccuracies occurring during the solid and liquid dispensing processes are technical in nature and are negligible given the fidelity assessment presented in the section “Interactions and method fidelity”. The error bar illustrates the conductivity error by reporting the maximum and minimum values among the repeated measurements.

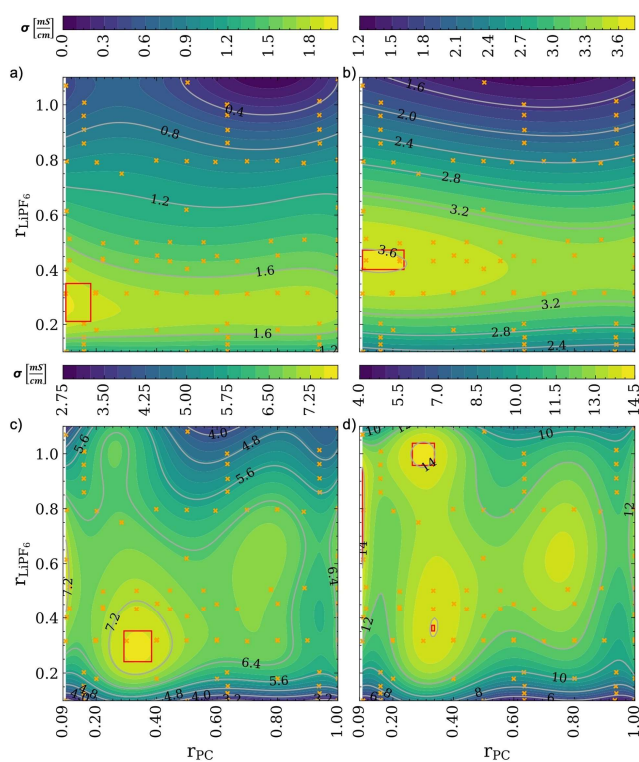


**Figure 1.** Trends in electrolyte conductivity at a)  $-30^{\circ}\text{C}$ , b)  $-10^{\circ}\text{C}$ , c)  $20^{\circ}\text{C}$ , d)  $60^{\circ}\text{C}$  as obtained from model M1. Orange data points represent the  $r_{\text{PC}}$  and  $r_{\text{LiPF}_6}$  position of formulations, which were experimentally measured. There is an overall incremental trend for higher  $r_{\text{LiPF}_6}$  from  $-30^{\circ}\text{C}$  to  $-10^{\circ}\text{C}$  and narrow optima in electrolyte conductivity at higher  $r_{\text{PC}}$  at unsampled formulations for the higher temperatures. The red boxes in the plots represent the range of formulations corresponding to the top percentile of the conductivity as obtained from the predictions of the model M1.

Figure 2(a) shows predicted and measured conductivities at a temperature of  $-30^{\circ}\text{C}$ . Formulations predicted to be optimally conducting electrolytes at  $-30^{\circ}\text{C}$  are verified experimentally to be among the best conducting at this temperature. The evaluation metric here should therefore not be the exact value prediction, as all originate from a narrow distribution of only 1% variance, which is significantly lower than the experimental noise, i.e., all points are virtually indistinguishable. All but one formulation optimized for  $-30^{\circ}\text{C}$  fall within the top percentile, i.e., the success rate is 87%, see also Figure 4. The formulations optimized for  $20^{\circ}\text{C}$  and  $60^{\circ}\text{C}$  exhibit a significantly lower conductivity at  $-30^{\circ}\text{C}$ , also with relatively large deviations between M1 prediction and measurement. This data suggests that there exists no electrolyte with a globally optimal conductivity. Differences in performance between formulations optimized for the temperature of interest and those not optimized for this temperature can amount up to 100%.

The measured conductivities for the requested formulations are added as prior knowledge and the model is retrained using dataset DS3.

#### Post-shot model refinement

After one-shot active learning and the Bayesian hyperparameter tuning<sup>[29]</sup> as described in the methods section, the models are significantly improved. The predicted trends for low temperatures changed only marginally, whereas the improvements for temperatures of  $20^{\circ}\text{C}$  and  $60^{\circ}\text{C}$  are significant, as shown in Figure 3. Additional temperatures can be found in S3. Together with the low temperature trends there is now a coherent trend across temperatures suggesting higher  $r_{\text{PC}}$  and  $r_{\text{LiPF}_6}$  for optimal conductivity at elevated temperatures.<sup>[23,26]</sup> Also, the range of formulations, for which the maximum



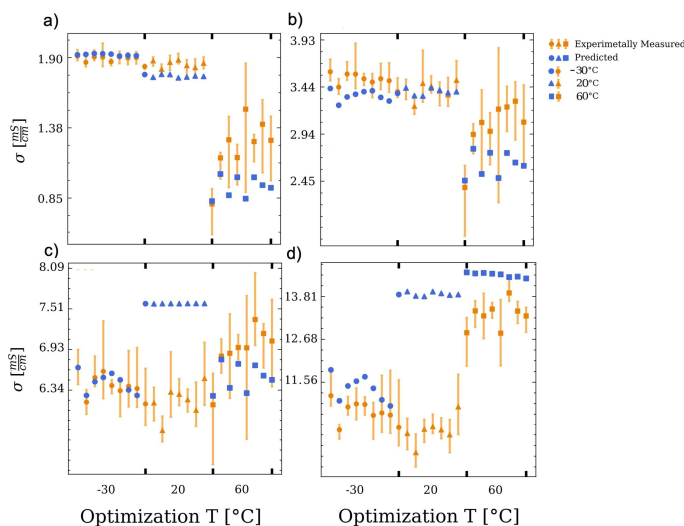


**Figure 2.** Comparison between measured and predicted conductivity values at a)  $-30^{\circ}C$ , b)  $-10^{\circ}C$ , c)  $20^{\circ}C$ , and d)  $60^{\circ}C$  for the formulations selected based on the predictions of model M1. Orange points represent the mean values of measured conductivities with error bars relating to the min/max spread from repeated measurements. The high accuracy for low temperature predictions is best observed in a) where the formulations predicted to be best at  $60^{\circ}C$  and the ones optimized for conductivity at  $20^{\circ}C$  perform worse at  $-30^{\circ}C$ . Overall, this suggests, that there exists no globally optimal electrolyte and performance can vary by up to a factor of two.

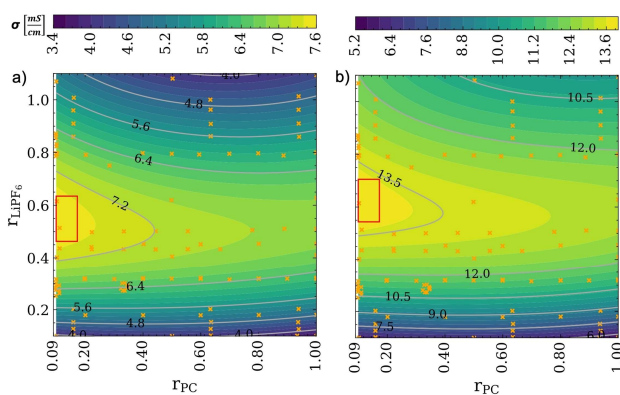


**Figure 3.** Trends in electrolyte conductivity after one-shot active learning for a)  $20^{\circ}C$ , and b)  $60^{\circ}C$  as predicted by M2. The red boxes correspond to the top percentile, which was obtained from M1. The selected formulations which were suggested by M1 and used for conductivity determination (DS2), were added to the training set as an additional prior knowledge (DS3). Model parameter tuning and uncertainty measurement were implemented at this stage of active learning (see S4). Trends for additional temperatures can be seen in the S3.

conductivity was predicted by M1, changed significantly with M2. Therefore, the region of the formulations constituting the top percentile obtained from M1, represented as a red

rectangle in Figure 3, is far from the top percentile of the improved model M2.

The improvement of the model's predictions towards a more physically meaningful trend highlights the significance of

active learning in model refinement as we only added an additional 30% of data points to the dataset whilst qualitatively improving the model. Comparing these results to the symbolic regression model by Flores et al.<sup>[13]</sup> reveals significant differences in the mass ratios required for maximum conductivity.

Figure 4 shows the conductivity as predicted by M1 and measured experimentally for the formulations comprised in dataset DS2 at the temperature for which the respective formulation was optimized. Furthermore, the top percentiles obtained from M1 (red areas) and M2 (green areas) are shown. Overall, the optimization and prediction worked best at low temperatures. The measured conductivity values are close to the predicted ones at  $-30^{\circ}\text{C}$ . Hence, the measured values are within the top percentile of M1. Unsurprisingly, the top percentile does not change significantly after the one-shot active learning and the formulations are also within the top percentile of M2. From the plots corresponding to  $20^{\circ}\text{C}$  and  $60^{\circ}\text{C}$ , a poorer performance is observed. At  $20^{\circ}\text{C}$ , the model significantly overestimates the highest conductivity. The measured conductivity values at  $20^{\circ}\text{C}$  remain below the predictions and below the top percentile. The results for  $60^{\circ}\text{C}$  reveal a less severe deviation between the predictions and the measured conductivity values. However, the measured values are still below the predicted ones and below the top one percentiles of both, M1 and M2. This can be understood based on the results obtained from Figure 3. Therefore, the success rate is only about 12% as only one formulation is within the pre-shot top percentile. The significant changes in the position of the conductivity maxima upon one-shot active learning result in the formulations contained in dataset DS2 not being the highest conducting ones anymore. The range of the top percentile in conductivity does not change severely, however the formulations corresponding to these conductivity values differ strongly. This indicates that M1, which is trained solely on DS1, is not fit well for temperatures around  $20^{\circ}\text{C}$  and above. Based on the differences between Figure 3 and Figure 4, it can be assumed, that the quality of the models significantly increases through active learning.

The drastic improvement of the model becomes even more obvious upon plotting the temperature maxima with the spread of the top percentile as displayed in Figure 5. Before the

learning shot, the optima followed no physically meaningful or interpretable trend whereas after adding the extra data contained in DS2, the very fine trends in optima towards higher  $r_{\text{LiPF}_6}$  and slightly more  $r_{\text{PC}}$  become obvious. Uncertainty quantification was performed using the jackknife plus<sup>[30,31]</sup> strategy resulting in an average 95% prediction interval of  $3^*10^{-1} \text{ mS cm}^{-1}$  (see S4). However, the incorporation of the model agnostic prediction technique allows the measurement of aleatoric and epistemic uncertainty at any point. Comparing the results for electrolyte conductivity found by our one-shot active learning approach to literature such as Ding et al.<sup>[24]</sup> at  $60^{\circ}\text{C}$ , and  $-30^{\circ}\text{C}$  suggests that the herein reported maxima correspond to the globally maximum conductivity in this system, which is approximately  $12 \text{ mS cm}^{-1}$  and  $1.9 \text{ mS cm}^{-1}$ , respectively. In another study, Landesfeind et al.<sup>[23]</sup> indicate global maxima of  $4.7 \text{ mS cm}^{-1}$ ,  $7.6 \text{ mS cm}^{-1}$  and  $9.25 \text{ mS cm}^{-1}$  at  $-10^{\circ}\text{C}$ ,  $20^{\circ}\text{C}$ , and  $30^{\circ}\text{C}$ , respectively. Their results are in agreement with our findings.

#### Interactions and method fidelity

Through the availability of a machine learning model M2 that accurately and precisely predicts the trends in conductivity for all temperatures, an assessment of confounding inputs and method fidelity can be pursued. The model has two inputs:  $r_{\text{PC}}$  and  $r_{\text{LiPF}_6}$ , and through the polynomial nature an analytical derivation is facile. The post-shot regularized polynomial equation [Eq. (1)] for conductivity ( $\sigma$ ) post hyperparameter tuning is:

$$\sigma = C_0 + C_1 r_{\text{PC}} + C_2 r_{\text{LiPF}_6} + C_3 r_{\text{PC}}^2 + C_4 r_{\text{PC}} r_{\text{LiPF}_6} + C_5 r_{\text{LiPF}_6}^2 + C_6 r_{\text{PC}}^3 + C_7 r_{\text{PC}}^2 r_{\text{LiPF}_6} + C_8 r_{\text{PC}} r_{\text{LiPF}_6}^2 + C_9 r_{\text{LiPF}_6}^3 \quad (1)$$

i.e., a polynomial of degree 3 with the individual parameters shown in Table 1. Some coefficients change drastically with temperature whilst others barely change. Upon careful comparison to Equation (1), one can see that those coefficients corresponding to a conducting-salt-ratio-only term, scale almost exponentially whilst all others, i.e., solvent-ratio-only and

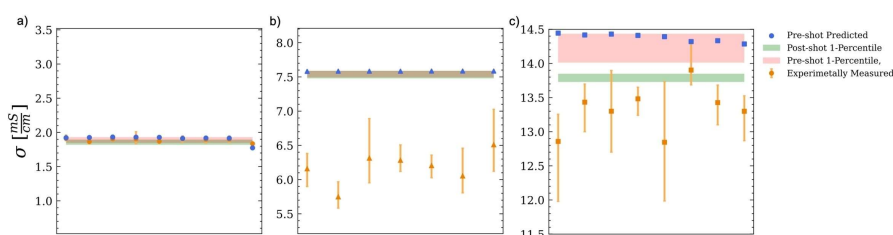


**Figure 4.** Predicted and measured conductivities for the formulations contained in dataset DS2 optimized regarding conductivity at the temperatures a)  $-30^{\circ}\text{C}$ , b)  $20^{\circ}\text{C}$  and c)  $60^{\circ}\text{C}$ . Each subfigure shows the data for the formulations optimized at the respective temperature. Predictions originating from M1 are shown. Additionally, the range of conductivities spanned by the top percentile as predicted by M1 (red areas) and M2 (green areas) are shown.

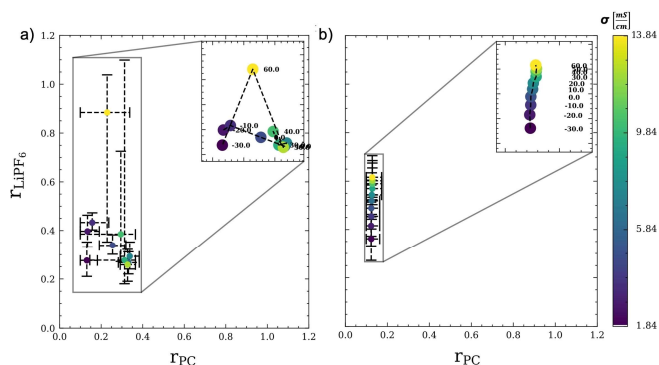


**Figure 5.** Trends of maximum conductivity a) before (M1) and b) after (M2) one-shot active learning and model optimization. Each point corresponds to the mean conductivity value of the top percentile obtained from the respective model trained for the temperature of interest. The error bars represent the spread of  $r_{LiPF_6}$  and  $r_{PC}$  within the top percentile. Before introduction of the additional 24 electrolyte formulations (DS2), the trends are neither physically nor qualitatively interpretable. Overall, higher  $r_{LiPF_6}$  is needed at higher temperatures to reach the optima, with a minutely higher  $r_{PC}$  from 20 °C onward.

**Table 1.** Polynomial coefficients incorporating ridge regularization after one-shot active learning for  $T = -30$  °C to 60 °C.

$T$ [°C] / $c \times 10^{-3}$	$c_0$	$c_1$	$c_2$	$c_3$	$c_4$	$c_5$	$c_6$	$c_7$	$c_8$	$c_9$
-30	1.0	-0.3	5.6	0.9	-2.3	-9.7	-0.6	1.4	0.6	4.0
-20	1.2	-0.3	8.9	0.9	-3.2	-13.6	-0.7	1.9	0.8	5.1
-10	1.4	1.0	12.1	0.1	-3.9	-17.1	-0.3	2.4	0.9	6.1
0	1.5	0.4	15.9	-0.1	-4.9	-21.2	-0.4	3.3	0.9	7.3
10	1.5	1.2	20.4	-0.9	-5.9	-26.1	-0.4	4.2	0.7	8.8
20	1.6	1.7	25.0	-1.4	-6.8	-31.0	-0.3	5.1	0.5	10.5
30	1.6	2.7	29.7	-3.2	-6.9	-35.8	0.4	5.6	0.0	12.2
40	1.6	3.0	35.1	-3.2	-7.3	-41.9	1.0	6.2	-0.6	14.6
50	1.6	3.2	41.3	-3.2	-7.6	-49.5	0.0	6.4	-0.7	17.6
60	1.6	3.0	47.4	-2.5	-6.9	-57.2	-0.7	6.6	-1.8	21.1

solvent-conducting-salt-ratio terms scale sigmoidal with temperature (see S6b). These interaction coefficients allow for further research into the relationship governing the solvation shell properties upon electrolyte solvent variation.<sup>132</sup>

A long-lasting debate of how precise the electrolyte formulation needs to be answered using model M2. An error propagation estimation can be done when the gradient of a function and the uncertainty of the underlying input is known. From the herein reported measurements, we know the uncertainty of the conductivity and we can easily calculate the gradient of the conductivity w.r.t. the formulation. Here, we take the median uncertainty of the conductivity measurements ( $\Delta\sigma_{exp} = 0.3527 \text{ mS cm}^{-1}$ ) and divide it by the largest gradient of conductivity w.r.t. to formulation (both uni- and bivariate) at every temperature (Figure 6, Table 2) to obtain a conservative estimate of the maximally allowed formulation error [Eq. (2)] that would be on the same order of magnitude like the measurement noise. Unsurprisingly one can have larger errors in solvent-to-co-solvent ratios as in conducting-salt-to-solvent ratios. Interesting, however, is that an error of about 10% in the solvents is acceptable for most temperatures. Dosing of the conducting salt should however be as precise as possible as at high temperatures the error should not exceed 1.5%.

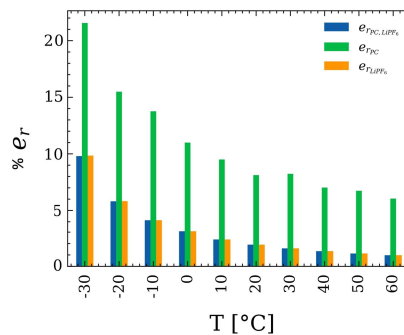


**Figure 6.** The maximum formulation error calculated by Equation (2) with the median  $\Delta\sigma_{exp}$  of approximately  $0.3527 \text{ mS cm}^{-1}$  with respect to uni- and bivariate combination of  $r_{LiPF_6}$  and  $r_{PC}$  between  $-30$  °C and  $60$  °C.

Table 2. The maximum norm of the predicted conductivity gradient.

$T [^{\circ}\text{C}] / \max(\partial\sigma) \left(\frac{\text{mS}}{\text{cm}}\right)$	$\partial\sigma_{r_{\text{LiPF}_6}}$	$\partial\sigma_{r_{\text{PC}}}$	$\partial\sigma_{r_{\text{EMC}}}$
-30	3.598	1.636	3.582
-20	6.071	2.277	6.057
-10	8.526	2.563	8.523
0	11.454	3.208	11.455
10	14.955	3.711	14.947
20	18.535	4.341	18.516
30	22.345	4.283	22.294
40	26.462	5.024	26.404
50	31.307	5.234	31.248
60	36.173	5.831	35.999

$$\left(\alpha\left(\frac{\partial\sigma}{\partial r_{\text{PC}}}\right)^2 + \beta\left(\frac{\partial\sigma}{\partial r_{\text{LiPF}_6}}\right)^2\right)^{0.5} \cdot e_{r_{\text{PC}}, \text{LiPF}_6} \leq \Delta\sigma_{\text{exp}} \quad (2)$$

for  $\alpha, \beta \in \{(0, 1), (1, 0), (1, 1)\}$

## Conclusion

This study shows the utility of active learning to improve model accuracy and precision on complex data with few examples. The pre-shot model M1 significantly underfit the data such that obtained trends did not follow a physically meaningful trend. After one-shot active learning, the discovered model M2 produced smooth optima across the temperatures under investigation even though temperature was not a parameter in model training. Obtained trends in the optima suggest that for low temperatures, the conducting salt concentration should be minimized whilst for higher temperatures the salt concentration should be increased. We find that a globally optimally conducting electrolyte does not exist as those optimal at low temperatures perform poorly at higher temperatures. Those electrolytes optimized for near room temperature show approximately 20% less conductivity at low and about half the conductivity at high temperatures compared to the formulations optimized for the respective temperature range. Through the availability of an easily differentiable model M2, we can discuss electrolyte solvent-conducting salt interactions and find mostly sigmoidal or exponential temperature trends hinting at two different mechanisms. The differentiable model M2 also allows an elucidation of maximally allowed formulation errors which lie at approximately 10% for the solvent composition and 1.5% for the conducting salt ratio at most temperatures. Through the conservative choice of a low degree polynomial model, we were able to obtain optima and interpretable insights translatable to existing physicochemical laws such as the DHO theory, however at high salt concentrations.

We believe, our approach can be transferred to novel electrolyte systems e.g., for Na-ion batteries. In our opinion, this could accelerate knowledge generation when starting from small datasets and unravel complex interrelations early in the research process.

## Experimental

### Workflow

The overall idea of this study is the optimization through a one-shot active learning iteration. To this end a pre-existing dataset DS1 was utilized to pre-train a model M1. From M1, a set of optimally conducting electrolytes was suggested to the experimentalists. The experimentalists measured the conductivity of the newly suggested formulations and reported the results back to the machine learning team. The newly measured data collected in the dataset DS2 was merged with dataset DS1 to obtain an extended dataset DS3. The dataset DS3 is then used to retrain the model to provide refined trends with formulation and temperature. In the following we will refer to the retrained model as M2. The predicted conductivities obtained from M2 are also used to understand error propagation.

Further details about the model training can be found in the section "Model training and one-shot active learning". A schematic of this study's workflow is shown in Figure 7. Summarizing, there are three stages in this pipeline: 1) model training, 2) formulation suggestions and measurement, 3) retraining and refinement of the model and uncertainty quantification.

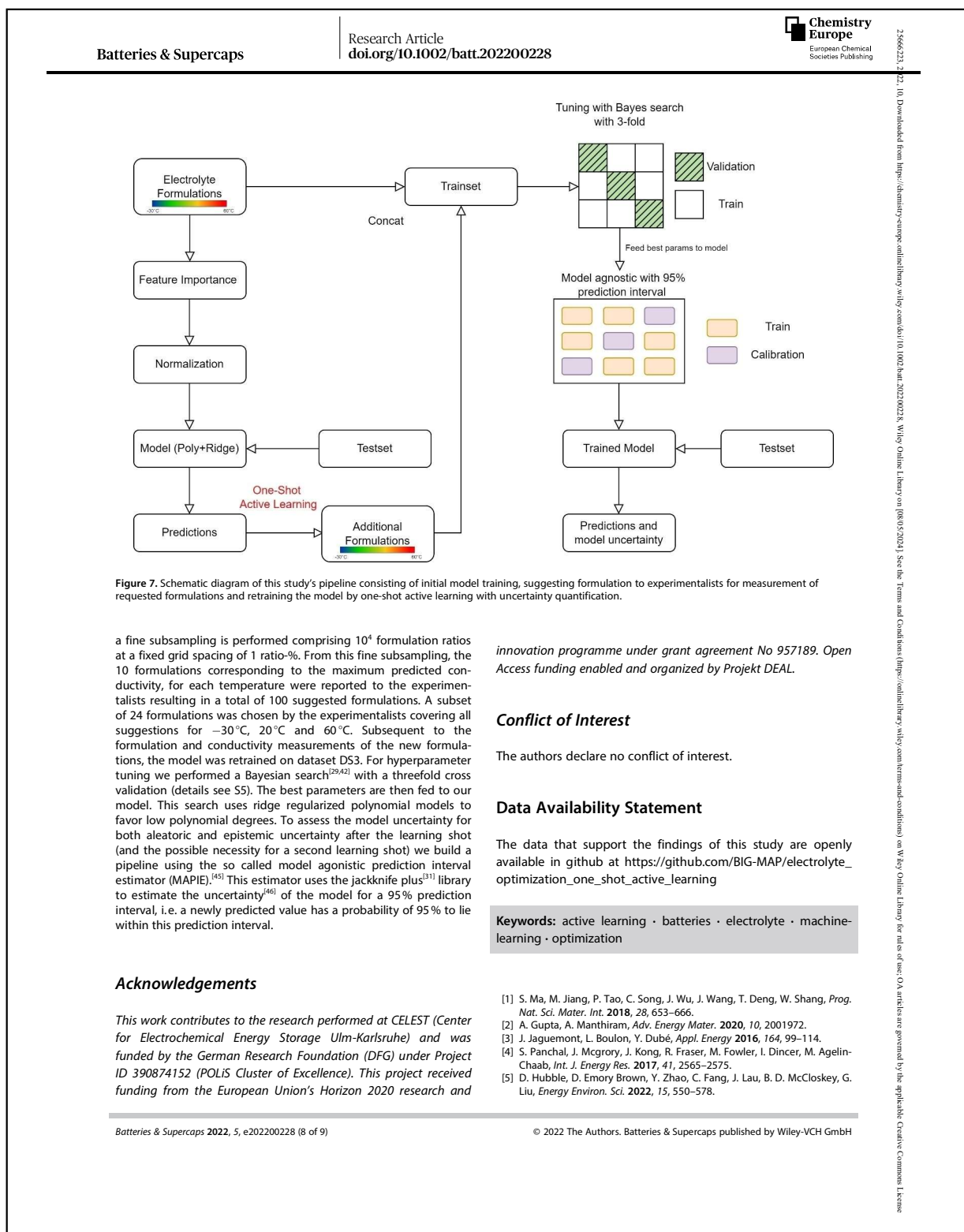
### Description of the initial dataset DS1 and Measurements

The initial dataset DS1 used herein to pre-train the model M1, totals 80 distinct electrolyte formulations measured at Helmholtz-Institute Münster for general purpose, using their automated formulation and characterization setup described in detail in Krishnamoorthy et al.<sup>[14]</sup> The formulations reported in DS1 contain ethylene carbonate (EC), propylene carbonate (PC), and ethyl methyl carbonate (EMC) in a solvent/co-solvent mixture and lithium hexafluorophosphate (LiPF<sub>6</sub>) as the conducting salt. The data reported in DS1 covers temperatures between -30 °C and 60 °C, at increments of 10 °C as described by Krishnamoorthy et al.<sup>[14]</sup> Conductivity measurements were repeated 5 to 7 times. For each datapoint the electrolyte formulation, conductivity and measurement temperature were recorded. Across all formulations, the ratio of (EC + PC) : EMC was fixed either at 3:7 or 1:1 by weight and the concentration of LiPF<sub>6</sub> was varied between 0.2 and 2.1 mol kg<sup>-1</sup>.

We express the uncertainties for the experimental values by the min/max spread of the individual measurements. The mass ratios of PC and LiPF<sub>6</sub> were normalized and referenced as  $r_{\text{PC}} = \frac{\text{PC}}{\text{PC} + \text{EC}}$  and  $r_{\text{LiPF}_6} = \frac{\text{LiPF}_6}{\text{PC} + \text{EC} + \text{EMC}}$  for using them as inputs for model training and one-shot active learning. The (EC + PC):EMC ratio was not considered during model training as it is not an independent variable.

### Model training and one-shot active learning

The dataset size poses the challenge of finding well performing models that are simple and interpretable.<sup>[33]</sup> We therefore settle on polynomial regression<sup>[34]</sup> for our study. Contrary to Flores et al.<sup>[13]</sup> we do not consider temperature as a parameter in model training and train our model independently for each temperature. The basic model is a strongly regularized polynomial regressor aiming to avoid multicollinearity,<sup>[35,36]</sup> i.e., linear correlations among the input parameters, which would negatively affect the estimates of the coefficients in the regression model.<sup>[37-40]</sup> The polynomial regression,<sup>[34]</sup> ridge regularization,<sup>[41]</sup> and in step two for optimization purposes hyperparameter tuning are performed. All of the machine learning steps were performed using the scikit-learn library<sup>[42-44]</sup> available for Python. From the fitted polynomial model



- [6] M. C. Smart, B. V. Ratnakumar, K. B. Chin, L. D. Whitcanack, *J. Electrochem. Soc.* **2010**, *157*, A1361.
- [7] X. Fan, X. Ji, L. Chen, J. Chen, T. Deng, F. Han, J. Yue, N. Piao, R. Wang, X. Zhou, X. Xiao, L. Chen, C. Wang, *Nat. Energy* **2019**, *4*, 882–890.
- [8] Q. Zhou, S. Dong, Z. Lv, G. Xu, L. Huang, Q. Wang, Z. Cui, G. Cui, *Adv. Energy Mater.* **2020**, *10*, 1903441.
- [9] Y. Yang, Y. Yin, D. M. Davies, M. Zhang, M. Mayer, Y. Zhang, E. S. Sablina, S. Wang, J. Z. Lee, O. Borodin, C. S. Rustomji, Y. Shirley Meng, *Energy Environ. Sci.* **2020**, *13*, 2209–2219.
- [10] X. Lin, G. Zhou, J. Liu, J. Yu, M. B. Effat, J. Wu, F. Ciucci, *Adv. Energy Mater.* **2020**, *10*, 2001235.
- [11] A. Dave, J. Mitchell, K. Kandasamy, H. Wang, S. Burke, B. Paria, B. Póczos, J. Whitacre, V. Viswanathan, *Cell Rep. Phys. Sci.* **2020**, *1*, 100264.
- [12] A. Dave, J. Mitchell, S. Burke, H. Lin, J. Whitacre, V. Viswanathan, *ArXiv211114786 Cs* **2021**.
- [13] E. Flores, C. Wölke, P. Yan, M. Winter, T. Vegge, I. Cekic-Laskovic, A. Bhowmik, **2022**, DOI 10.26434/chemrxiv-2022-nmmd4.
- [14] A. N. Krishnamoorthy, C. Wölke, D. Diddens, M. Maiti, Y. Mabrouk, P. Yan, M. Grünebaum, M. Winter, A. Heuer, I. Cekic-Laskovic, **2022**, DOI 10.26434/chemrxiv-2022-vbl5d.
- [15] A. D. Sendek, E. D. Cubuk, B. Ransom, J. Nanda, E. J. Reed, in *Transit. Met. Oxides Electrochem. Energy Storage*, John Wiley & Sons, Ltd, **2022**, pp. 393–409.
- [16] P. M. Attia, A. Grover, N. Jin, K. A. Severson, T. M. Markov, Y.-H. Liao, M. H. Chen, B. Cheong, N. Perkins, Z. Yang, P. K. Herring, M. Aykol, S. J. Harris, R. D. Braatz, S. Ermon, W. C. Chueh, *Nature* **2020**, *578*, 397–402.
- [17] T. Lombardo, M. Duquesnoy, H. El-Bouysidy, F. Àrén, A. Gallo-Bueno, P. B. Jørgensen, A. Bhowmik, A. Demortière, E. Ayerbe, F. Alcaide, M. Reynaud, J. Carrasco, A. Grimaud, C. Zhang, T. Vegge, P. Johansson, A. A. Franco, *Chem. Rev.* **2022**, *122*, 10899–10969.
- [18] T. Mueller, A. G. Kusne, R. Ramprasad, in *Rev. Comput. Chem.*, Wiley Hoboken, NJ, **2016**, pp. 186–273.
- [19] Z. Wang, Z. Sun, H. Yin, X. Liu, J. Wang, H. Zhao, C. H. Pang, T. Wu, S. Li, Z. Yin, X. Yu, *Adv. Mater.* n.d., n/a, 2104113.
- [20] B. Rohr, H. S. Stein, D. Guevarra, Y. Wang, J. A. Haber, M. Aykol, S. K. Suram, J. M. Gregoire, *Chem. Sci.* **2020**, *11*, 2696–2706.
- [21] F. Rahmanian, J. Flowers, D. Guevarra, M. Richter, M. Fichtner, P. Donnelly, J. M. Gregoire, H. S. Stein, *Adv. Mater. Interfaces* **2022**, 2101987.
- [22] L. Onsager, *Trans. Faraday Soc.* **1927**, *23*, 341–349.
- [23] J. Landesfeind, H. A. Gasteiger, *J. Electrochem. Soc.* **2019**, *166*, A3079.
- [24] M. S. Ding, T. R. Jow, *ECS Trans.* **2009**, *16*, 183.
- [25] M. S. Ding, T. R. Jow, *J. Electrochem. Soc.* **2003**, *150*, A620.
- [26] M. S. Ding, Q. Li, X. Li, W. Xu, K. Xu, *J. Phys. Chem. C* **2017**, *121*, 11178–11183.
- [27] M. S. Ding, T. R. Jow, *J. Electrochem. Soc.* **2004**, *151*, A2007.
- [28] R. Naejus, D. Lemordant, R. Coudert, P. Willmann, *J. Chem. Thermodyn.* **1997**, *29*, 1503–1515.
- [29] J. Wu, X.-Y. Chen, H. Zhang, L.-D. Xiong, H. Lei, S.-H. Deng, *J. Electron. Sci. Technol.* **2019**, *17*, 26–40.
- [30] A. F. Bissell, *J. Appl. Stat.* **1977**, *4*, 55–64.
- [31] R. F. Barber, E. J. Candès, A. Ramdas, R. J. Tibshirani, *Ann. Stat.* **2021**, *49*, 486–507.
- [32] D. J. Siegel, L. Nazar, Y.-M. Chiang, C. Fang, N. P. Balsara, *Trends Chem.* **2021**, *3*, 807–818.
- [33] X. Cheng, B. Khomtchouk, N. Matloff, P. Mohanty, *ArXiv180606850 Cs Stat* **2019**.
- [34] E. Ostertagová, *Procedia Eng.* **2012**, *48*, 500–506.
- [35] K. M. Marcoulides, T. Raykov, *Educ. Psychol. Meas.* **2019**, *79*, 874–882.
- [36] R. Johnston, K. Jones, D. Manley, *Qual. Quant.* **2018**, *52*, 1957–1976.
- [37] J. M. Wooldridge, *Introductory Econometrics: A Modern Approach*, Cengage Learning, **2015**.
- [38] E. Vittinghoff, D. V. Glidden, S. C. Shiboski, C. E. McCulloch, in *Regres. Methods Biostat. Linear Logist. Surviv. Repeated Meas. Models* (Eds.: E. Vittinghoff, D. V. Glidden, S. C. Shiboski, C. E. McCulloch), Springer US, Boston, MA, **2012**, pp. 69–138.
- [39] G. James, D. Witten, T. Hastie, R. Tibshirani, *An Introduction to Statistical Learning: With Applications in R*, Springer US, New York, NY, **2021**.
- [40] S. Menard, *Applied Logistic Regression Analysis*, SAGE, **2002**.
- [41] G. C. McDonald, *WIREs Comput. Stat.* **2009**, *1*, 93–100.
- [42] L. Buitinck, G. Louppe, M. Blondel, F. Pedregosa, A. Mueller, O. Grisel, V. Niculae, P. Prettenhofer, A. Gramfort, J. Grobler, R. Layton, J. Vanderplas, A. Joly, B. Holt, G. Varoquaux, *ArXiv13090238 Cs* **2013**.
- [43] G. Hackeling, *Mastering Machine Learning with Scikit-Learn*, Packt Publishing Ltd, **2017**.
- [44] O. Kramer, in *Mach. Learn. Evol. Strateg.* (Ed.: O. Kramer), Springer International Publishing, Cham, **2016**, pp. 45–53.
- [45] “MAPIE - Model Agnostic Prediction Interval Estimator – MAPIE 0.3.2 documentation,” can be found under <https://mapie.readthedocs.io/en/latest/index.html>, n.d.
- [46] E. Hüllermeier, W. Waegeman, *ArXiv191009457 Cs Stat* **2020**.

Manuscript received: May 19, 2022  
 Revised manuscript received: July 13, 2022  
 Version of record online: August 23, 2022

### 4.3.3. Supporting Information

# Batteries & Supercaps

## Supporting Information

### **One-Shot Active Learning for Globally Optimal Battery Electrolyte Conductivity\*\***

Fuzhan Rahmanian, Monika Vogler, Christian Wölke, Peng Yan, Martin Winter, Isidora Cekic-Laskovic, and Helge S. Stein\*

### Supplementary information

**Initial model training (M1):** In the first round of optimization, for every temperature, the polynomial degree varied between 1 to 9. The degree which results in lowest root mean square error (RMSE) after every fit, is considered as an optimal degree. The split ratio between train set and validation set is 70:30. A constant value of  $10^{-4}$  is selected for regularisation coefficient parameter. The trends of predicted conductivity for additional temperatures including -20 °C, 0 °C, 10 °C, 30 °C, 40 °C, 50 °C can be seen in Figure.S1. The validation scores from the 70:30 split at all temperatures are shown in Figure S1.1.

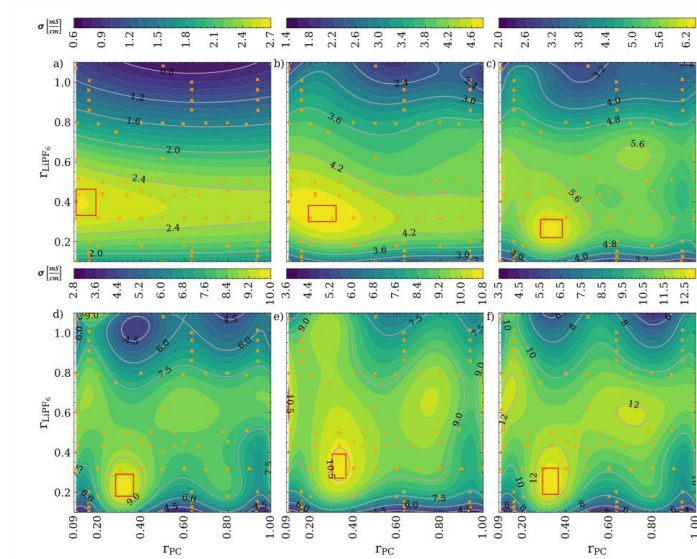


**Figure S1:** Trends in electrolyte conductivity at a) -20 °C, b) 0 °C, c) 10 °C, d) 30 °C, e) 40 °C, f) 50 °C

temperature	validation $R^2$ score from splitting DS1 in 70:30 (pre-shot)	model training $R^2$ score from DS1 / pre-shot
-30	0.8	0.724297226
-20	0.81	0.70787434
-10	0.73	0.72662187
0	0.75	0.712614466
10	0.8	0.72145169
20	0.72	0.717343607
30	0.78	0.730915979
40	0.79	0.744500333
50	0.8	0.75248152
60	0.79	0.7590995

**Table T1:**  $R^2$  scores for the training of the model M1 on dataset DS1.

**One-shot predictions and measurements:** Figure.S2 compares the experimentally measured conductivity versus the predicted one for the suggested 24 formulations (DS2) for additional temperatures including -20 °C, 0 °C, 10 °C, 30 °C, 40 °C, 50 °C.



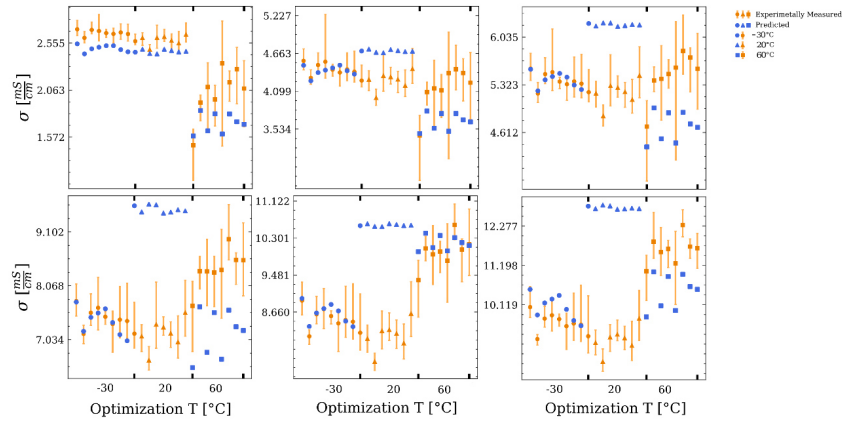


**Figure S2:** Comparison between measured and predicted conductivity values at a) -20 °C, b) 0 °C, c) 10 °C, d) 30 °C, e) 40 °C, f) 50 °C at the respective temperature. Orange points represent the mean of measured conductivities with error bars relating to the min/max from repeated measurements.

**Post-shot model refinement (M2):** The parameters of the regularized polynomial pipeline (M2) for DS3 is optimized using Bayesian search with 3-fold cross validation. Figure.S3 shows the trends of electrolyte conductivity after one-shot active learning for additional temperatures including -20 °C, 0 °C, 10 °C, 30 °C, 40 °C, 50 °C.

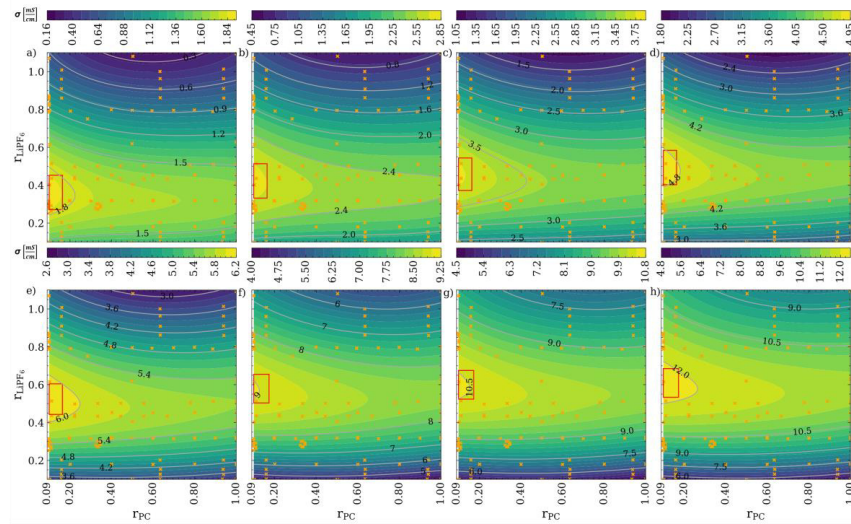


**Figure S3:** The refinement of conductivity trends after one-shot active learning at a) -30 °C, b) -20 °C, c) -10 °C, d) 0 °C, e) 10 °C, f) 30 °C, g) 40 °C, h) 50 °C can be seen.

temperature	model training R <sup>2</sup> score from DS3 / post-shot
-30	0.760282478
-20	0.747042491
-10	0.773409518
0	0.823519509
10	0.813040842
20	0.859029562
30	0.828545608
40	0.855524487
50	0.830341705
60	0.763871653

**Table T2:** R<sup>2</sup> scores for the training of the model M2 on dataset DS3.

**Model Uncertainty:** In Figure.S4, prediction intervals with 95 % of confidence ( $\alpha = 0.05$ ) for predicted conductivity values can be seen. For incorporating these calculations, model agnostic prediction interval estimator (MAPIE) using sklearn-contrib module is implemented <sup>[1]</sup>.

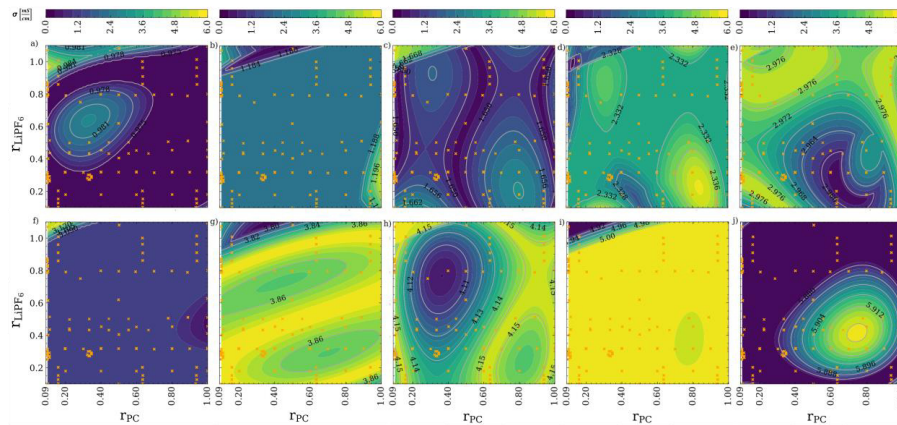


**Figure S4:** Uncertainty quantification for predicted conductivity values using 95 % prediction interval at a) -30 °C, b) -20 °C, c) -10 °C, d) 0 °C, e) 10 °C, f) 20 °C, g) 30 °C, h) 40 °C, i) 50 °C, j) 60 °C

**Bayesian optimization:** hyperparameter tuning was applied using the Bayesian optimization method <sup>[2,3]</sup>. The cross-validation search set to 3 for 20 iterations and the parameters setting includes polynomial features degree and ridge coefficient which can vary between (2 to 5) and ( $5 \cdot 10^{-4}$  to 0.03) respectively. The objective plot of hyperparameter parameters can be observed in figure S5.

**Summary:** In figure S6.a, an overall trend of conductivity for molal ratio of salt at considered temperatures range is observable. The line plots represent the predicted conductivity trend and the measured conductivity for the selected formulations at Helmholtz-Institute Münster are shown with scatter points. Figure S7 shows the molar conductivity comparison to the conductivity. Trends are overlapping for solvent ratios but not for salt concentrations.

According to Table.1, the coefficient relations extracted from our polynomial fit after one shot active learning can be seen in figure S6.b.

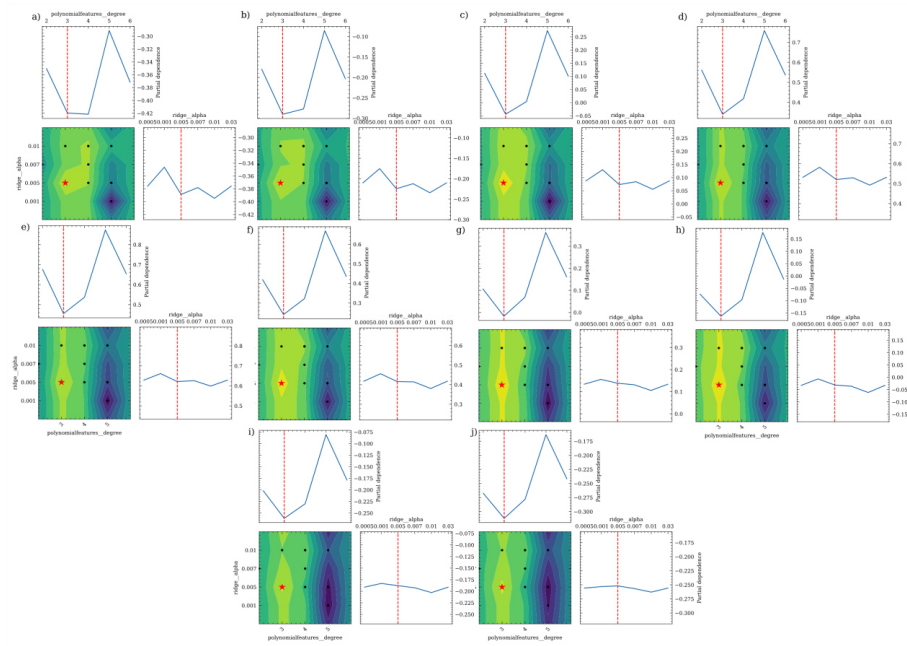


**Figure S5:** Hyperparameter tuning using Bayes search on pipeline consists of polynomial and ridge regression at a) -30 °C, b) -20 °C, c) -10 °C, d) 0 °C, e) 10 °C, f) 20 °C, g) 30 °C, h) 40 °C, i) 50 °C, j) 60 °C.

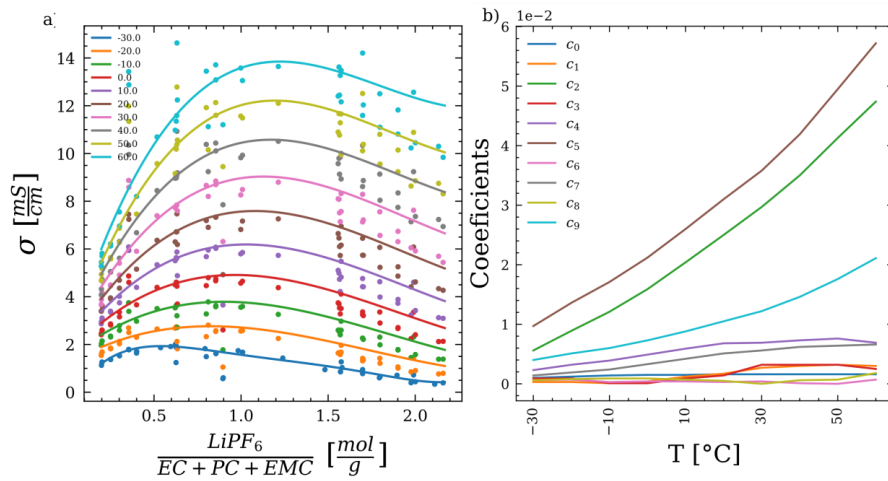


**Figure S6:** a) An overall trend of conductivity prediction for molal ratio of salt for temperature range between -30 °C and 60 °C applied on a full exploit search space can be seen. The lines represent the prediction trend of conductivity while the points refer to the measured conductivity for the selected formulations. Each colour specifies the corresponding temperature. b) The relation between polynomial coefficients incorporating ridge regularisation after one shot active learning.

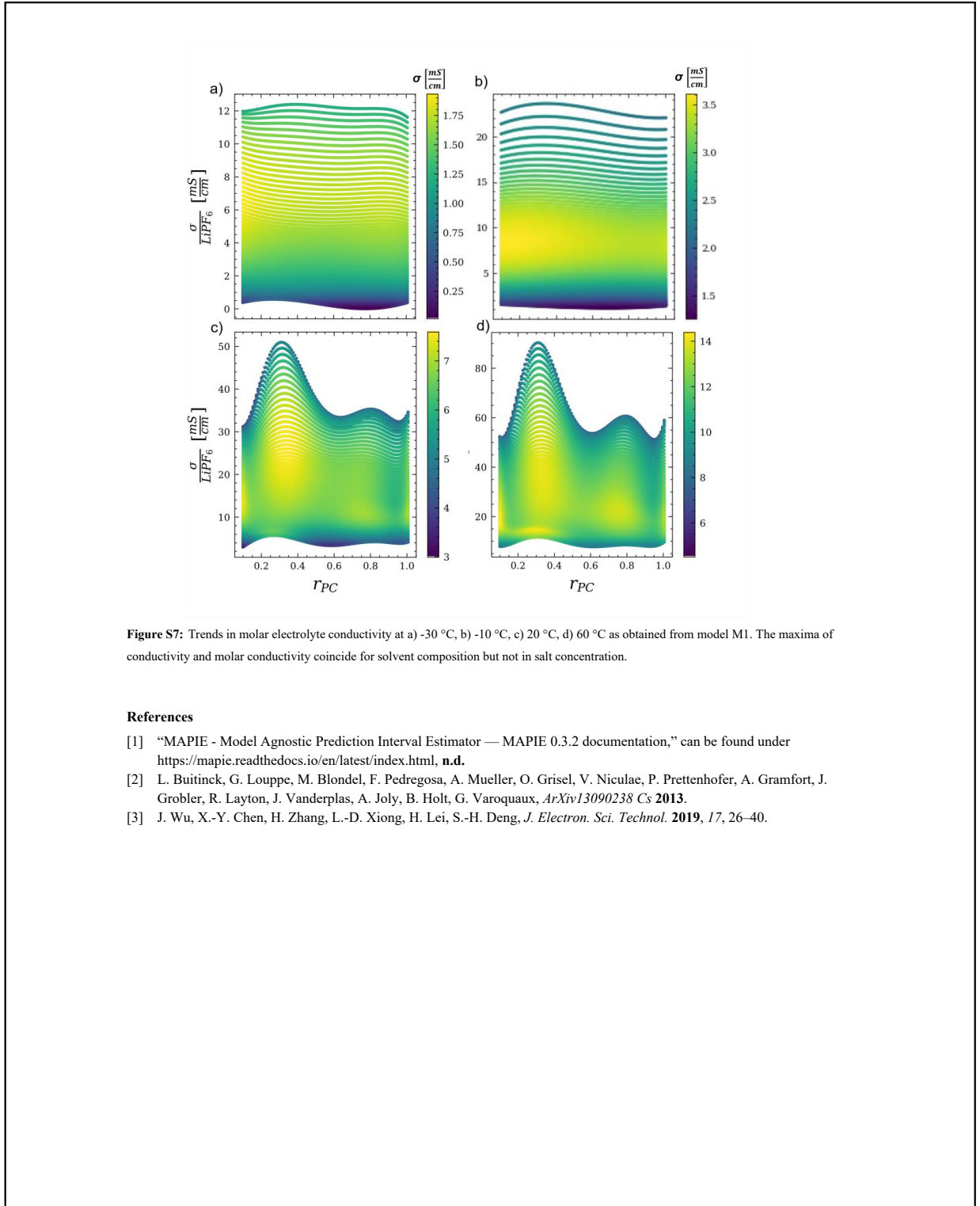


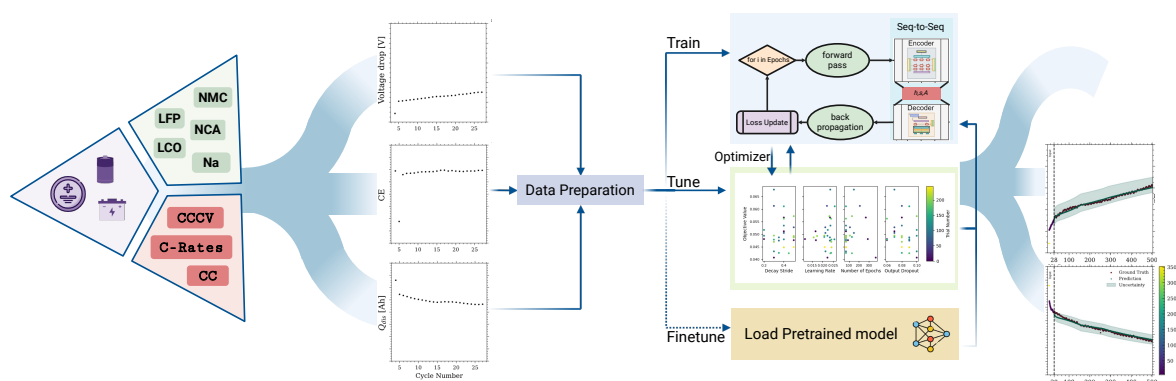
**Figure S7:** Trends in molar electrolyte conductivity at a) -30 °C, b) -10 °C, c) 20 °C, d) 60 °C as obtained from model M1. The maxima of conductivity and molar conductivity coincide for solvent composition but not in salt concentration.

#### References

- [1] “MAPIE - Model Agnostic Prediction Interval Estimator — MAPIE 0.3.2 documentation,” can be found under <https://mapie.readthedocs.io/en/latest/index.html>, **n.d.**
- [2] L. Buitinck, G. Louppe, M. Blondel, F. Pedregosa, A. Mueller, O. Grisel, V. Niculae, P. Prettenhofer, A. Gramfort, J. Grobler, R. Layton, J. Vanderplas, A. Joly, B. Holt, G. Varoquaux, *ArXiv13090238 Cs* **2013**.
- [3] J. Wu, X.-Y. Chen, H. Zhang, L.-D. Xiong, H. Lei, S.-H. Deng, *J. Electron. Sci. Technol.* **2019**, *17*, 26–40.

## 4.4. Attention towards chemistry agnostic and explainable battery lifetime prediction

### 4.4.1. Publication Details



**Title:** "Attention towards chemistry agnostic and explainable battery lifetime prediction"

**Journal:** *npj Computational Materials - Nature\** 2024

**Publisher:** Springer Nature

**Authors:** **Rahmanian, Fuzhan** and Lee, Robert M. and Linzner, Dominik and Michel, Kathrin and Merker, Leon and Berkes, Balazs B. and Nuss, Leah and Stein, Helge Sören

**Status:** Accepted: 24. April 2024

**DOI:** <https://10.1038/s41524-024-01286-7>

**Developed Software:**  <https://github.com/basf/ARCANA>

\* For reprint permission refer to Section A.1

## Publication Content

Monitoring and predicting the lifetime of batteries is a lengthy and complex undertaking that requires an understanding of numerous factors, including the manufacturing processes, their chemistry, design, and cycling procedures. Among data-centric approaches, traditional DL models can capture non-linear relationships between parameters. However, they often suffer from overfitting due to their extensive parameter requirements, which impedes their generalizability and interpretability. Considering the aforementioned challenges, this study introduces a novel Seq-to-Seq architecture designed to efficiently capture temporal dependencies across variables. This architecture integrates advanced modeling techniques, including the utilization of pinball loss for uncertainty measurements, an adjusted teacher forcing technique, and an attention mechanism at the decoder level to dynamically prioritize important features in long sequences. It also incorporates other strategies, such as learning rate scheduling and customized early stopping, to accelerate model convergence. Additionally, the architecture enables multi-output predictions, which enhances the model's explainability of its decision-making process.

The framework, anointed as Attention-based ReCurrent Algorithm for Neural Analysis (ARCANA), offers flexibility through the implementation of four operational modes, namely training, tuning, prediction, and fine-tuning. The tuning mode utilizes the Optuna library<sup>287</sup> to optimize model parameters. During prediction, the model delivers immediate results and generates a detailed report on evaluation metrics, prediction uncertainties, and the impact of input parameters through saliency analysis, along with visual plots. The fine-tuning mode adjusts the pre-trained model to optimize performance on the provided user-specific datasets, which is especially effective in data-scarce scenarios. This pip-installable package (`pip install arcana-batt`) is implemented as a modular and user-friendly platform. The robustness of the model was validated in two separate case studies. Initially, the model was trained on an extensive coin cell dataset provided in a collaborative project with BASF company; in the second phase, a diverse, publicly available dataset comprising a variety of battery types, manufacturers, and charge-discharge protocols was collected. The number of cells was comparatively small to the initial dataset, amounting to just 4% of the total. The model processed static inputs, such as discharge current and nominal capacity,

and dynamic inputs from past cycling sequences, including discharge capacity, voltage drop, and CE. Following training, both models were evaluated on entirely unseen datasets from varied locations and manufacturers, demonstrating a high degree of generalization. The model trained with a larger dataset from BASF possesses richer prior knowledge of coin cell behaviors, while the smaller data facilitated broader predictions across different battery types, albeit with higher uncertainty. Both models were further fine-tuned for sodium batteries to showcase their adaptability across different chemistries. ARCANA, therefore, demonstrates potential scalability from laboratory settings to industrial production. Additionally, the framework is suitable for applications such as on-the-fly monitoring to reduce testing durations and costs and accelerate decision-making processes, and can also extend to active learning for continuous optimization of experimental protocols or other applications.

### Individual Contribution

The model idea for ARCANA was conceptualized by **Fuzhan Rahmanian** who contributed to the complete data lifecycle, including data collection, feature extraction, data cleaning, and curation for BASF and public datasets. The raw dataset of BASF was provided by K.M. and B.B. while L.M. and L.N. conducted the experiment for the data creation of Li-ion and Na-ion batteries at KIT and IPC. **F.R.** designed and implemented the OOP model and incorporated uncertainty measures and an evaluation framework, which included calculation and visualization of saliency analysis and attention mechanism **F.R.** run training on the *curiosity* supercomputer of BASF, gathered, evaluated, plotted, and reported the results, curated the codebase and the repository, implemented documentation, and automatic deployment. **F.R.** assembled the manuscript. R.L. and D.L. supervised the development of the model, while H.S., K.M., R.L., and D.L. oversaw the research. All authors reviewed the publication.



## 4.4.2. Manuscript

npj | computational materials

Article

Published in partnership with the Shanghai Institute of Ceramics of the Chinese Academy of Sciences

<https://doi.org/10.1038/s41524-024-01286-7>

# Attention towards chemistry agnostic and explainable battery lifetime prediction

Check for updates

Fuzhan Rahmanian<sup>1,2,3,4,5</sup>✉, Robert M. Lee<sup>6</sup>, Dominik Linzner<sup>6</sup>, Kathrin Michel<sup>6</sup>, Leon Merker<sup>1,2</sup>, Balazs B. Berkes<sup>6</sup>, Leah Nuss<sup>1,3,4,5</sup> & Helge Sören Stein<sup>3,4,5</sup>✉

Predicting and monitoring battery life early and across chemistries is a significant challenge due to the plethora of degradation paths, form factors, and electrochemical testing protocols. Existing models typically translate poorly across different electrode, electrolyte, and additive materials, mostly require a fixed number of cycles, and are limited to a single discharge protocol. Here, an attention-based recurrent algorithm for neural analysis (ARCANA) architecture is developed and trained on an ultra-large, proprietary dataset from BASF and a large Li-ion dataset gathered from literature across the globe. ARCANA generalizes well across this diverse set of chemistries, electrolyte formulations, battery designs, and cycling protocols and thus allows for an extraction of data-driven knowledge of the degradation mechanisms. The model's adaptability is further demonstrated through fine-tuning on Na-ion batteries. ARCANA advances the frontier of large-scale time series models in analytical chemistry beyond textual data and holds the potential to significantly accelerate discovery-oriented battery research endeavors.

Lithium-ion batteries (LIBs) enable the electrification of everything, yet there is a maze of challenges that must be navigated in order to optimize the batteries of the future<sup>1–4</sup>. Critical to the advancement of battery research is the rapid understanding of why and how some batteries degrade and what needs to be changed to prevent premature capacity fade<sup>5</sup>. Material degradation can occur due to numerous factors, including unpreventable solid electrolyte interphase growth, loss of active material, and other electrochemical phenomena<sup>6</sup>. However, investigating battery degradation is a time-consuming task, as non-linear capacity loss can occur over hundreds or thousands of cycles<sup>7</sup>. Another challenge in early lifetime prediction is the diversity of battery chemistries in the anode, cathode, and electrolyte, along with various form factors and testing protocols.

Battery lifetime can be evaluated through various methods, such as conventional cycling until the end of life (EOL) under constant current-constant voltage (CC-CV) conditions or cycling for a predetermined number of cycles. From these data, measures such as coulombic efficiency (CE) can be calculated<sup>8</sup> and correlated to more in-depth techniques such as electrochemical impedance spectroscopy (EIS)<sup>9</sup> to fundamentally assess the underlying degradation mechanisms. Accurate measurement of CE<sup>10,11</sup> does, however, require bespoke instrumentation and a considerable amount

of time, i.e., cycling a battery for 1000 cycles at 1C/1D takes approximately 11 weeks. Reducing the required number of cycles by a factor of 10 while maintaining a high level of fidelity is, therefore, of great interest<sup>12</sup>. Machine Learning (ML) and deep learning (DL) can accelerate testing by lowering the number of cycles required to understand the underlying chemistries<sup>13</sup>. An example of predicting the EOL of batteries using initial discharge capacity curves was demonstrated by Severson et al.<sup>3</sup>, who used regression models. They integrated data generation with data-driven models to forecast the lifetime of LFP/graphite cells based on  $\Delta Q(V)$  and classified their longevity. In further work, Attia et al.<sup>12</sup> employed a Bayesian algorithm to accelerate the optimization of fast-charging protocols. By using early-cycle data for low-fidelity predictions, the approach enabled the optimization of high-fidelity experimental outcomes, thus significantly reducing the experimental duration from 500 to 16 days.

The most reliable models do not, however, merely predict just predict a quantity but also allow assessment of the model's uncertainty. Emblematic of this is the work by Tong et al.<sup>14</sup>, who introduced ADLSTM-MC, a hybrid predictive model using adaptive dropout long short-term memory (LSTM) with Monte Carlo simulations. This approach, which requires minimal training data, enhances robustness through Bayesian-optimized dropout

<sup>1</sup>Helmholtz Institute Ulm, Applied Electrochemistry, Helmholtzstr. 11, 89081 Ulm, Germany. <sup>2</sup>Karlsruhe Institute of Technology, Institute of Physical Chemistry, Fritz-Haber-Weg 2, 76131 Karlsruhe, Germany. <sup>3</sup>Technische Universität München, School of Natural Sciences, Department of Chemistry, Lichtenbergstr 4, 85748 Garching, Germany. <sup>4</sup>Technische Universität München, Munich Data Science Institute, Walther-von-Dyck-Straße 10, 4, 85748 Garching, Germany. <sup>5</sup>Technische Universität München, Munich Institute for Robotic and Machine Intelligence, Georg-Brauchle-Ring 60-62, 80992 Munich, Germany. <sup>6</sup>BASF SE, Ludwigshafen, Germany. ✉e-mail: [fuzhan.rahmanian@tum.de](mailto:fuzhan.rahmanian@tum.de); [helge.stein@tum.de](mailto:helge.stein@tum.de)

<https://doi.org/10.1038/s41524-024-01286-7>

Article

rates and improves the remaining useful life of two types of LIBs. In a correlative study<sup>15</sup>, a recurrent autoregressive deep ensemble network with aleatoric and epistemic uncertainties was developed along with saliency analysis to assess the impact of input parameters on output prediction. This provided an intuitive understanding of feature importance. Another advantage of using DL algorithms is their ability to use raw data, which has gained interest in the estimation of battery State of Health (SOH). For instance, Yang et al.<sup>16</sup> developed a hybrid convolutional neural network architecture with parallel residual connections, which utilizes raw data across multiple dimensions. By incorporating attention mechanisms, their model achieves remarkable accuracy in predicting the early stages of degradation. These advances support the increased focus on more adaptive and generative modeling frameworks, of which recent efforts include reinforcement learning from human feedback (RLHF) and the prompt paradigm in Generative Artificial Intelligence (GAI) techniques regarded for their potential to unravel complex structure–activity relationships in material behavior<sup>17</sup>. Although these approaches are applied in battery research<sup>18,19</sup>, their prominence is not as widespread as in other scientific fields. However, this lesser emphasis provides an opportunity for further exploration and discovery.

Beyond these early lifetime prediction models, sequence-to-sequence (Seq-to-Seq) models have been used to monitor battery lifetime and (SOH)<sup>18,20,21</sup>. They leverage intrinsic temporal dependencies in degradation data, providing high predictive accuracy and computational efficiency. Li et al.<sup>20</sup> developed a one-shot LSTM-based Seq-to-Seq framework that not only predicts future capacities but also identifies knee points in the degradation curve, maintaining stability even in the face of stochastic disturbances. Although Seq-to-Seq models demonstrate robust predictions, they also exhibit limitations in generalization and require large and diverse datasets to enhance performance<sup>4</sup>.

Despite the promises made by ML and DL for lifetime predictions<sup>22–24</sup>, these models, while robust, face challenges of precision and trustworthiness<sup>25</sup>. Existing models often focus on single-task learning, neglecting the potential benefits of multi-objective learning for various predictive settings<sup>4</sup>. In particular, data-driven approaches<sup>26,27</sup> tend to overlook the inherent variations between, for example, production batches or individual cells<sup>28</sup>. Such discrepancies, originating from manufacturing processes or aging mechanisms, can profoundly impact lifetime predictions. Addressing these variations requires integrating domain knowledge into the learning process to enhance the model's ability to adapt and accurately forecast across diverse conditions<sup>27</sup>. Furthermore, despite the assertions of recent studies that they are chemistry-agnostic<sup>15,29</sup>, they often require enhanced explainability to optimize their effectiveness in various chemistry settings. Transfer learning offers a promising solution to the challenge of scarce data but requires more investigation for transparency and interpretability<sup>30</sup>. The acquisition of extensive datasets, essential for DL algorithms<sup>31</sup>, remains a significant hurdle<sup>36,32,33</sup>. Nevertheless, innovative strategies, such as the use of common features in databases and the documentation of various chemistries and protocols<sup>34</sup>, establish the foundation for more in-depth research<sup>31</sup>. Our goal is to develop a model characterized by its adaptable design and robustness, with the capability to provide both uncertainty quantification and explainability. The model's strength is underlined by its adaptability in dynamically fine-tuning to specific chemical domains. Such a model would be invaluable to the academic community and would find marketable applications in the real world<sup>31</sup>, accelerating battery design and data collection based on active learning.

## Results

### Data resources

Developing a model that generalizes well necessitates a diverse and large dataset<sup>35</sup> that ideally covers a spectrum of chemistries and formats given high-dimensional correlations and cell variations<sup>30,35</sup>, obtained from various laboratories and measured under different operating conditions<sup>12</sup>. Data diversity not only ensures an accurate representation of different cycling behaviors but also tames the irreducible uncertainty in the predictions while

mitigating the risk of overfitting. However, the scarcity of large and comprehensive datasets<sup>25</sup> that include both high and low-performing cells creates a challenge for training generalized models, i.e., to overcome a positive bias<sup>30,36</sup>. Available data often exhibit noise, discontinuities, and varying formats that require extensive curation, adding a layer of complexity. Initiatives such as Battery Archive<sup>37</sup> or other cloud services<sup>38</sup> are therefore commendable in promoting Findable, Accessible, Interoperable, and Reusable (FAIR) data<sup>39,40</sup> handling in battery research<sup>32,33</sup>.

In this study, we develop a model trained on ca. 17,400 batteries from BASF research laboratories that cover a diverse range of LIBs chemistries and multiple cycling protocols. Exposure of our model to such a wide variety of data enables robust generalization. Utilizing our pre-trained model on a set of unseen data, we effectively predict the early degradation trajectory. The ultimate test of our model, therefore, is to apply it to data from cells produced in a different location and with varying chemistries. Due to intellectual property constraints that prevent the authors from making the model trained on the BASF dataset openly accessible, we have retrained our model by leveraging a diverse array of publicly available datasets from respected institutions and research groups, including the Toyota Research Institute (TRI) in partnership with MIT and Stanford<sup>41,42</sup>, NASA<sup>43</sup>, the Center for Advanced Life Cycle Engineering (CALCE)<sup>44</sup>, Karlsruhe Institute of Technology (KIT)<sup>45</sup>, Hawaii Natural Energy Institute (HNEI)<sup>46</sup>, and Sandia National Laboratories (SNL)<sup>46</sup>. Furthermore, we have incorporated data from our in-house cycled cells<sup>47–50</sup> with successful and failed experiments to further enrich model training and reduce bias. In Supplementary Section 1, we provide an overview of all datasets; we include a brief summary in Table 1 with an indication of which datasets were used during training and which remained completely unseen for model testing. This approach ensures a thorough understanding of the data sources, thus improving the transparency and reproducibility of our research.

### Architecture overview

Central to this study is the Attention-based ReCurrent Algorithm for Neural Analysis with LSTM (ARCANA) model. This is an attention-based Seq-to-Seq architecture specifically engineered to assess early-stage battery degradation and perform lifecycle monitoring. The model demonstrates superior multi-output predictive capabilities, supported by its high modularity and dynamic adaptability. It is designed to utilize a flexible range of past battery cycle data, known as historical temporal segments, for input. In addition, the model includes predetermined parameters for future conditions, such as discharge rates and cycle numbers. These parameters are known in advance of the experiment, i.e., they are controlled by the measurement device and are referred to as encoded temporal segments. This dual capability offers multifaceted advantages, from cost and time savings to improved material selection and protocol optimization.

The ARCANA model is augmented with additional features such as the attention mechanism, which provides insight into the decision-making process of the model. This feature distinguishes between predictions based on underlying patterns and those arising from stochastic variability. Saliency analysis is additionally performed to emphasize the relative importance of each parameter through a computation of the absolute gradient of the model output relative to the input of the test set. It quantifies the sensitivity of the input parameters, revealing how minor variations significantly alter the output results<sup>15</sup>, thus aligning the internal logic of the model with domain-specific knowledge. Adding another layer of robustness is uncertainty quantification, which is valuable not only for understanding the reliability of cycling protocols but also for assessing material performance across different battery chemistries.

As illustrated in the unified modeling language (UML) diagram (Fig. 1), the ARCANA model consists of four principal classes, each performing a different function, and is designed to accept raw data, thus negating the need for preliminary feature engineering. This design versatility extends to its operational modes with Naive Training for initial experiments, Dynamic Tuning for real-time adaptability via extensive hyperparameter optimization, Fine-Tuning for integration of a pre-trained model with selective

<https://doi.org/10.1038/s41524-024-01286-7>

Article

**Table 1 | Collected cycling data for training and testing**

Location	Cell form	Cell chemistry	Protocol charge/discharge	No. cell	Cycle range	Nominal capacity [Ah]	Usage
BASF	Coin	Heterogenous	Multimodal	17400	Multimodal	Multimodal	$M(B)$ Train\Val
TRI <sup>41</sup>	Cylindrical commercial	LFP\graphite	CC1(Q1)CC2, CC-CV@1C, 4.2V\CC@4C	124	169–2235	1.1	$M(P)$ Train\Val
TRI <sup>42</sup>	Cylindrical commercial	LFP\graphite	CC1(20%)CC2(40%)CC3(60%)CC4(80%), CC-CV@1C, 4.2V\CC-CV@4C, 2V	233	100–862	1.1	$M(P)$ Train\Val
CALCE <sup>44</sup>	Prismatic commercial CX2	LCO\graphite	CC-CV@0.5C, 4.2V, \CC@(0.5C, 1C)	6	781–1082	1.35	Testing
CALCE <sup>44</sup>	Prismatic commercial CS2	LCO\graphite	CC-CV@0.5C, 4.2V, \CC@0.5C	6	1701–2016	1.1	$M(P)$ Train\Val
KIT <sup>45</sup>	Cylindrical commercial	NCA\graphite-Si	CC-CV@(0.25C, 0.5C, 1C), 4.2V, \CC@1C	58	29–800	3.5	$M(P)$ Train\Val
KIT <sup>45</sup>	Cylindrical commercial	NCM\graphite-Si	CC-CV@(0.25C, 0.5C, 1C), 4.2V, \CC@1C	55	43–1277	3.5	$M(P)$ Train\Val
KIT <sup>45</sup>	Cylindrical commercial	NCM+NCA\graphite	CC-CV@0.5C, 4.2V, \CC@(1C, 2C, 4C)	9	912–1031	2.5	Testing
KIT <sup>47</sup>	Coin self-made	LNO\graphite	CC-CV@1C, 4.2V, \CC@1C	43	82–505	0.004618	60% for $M(P)_{Na}$ , 40% Testing
KIT <sup>48</sup>	Coin commercial	LCO\graphite	CC-CV@1C, 4.25V, \CC-CV@1C, 2.75V	26	150–600	0.045	$M(P)$ Train\Val
KIT <sup>49</sup>	Coin self-made	NMC622\graphite	CC-CV@1C, 4.2V, \CC@1C	11	228–501	0.00328	Testing
KIT <sup>50</sup>	Coin self-made	$Na_{0.9}[...]\text{O}_2$ \graphite	CC@1C \CC@1C or C-rates test	44	40–140	0.00015	60% for $M(P)_{Na}$ and $M(B)_{Na}$ , 40% Testing
NASA <sup>43</sup>	Cylindrical commercial	NCA\graphite	CC-CV@0.75C, 4.2V, \CC@(0.5C, 1C, 2C)	34	24–196	2.0	$M(P)$ Train\Val
HNEI <sup>45</sup>	Cylindrical commercial	LCO-NMC\graphite	CC-CV@0.5C, 4.3V, \CC@1.5C	14	1102–1133	2.8	$M(P)$ Train\Val
SNL <sup>46</sup>	Cylindrical commercial	LFP\graphite	CC-CV@0.5C, 4.2V, \CC@(0.5C, 1C, 2C, 3C)	28	2621–19,174	1.1	$M(P)$ Train\Val
SNL <sup>46</sup>	Cylindrical commercial	NCA\graphite	CC-CV@0.5C, 4.2V, \CC@(0.5C, 1C, 2C)	24	463–7877	3.2	$M(P)$ Train\Val
SNL <sup>46</sup>	Cylindrical commercial	NMC\graphite	CC-CV@0.5C, 4.2V, \CC@(0.5C, 1C, 2C, 3C)	25	388–11,149	3.0	$M(P)$ Train\Val

An overview of the collected cycling data utilized for training and testing. The model  $M(B)$ , was trained with data provided by BASF, and the model  $M(P)$  was trained with publicly available data. The model  $M(P)_f$  represents a fine-tuned version of  $M(P)$  for lithium-ion coin cell data.  $M(P)_{Na}$  and  $M(B)_{Na}$  models are fine-tuned  $M(B)$  and  $M(P)$ , respectively, adapted for sodium coin cells.

gradient updating, and prediction for efficient inference. Through modularity, a logging mechanism ensures data integrity and traceability, adhering to FAIR data principles<sup>40</sup>. The open-source codebase uses the PyTorch library<sup>51</sup> for model development and the Optuna library<sup>52</sup> for hyperparameter optimization.

**The encoder-decoder framework.** The encoder (Fig. 2a) initiates the Seq-to-Seq model in the ARCANA framework by processing historical temporal segments of the past battery life cycles. Employing an LSTM network, it is designed to capture complex, non-linear relationships and time dependencies inherent in sequence data. The encoder processes the input tensor to accommodate sequences of different lengths, employing a padding mechanism that enables the LSTM to efficiently process these sequences without being constrained by their varying lengths. Within the LSTM, the temporal data is transformed into a tensor, constructing hidden and cell states that capture sequential information. A skip connection incorporates the initial input into the LSTM output, thus preserving crucial temporal features and stabilizing the learning process. Layer normalization, when applied to the LSTM output, not only accelerates convergence but also leads to robust performance, mitigating the challenges associated with long-sequence dependencies<sup>53</sup>. The encoder returns a rich latent representation of the historical data, consisting of the output tensor and the updated hidden and cell states, which are then utilized by the decoder to enable accurate forecasting in subsequent steps.

The decoder (Fig. 2a) takes on the task of generating future state predictions. It is initialized with the hidden and cell states from the encoder and begins by processing the most recent historical cycle data. The model then integrates its own previous predictions and known future conditions, such as the expected discharge current and the cycle number. These two inputs are temporally encoded to capture their positional relevance<sup>54</sup>, ensuring that the decoder is informed of the predefined condition and the timing of each data point within the life cycle. The decoder employs an attention mechanism that can dynamically adjust sequence weights, identifying critical information at each prediction step. This approach overcomes the limitations of static-length vector representation in conventional encoder-decoder models<sup>55</sup>, allowing the decoder to focus on the most relevant parts of historical data. The attention mechanism then computes a context vector associated with the encoder's output, which highlights the encoder sequences with the highest relevance to the current decoding task. This context vector, combined with the current input, forms a feature-rich tensor that is subsequently processed by an LSTM layer. Post-LSTM, the output layer is passed through a fully connected layer with a leaky ReLU activation function, crucial in maintaining network stability, and enhanced with a dropout layer placed to reduce overfitting risks. The culmination of this process is a decoder that generates forecasts for the 0.1, 0.5, and 0.9 quantiles. These provide a probabilistic range indicative of the inherent uncertainty and offer a statistical interpretation of the potential future states of the degradation profile.

<https://doi.org/10.1038/s41524-024-01286-7>

Article

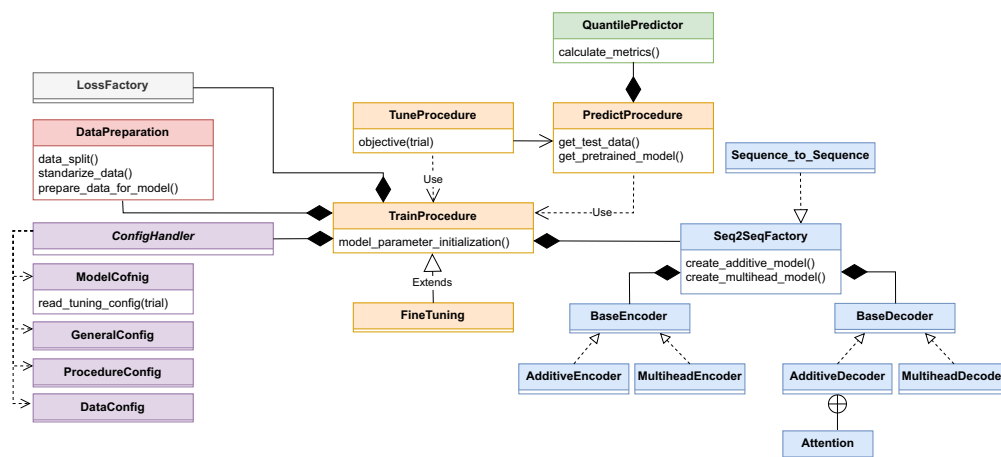


**Fig. 1 | An UML diagram of the computational framework.** The framework is designed around three principal class clusters. The first includes a `ConfigHandler` engineered to manage a comprehensive set of user-defined configurations and establishes a blueprint for handling various subconfigurations such as general settings, data properties, and model specifications. During hyperparameter optimization tasks, `ConfigHandler` interfaces with the Optuna optimization library to adaptively create and update the tuning configuration. The second key class structure includes `TrainProcedure`, which serves as an architectural template for the training process. Its attributes are employed throughout the computational pipeline, starting with data preparation and extending to the instantiation of specialized loss functions and `Seq2Seq` models via the `LossFactory` and `Seq2SeqFactory`.

`FineTuning` is a specialized subclass that inherits from `TrainProcedure` while `TuneProcedure` and `PredictProcedure`, the latter of which uses the `QuantilePredictor`, are incorporated into the pipeline depending on the desired use case and settings. The tuning operates on single trials with a `TPESampler` when multiple runs are desired. Lastly, `Seq2SeqFactory` is engineered to govern the instantiation of encoder-decoder architectures. Depending on the user-defined configurations, it can orchestrate a multihed or an additive encoder-decoder mechanism. The inclusion of custom attention mechanisms within the architecture is handled by the `AdditiveDecoder` class or the `MultihedDecoder`, conditional upon the configuration stipulations.

**Seq-to-seq integration.** In the broader Seq-to-Seq model, the encoder and decoder are orchestrated to facilitate the overall predictions, as can be seen in Fig. 2b. Here, the model processes the temporal data using a sliding window approach that enhances the ability to discern local patterns within long input sequences<sup>54</sup>. This technique allows for the integration of the last observed data or transitions to the decoder's self-generated predictions, supplemented with temporally encoded future conditions. During training, a dynamic teacher forcing strategy is employed, in which actual target outputs are used as inputs in lieu of previous predictions to promote model convergence, prediction fidelity, and generalizability in the model. This hybrid training strategy allows effective learning from the ground truth while gradually becoming equipped for self-guided predictions. At the end of the processing of this sequence, quantile-based predictions are collected into a stack of tensors, encapsulating a comprehensive forecast for subsequent decision-making processes. Thus, this forward pass provides a fine-grained, probabilistic understanding of the evolving battery life-cycle stages, with the potential to inform risk assessment and optimize operational efficiency.

#### Experimental configuration

This study evaluates the ARCANA architectural model through a two-stage experimental process. Our aim is to present findings that resonate across multiple disciplines, highlighting both the complexity and versatility of our approach. The first stage involved training model  $M$  with the coin cell dataset  $B$  from BASF. The resulting trained model is here denoted  $M(B)$ . We encoded predetermined parameters, including cycle number and discharge current, into temporal segments to capture past and future discharge conditions. The training used an additive attention mechanism in the ARCANA architecture for initial learning, with a detailed explanation in Section "Methods". In the second stage, the model  $M$  is re-trained from scratch (parameters available in Supplementary Table 1), with publicly

available datasets as mentioned in Table 1 and denoted as  $M(P)$ . This entails various cell types, including 26 coin cells and 6 prismatic cells with Lithium-Cobalt-Oxide (LCO) cathodes, with the majority being cylindrical cells with Lithium-Iron-Phosphate (LFP), Nickel-Manganese-Cobalt (NMC), and Nickel-Cobalt-Aluminum Oxide (NCA) cathode materials. To address these cell chemistry variations, we introduced an additional predefined parameter, the nominal capacity of each cell in logarithmic format. This inclusion was critical for the model to effectively differentiate and interpret response characteristics<sup>56</sup>. The public dataset selected for  $M(P)$  was significantly smaller, comprising 627 cell entries and accounting for only 3.35% of the total data size of the initial model  $M(B)$ . The dataset was distributed with 65% for training, 30% for validation, and 5% for testing.

To emphasize generalizability and test model performance, we incorporated four distinct test datasets, each sourced from different locations and created by various experts. The first two test sets, denoted ( $D_{LNO}$ ) and  $D_{NMC}$  comprise coin cell measurements made at the Institute of Physical Chemistry (IPC) of KIT, featuring the Lithium-Nickel-Oxide (LNO) and NMC materials, respectively. The third dataset consisted of cylindrical cells from the Institute of Applied Materials (IAM) of KIT, containing NMC blended with NCA cathode materials ( $D_{NMC+NCA}$ ). The final dataset involved prismatic cells of the CALCE institute with LCO materials ( $D_{LCO}$ ). The complete description of these cells is provided in the Supplementary Section 1. This approach in dataset selection and testing allowed an in-depth evaluation of  $M(P)$  for its adaptability to various cell types and experimental setups.

The publicly available data for  $M(P)$  presented distinctive challenges, as they included prematurely failed cells and high experimental noise, in contrast to the high-quality data used for training  $M(B)$ . These complexities required a change from an additive to a multihed attention mechanism in  $M(P)$ . We also encountered a wide range of cycles, from as few as 196 to as many as 19176. However, most of the tests we considered had fewer than

<https://doi.org/10.1038/s41524-024-01286-7>

Article

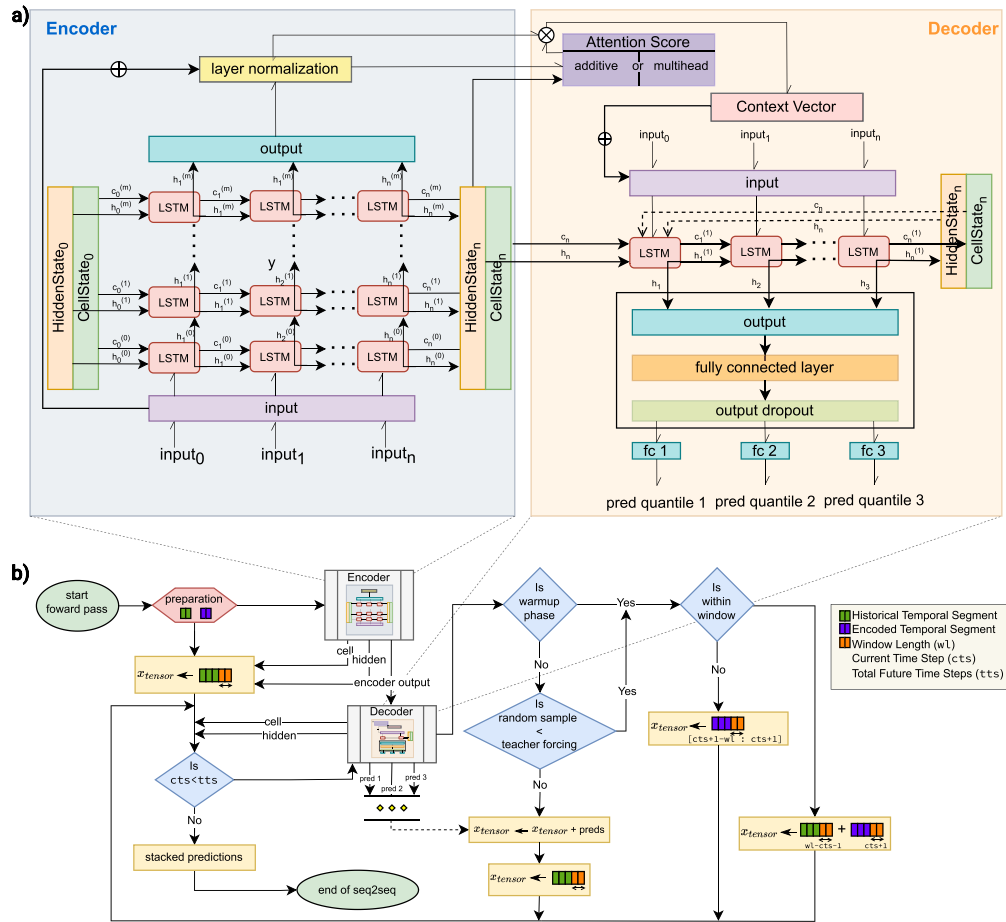


**Fig. 2 | Architectural overview of Seq-to-Seq model.** In this overview subfigure a depicts the detailed architecture of the encoder and decoder components. The LSTM-based encoder processes historical temporal segments to capture the intricate pattern of battery life cycles. It integrates skip-connection and layer normalization to preserve and stabilize essential key temporal features. The decoder is initialized with the encoder's final states and applies an attention mechanism to focus on relevant temporal features from the encoder output and enrich the context of its predictions. The attention-enhanced representations are combined with the initial decoder input and subsequently propagated through LSTM layers. A fully connected layer with leaky ReLU activation and a dropout layer—used solely during training and inactive

during inference—for regularization follow the LSTM outputs. The model outputs are then fed into three separate fully connected layers for predicting a specific quantile of the future distribution based on the pattern learned during training, thus providing a probabilistic characterization of the forecast. Subfigure b illustrates the integrated Seq-to-Seq model flow, depicting the progression from encoding historical data to multi-output future forecasts. It highlights the sliding-window approach that underpins the model's capability to handle both the tail-end of historical data and the integration of self-generated forecasts with known future conditions. This process also captures the dynamic training process, which incorporates teacher forcing to enhance the predictive fidelity of the model.

500 cycles. This variability posed a potential risk of gradient instability and inconsistent learning in the training process. To mitigate the risk of poor convergence and the possibility of overfitting, we adopted a standardization approach in which all cells were limited to a maximum of 500 cycles, ensuring better balance in the training data and reducing bias, thus increasing reliability.

Both  $M(B)$  and  $M(P)$  focused on predicting three parameters, which were selected for their established significance in the existing literature and their availability across the datasets. They included discharge capacity, crucial for understanding the (SOH)<sup>3</sup>, CE, as emphasized in studies by Burns et al.<sup>57,58</sup>

as the key to understanding the impact of electrode additives and electrode materials on battery long-term performance, and the voltage drop during the relaxation phase between charging and discharging cycles. The last parameter is less explored but, as described by e.g. Zhu et al.<sup>59</sup>, it offers valuable insights independent of the charging process. This parameter is easily calculated from cycling data, even if the studies where the data originated did not directly measure it. In this section, we evaluate our model's performance on various scenarios, focusing on the impact of data quality on model generalization and interpretability, investigating its adaptability to different chemistries, and deriving insights from attention mechanisms and saliency analysis.

<https://doi.org/10.1038/s41524-024-01286-7>

Article

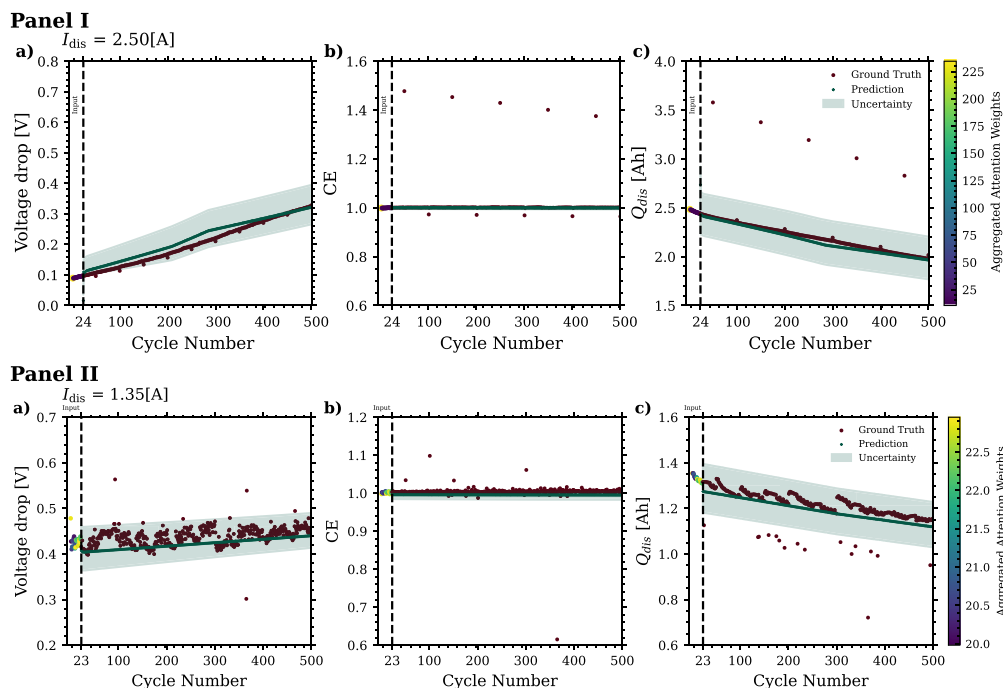


**Fig. 3 |** ARCANA's predictive performance on cylindrical sample cells. The performance of the proposed framework on two unseen datasets, namely cylindrical  $D_{NMC+NCA}$  in Panel I and prismatic  $D_{LCO}$  in Panel II, when predicting battery behavior over 500 cycles for three predictors of Voltage drop [V] (a), CE (b) and  $Q_{dis}$

[Ah] (c). The uncertainty at the 10th and 90th percentiles effectively captures underlying data variability and highlights the model's predictive reliability and adaptability across diverse unseen datasets, demonstrating deep insight into data characteristics.

### Model performance across battery types

The hyperparameters of  $M(P)$  were selected using Optuna's hyperparameter tuning with 250 trials and are described in Supplementary Fig. 2, along with its training performance (Supplementary Fig. 3). The model generalization is evaluated on two datasets; cylindrical cells of  $D_{NMC+NCA}$  and prismatic cells of  $D_{LCO}$ , neither of which were seen by the model during training. Here, the objective was to determine how effectively the model generalizes across different battery configurations despite the presence of noisy data.

As shown in Fig. 3, the model handles multidimensional predictions for both  $D_{NMC+NCA}$  and  $D_{LCO}$  well. For  $D_{NMC+NCA}$ , it accurately forecasts up to 500 cycles based on 24 input cycles (see Panel I, Fig. 3) even though the extracted data exhibits occasional jumps despite the discharge current remaining constant throughout. Given that these unexpected jumps are not annotated in the original dataset, we have chosen to acknowledge their presence but not alter them for the sake of data integrity. Aggregated attention weights in early cycles indicate their importance for long-term forecasting. Emblematic is  $D_{LCO}$ , which starts from a 23-cycle profile (Panel II, Fig. 3); the model demonstrates robustness even in the presence of more complex noise patterns. Here, the attention weights are distributed not only in the initial cycles but also in later cycles, proving the necessity of incorporating an attention mechanism. Illustrating the model's generalization capabilities, a detailed analysis of  $Q_{dis}$  in Fig. 4 is presented. In both  $D_{NMC+NCA}$  and  $D_{LCO}$ , there is good agreement between the model's predictions and actual values (Panel I & II, Fig. 4a), as complemented by the density graphs in Fig. 4b. For  $D_{NMC+NCA}$ , the predicted and actual densities closely overlap. For  $D_{LCO}$ , the predicted density is highly similar, with a

slightly skewed distribution towards lower  $Q_{dis}$ . The better density distributions for  $D_{NMC+NCA}$  are likely attributable to the larger proportion of cylindrical cells in the training data, which accounts for 94.9% of the total. A detailed evaluation of the uncertainty of the model  $M(P)$  is provided in Fig. 4c–e for both datasets. Panel I & II of Fig. 4c evaluate the calibration by comparing the observed quantile proportions to the expected proportions under the assumption of a normal distribution. This continuous curve indicates the model's general performance across the entire probability distribution. The miscalibration area, quantified by the degree of deviation from the ideal diagonal line, represents the aggregate of discrepancies<sup>60</sup>. For  $D_{NMC+NCA}$ , the predicted distribution of  $Q_{dis}$  is well calibrated around the median but diverges at the tail, with calibration points showing underconfidence at higher quantiles. For  $D_{LCO}$ , the individual calibration points suggest a slight overconfidence in the 10th–50th percentile and underconfidence in the ranges 50th–90th and 10th–90th percentile. The miscalibration area for  $D_{LCO}$  is 0.16, which is slightly higher than  $D_{NMC+NCA}$ , likely due to noisier data. The overall calibration performance across both datasets is comparable. Figure 4e shows a histogram of prediction interval quantiles, revealing the spread between the 10th and 90th percentiles and evaluating the concentration of its predictive distribution as indicated by sharpness. The lower values suggest higher confidence in the prediction<sup>61</sup>. For  $D_{NMC+NCA}$ , a bimodal distribution highlights variable prediction certainty across cycles, suggesting potential fluctuations in battery behavior.  $D_{LCO}$  shows two clusters of distributions, mostly around a central quantile with a sharpness of 0.19, indicative of consistent uncertainty. Figure 4d further supports these findings by illustrating the model's median prediction uncertainty and the variability of these predictions by interquartile range

<https://doi.org/10.1038/s41524-024-01286-7>

Article

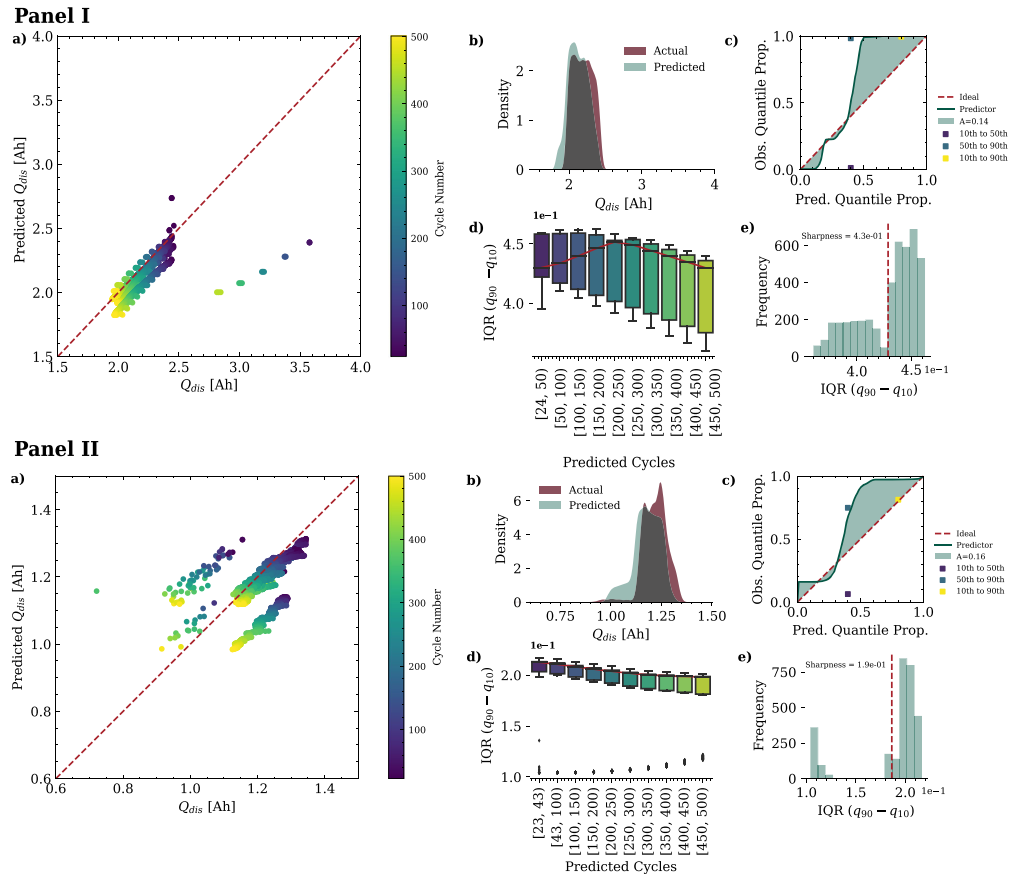


**Fig. 4 | Comparative analysis of model predictions and its uncertainty and calibration for  $Q_{dis}$  in cylindrical sample cells.** Analytical comparison for  $Q_{dis}$  for two datasets:  $D_{NMC+NCA}$  (Panel I) and  $D_{LCO}$  (Panel II), where **a** depicts the relationship between predicted and actual values of  $Q_{dis}$  with the diagonal dashed line indicating perfect prediction accuracy, **b** illustrates the density distributions of predicted versus actual  $Q_{dis}$ . The calibration plot in **c** assumes a normal distribution, where the mean and standard deviation are estimated from the 10th, 50th, and 90th percentiles of predictions. It depicts the cumulative proportion of actual  $Q_{dis}$  values that fall at or below the predicted quantile values rather than within symmetric intervals around the predictions. The ideal diagonal line represents perfect calibration with the shaded area indicating the degree of miscalibration, denoted  $A$ . The approximately diagonal trend of the calibration line up to the 0.5 quantile shows that data with residuals below the median are well described by the predictive distribution. The jump from 0.5 to 1 indicates that the predictive distribution extends further

to positive values than the observed distribution of residuals; almost all test data are already covered by the predicted 0.6 quantiles for both datasets. However, the overall miscalibration areas for both datasets are quite similar, indicating that despite different patterns of over- and underconfidence at specific quantiles, the general calibration performance across both datasets is comparable. Box plots at **d** show the prediction intervals over multiple cycles, demonstrating the median and variability of the model prediction uncertainty over the battery's lifespan. **e** provides histograms that depict the quantile-based prediction interval width between the 10th and 90th percentiles as a measure of sharpness. The red dashed line indicates the sharpness as the mean interval width and shows the concentration of the predictive distributions that indicate narrower distribution and, consequently, higher confidence in predicting  $Q_{dis}$  for  $D_{NMC+NCA}$  in Panel I. Further comparisons are in Supplementary Figs. 7, 8, 10, and 12.

(IQR). Here,  $D_{NMC+NCA}$  in Panel I shows varying IQR, suggesting changes in model confidence over the lifespan. In contrast,  $D_{LCO}$  maintains a more uniform IQR, indicating steady prediction uncertainty and aligning with the model's attention on later cycles to contend with the increased complexity and noise. These metrics complement the information provided in Fig. 4c–e, serving as a benchmark for the model's reliability and its capacity to generalize within a precise estimate range.

The multi-output predictive capabilities of  $M(P)$  are further highlighted by its performance in predicting the second parameter, voltage drop

(Supplementary Fig. 4). The model exhibits strong prediction accuracy with both datasets.  $D_{NMC+NCA}$  shows a smaller range of predictions over increasing cycles, and  $D_{LCO}$  shows a stable range with decreasing median intervals, while the calibration accuracy and the reliability of the predictions remain high across both datasets. The performance on the third predictor, CE (Supplementary Figs. 6 and 11), shows consistency and low prediction uncertainty, although the high measurement noise present in this dimension poses a challenge and makes convergence more demanding<sup>22</sup>. Additional examples are shown in Supplementary Figs. 5 and 9. The evaluation



<https://doi.org/10.1038/s41524-024-01286-7>

Article

metrics for  $M(P)$  (Supplementary Table 2) demonstrate its predictive strengths for both  $D_{NMC+NCA}$  and  $D_{LCO}$ . For the  $D_{LCO}$  dataset, the voltage drop is predicted with a root mean square error (RMSE) of 0.0335 and a mean absolute percentage error (MAPE) of 6.6052. However,  $D_{NMC+NCA}$  outperforms CE with significantly lower error rates of 0.0256 and 0.2489 for the RMSE and MAPE, respectively. However, both datasets present higher error rates in the predicted discharge capacity. To counteract the impact of systematic noise, Median Absolute Error (medAE) is used along with MAE for a more robust error analysis. These metrics highlight  $M(P)$ 's versatile predictive capabilities in handling diverse dataset requirements for multiple features and long-term predictions<sup>63</sup>.

We further examine  $M(P)$ 's performance on unseen coin cell datasets,  $D_{LNO}$  and  $D_{NMC}$ . The model predicts the voltage drop and CE well but shows limitations and high uncertainty when predicting the discharge capacity with an RMSE of 0.5827. This may stem from the low representation of coin cells in the training data, just 4.1% of the total. To alleviate this problem, we fine-tuned the decoder weights of  $M(P)$  using the data of 17 coin cells from  $D_{LNO}$ , resulting in an updated model,  $M(P)_f$ . This fine-tuning process and training performance are detailed in Supplementary Figs. 13 and 14 and led to a substantial improvement in predicting  $Q_{dis}$ , dropping the RMSE to 0.0002, indicating a significantly enhanced precision.  $M(P)_f$ 's performance will be compared with  $M(B)$ , trained with the BASF dataset  $B$ , in the following section.

#### Model performance on coin cell data for generalization insights

While comparing the predictive performance of models  $M(B)$  and  $M(P)$  on subsets of unseen  $D_{LNO}$  (Supplementary Figs. 15 and 20) and  $D_{NMC}$  dataset (Supplementary Figs. 21 and 23),  $M(P)_f$  demonstrates reliable predictive alignment for voltage drop, CE, and  $Q_{dis}$ . In contrast,  $M(B)$  shows a divergent pattern in voltage drop predictions, which may be due to its training on data with inherently long relaxation time profiles compared to those in  $D_{LNO}$ , where measurements are taken shortly after state changes. However, it maintains consistency in CE predictions and adjusts  $Q_{dis}$  predictions in response to changes in the test protocol.

In our analysis of  $D_{LNO}$  for  $Q_{dis}$ , Fig. 5 demonstrates that  $M(P)_f$  achieves high predictive fidelity. This is evident from the dense alignment of the predictions with the actual values in the scatter plot (Fig. 5a), and the significant overlap in distributions seen in the density plot (Fig. 5b). The model's precision is further highlighted by concentrated prediction intervals and a calibration curve that closely traces the diagonal (Fig. 5c–e). It achieves a high proportion of data points within the predictive bounds, indicative of accuracy, without excessively wide intervals that could decrease the utility of the predictions. Panel II for  $M(B)$  also demonstrates a close tracking of the actual values, with a marginally broader prediction interval and higher miscalibrated area of 0.16 compared to  $M(P)_f$ 's of 0.022 (Panel I). Despite this variance,  $M(B)$  maintains a reasonable estimate range. Qualitatively (Table 2),  $M(P)_f$  achieves a lower MAPE (9.2285) for predicting voltage drop, indicating its capability for learning trends commonly observed in training datasets with short relaxation times during cycling. On the other hand, the  $M(B)$  model demonstrates a notably lower MAPE in  $Q_{dis}$  (8.8914), showcasing its superior ability to capture proportional changes across a broader dataset. This performance illustrates the impact of prior knowledge and training data diversity on the learning outcomes of the models. Detailed analyses of additional predictive dimensions for  $D_{LNO}$  for both models and the complete dataset  $D_{NMC}$  are available in Supplementary Figs. 16–19, 22, 24, 25 and Supplementary Table 3. Despite the  $D_{LNO}$  data originating from another institute, the generalization of  $M(B)$  highlights the potential of well-trained DL models to overcome the variability of data sources.

#### Adaptive chemical modeling

ARCANA has so far been demonstrated to generalize well across battery formats, electrolyte formulations, cathode chemistries, and cycling procedures for LIBs. The ultimate generalization would be achieved if the model could also be deployed to Na-ion batteries. Since the underlying degradation mechanism of Na-ion batteries is very different, we performed fine-tuning

to test the adaptability of  $M(B)$  and  $M(P)$  to this distinct chemical domain<sup>30,64</sup>. These fine-tuned models are denoted  $M(B)_{Na}$  and  $M(P)_{Na}$  and are trained on Na-ion cycling data with CC-CV and pulse discharge settings. Details on the fine-tuning parameters and training performance for both models are available in Supplementary Figs. 26–29.

In Figs. 6 and 7, we evaluate the fine-tuned  $M(B)_{Na}$  and  $M(P)_{Na}$  models on an unseen C-rate test protocol (Figs. 6a and 7a). Both models demonstrate flexibility in adjusting to changes in C-rates, with voltage drop, CE, and  $Q_{dis}$  depicted in Figs. 6b–d and 7b–d. The model  $M(B)_{Na}$  shows narrower prediction intervals, indicative of lower uncertainty and greater predictive robustness. This trend is consistent across all predictive dimensions, and the model is probably benefiting from the larger initial dataset on which it was trained, since it provided a richer learning environment for the model to become more 'protocol-agnostic'. Its precision is especially notable in predicting the voltage drop and CE estimations, closely following the ground truth despite the substantial experimental noise. The aggregated attention mechanism in  $M(B)_{Na}$  (Fig. 7d) also appears more fine-tuned, with greater weights on the latest cycle data, which is consistent with its precise predictions. While  $M(P)_{Na}$  is adaptable, it shows a marginally wider uncertainty (Fig. 6b–d).

Sensitivity analysis, as shown in Figs. 7e–g and 6e–g evaluates the input parameter influence on future predictions for  $M(B)_{Na}$  and  $M(P)_{Na}$ . Both models demonstrate increased sensitivity to the most recent input data, i.e., cycles 7–9 in this provided example, aligned with their attention distributions, with cycle 9 receiving the highest attention. This increased emphasis on the last input cycles corresponds to the rapid degradation patterns in this sodium coin cell. As the model receives each successive cycle, the most recent data, here in cycle 9, becomes important in shaping its predictions, allowing the model to more accurately predict ongoing trends.

In Fig. 7,  $M(B)_{Na}$  shows a greater overall sensitivity across input cycles, particularly for the dimensions of voltage drop and  $Q_{dis}$ . This is further illustrated in sensitivity profiles and cumulative plots (Fig. 7h–j), highlighting a refined input-response relationship and a lower uncertainty interval in the primary prediction (Fig. 7a–c). Such a distinct sensitivity indicates  $M(B)_{Na}$ 's ability to precisely identify and respond to subtle variations. Despite the high experimental noise and limited battery performance, the saliency and attention trends of both models remain remarkably similar. This suggests that both mechanisms are intrinsic to the model's architecture, enabling them to perform consistently in diverse scenarios.

To further substantiate our initial findings, the plots in Fig. 8, show both models'  $Q_{dis}$  predictions aligning well with the ground truth.  $M(P)_{Na}$  exhibits a tighter clustering around the actual values, while  $M(B)_{Na}$  exhibits a broader spread. The prediction intervals and the distribution of quantiles across the 10th and 90th percentile for both models confirm their consistency and calibrated confidence. Further assessments are found in Supplementary Figs. 30–32 and Supplementary Table 4. These evaluations provide insights into the model's robustness. The performance of  $M(B)_{Na}$ 's especially underscores the advantage of extensive and diverse pretraining datasets in enhancing model generalization across different battery chemistries.

#### Discussion

We demonstrated the chemistry-, format- and cycling procedure-agnostic ARCANA framework and its ability to reliably monitor battery life and SOH by utilizing multitask learning with an attention mechanism. ARCANA excelled across three predictive settings, demonstrating that augmenting the model with diverse knowledge streams enhances its generalization across virtually all variations possible in batteries, such as anode, cathode, electrolyte, and shuttle ion chemistry and format. The ARCANA model integrates uncertainty quantification and attention mechanisms for each and every cycle to elucidate the model's focus for each prediction and is essential for uncovering complex patterns associated with multiple factors. Further evaluation involves saliency and sensitivity assessments, allowing us to understand the impact of perturbation of input parameters on output predictions. By examining whether saliency and attention are directly



<https://doi.org/10.1038/s41524-024-01286-7>

Article

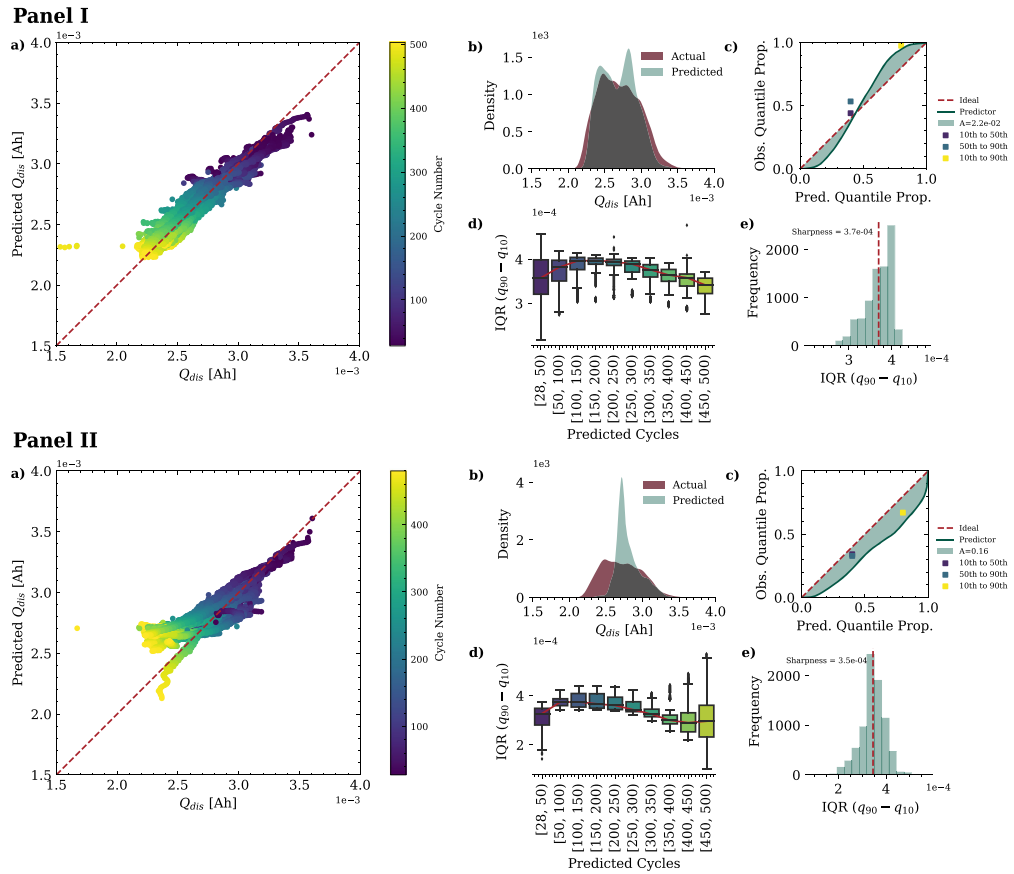


**Fig. 5 | Performance analysis of  $M(P)_j$  and  $M(B)$  for  $Q_{dis}$  in coin sample cells.** Performance of  $M(P)_j$  (Panel I) and  $M(B)$  (Panel II) on  $D_{LNO}$  for  $Q_{dis}$  prediction. Plot **a** illustrates the relationship between models' predictions and the actual  $Q_{dis}$  with the diagonal line representing perfect prediction accuracy, plot **b** compares the density distribution of actual and predicted  $Q_{dis}$ , plot **c** presents calibration curves that reflect the degree of alignment between predicted probabilities and observed frequencies under a normal distribution assumption. The discrete points on the calibration curve show the observed proportions of actual values that fall within three specific intervals based on the quantiles: between the 10th and 50th, 50th and 90th, and 10th and 90th percentiles. Model  $M(P)_j$  shows a high level of calibration for predicting  $Q_{dis}$  of  $D_{LNO}$  samples with a minimal miscalibrated area of 0.022. The points for the 10th, 50th, 50th, and 90th percentiles lie close to the diagonal line, indicating a nearly perfect calibration for these intervals.  $M(B)$  exhibits a slight overconfidence by deviating

from the ideal line, with a miscalibration area of 0.16. The three calibration markers for  $M(B)$  are all positioned just below the diagonal line, showing uniform overconfidence across these quantile ranges, yet they remain close to this line, indicating a generally well-calibrated model. Plots **d** show the prediction intervals across lifespan cycles, highlighting models' uncertainty over time, and plot **e** details the distribution of prediction intervals' quantiles between the 10th and 90th percentiles, which convey the models' prediction uncertainty; a distribution skewed towards the lower quantiles suggests a higher confidence in predictions at these quantiles. The sharpness, as a measure of mean interval width, is approximately similar for both models at  $3.7 \times 10^{-4}$  and  $3.5 \times 10^{-4}$  for  $M(P)_j$  and  $M(B)$ , respectively. Together, these plots demonstrate the  $M(P)_j$ 's precision in capturing discharge capacity behavior and  $M(B)$ 's robust generalization.

correlated or orthogonal to each other, we gain a comprehensive understanding of input–output relationships, increasing the model's explainability and reliability in extrapolation. Incorporating raw data and failed experiments, as suggested in prior studies<sup>4,36</sup> is a deliberate strategy to teach our models to recognize variations across similar cell types and manufacturers. This inclusion not only enables uncertainties to be quantified more accurately but also deepens reliability insights, reduces bias, and offers a more meaningful understanding of the data. A conceptually straightforward extension to this work would be to incorporate additional features, such as the rate of change of voltage with respect to capacity ( $dQ/dV$ )<sup>34,65</sup>, and

leverage different characterization methods, like spectroscopy, to enhance the predictive power of the models. This will not only enhance multi-feature predictions but also deepen the understanding of degradation processes.<sup>34,63</sup>

We observed that  $M(P)$ , trained on public data, offers broader generalization across various battery types and protocols, albeit with increased uncertainty.  $M(B)$ , trained on a more extensive dataset, demonstrates a lower uncertainty. This further motivates the importance of data sharing and management. Our findings also reveal that fine-tuning the models with few labels significantly improves their generalization to different chemistries, especially for  $M(B)$ . The methodology outlined in this paper presents

<https://doi.org/10.1038/s41524-024-01286-7>

Article

**Table 2 | Evaluation metrics for  $M(P)_t$  and  $M(B)$  using  $D_{LNO}$**

Metrics	$M(P)_t$			$M(B)$		
	Voltage drop [V]	CE	$Q_{dis}$ [Ah]	Voltage drop [V]	CE	$Q_{dis}$ [Ah]
RMSE	0.0703	0.0331	0.0002	0.1247	0.0588	0.0003
MAPE	9.2285	1.1922	20.7946	34.8638	4.4560	8.8914
MAE	0.0353	0.0076	0.0001	0.0867	0.0335	0.0002
medAE	0.0181	0.0021	0.0001	0.0513	0.0104	0.0001

Summary of the evaluation metrics for  $M(P)_t$  and  $M(B)$ , tested on 26 unseen coin cells ( $D_{LNO}$ ), using 27 initial cycles of historical data, to predict the cell behavior up to the 500th cycle. Note that the number of initial cycles was chosen randomly to resemble practical scenarios with limited initial data. The user can specify any preferred number of initial cycles in the provided configuration file, which is detailed at <https://github.com/basf/ARCANA/blob/master/config/>.

an opportunity for other researchers to create their own high-performance models. By retraining or fine-tuning with different datasets, researchers can tailor these predictive models to their specific experimental setups and desired outcomes. This flexibility allows for the exploration of different perspectives and approaches, facilitating the development of more accurate and specialized models. One could envision a model-sharing and transfer-learning community similar to those found today in the fields of computer vision and language modeling. Furthermore, the performance metrics explored here raise the tantalizing prospect of further improving model quality via a federated learning approach. This could enable researchers from diverse backgrounds and institutions to pool their data and expertise, leading to more powerful models.

The modular design of the ARCANA pipeline enables real-time monitoring of battery degradation profiles, promoting timely and cost-effective interventions. This proactive approach prevents prolonged sub-optimal testing conditions, improves the R&D process, and contributes to more informed material selection and protocol optimization. By automating data collection, processing, and analysis, researchers can streamline their experimental workflows and reduce human error. Furthermore, ML models can continuously learn from upcoming data, adapt to evolving experimental conditions, and provide real-time insights. This integration of ML and laboratory workflows has the potential to transform battery research, enabling researchers to make data-driven decisions, uncover insights more rapidly, and accelerate the pace of discovery.

Overall, we demonstrated that incorporating multitask learning with an attention mechanism creates a framework that can achieve chemistry agnosticism as envisioned by Battery 2030+<sup>1</sup> and the interesting fact that a DL architecture trained on a smaller, noisier, but more diverse dataset yields better generalization at the cost of higher uncertainty. We hope that the pipeline will emerge as an indispensable and transformative tool to bridge the gap between lab-scale research and commercial viability and will become essential for the development of applications and insightful predictive models in the energy storage field.

## Methods

In the following section, some of the key components of the ARCANA framework are explained to underscore their contribution to the overall efficacy and reliability of the model. This includes an exploration of attention mechanisms, a teacher forcing scheduler, methods to quantify predictive uncertainty, a strategic early stopping protocol, a training procedure, and evaluation metrics.

### Attention mechanism

Within the proposed ARCANA framework, two distinct attention mechanisms are implemented. The first, termed additive attention, is also known as Bahdanau attention<sup>55</sup>. This mechanism aligns the hidden state of the decoder  $h_t$  at each time step  $t$  with the hidden states of the encoder ( $h_s$ ), thus producing a context vector that encapsulates the weighted relevance of each historical temporal segment from the past cycles. This vector provides a

dynamically focused representation of the input sequence pertinent to the current decoding step. This mechanism is functional through a parameterized attention model. The model calculates an attention score  $e_{ts}$  (Eq. (1)) for each encoder state  $h_s$  given by:

$$e_{ts} = v^T \tanh(W_1 h_t + w_2 h_s) \quad (1)$$

where  $W_1$  and  $W_2$  are the weight matrices that transform the respective hidden states into a common feature space and  $v$  is a weight vector that projects the activated sum into a scalar score. Attention weights  $\alpha_{ts}$  are then determined by normalizing these scores using the softmax function (Eq. (2)):

$$\alpha_{ts} = \frac{\exp(e_{ts})}{\sum_{k=1}^{T_e} \exp(e_{tk})} \quad (2)$$

where,  $T_e$  is the total number of time steps in the encoder sequence.

The context vector  $c_t$  results from aggregating the encoder hidden states, each weighted by its respective attention weight, as can be seen in Eq. (3), and can improve the model's capacity for handling Seq-to-Seq predictions<sup>66</sup>.

$$c_t = \sum_{s=1}^{T_e} \alpha_{ts} h_s \quad (3)$$

Another attention mechanism that can be employed within the ARCANA architecture is multihead attention. This mechanism expands the model's capacity to focus on different positions of the input sequence simultaneously<sup>67</sup>, which is crucial for capturing a wider range of dependencies inherent in battery lifetime data. This attention mechanism operates by projecting the decoder's hidden states and the encoder outputs, representing the past cycle's information, into multiple subspaces. This is formulated as: (Eq. (4))

$$\text{MultiHead}(Q, K, V) = \text{Concat}(\text{head}_1, \dots, \text{head}_h) W^0 \quad (4)$$

$$\text{head}_i = \text{Attention}(QW_i^Q, KW_i^K, VW_i^V) \quad (5)$$

where each head ( $\text{head}_i$ ) captures different aspects of the input data and is computed as shown in Eq.(5). The operation applied in each head is defined by the attention of the scaled dot product and is presented in Eq. (6).

$$\text{Attention}(Q, K, V) = \text{softmax}\left(\frac{QK^T}{\sqrt{d_k}}\right)V \quad (6)$$

Here,  $Q$ ,  $K$ , and  $V$  are the query, key, and value matrices, respectively.  $Q$  is generated from the hidden states of the decoder, while  $K$  and  $V$  are derived from the encoder outputs. This arrangement enables the decoder to integrate the current state information with historical data provided by the encoder. The parameter matrices  $W_i^Q$ ,  $W_i^K$ , and  $W_i^V$  for each head  $i$ , along with the output weight matrix  $W^0$ , are optimized during the training process. These matrices are instrumental in transforming the input data into different representational subspaces to capture various aspects and dependencies within the data. The parameter  $d_k$ , representing the dimension of the key vectors, scales the dot product within the attention mechanism. In Eq. (6), the softmax function is applied to these scaled attention scores, which originate from the interactions between the query and key matrices. This process results in the production of a context vector, which integrates information from different representational subspaces and allows the model to consider multiple aspects of historical data<sup>54,68</sup>.

<https://doi.org/10.1038/s41524-024-01286-7>

Article

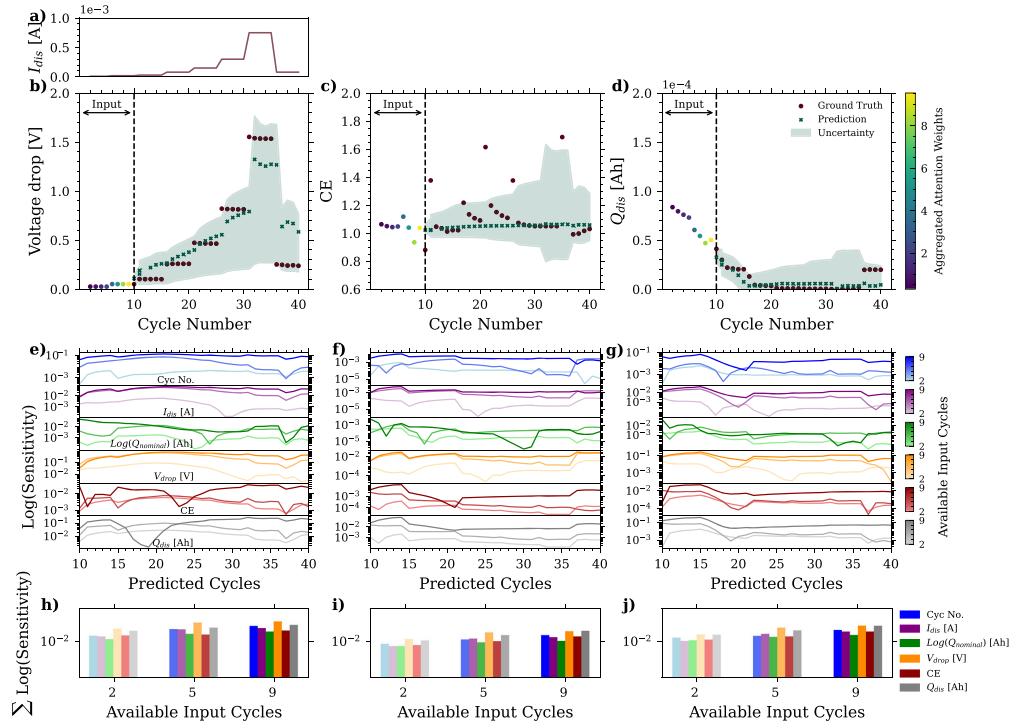


**Fig. 6 | Analysis of  $M(P)_{Na}$ 's predictive accuracy and input sensitivity on Na-ion data.** Plot a presents the C-rate profile for cycling one battery, while plots b–d compare the model's prediction to actual data, showing consistency and adaptability. Sensitivity to input parameters across predicted cycles is analyzed in plots e–g on a logarithmic scale. The color intensity in these plots denotes the specific

cycles from which the input parameter originates. Plots h–j show the sum of the logarithmic contribution of each input parameter towards predicting future cycles with a selective representation of three past cycle data. These visualizations confirm the model's attentive adjustment to the latest available input data and its capacity for generalization, despite the high experimental noise and limited battery performance.

#### Teacher forcing

Teacher forcing optimizes the learning of temporal dependencies. By integrating the real data from previous time steps, the technique promotes rapid stabilization and convergence of the model. In the present study, the implementation of the teacher forcing strategy is applied through a calculated division of training epochs. This division is reflective of the model's incremental improvement in processing sequences with varying lengths over time by prioritizing shorter sequences at the early stages of training to ensure intensive guidance. This preferential focus ensures that the model does not prematurely plateau when learning to predict longer-term dependencies.

To quantitatively define this approach, the training period consisting of  $E$  epochs is divided into  $D$  equal segments  $s$ . Within the  $i$ -th segment, the teacher forcing ratio is adjusted through a decay parameter  $\lambda$ , which represents how quickly the training procedure switches from using real data as decoder inputs to using model predictions from the previous cycle, as depicted in Fig. 2b. The allocation of epochs per division  $d_i$  is calculated as can be seen in Eq. (7)

$$d_i = \text{round} \left( \frac{s \cdot e^{-\lambda i}}{\sum_{j=0}^{D-1} s \cdot e^{-\lambda j}} \cdot E \right) \quad (7)$$

Following this, the teacher forcing ratio for the  $t$ -th epoch in the  $i$ -th segment is linearly reduced from a starting ratio  $R_{start}$  to an ending ratio  $R_{end}$

using the following equation, Eq. (8).

$$\begin{aligned} A &= \left( \frac{R_{start} - R_{end}}{d_i + \epsilon} \right) \\ R_{t_i} &= R_{start} - A \cdot t \end{aligned} \quad (8)$$

Here,  $R_{t_i}$  indicates the teacher forcing ratio at epoch  $t$  for the  $i$ th segment. The expression  $A$  represents the decrease per epoch in that segment. To ensure numerical stability and avoid division by zero, a small constant  $\epsilon$ , set to  $10^{-8}$ , is included in the calculation as indicated in Eq. (8). The teacher forcing ratio, as a probabilistic measure, represents the likelihood that the model will utilize the actual observation from the training data at a given prediction step. This approach modulates the ratio to facilitate a smooth transition from guided to self-generated sequence prediction. The adjusted ratios are indicative of the model's learning trajectory, enhancing its independent predictive accuracy across different sequence lengths.

#### Uncertainty quantification

The pinball loss, in this study, provides a robust metric for predicting a range of potential outcomes, rather than a single point estimation. This is an effective measure for forecasting scenarios where the impacts of over-prediction and under-prediction are asymmetric<sup>36</sup>. It is defined for a set of quantiles  $Q = \{q_1, q_2, q_3\}$  where  $q_1 < q_2 < q_3$  and in this study, we select

<https://doi.org/10.1038/s41524-024-01286-7>

Article

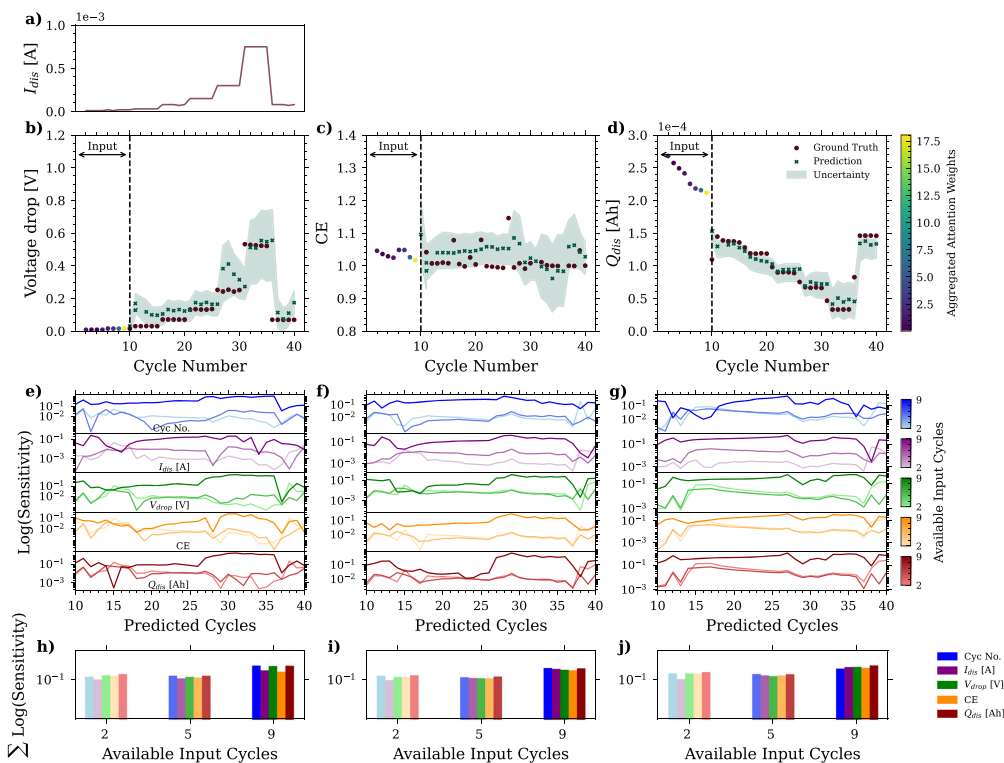


**Fig. 7 | Evaluation of  $M(B)_{N_t}$ 's predictive performance and input sensitivity on our in-house Na-ion data.** Plot a shows the discharge current profile, while plots b–d depict the predictions for voltage drop, CE, and  $Q_{dis}$  against the ground truth. The color bar here shows the aggregated attention weights across the input data.

Plots e–g provide a detailed logarithmic sensitivity analysis per predictive cycle for each input parameter, and plots h–j aggregate these sensitivities, highlighting the model's focus on different input cycles, especially the most recent ones, reflecting  $M(B)_{N_t}$ 's protocol adaptability and robust response to experimental noise.

$Q = \{0.1, 0.5, 0.9\}$  corresponding to the 10th, 50th, and 90th percentiles, respectively. For a given predicted value  $\hat{y}$  and the actual target value  $y$ , the pinball loss for a single quantile  $q$  is calculated as:

$$L_q(\hat{y}, y) = \begin{cases} (1 - q) \cdot (\hat{y} - y) & \text{if } y < \hat{y} \\ q \cdot (y - \hat{y}) & \text{if } y \geq \hat{y} \end{cases} \quad (9)$$

In the implementation of this loss function, a mask is provided and applied to each quantile's loss to selectively evaluate certain predictions, allowing for the exclusion of outliers. The total pinball loss for multiple quantiles is then the sum of the individual losses for each quantile, averaged over all predictions, as shown in Eq. (10), reflecting the model's performance across the specified range of quantiles.

$$L(Q, \hat{Y}, Y) = \frac{1}{N} \sum_{i=1}^N \sum_{q \in Q} L_q(\hat{y}_{qi}, y_i) \quad (10)$$

Here,  $N$  is the number of observations,  $\hat{Y}$  is a stack of vectors, with each vector containing the predictions for all observations at one of the specified quantiles, and  $Y$  is the vector of the true target values. Each element  $\hat{y}_{qi}$  in  $\hat{Y}$  denotes the predicted value for the  $i$ th observation at quantile  $q$ . This configuration not only facilitates efficient computation of the loss function

across multiple quantiles and observations, but also captures the central tendency and variability of the predictions, making it a comprehensive loss function for probabilistic forecasting<sup>69,70</sup>.

#### Early stopping

To optimize training, a rigorous early stopping approach is incorporated. This method was originally proposed by Prechelt et al.<sup>71</sup> and combines criteria to prevent overfitting while ensuring substantial training progress, especially in the presence of noisy data. Here, a dual-criteria strategy is implemented. The first criterion assesses the ratio between generalization loss (GL) and training progress, which is shown in Eq. (11), where  $E_{val}$  represents the validation error at the current epoch,  $E_{min\ val}$  is the lowest validation error obtained up to the current epoch, and  $E_{train\ strip}$  denotes the training errors within a recent sequence of epochs. This sequence, or strip, is a designated period in which the progress quotient (PQ) is measured. If the generalization-loss-to-progress-quotient-ratio (GL/PQ) surpasses a predefined value, it may indicate that further training will not be beneficial for the model's generalizability.

$$\begin{aligned} \text{GL} &= 100 \cdot \left( \frac{E_{val}}{E_{min\ val}} - 1 \right) \\ \text{PQ} &= 1000 \cdot \left( \frac{\text{Mean}(E_{train\ strip})}{\text{Min}(E_{train\ strip})} - 1 \right) \end{aligned} \quad (11)$$

<https://doi.org/10.1038/s41524-024-01286-7>

Article

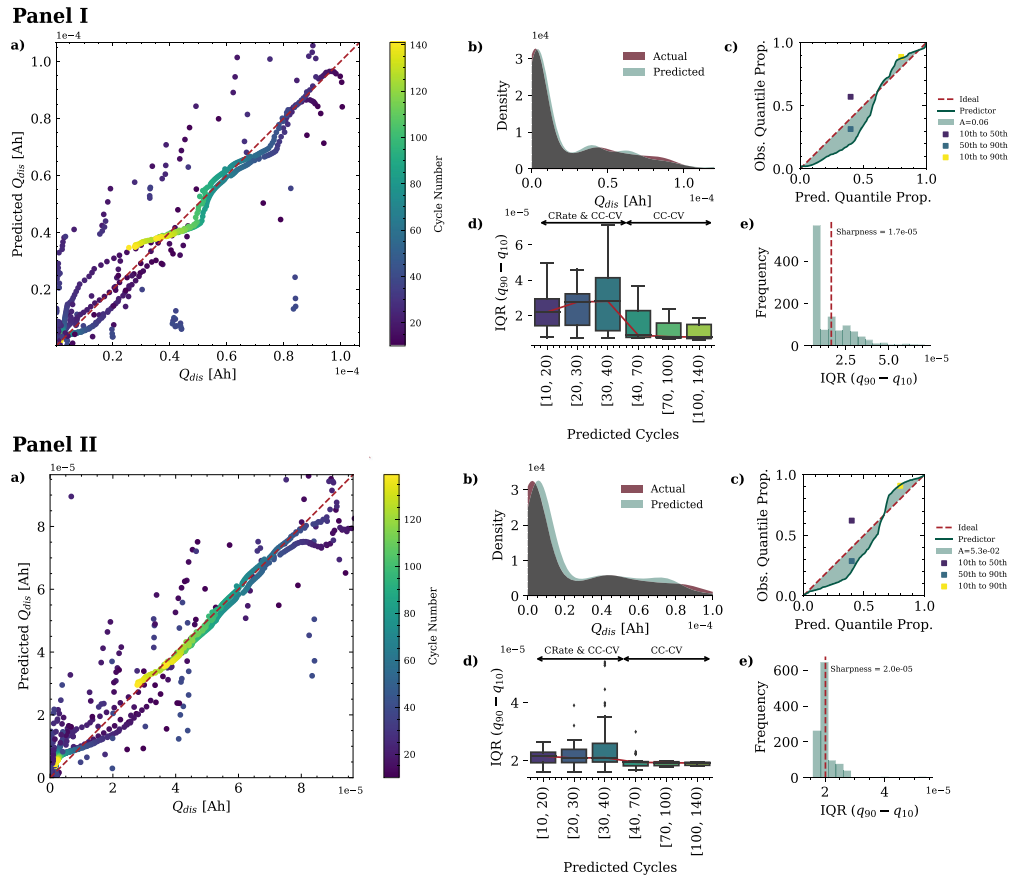


**Fig. 8 | Comparative analysis of  $M(P)_{Na}$  and  $M(B)_{Na}$  on  $Q_{dis}$  prediction for Na-ion batteries.** Prediction analysis for  $M(P)_{Na}$  (Panel I) and  $M(B)_{Na}$  (Panel II) for  $Q_{dis}$  prediction of Na-ion batteries. The scatter plots **a** illustrate the models' alignment with actual measurements. Density plots **b** compare the distributions of predicted and actual values, demonstrating the models' accuracy in estimating  $Q_{dis}$ . Calibration plots in **c** depict how well the predicted probabilities match the observed outcomes against the benchmark line, with the discrete points representing the observed proportions of actual values that fall within three quantile intervals. Both models demonstrate a pattern of marginal overconfidence below the 70th percentile and a slight underconfidence above this percentile, as evidenced by the calibration points

positions beneath and above the diagonal line, respectively.  $M(P)_{Na}$  shows a larger area of divergence,  $A = 0.06$ , while  $M(B)_{Na}$  presents a closer fit with a miscalibration of 0.053, highlighting both models' well-calibrated prediction capabilities across different chemistries. Boxplots **d** visualize the spread and consistency of prediction intervals across predicted cycles. Histograms in **e** represent the distribution of the quantile intervals of the models' prediction, highlighting uncertainty; these distributions indicate where, within the prediction range, the models' confidence is concentrated, with sharpness values of  $1.7 \times 10^{-5}$  for  $M(P)_{Na}$  and  $2.0 \times 10^{-5}$  for  $M(B)_{Na}$ , demonstrating a precise estimation of uncertainty.

The second criterion implements a conventional check and is applied to monitor the trend in validation error. An increased trend over the epoch sequence suggests that overfitting could be occurring. Training is discontinued when both the ratio criterion and the error-trend criterion indicate that further training is unlikely to yield significant gains. In general, this strategy offers a control mechanism that aligns the duration of training with the achievement of a well-generalized model capable of accurate predictions.

**Training procedure**

Expanding on Seq-to-Seq integration, the training phase begins by initializing the data loaders for batch processing and configuring the parameters

of the Seq-to-Seq model, the loss criteria, the optimizer, and a dynamic learning rate scheduler<sup>62</sup>. Hyperparameter optimization, through a series of trials using Optuna's<sup>52</sup> Tree-structured Parzen Estimator (TPE) Sampler, employs a probabilistic model to specify the most promising parameter configuration, navigating the search space while balancing exploration and exploitation within a complex and high-dimensional domain<sup>72</sup>. Training unfolds over several epochs, with each iteration starting with a reset of the model's hidden states and zeroing gradients to ensure clean computation for the forward pass. The pinball loss function is selected for its effectiveness in probabilistic forecasting, eliminating the need for a presumptive data distribution model<sup>70</sup>, unlike traditional metrics<sup>69</sup>, which are more sensitive to noise and anomalies. These asymmetric and non-parametric criteria assess

<https://doi.org/10.1038/s41524-024-01286-7>

Article

forecast accuracy by penalizing deviations from three targeted quantiles, namely 0.1, 0.5, and 0.9, enhancing robustness to outliers and the efficacy of LSTM-based networks<sup>69</sup>. At the same time, a masking technique<sup>63</sup> is implemented to filter out padding-induced distortions from the loss calculation, ensuring the integrity of the learning signal. Backpropagation follows loss computation, incorporating gradient clipping to prevent divergence and gradient explosion in recurrent network architectures. Additionally, learning rate adjustments encourage robust convergence. The validation phase alternates with training, where performance is assessed, and early stopping criteria are applied to mitigate overfitting. Optuna enhances optimization by pruning the less promising trials. Once the training is completed, the model parameters are saved and a comprehensive report is generated detailing the training results. The training procedure steps described are schematically depicted in Supplementary Fig. 1.

#### Evaluation metrics

For this study, the following metrics are implemented, including both average errors and variability of individual predictions, to evaluate the performance of the model. These metrics are RMSE (Eq. (12)) which provides a measure of the magnitude of prediction errors, MAPE (Eq. (13)), which measures the average magnitude of errors as a percentage, medAE (Eq. (14)) to capture the median error, reducing the influence of outliers, and mean absolute error (MAE) (Eq. (15)) which represents the mean absolute differences.

$$\text{RMSE} = \sqrt{\frac{1}{n} \sum_{i=1}^n (y_i - \hat{y}_i)^2} \quad (12)$$

$$\text{MAPE} = \frac{100\%}{n} \sum_{i=1}^n \frac{|y_i - \hat{y}_i|}{y_i} \quad (13)$$

$$\text{medAE} = \text{median}(|y_i - \hat{y}_i| : i = 1, 2, \dots, n) \quad (14)$$

$$\text{MAE} = \frac{1}{n} \sum_{i=1}^n |y_i - \hat{y}_i| \quad (15)$$

#### Data availability

Open source data supporting the findings of this study are available online, with access details provided in Table 1 and can be found in the corresponding literature<sup>41–48,50</sup>. In addition, public pre-trained model weights can be accessed at <https://doi.org/10.5281/zenodo.10293072>.

#### Code availability

The ARCANA framework can be installed using `pip install arcana-batt` or cloned from <https://github.com/basf/ARCANA>.

Received: 5 January 2024; Accepted: 24 April 2024;

Published online: 10 May 2024

#### References

- Amici, J. et al. A roadmap for transforming research to invent the batteries of the future designed within the European large scale research initiative battery 2030+. *Adv. Energy Mater.* **12**, 2102785 (2022).
- Xu, Y., Ge, J. & Ju, C.-W. Machine learning in energy chemistry: introduction, challenges and perspectives. *Energy Adv.* **2**, 896–921 (2023).
- Severson, K. A. et al. Data-driven prediction of battery cycle life before capacity degradation. *Nat. Energy* **4**, 383–391 (2019).
- Che, Y., Hu, X., Lin, X., Guo, J. & Teodorescu, R. Health prognostics for lithium-ion batteries: mechanisms, methods, and prospects. *Energy Environ. Sci.* **16**, 338–371 (2023).
- Stein, H. S. Nonlinear potentiodynamic battery charging protocols for fun, education, and application. *ACS Eng. Au* **0**, 0 (2023).
- Kabir, M. & Demirocak, D. E. Degradation mechanisms in li-ion batteries: a state-of-the-art review. *Int. J. Energy Res.* **41**, 1963–1986 (2017).
- Attia, P. M. et al. "knees" in lithium-ion battery aging trajectories. *J. Electrochem. Soc.* **169**, 060517 (2022).
- Yang, F., Song, X., Dong, G. & Tsui, K.-L. A coulombic efficiency-based model for prognostics and health estimation of lithium-ion batteries. *Energy* **171**, 1173–1182 (2019).
- Rahmanian, F. et al. Conductivity experiments for electrolyte formulations and their automated analysis. *Sci. Data* **10**, 43 (2023).
- Dahn, J., Burns, J. & Stevens, D. Importance of coulombic efficiency measurements in r&d efforts to obtain long-lived li-ion batteries. *Interface* **25**, 75 (2016).
- Smith, A., Burns, J., Trussler, S. & Dahn, J. Precision measurements of the coulombic efficiency of lithium-ion batteries and of electrode materials for lithium-ion batteries. *J. Electrochem. Soc.* **157**, A196 (2009).
- Attia, P. M. et al. Closed-loop optimization of fast-charging protocols for batteries with machine learning. *Nature* **578**, 397–402 (2020).
- Adamu, H., Abba, S. I., Anyin, P. B., Sani, Y. & Qamar, M. Artificial intelligence-navigated development of high-performance electrochemical energy storage systems through feature engineering of multiple descriptor families of materials. *Energy Adv.* **2**, 615–645 (2023).
- Tong, Z., Miao, J., Tong, S. & Lu, Y. Early prediction of remaining useful life for lithium-ion batteries based on a hybrid machine learning method. *J. Cleaner Prod.* **317**, 128265 (2021).
- Rieger, L. H. et al. Uncertainty-aware and explainable machine learning for early prediction of battery degradation trajectory. *Digit. Discov.* **2**, 112–122 (2023).
- Yang, Y. A machine-learning prediction method of lithium-ion battery life based on charge process for different applications. *Appl. Energy* **292**, 116897 (2021).
- Liu, Y. et al. Generative artificial intelligence and its applications in materials science: current situation and future perspectives. *J. Materiomics* **9**, 798–816 (2023).
- Gong, Q., Wang, P. & Cheng, Z. An encoder-decoder model based on deep learning for state of health estimation of lithium-ion battery. *J. Energy Storage* **46**, 103804 (2022).
- Zhu, C., He, Z., Bao, Z., Sun, C. & Gao, M. Prognosis of lithium-ion batteries' remaining useful life based on a sequence-to-sequence model with variational mode decomposition. *Energies* **16**, 803 (2023).
- Li, W. et al. One-shot battery degradation trajectory prediction with deep learning. *J. Power Sources* **506**, 230024 (2021).
- Deng, Z., Lin, X., Cai, J. & Hu, X. Battery health estimation with degradation pattern recognition and transfer learning. *J. Power Sources* **525**, 231027 (2022).
- Bhowmik, A. et al. Implications of the battery 2030+ AI-assisted toolkit on future low-trl battery discoveries and chemistries. *Adv. Energy Mater.* **12**, 2102698 (2022).
- Fichtner, M. et al. Rechargeable batteries of the future—the state of the art from a battery 2030+ perspective. *Adv. Energy Mater.* **12**, 2102904 (2022).
- Strange, C. & Dos Reis, G. Prediction of future capacity and internal resistance of li-ion cells from one cycle of input data. *Energy and AI* **5**, 100097 (2021).
- Ling, C. A review of the recent progress in battery informatics. *npj Comput. Mater.* **8**, 33 (2022).
- Ng, M.-F., Zhao, J., Yan, Q., Conduit, G. J. & Seh, Z. W. Predicting the state of charge and health of batteries using data-driven machine learning. *Nat. Mach. Intell.* **2**, 161–170 (2020).
- Liu, Y. et al. Data quantity governance for machine learning in materials science. *Natl. Sci. Rev.* **10**, nwad125 (2023).
- Baumhöfer, T., Brühl, M., Rothgang, S. & Sauer, D. U. Production caused variation in capacity aging trend and correlation to initial cell performance. *J. Power Sources* **247**, 332–338 (2014).



<https://doi.org/10.1038/s41524-024-01286-7>

Article

29. Roman, D., Saxena, S., Robu, V., Pecht, M. & Flynn, D. Machine learning pipeline for battery state-of-health estimation. *Nat. Mach. Intell.* **3**, 447–456 (2021).
30. Jha, S. et al. Learning-assisted materials development and device management in batteries and supercapacitors: Performance comparison and challenges. *J. Mater. Chem. A* **11**, 3904–3936 (2023).
31. Yao, Z. et al. Machine learning for a sustainable energy future. *Nat. Rev. Mater.* **8**, 202–215 (2023).
32. Dos Reis, G., Strange, C., Yadav, M. & Li, S. Lithium-ion battery data and where to find it. *Energy AI* **5**, 100081 (2021).
33. Wu, B., Widanage, W. D., Yang, S. & Liu, X. Battery digital twins: perspectives on the fusion of models, data and artificial intelligence for smart battery management systems. *Energy AI* **1**, 100016 (2020).
34. Li, X., Wang, Z. & Yan, J. Prognostic health condition for lithium battery using the partial incremental capacity and gaussian process regression. *J. Power Sources* **421**, 56–67 (2019).
35. Zhang, Y. et al. Identifying degradation patterns of lithium ion batteries from impedance spectroscopy using machine learning. *Nat. Commun.* **11**, 1706 (2020).
36. Raccuglia, P. et al. Machine-learning-assisted materials discovery using failed experiments. *Nature* **533**, 73–76 (2016).
37. De Angelis, V., Preger, Y. & Chalamala, B. R. Battery lifecycle framework: a flexible repository and visualization tool for battery data from materials development to field implementation. Preprint at [osf.io/preprints/ecsarxiv/h7c24](https://arxiv.org/abs/2011.07244) (2021).
38. Li, W. et al. Digital twin for battery systems: cloud battery management system with online state-of-charge and state-of-health estimation. *J. Energy Storage* **30**, 101557 (2020).
39. Draxl, C. & Scheffler, M. Nomad: the fair concept for big data-driven materials science. *Mrs Bulletin* **43**, 676–682 (2018).
40. Wilkinson, M. D. et al. The fair guiding principles for scientific data management and stewardship. *Sci. Data* **3**, 1–9 (2016).
41. Toyota Research Institute (TRI). Experimental data platform: project data-driven prediction of battery cycle life before capacity degradation. [data.mtr.io](https://data.mtr.io)
42. Toyota Research Institute (TRI). Experimental data platform: Project closed-loop optimization of extreme fast charging for batteries using machine learning. [data.mtr.io](https://data.mtr.io/1/projects/5c48dd2bc625d700019f3204)
43. Saha, B. & Goebel, K. Nasa. *Prognostics Data Repository* <https://www.nasa.gov/content/prognostics-center-of-excellence-data-set-repository> (2007).
44. Center for Advanced Life Cycle Engineering (CALCE), *University of Maryland* <https://calce.umd.edu/data> (2011).
45. Zhu, J. et al. Data-driven capacity estimation of commercial lithium-ion batteries from voltage relaxation. *Zenodo* <https://doi.org/10.5281/zenodo.6405084> (2022).
46. Battery Archive, Homepage of Battery Archive. <https://www.batteryarchive.org>, (2021).
47. Zhang, Merker, Sanin & Stein. Cycling data of 64 cells manufactured by autobass. *Zenodo* <https://doi.org/10.5281/zenodo.7299473> (2022).
48. Merker, L. 2023 commercial coin cell 45mah. *Zenodo* <https://doi.org/10.5281/zenodo.10102627> (2023).
49. Merker, L. Inzpro inform 300 cycles cccv after eol. *Zenodo* <https://doi.org/10.5281/zenodo.10102508> (2023).
50. Nuss, L., Merker, L., Zhang, B. & Stein, H. Formation and cycling data for Na-ion batteries from high-throughput synthesis, coating, and assembly. *Zenodo* <https://doi.org/10.5281/zenodo.7981011> (2023).
51. Paszke, A. et al. Pytorch: An imperative style, high-performance deep learning library. *Adv. Neural Inf. Process Syst.* **32**, 8024–8035 (2019).
52. Akiba, T., Sano, S., Yanase, T., Ohta, T. & Koyama, M. Optuna: a next-generation hyperparameter optimization framework. *DLP-KDD '19* 2623–2631 (2019).
53. Cooijmans, T., Ballas, N., Laurent, C., Gülçehre, Ç. & Courville, A. Recurrent batch normalization. Preprint at <https://arxiv.org/abs/1603.09025> (2017).
54. Yoo, J., Kim, B., Lee, B., Song, J.-h & Kang, K. An artificial neural network using multi-head intermolecular attention for predicting chemical reactivity of organic materials. *J. Mater. Chem. A* **11**, 12784–12792 (2023).
55. Bahdanau, D., Cho, K. & Bengio, Y. Neural machine translation by jointly learning to align and translate. Preprint at <https://arxiv.org/abs/1409.0473> (2016).
56. Smith, A. et al. Potential and limitations of research battery cell types for electrochemical data acquisition. *Batter. Supercaps* **6**, e202300080 (2023).
57. Burns, J. et al. Evaluation of effects of additives in wound li-ion cells through high precision coulometry. *J. Electrochem. Soc.* **158**, A255 (2011).
58. Burns, J. et al. Predicting and extending the lifetime of li-ion batteries. *J. Electrochem. Soc.* **160**, A1451 (2013).
59. Zhu, J. et al. Data-driven capacity estimation of commercial lithium-ion batteries from voltage relaxation. *Nat. Commun.* **13**, 2261 (2022).
60. Guo, C., Pleiss, G., Sun, Y. & Weinberger, K. Q. On calibration of modern neural networks. Preprint at <https://arxiv.org/abs/1706.04599> (2017).
61. Gneiting, T., Balabdaoui, F. & Raftery, A. E. Probabilistic forecasts, calibration and sharpness. *J. R. Stat. Soc. Series B Stat. Methodol.* **69**, 243–268 (2007).
62. Goldberg, Y. A primer on neural network models for natural language processing. *J. Artif. Intell. Res.* **57**, 345–420 (2016).
63. Li, W., Zhang, H., van Vlijmen, B., Dechent, P. & Sauer, D. U. Forecasting battery capacity and power degradation with multi-task learning. *Energy Storage Mater.* **53**, 453–466 (2022).
64. Chen, G., Song, Z., Qi, Z. & Sundmacher, K. Generalizing property prediction of ionic liquids from limited labeled data: a one-stop framework empowered by transfer learning. *Digit. Discov.* **2**, 591–601 (2023).
65. Bloom, I. et al. Differential voltage analyses of high-power, lithium-ion cells: 1. Technique and application. *J. Power Sources* **139**, 295–303 (2005).
66. Niu, Z., Zhong, G. & Yu, H. A review on the attention mechanism of deep learning. *Neurocomputing* **452**, 48–62 (2021).
67. Ross, J. et al. Large-scale chemical language representations capture molecular structure and properties. *Nat. Mach. Intell.* **4**, 1256–1264 (2022).
68. Xu, C., Wang, Y. & Barati Farimani, A. Transpolymer: a transformer-based language model for polymer property predictions. *npj Comput. Mater.* **9**, 64 (2023).
69. Wang, Y. et al. Probabilistic individual load forecasting using pinball loss guided lstm. *Appl. Energy* **235**, 10–20 (2019).
70. Liu, B., Nowotarski, J., Hong, T. & Weron, R. Probabilistic load forecasting via quantile regression averaging on sister forecasts. *IEEE Trans. Smart Grid* **8**, 730–737 (2015).
71. Prechelt, L. Early stopping—but when? In *Neural Networks: Tricks of the Trade: Second Edition*, 53–67 (2012).
72. Bergstra, J., Bardenet, R., Bengio, Y. & Kégl, B. Algorithms for hyperparameter optimization. *Adv. Neural Inf. Process Syst.* **24** (2011).

#### Acknowledgements

This work contributes to TUM.Battery, the Munich Data Science Institute, and the Munich Institute for Robotic and Machine Intelligence. This work contributes to the research performed at CELEST (Center for Electrochemical Energy Storage Ulm-Karlsruhe) and was partly funded by the German Research Foundation (DFG) under Project ID 390874152 (POLiS Cluster of Excellence). This project also received funding from the European Union's Horizon 2020 research and innovation program under grant agreement No. 957189 (BIG-MAP). The project is part of BATTERY 2030+, the large-scale European research initiative for inventing sustainable batteries for the future, funded by the European Union's Horizon 2020 research

<https://doi.org/10.1038/s41524-024-01286-7>

Article

and innovation program under Grant Agreement No. 957213. HSS acknowledges funding from the German Research Foundation (DFG) under Project ID 390776260 (eConversion Cluster of Excellence).

#### Author contributions

K.M. and B.B. provided the comprehensive BASF dataset, and L.M. and L.N. conducted all cycling data for Li-ion and Na-ion batteries at KIT/IPC, respectively. Data assembly, data cleaning, model idea including the design architecture, code implementation, repository curation, training, evaluation, and package creation is conducted by F.R. R.L. and D.L. supervised the model development. K.M., B.B., H.S., R.L. and D.L. supervised this research. All authors reviewed the paper.

#### Funding

Open Access funding enabled and organized by Projekt DEAL.

#### Competing interests

The authors declare no competing interests.

#### Additional information

**Supplementary information** The online version contains supplementary material available at <https://doi.org/10.1038/s41524-024-01286-7>.

**Correspondence** and requests for materials should be addressed to Fuzhan Rahmanian or Helge Sören Stein.

**Reprints and permissions information** is available at

<http://www.nature.com/reprints>

**Publisher's note** Springer Nature remains neutral with regard to jurisdictional claims in published maps and institutional affiliations.

**Open Access** This article is licensed under a Creative Commons Attribution 4.0 International License, which permits use, sharing, adaptation, distribution and reproduction in any medium or format, as long as you give appropriate credit to the original author(s) and the source, provide a link to the Creative Commons licence, and indicate if changes were made. The images or other third party material in this article are included in the article's Creative Commons licence, unless indicated otherwise in a credit line to the material. If material is not included in the article's Creative Commons licence and your intended use is not permitted by statutory regulation or exceeds the permitted use, you will need to obtain permission directly from the copyright holder. To view a copy of this licence, visit <http://creativecommons.org/licenses/by/4.0/>.

© The Author(s) 2024



### 4.4.3. Supporting Information

#### Attention towards chemistry agnostic and explainable battery lifetime prediction

Fuzhan Rahmanian<sup>1,2,4,5,6\*</sup>, Robert M. Lee<sup>3</sup>, Dominik Linzner<sup>3</sup>, Kathrin Michel<sup>3</sup>, Leon Merker<sup>1,2</sup>, Balazs B. Berkes<sup>3</sup>, Leah Nuss<sup>1,4,5,6</sup>, and Helge Sören Stein<sup>4,5,6\*</sup>

<sup>1</sup>Helmholtz Institute Ulm, Applied Electrochemistry, Helmholtzstr. 11, 89081 Ulm, Germany

<sup>2</sup>Karlsruhe Institute of Technology, Institute of Physical Chemistry, Fritz-Haber-Weg 2, 76131 Karlsruhe, Germany

<sup>3</sup>BASF SE, Ludwigshafen, Germany

<sup>4</sup>Technische Universität München, School of Natural Sciences, Department of Chemistry Lichtenbergstr 4, 85748 Garching, Germany

<sup>5</sup>Technische Universität München, Munich Data Science Institute, Walther-von-Dyck-Straße 10, 4, 85748 Garching, Germany

<sup>6</sup>Technische Universität München, Munich Institute for Robotic and Machine Intelligence, Georg-Brauchle-Ring 60-62, 80992 Munich, Germany

\*corresponding author(s): Helge Sören Stein (helge.stein@tum.de), Fuzhan Rahmanian (fuzhan.rahmanian@tum.de)

## Supplementary Information

### 1 Multisource Battery Cycling Protocols

In this section, a detailed description of the data is provided, along with their cycling protocols collected at various locations.

#### Toyota Research Institute

In a joint venture with MIT and Stanford<sup>1,2</sup>, the Toyota Research Institute (TRI) has made available two substantial high-throughput cycling datasets<sup>3,4</sup>, which form an integral part of our study. The initial dataset encompasses data from 124 commercial lithium iron phosphate (LFP)/graphite cells manufactured by A123 Systems (APR18650M1A), each with a nominal capacity of 1.1 Ah. The cells were cycled under a diverse array of fast charging protocols, ranging from single-step to dual-step policies, within a temperature-controlled environment maintained at 30 °C. The objective was to investigate the impact of varied charging protocols on the lifespan of the cells from 150 to 2300 cycles. The charging protocol, 'C1(Q1)-C2', involves two constant-current steps, C1 and C2, with a transition at a State of Charge (SOC) Q1. Following the second stage at 80% SOC, cells proceeded to charge at a 1 C constant current-constant voltage (CC-CV) rate within the 3.6 V and 2.0 V boundaries. The cells were consistently discharged at 4 C. The datasets, segmented into three batches, included a broad spectrum of measurements. The first two batches featured non-calendar aged batteries, while the third included calendar-aged ones, exhibiting significant capacity degradation over time.

In another relevant study, Attia et al. (2020)<sup>2</sup>, compiled a second dataset comprising 233 cells, with an emphasis on improving fast charging protocols. The dataset, segmented into five sequential batches, began with the first batch of cells, each assigned one of 224 distinct six-step charging protocols at random. After undergoing 100 cycles, an end of life (EOL) prediction model, based on initial data, guided the selection of charging protocols for the next batch. This iterative process was repeated

for the first four batches. The final batch was subjected to extended testing until EOL, providing a comparative analysis of various charging protocols. The discharge was carried out following a CC-CV profile at a 4 C rate to 2 V. Despite the absence of internal resistance (IR), efforts have been made by Strange et al.<sup>5</sup> and Ibraheem et al.<sup>6</sup> to recover these data and assemble them with the original study. The IR has been predicted using a Convolutional Neural Network (CNN) model trained on the initial work by Severson et al.<sup>1</sup>. Strange et al.<sup>5</sup> indicated that the predicted internal resistance drops that exceeded the EOL of the training set were unreliable and showed a high uncertainty. The predicted IR can be accessed online<sup>7</sup>.

#### Karlsruhe Institute of Technology

The Karlsruhe Institute of Technology (KIT) has contributed six distinct categories of cycling data, sourced from two of its departments; The Institute of Applied Materials (IAM) and the Institute of Physical Chemistry (IPC).

In a comprehensive study conducted by IAM, three commercial 18650-type lithium-ion batteries, namely NCA, NCM, and NCM + NCA, were cycled<sup>8</sup>. The cycling occurred within a temperature-controlled chamber at  $25 \pm 0.2$  °C,  $35 \pm 0.2$  °C, and  $45 \pm 0.2$  °C. The charging protocol involved constant current (CC) with rates ranging from 0.25 C to 1 C, then transitioning to constant voltage (CV) at 4.2 V until the current reached 0.05. Discharge was treated as residual capacity during cycling, with a relaxation time of 30 minutes for NCA and NCM batteries and 60 minutes for NCM + NCA batteries. This dataset initially was intended to improve the understanding of the reliable and safe operation of lithium-ion (Li-ion) batteries<sup>9</sup>.

The contribution of IPC is marked by a series of studies involving various types of coin cells, all automatically assembled using the AUTOBASS system<sup>10</sup>. A subset of the research focuses on 43 LNO coins<sup>11</sup> with cathode sheets of LNO and anode sheets of Si-C, supplied by BASF and CIDETEC, respectively. These cells were subjected to a standard cycling procedure that involved charging at a CC of 1 C until reaching 4.2 V, followed by a CV until the current dropped to 0.23 mA and discharged at a CC of 1 C.

Furthermore, commercial coin cells were introduced utilizing Lithium Cobalt Oxide (LCO) material<sup>12</sup>. With a nominal capacity of 45 mA h, these cells were charged by a CC-CV protocol of 1 C until 4.25 V, and discharged similarly until 2.75 V. Additionally, they also included an examination of NMC622/graphite cells<sup>13</sup> with a nominal capacity of 3.28 mA h, provided by the ZSW institute. The charging procedure followed a CC-CV protocol at 1 C and 4.2 V with a cutoff of 0.164 mA, and discharge was at 1 C until 2.9 V.

Finally, KIT included self-made Na-ion cells<sup>14</sup>, with a calculated nominal capacity of 0.15 mA h. These cells were characterized by the utilization of synthesized cathode material and hard carbon as anode, complemented by a glass fiber separator and a 1M NaPF<sub>6</sub> and EC: EMC 3: 7 electrolyte with 2 wt% FEC. The charging and discharging protocols remained at aCC of 1 C. Furthermore, C-rate testing was conducted, covering CC for charge and discharge at various rates, including C/20, C/10, C/5, C/2, 1 C, 2 C, and 5 C. Despite the inherently short lifetime of these cells, their inclusion provided valuable insights. In summary, the coins, composed of various materials and subjected to different charging and discharging protocols, contribute to a dataset of considerable diversity. Here, some tests are characterized by elevated noise levels, owing to factors such as temperature fluctuations, environmental shifts, or inherent instability leading to test failures; these have been retained for their potential to enrich the model's predictive performance.

#### Advanced Life Cycle Engineering

The research carried out by the Center for Advanced Life Cycle Engineering (CALCE)<sup>15</sup> has provided significant insights into the health prognostics of Li-ion batteries<sup>16,17</sup>, with a particular focus on two distinct groups, CS2 and CX2<sup>18</sup>. These groups consist of prismatic cells, each with LCO as the defining cell chemistry. In the scope of this study, a total of six CS2 cells and six CX2 cells of types 1 and 2, respectively, were chosen. The CS2 group, with a nominal capacity of 1.1 A h, were subjected to cycling at a room temperature of 23 °C following a CC-CV protocol. This phase was carried out at a 0.5 C rate, continuing until a voltage 4.2 V was attained, and subsequently maintained, until the current fell below 0.05A, with the discharge process ceasing at 2.7 V. The CX2 group, which has a nominal capacity of 1.35 A h followed an identical procedure. The discharge protocols for both groups were conducted at two distinct C-rates, namely 0.5 C and 1 C. All tests were carried out using the Arbin Battery Tester<sup>15</sup>.

### NASA Prognostics Center of Excellence

Saha et al.<sup>19</sup>, explored the behavior of 34 commercial 18650 Li-ion cells with a 2 Ah capacity, tailored for small aircraft and satellite applications<sup>20</sup>, as detailed in the NASA Prognostics Center of Excellence (PCoE) dataset<sup>19,21</sup>. Here, the charging processes were identical, using a CC of 1.5 A until 4.2 V, then a CV applied until the current reached 10 . During discharge cycles, a subset of batteries was subjected to constant current levels of 1 A, 2 A and 4 A, and the process was stopped at specific voltages among different test cells, including 2.0 V, 2.2 V, 2.5 V, and 2.7 V. Cells were cycled to 70% or 80% of their initial capacity in various temperatures of 4 °C, 24 °C, and 43 °C. Additionally, electrochemical impedance spectroscopy (EIS) was performed using a frequency sweep from 0.1 Hz to 5 kHz. This procedure facilitates understanding of Li-ion cell degradation under various operational conditions<sup>21</sup>.

### Hawaii Natural Energy Institute

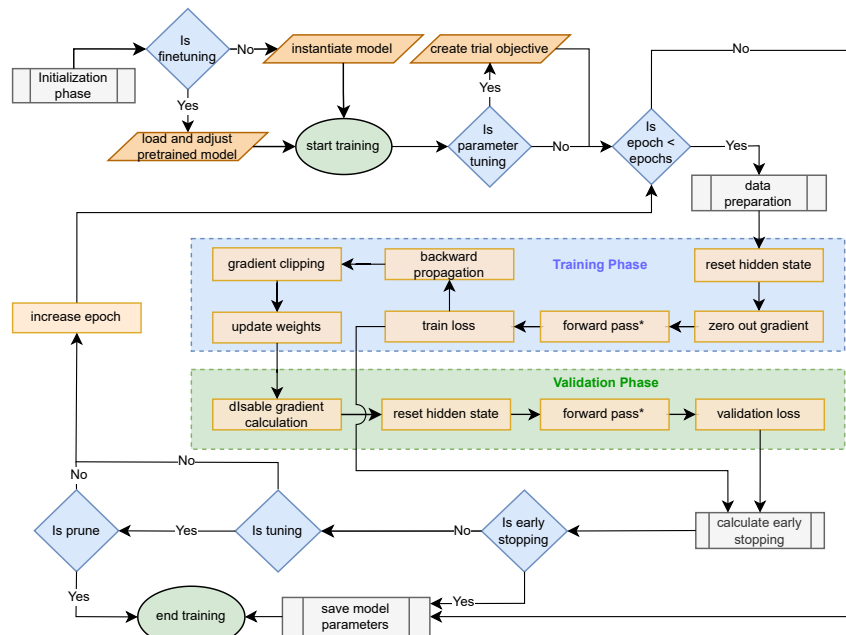
The Hawaii Natural Energy Institute (HNEI) dataset<sup>22</sup>, available for download from the Battery Archive<sup>23</sup>, includes an analytical study of 14 commercial 18650 Li-ion cells, manufactured under the model "ICR18650 C2" by LG Chemical Limited. These cells, designed for the use of PC notebooks, feature a graphite negative electrode and a composite positive electrode containing LCO and NMC. The cell's calculated energy density is approximately 208 Whkg<sup>-1</sup>, and has a nominal capacity of 2.8 Ah. The charging process was carried out with a CC-CV protocol at a rate of C/2, with a cutoff voltage of 4.3 V, accompanied by a 50 mA cutoff current. The discharge process was conducted at a 1.5 C rate to a full Depth of Discharge (DoD), with a cutoff voltage of 3 V. The study spanned over 1000 cycles at room temperature and was aimed at understanding the effects of inherent variations between cells on their aging process<sup>22</sup>.

### Sandia National Laboratories

The Sandia National Laboratories (SNL) dataset<sup>24</sup> encompasses data from 77 commercial 18650 cells, including chemistries of LFP, NCA, and NMC, cycled between 388 – 19,174 ranges. Available on the Battery Archive website<sup>23</sup>, the study aimed to evaluate the effects of temperature at 15 °C, 25 °C, and 35 °C, as well as DoD at 0 – 100%, 20 – 80%, and 40 – 50%, and discharge current at 0.5 C, 1 C, 2 C, and 3 C on long-term degradation. The charge/discharge protocol began with thermal equilibration, followed by a discharge. The cells were charged at a consistent rate of 0.5 C, continuing the cycling process until they reached State of Health (SOH) of 80%. An exception was made for NCA cells, where a 3 C discharge was applied instead. The SNL dataset offers valuable insights into the behavior of different battery chemistries under varied conditions,<sup>24</sup>.

## 2 Training Procedure

The steps outlined in the training procedure in the Attention-based ReCurrent Algorithm for Neural Analysis with LSTM (ARCANA) architecture can be seen in Supplementary Figure 1.



Supplementary Figure 1: Illustration of the sequence-to-sequence (Seq-to-Seq) model training in the ARCANA workflow, outlining data loader initialization, parameter configuration, and model hyperparameter tuning. Additionally, the configuration allows for specifying whether the model will initiate training from scratch, be instantiated for baseline learning, or follow a fine-tuning procedure. In the latter, a pre-trained model is loaded, and only selected layers are subject to gradient updates, while the remaining layers are kept frozen to maintain pre-learned features. After this stage, the training procedure will be initiated. The process details the epoch-based training with hidden state resets, gradient zeroing, pinball loss computation for quantile accuracy, the use of masking to maintain loss metric fidelity and gradient clipping. The figure also includes the adaptive learning rate adjustments and validation phase with early stopping and the Optuna-driven pruning strategy. In the final stage, all the model parameters will be saved, and a detailed training report will be generated.  
 \*The details of the forward pass are comprehensively described in Figure 2 of the main Manuscript.

### 3 Model $M(P)$ Performance

For training  $M(P)$ , the model parameters, architecture components, and their descriptions are detailed in Table 1. The configurations include input and output sizes, hidden layer dimensionality, batch sizes, sequence window lengths, and the teacher forcing strategy, which specifies the start and end ratios and the decay step for gradual adjustment. Encoder- and decoder-specific parameters such as dropout rates, number of layers, and attention heads are also enumerated. It is important to note that all models utilize a consistent training strategy, incorporating early stopping criteria based on a combination of generalization-loss-to-progress-quotient-ratio (GL/PQ) and error-trend evaluation, alongside a learning rate scheduler using the one-cycle policy for optimal convergence. Additionally, an activation layer using Leaky ReLU with a negative slope of 0.01 is integrated into the decoder architecture in all model configurations to add non-linearity and learning capacity. The hyperparameters, optimized over 250 Optuna trials, consist of a learning rate of 0.0223, 370 epochs, a decay rate of 0.3, and an output dropout of 0.1 (Supplementary Figure 2). The performance of training and validation over the epochs, along with the one-cycle learning rate scheduler, is depicted in Supplementary Figure 3.

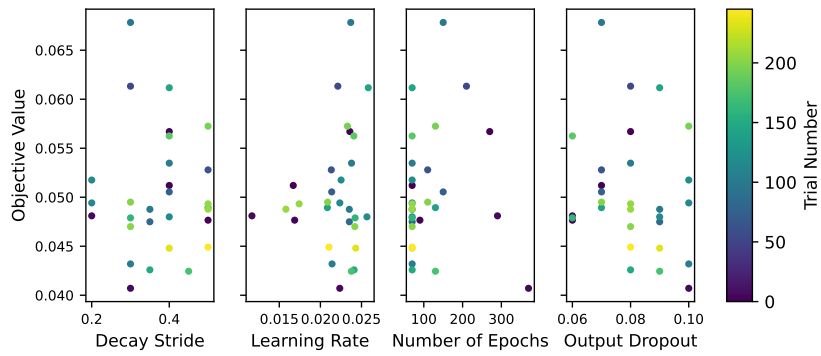
Supplementary Table 1: Summary of the model parameters and configurations, including their names, descriptions, involved components, types, and values for the architecture and the training strategy.

Variable Name	Parameter Name	Description	Relevant Component	Parameter Type	Model: $M(P)$
input_size	Input Size	Size of the input data	Model Architecture	Architecture Parameter	6
output_size	Output Size	Size of the model output		Architecture Parameter	3
hidden_dim	Hidden Layer Dimension	Dimensionality of hidden layers		Architecture Parameter	32
batch_size	Batch Size	Number of selected samples	Training Strategy	Hyperparameter	32
window_length	Sequence Window Length	Length of the input sequence for the Seq-to-Seq architecture	Seq-to-Seq	Architecture Parameter	5
warmup_steps	Warmup Steps	Number of steps of initial training phase to stabilize the model		Training Strategy	3
weight_decay	Weight Decay	Regularization parameter to prevent overfitting by penalizing large weights	Optimizer	Hyperparameter	1e-8
tl_start_ratio	Teacher Forcing Start Ratio	Starting ratio of teacher forcing in training	Teacher Forcing	Training Strategy	0.55
tl_end_ratio	Teacher Forcing End Ratio	Final ratio of teacher forcing, indicating when to decay the use of true data		Training Strategy	0.001
decay_stride	Teacher Forcing Decay Stride	Defines the rate and segments of teacher forcing ratio decay throughout training epochs		Training Strategy	0.3
bidirectional	Bidirectional Encoding	Indicates if the encoder processes data in both forward and backward directions	Encoder	Architecture Parameter	false
dropout_encoder	Encoder Dropout Rate	Dropout rate for layers within the encoder to prevent overfitting		Hyperparameter	0.2
num_layers_encoder	Encoder Layer Count	Number of layers in the encoder		Architecture Parameter	1
nhead_encoder	Encoder Attention Heads	Number of heads in the multi-head attention mechanism of the encoder		Architecture Parameter	8
dropout_decoder	Decoder Dropout Rate	Dropout rate for layers within the decoder to prevent overfitting	Decoder	Hyperparameter	0.15
num_layers_decoder	Decoder Layer Count	Number of layers in the decoder		Architecture Parameter	1
nhead_decoder	Decoder Attention Heads	Number of heads in the multi-head attention mechanism of the decoder		Architecture Parameter	4
output_dropout	Output Layer Dropout Rate	Dropout rate for the fully connected layer to prevent overfitting		Hyperparameter	0.1

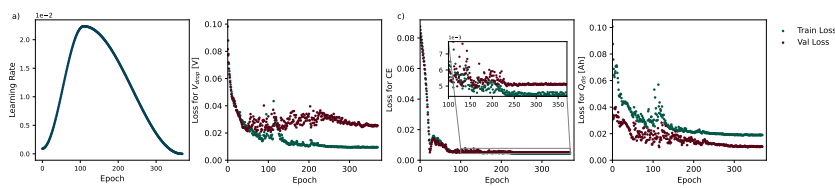
Supplementary Table 2: Summary of the evaluation metrics for  $M(P)$ , tested on nine unseen cylindrical cells ( $D_{NMC+NCA}$ ) and six unseen prismatic cells ( $D_{LCO}$ ), using 24 and 22 initial cycles of historical data\*, respectively, to predict the cell behavior up to the 500th cycle. Comparative studies by Roman et al.<sup>25</sup> and Tian et al.<sup>26</sup> using similar CALCE datasets report MAPE values ranging from 2 to 4.65. The evaluation by Zhang et al.<sup>27</sup> on a subset of the  $D_{NMC+NCA}$  shows a MAPE of less than 10. It is important to note that these comparisons are indirect, as the model provides multidimensional predictions on different data splits.

Metrics	$D_{NMC+NCA}$			$D_{LCO}$		
	Voltage drop [V]	CE	$Q_{dis}$ [Ah]	Voltage drop [V]	CE	$Q_{dis}$ [Ah]
<b>RMSE</b>	0.0566	0.0256	0.1009	0.0335	0.0300	0.0709
<b>MAPE</b>	12.4294	0.2489	2.9455	6.6052	0.9207	4.0527
<b>MAE</b>	0.0378	0.0029	0.0659	0.0258	0.0085	0.0484
<b>medAE</b>	0.0218	0.0009	0.0448	0.0213	0.0061	0.0289

\*The number of initial cycles was chosen randomly to resemble practical scenarios with limited initial data. The user can specify any preferred number of initial cycles in the provided configuration file, which is detailed at <https://github.com/basf/ARCANA/blob/master/config/>

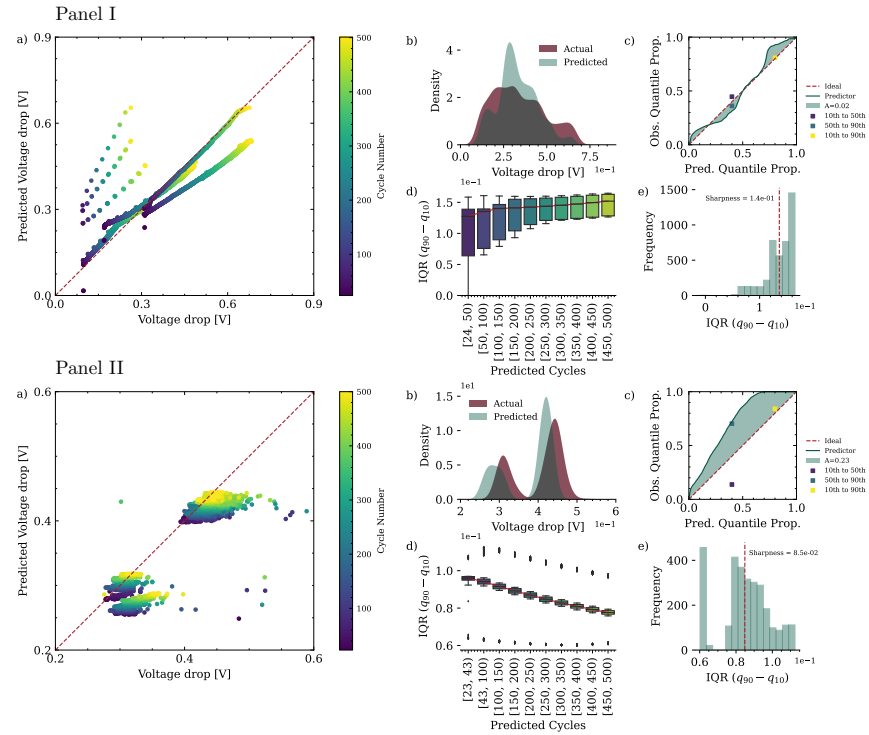


Supplementary Figure 2: Graphical representation of hyperparameter optimization using Optuna<sup>28</sup>; this slice plot delineates the multidimensional search space explored during the optimization process for Model  $M(P)$ . Each axis represents a distinct hyperparameter, illustrating the range of values explored.



Supplementary Figure 3: Model training and performance analysis for  $M(p)$ : a) Learning rate dynamics, which shows the adaptive adjustment of learning rates over epochs using a one-cycle scheduler, b) Loss trends for tracing training and validation loss during voltage drop c) Coulomb efficiency, and d) Discharge capacity.

#### 4 Comparison of $M(P)$ performance for $D_{NMC+NCA}$ and $D_{LCO}$

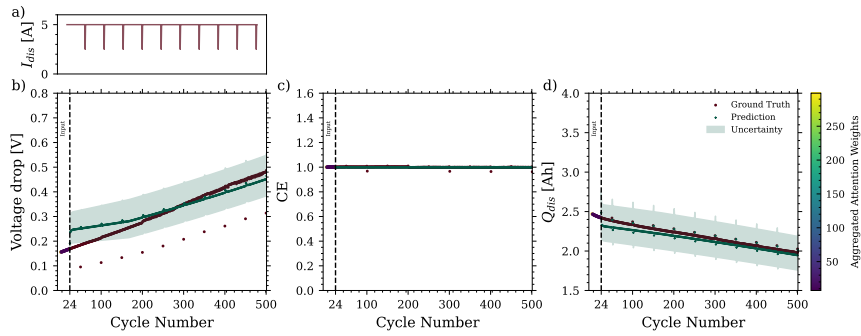


Supplementary Figure 4: Predictive accuracy and calibration of model  $M(P)$  for voltage drop across  $D_{NMC+NCA}$  (Panel I) and  $D_{LCO}$  (Panel II). a) Scatter plot shows close alignment of predicted versus actual values, with color gradients representing the cycle increment. The density plots in b) represent the model's predictive distribution against actual measurements. The calibration curve in c) assumes a normal distribution, where the mean and standard deviation are estimated from the 10th, 50th, and 90th percentile predictions. It depicts the proportion of values that fall within the predicted intervals defined by these quantiles, with the ideal diagonal line representing perfect calibration. The shaded area indicates the degree of miscalibration, denoted as  $A$ . Additionally, the points in this plot illustrate the observed proportions of actual values that fall within three specific intervals based on the quantiles: between the 10th and 50th, 50th and 90th, and 10th and 90th percentiles; the shaded area indicates the degree of miscalibration noted as  $A$ . Box plots d) illustrate narrow prediction intervals for  $D_{NMC+NCA}$  over cycles and a decreasing median for  $D_{LCO}$ . Histograms in e) provide the quantiles as the width of the prediction interval between the 10th and 90th percentiles as a measure of sharpness, revealing the skewness for both datasets and diversity for  $D_{LCO}$ . The red dashed line indicates the sharpness as the mean interval width and shows the concentration of the predictive distributions.

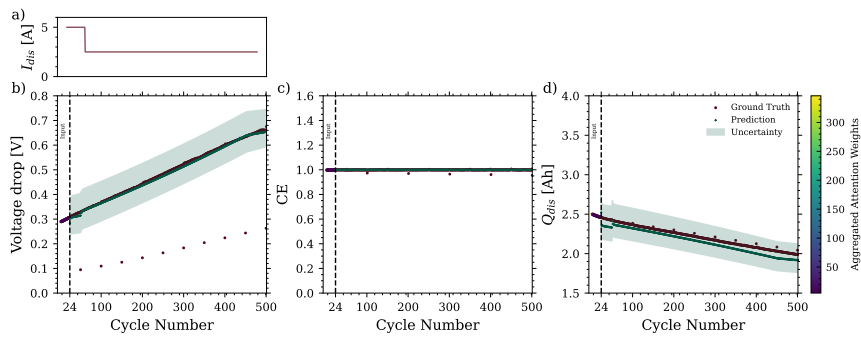
## 5 Evaluation on $D_{NMC+NCA}$

All analytical plots supporting the prediction of  $D_{NMC+NCA}$  using the pretrained  $M(P)$  can be seen here.

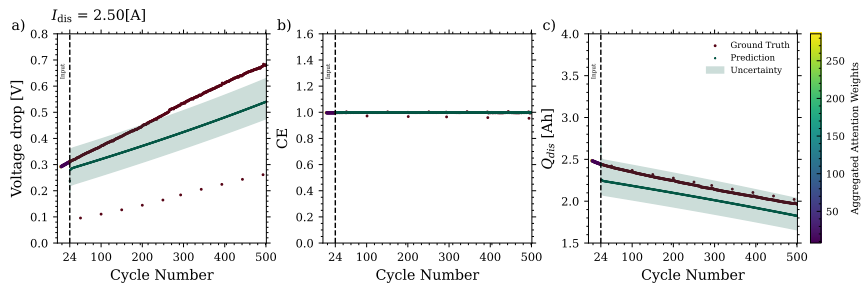
Panel I



Panel II

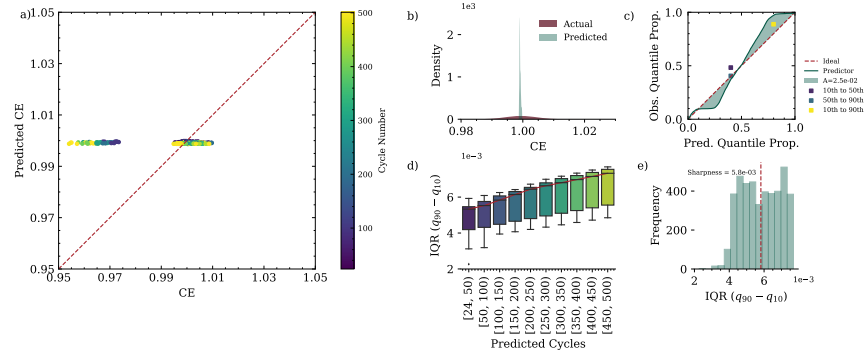


Panel III

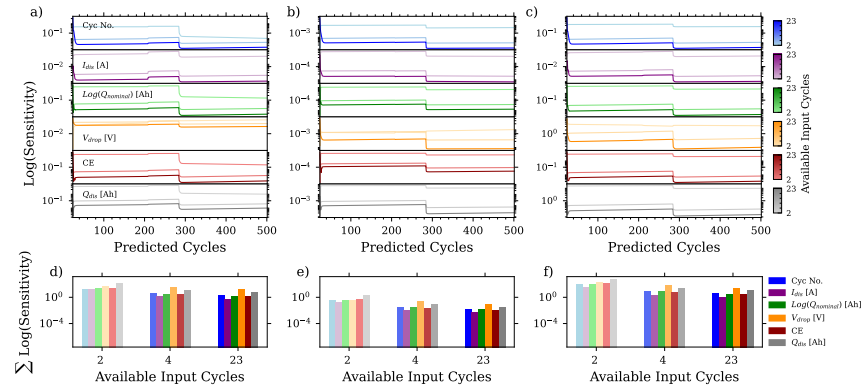


Supplementary Figure 5: Showcase of the predictive performance of  $M(P)$  for cylindrical  $D_{NMC+NCA}$  on three sample in Panel I, II and III to predict battery behavior over 500 cycles across different discharge current profile (plot a, Panel I and II) for three predictors (plots b-d, Panel I and plot a-c, Panel II): Voltage drop [V], CE and  $Q_{dis}$  [Ah].

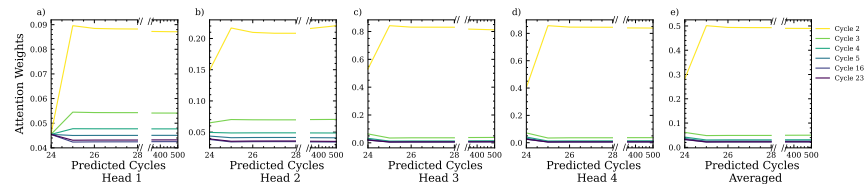




Supplementary Figure 6: Evaluation of  $M(P)$  prediction for Coulombic efficiency for  $D_{NMC+NCA}$ : a) shows the correlation between actual and predicted values with a representation of the cycle progression by color gradient, b) compares the density of actual and predicted values. The calibration curve in c) assumes a normal distribution, where the mean and standard deviation are estimated from the 10th, 50th, and 90th percentile predictions. It depicts the proportion of values that fall within the predicted intervals defined by these quantiles, with the ideal diagonal line representing perfect calibration. The shaded area indicates the degree of miscalibration, denoted as  $A$ . Additionally, the points in this plot illustrate the observed proportions of actual values that fall within three specific intervals based on the quantiles: between the 10th and 50th, 50th and 90th, and 10th and 90th percentiles. d) Illustrates the variability and central tendency of prediction intervals across cycles, e) provides a histogram of the quantiles as the prediction interval width between the 10th and 90th percentiles as a measure of sharpness. The dashed red line indicates sharpness as the mean interval width and shows the concentration of the predictive distributions.



Supplementary Figure 7: Comprehensive predictive performance and sensitivity assessment for  $M(P)$  on a selected sample from  $D_{NMC+NCA}$ . Plots a), b), and c) detail the model's sensitivity to each predictive cycle, represented on a logarithmic scale, demonstrating how input variations affect the output. Plots d), e), and f) aggregate the sensitivity data across all given cycles, providing an overview of the model's input responsiveness throughout the cycling process.

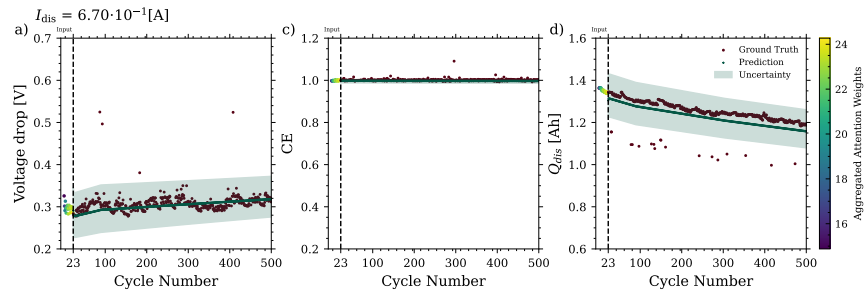


Supplementary Figure 8: Multi-head attention weight analysis of  $M(P)$  for a selected sample from  $D_{NMC+NCA}$ . The first four plots (a-d) represent the attention weights of separate heads for selected input cycles. The final plot (e) shows the average attention weights across all heads, providing an overview of the model's focus distribution throughout the prediction process. This composite view illustrates how the model prioritizes different cycles to optimize prediction accuracy.

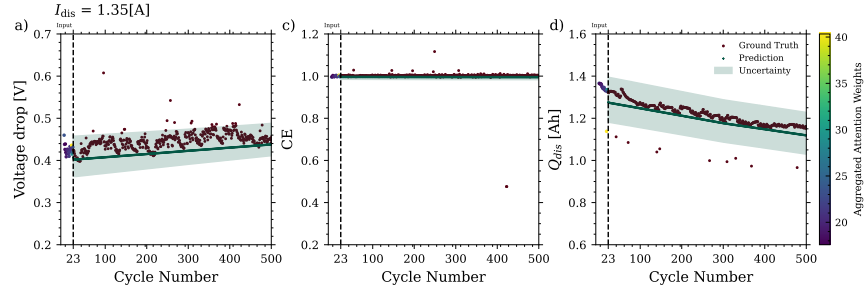
## 6 Evaluation of $D_{LCO}$

All analytical plots supporting the prediction of  $D_{LCO}$  using the pre-trained  $M(P)$  can be seen here.

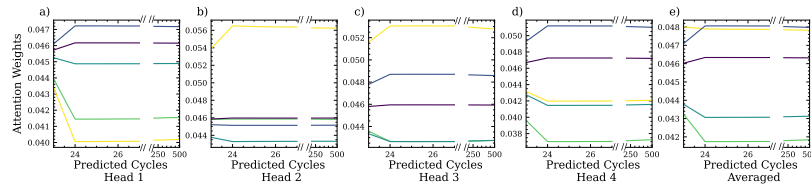
Panel I



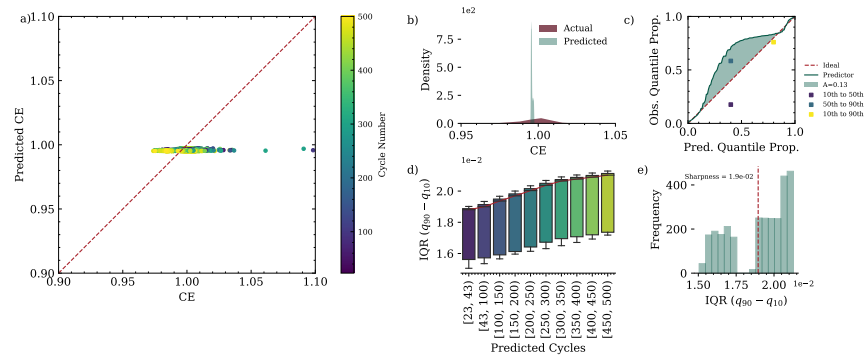
Panel II



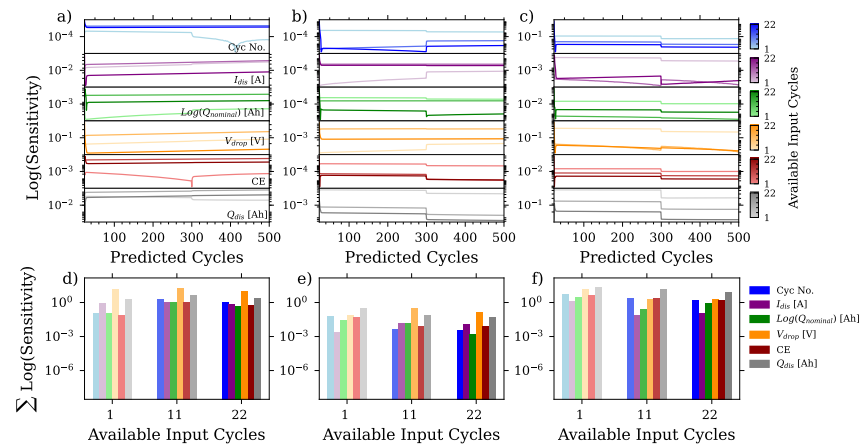
Supplementary Figure 9: Showcase of the predictive performance of  $M(P)$  for prismatic  $D_{LCO}$  on two samples in Panel I and II to predict battery behavior over 500 cycles for three predictors: Voltage drop [V], CE and  $Q_{dis}$  [Ah].



Supplementary Figure 10: Multi-head attention weight analysis of  $M(P)$  for a selected sample from  $D_{LCO}$ . The first four plots (a-d) represent the attention weights of separate heads for selected input cycles. The final plot (e) shows the average attention weights across all heads, providing an overview of the model's focus distribution throughout the prediction process. This composite view illustrates how the model prioritizes different cycles to optimize prediction accuracy.



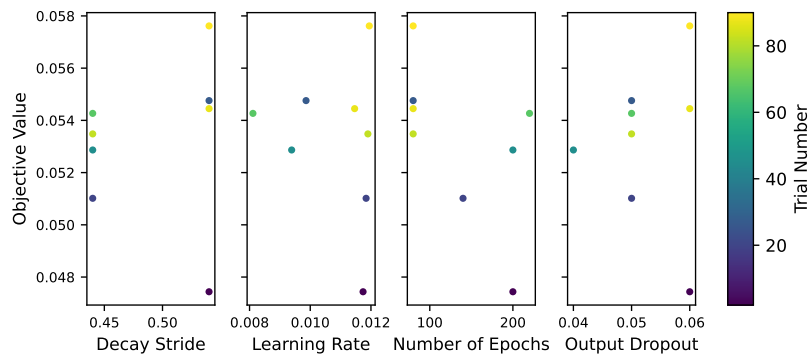
Supplementary Figure 11: Evaluation of  $M(P)$  prediction for Coulombic efficiency for  $DLCO$ : a) shows the correlation between actual and predicted values with a representation of the cycle progression by a color gradient, b) compares the density of actual and predicted values. The calibration curve in c) assumes a normal distribution, where the mean and standard deviation are estimated from the 10th, 50th, and 90th percentile predictions. It depicts the proportion of values that fall within the predicted intervals defined by these quantiles, with the ideal diagonal line representing perfect calibration. The shaded area indicates the degree of miscalibration, denoted as  $A$ . Additionally, the points in this plot illustrate the observed proportions of actual values that fall within three specific intervals based on the quantiles: between the 10th and 50th, 50th and 90th, and 10th and 90th percentiles, d) illustrates the variability and central tendency of prediction intervals across cycles. e) provides a histogram of the quantiles as the prediction interval width between the 10th and 90th percentiles as a measure of sharpness. The dashed red line indicates sharpness as the mean interval width and shows the concentration of the predictive distributions.



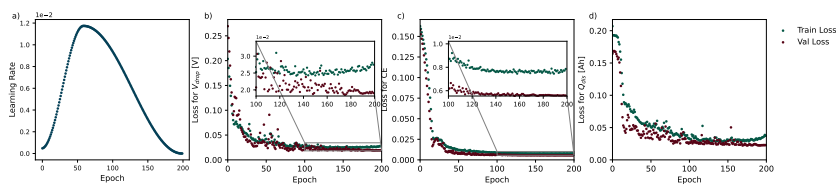
Supplementary Figure 12: Comprehensive predictive performance and sensitivity assessment for  $M(P)$  on a selected sample from  $DLCO$ . Plots a), b), and c) detail the model's sensitivity to each predictive cycle, represented on a logarithmic scale, demonstrating how input variations affect the output. Plot d), e), and f) aggregate the sensitivity data across all given cycles, providing an overview of the model's input responsiveness throughout the cycling process.

## 7 Model $M(P)_f$ Performance

Fine-tuning of  $M(P)$  for coin cells ( $M(P)_f$ ) is accomplished by loading the pre-trained model with all components initially frozen to preserve the model's foundational knowledge. For fine-tuning, the decoder layers are unfrozen; this includes the LSTM layers for capturing long-term dependencies across diverse degradation mechanisms of coin cells, the multi-head attention mechanism for identifying cycle-specific features and fully connected layers for mapping features from the LSTM and attention mechanism, to perform accurate lifetime predictions. During the fine-tuning, all the architecture parameters remain unchanged from the original configuration (Table 1), with the tuned hyperparameters selected from 85 trials through Optuna's hyperparameter optimization. These optimal settings include a learning rate of 0.0117, 200 epochs, a decay rate of 0.54, and an output dropout of 0.06 (Supplementary Figure 13). The fine-tuning process enabled the model to adjust its parameters and improve its predictive accuracy and reliability. Additionally, the training and validation performance associated with the one-cycle learning dynamics of the model over the epochs can be seen in Supplementary Figure 14.

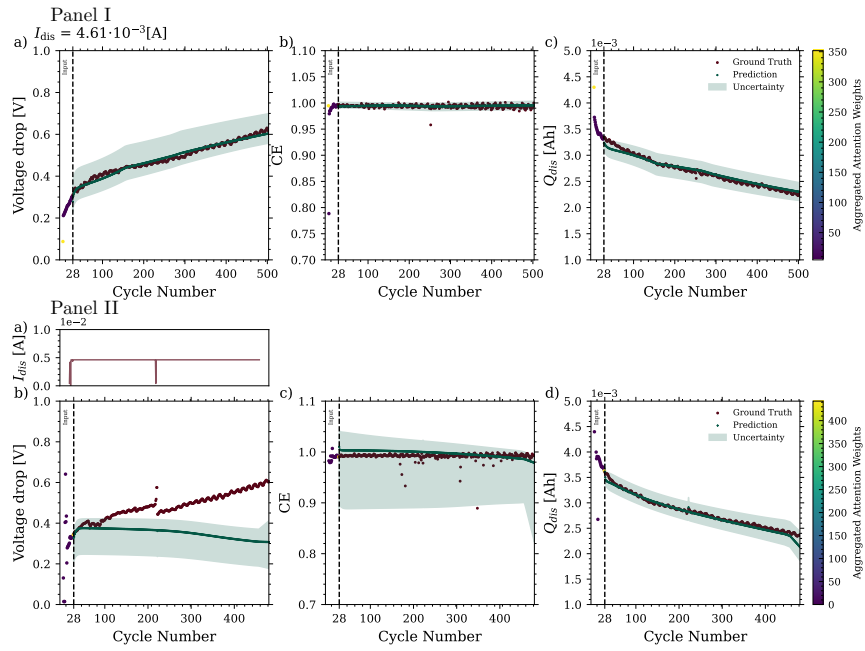


Supplementary Figure 13: Graphical representation of hyperparameter optimization using Optuna<sup>28</sup>; this slice plot delineates the multidimensional search space explored during the optimization process for Model  $M(P)_f$ . Each x-axis represents a distinct hyperparameter, illustrating the range of values explored.



Supplementary Figure 14: Comprehensive model training and performance analysis for  $M(p)_f$ : a) Learning rate dynamics, which shows the adaptive adjustment of learning rates over epochs using a one-cycle scheduler, b) loss trends for tracing training and validation loss during voltage drop, c) Coulomb efficiency, and d) Discharge capacity.

### 8 Performance comparison between $M(P)_f$ and $M(B)$

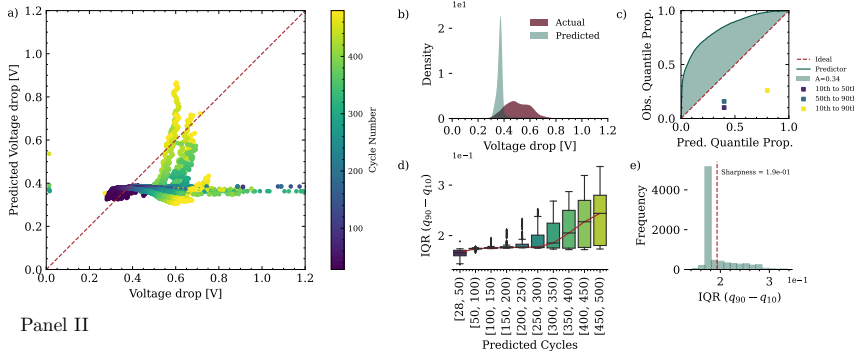


Supplementary Figure 15: Showcase the two model's predictive performances on coin data  $D_{LNO}$  from  $M(P)_f$  and  $M(B)$ . Panel I depicts the  $M(P)_f$  predictions, which closely match the actual measurements for a) voltage drop [V], b) CE and c)  $Q_{dis}$  [Ah], with a focused attention distribution on early cycle data. Panel II depicts the  $M(B)$ 's performance, indicating a responsive adjustment to mid-cycle protocol changes in  $Q_{dis}$  predictions, with attention weights shifted towards later cycles.

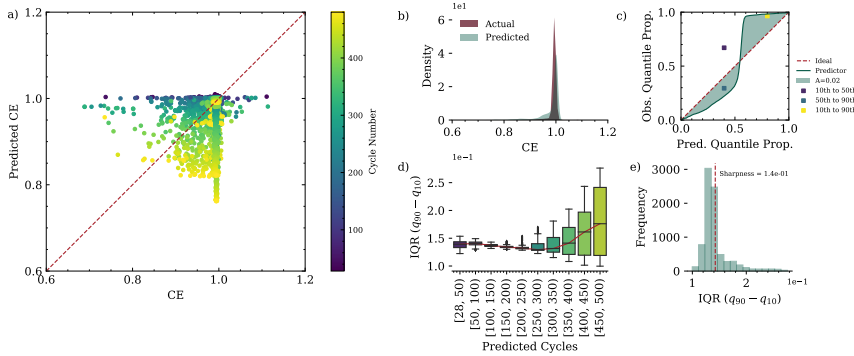
### 9 Evaluation of $D_{LNO}$

All the analytical plots supporting the prediction of  $D_{LNO}$  using the pretrained  $M(P)_f$  and  $M(B)$  can be seen here.

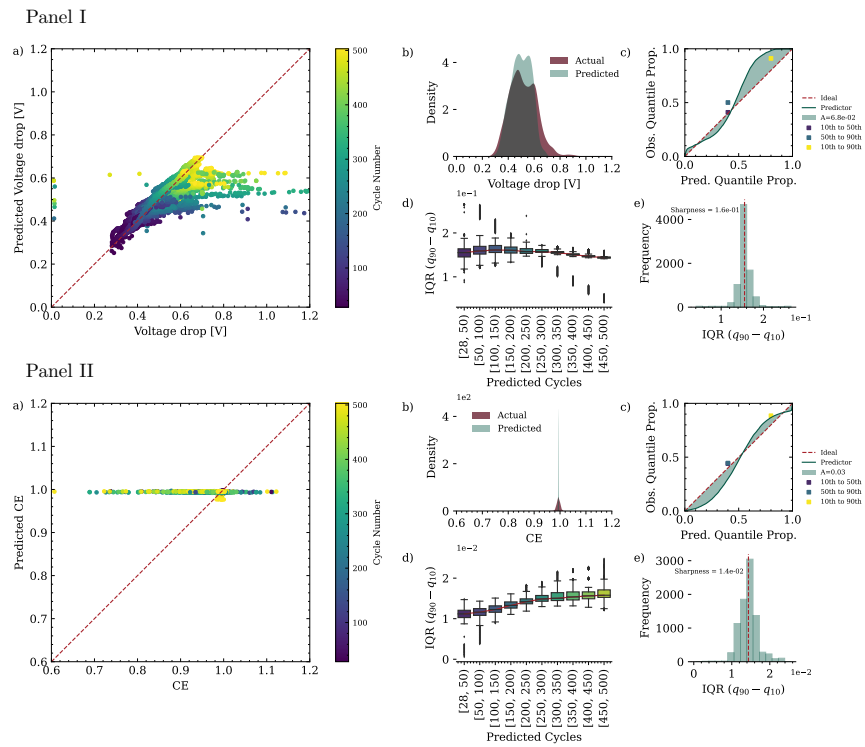
Panel I



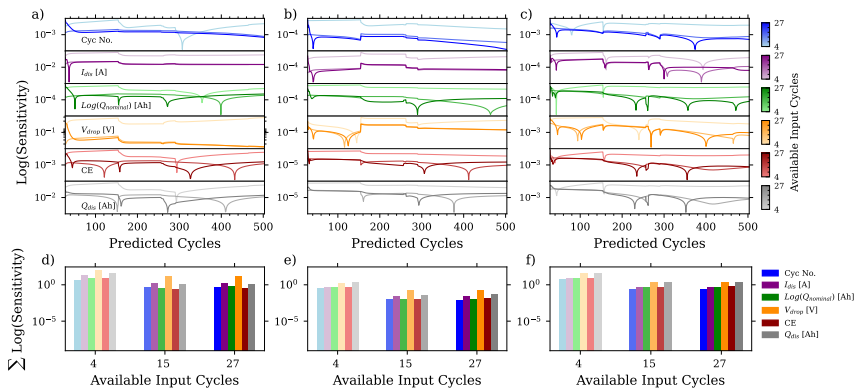
Panel II



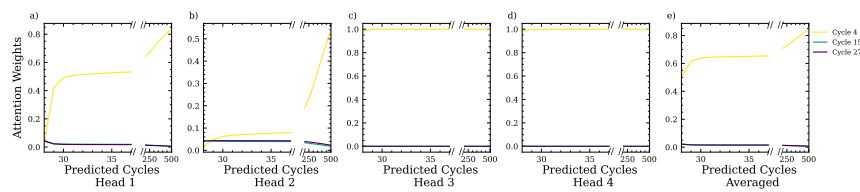
Supplementary Figure 16: Evaluation of  $M(B)$  prediction for Voltage drop (Panel I) and Coulombic efficiency (Panel II) for  $D_{LNO}$ . a) Shows the correlation between actual and predicted values with a representation of the cycle progression by a color gradient, b) compares the density of actual and predicted values. The calibration curves in c) assumes a normal distribution, where the mean and standard deviation are estimated from the 10th, 50th, and 90th percentile predictions. It depicts the proportion of values that fall within the predicted intervals defined by these quantiles, with the ideal diagonal line representing perfect calibration. The shaded area indicates the degree of miscalibration, denoted as  $A$ . Additionally, the points in this plot illustrate the observed proportions of actual values that fall within three specific intervals based on the quantiles: between the 10th and 50th, 50th and 90th, and 10th and 90th percentiles, d) illustrates the variability and central tendency of prediction intervals across cycles and e) provides a histogram of the quantiles as the prediction interval width between the 10th and 90th percentiles as a measure of sharpness. The dashed red line indicates sharpness as the mean interval width and shows the concentration of the predictive distributions.



Supplementary Figure 17: Evaluation of  $M(P)_f$  prediction for voltage drop (Panel I) and Coulombic efficiency (Panel II) for  $D_{LNO}$ . a) Shows the correlation between actual and predicted values with a representation of the cycle progression by a color gradient, b) compares the density of actual and predicted values. The calibration curves in c) assumes a normal distribution, where the mean and standard deviation are estimated from the 10th, 50th, and 90th percentile predictions. It depicts the proportion of values that fall within the predicted intervals defined by these quantiles, with the ideal diagonal line representing perfect calibration. The shaded area indicates the degree of miscalibration, denoted as  $A$ . Additionally, the points in this plot illustrate the observed proportions of actual values that fall within three specific intervals based on the quantiles: between the 10th and 50th, 50th and 90th, and 10th and 90th percentiles. d) illustrates the variability and central tendency of prediction intervals across cycles and e) provides a histogram of the quantiles as the prediction interval width between the 10th and 90th percentiles as a measure of sharpness. The dashed red line indicates sharpness as the mean interval width and shows the concentration of the predictive distributions.

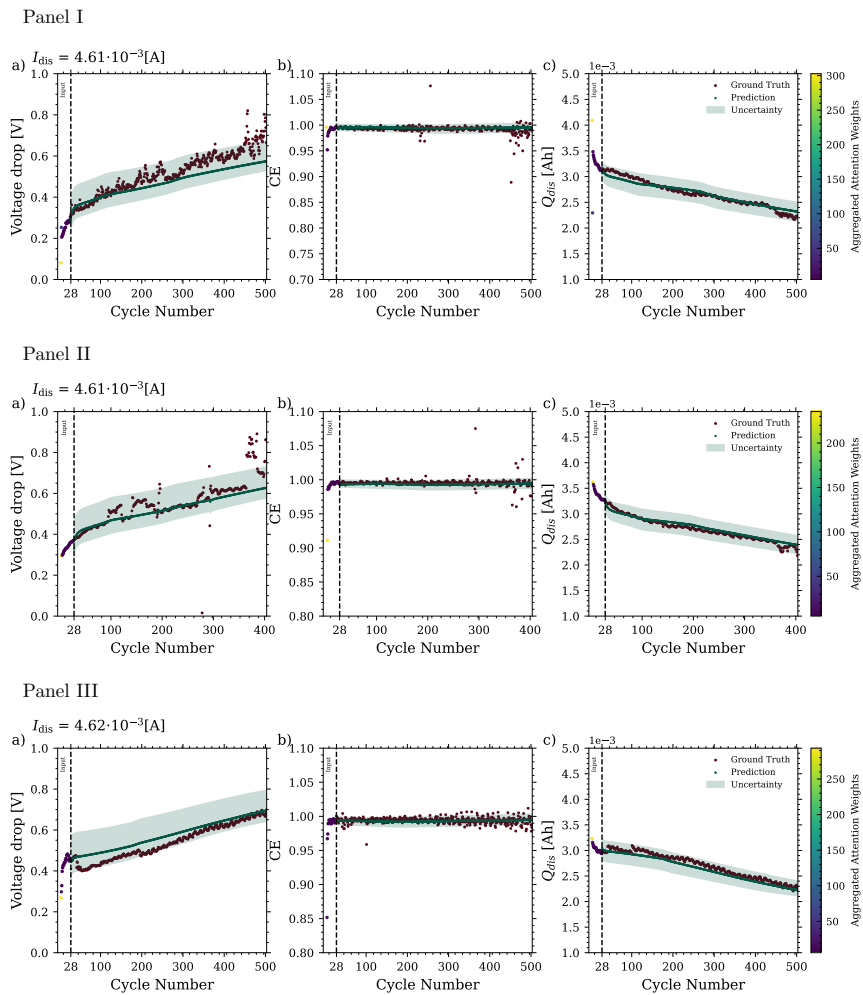


Supplementary Figure 18: Comprehensive predictive performance and sensitivity assessment for  $M(P)_I$  on a selected sample from  $DLNO$ . Plots a), b), and c) detail the model's sensitivity to each predictive cycle, represented on a logarithmic scale, demonstrating how input variations affect the output. Plot d), e), and f) aggregate the sensitivity data across all given cycles, providing an overview of the model's input responsiveness throughout the cycling process.



Supplementary Figure 19: Multi-head attention weight analysis of  $M(P)_I$  for a selected sample from  $DLNO$ . The first four plots (a-d) represent the attention weights from separate heads for selected input cycles. The final plot (e) shows the average attention weights across all heads, providing an overview of the model's focus distribution throughout the prediction process. This composite view illustrates how the model prioritizes different cycles to optimize prediction accuracy.





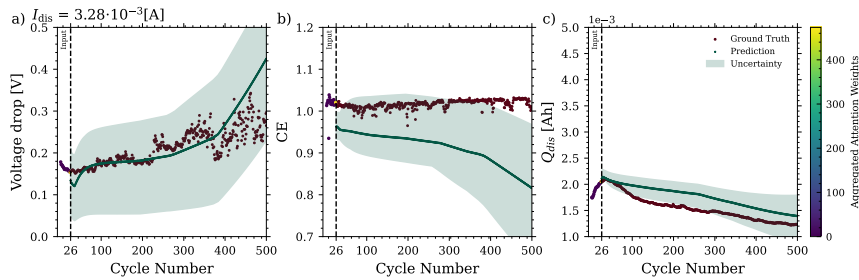
Supplementary Figure 20: Showcase the predictive performance of  $M(P)_f$  for coin  $D_{LNO}$  on three example samples in Panel I, II, III, to predict battery behavior over 500 cycles for three predictors of Voltage drop [V], Coulombic efficiency and  $Q_{dis}$  [Ah].

## 10 Evaluation of $D_{NMC}$

All the analytical plots and metrics supporting the prediction of  $D_{NMC}$  using  $M(P)_f$  and  $M(B)$  models can be seen here.

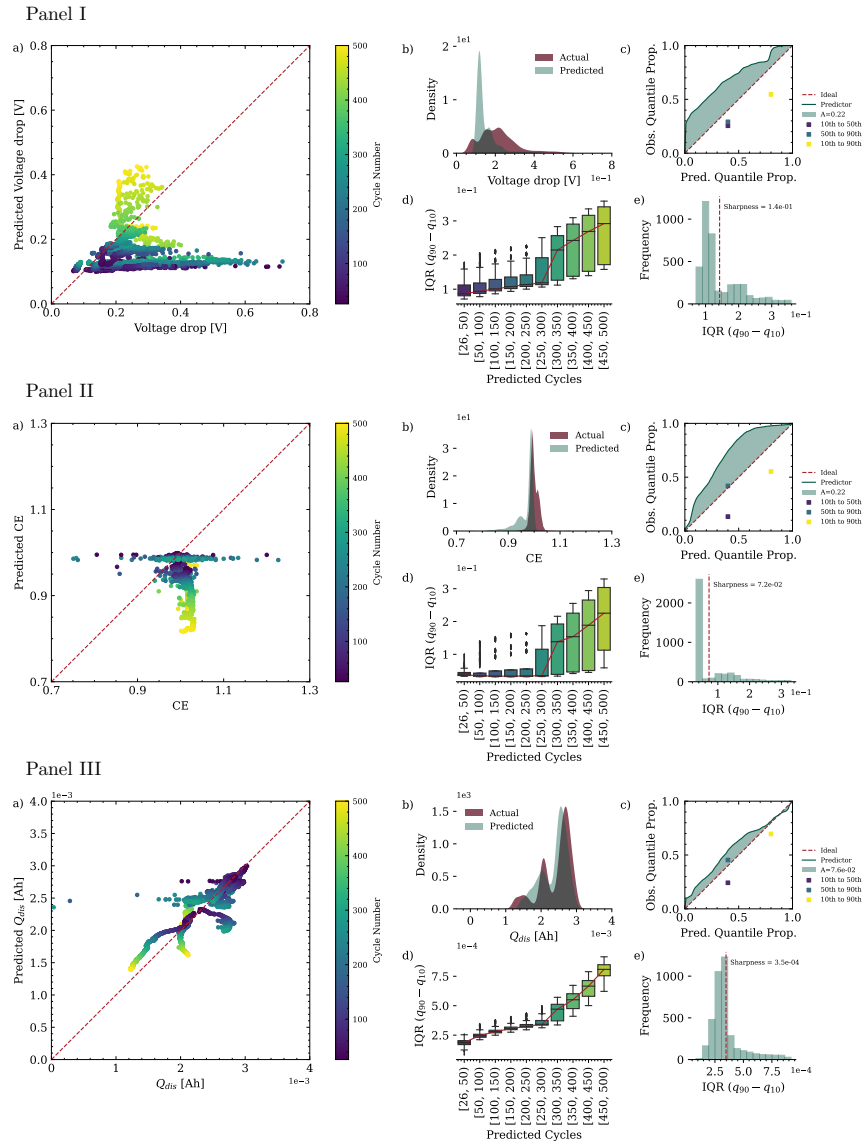
Supplementary Table 3: Summary of the evaluation metrics for  $M(P)_f$  and  $M(B)$ , tested on 11 unseen coin cells ( $D_{NMC}$ ), using 25 initial cycles of historical data\*, to predict the cell behavior up to the 500th cycle.

Metrics	$M(P)_f$			$M(B)$		
	Voltage drop [V]	CE	$Q_{dis}$ [Ah]	Voltage drop [V]	CE	$Q_{dis}$ [Ah]
<b>RMSE</b>	0.0697	0.0304	0.0002	0.1820	0.0524	0.0002
<b>MAPE</b>	19.2894	2.2022	9.5144	27.7655	2.8842	24.0902
<b>MAE</b>	0.0470	0.0103	0.0002	0.1448	0.0245	0.0002
<b>medAE</b>	0.0293	0.0060	0.0001	0.1240	0.0084	0.0001

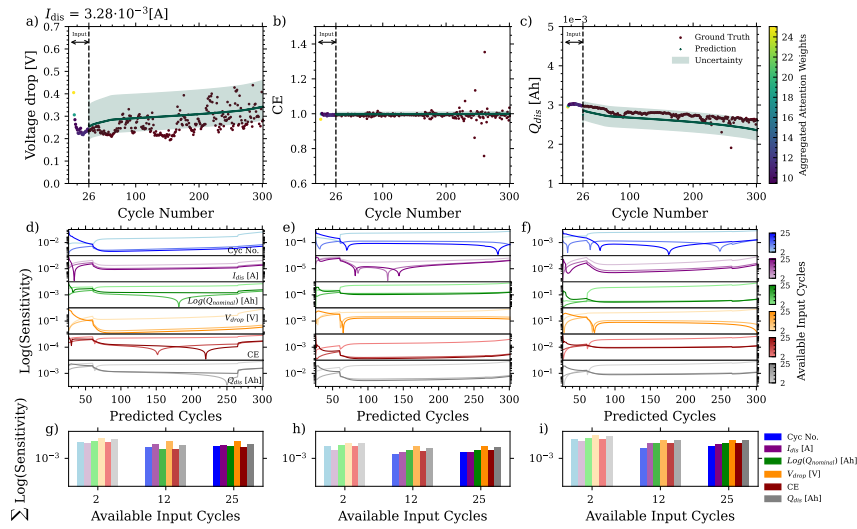


Supplementary Figure 21: Showcase the predictive performance of  $M(B)$  for coin  $D_{NMC}$  on an example sample to predict battery behavior over 500 cycles for three predictors of Voltage drop [V], Coulombic efficiency and  $Q_{dis}$  [Ah].

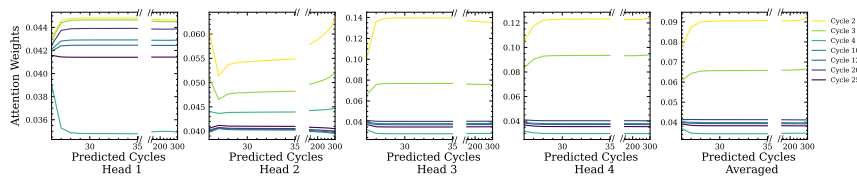
\*The number of initial cycles was chosen randomly to resemble practical scenarios with limited initial data. The user can specify any preferred number of initial cycles in the provided configuration file, which is detailed at <https://github.com/basf/ARCANA/blob/master/config/>



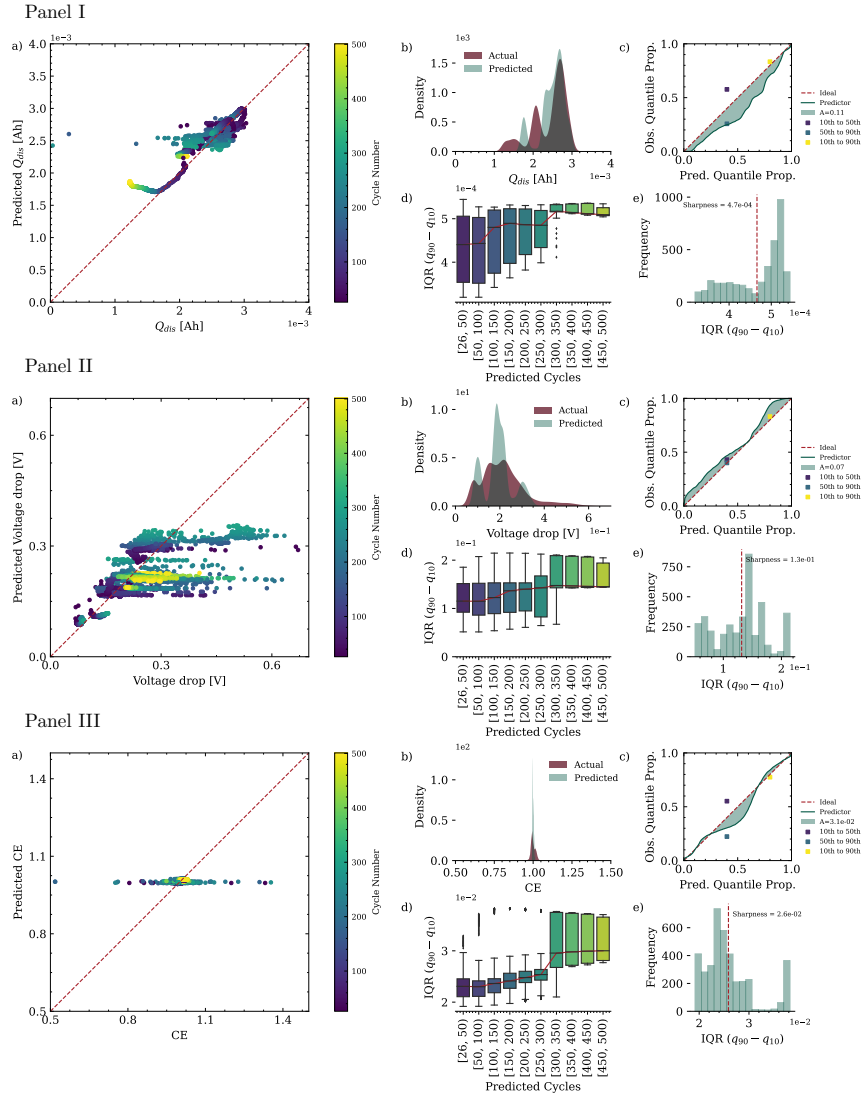
Supplementary Figure 22: Evaluation of  $M(B)$  prediction for Voltage drop, Coulombic efficiency and  $Q_{dis}$  on  $DNMC$  a) Shows the correlation between actual and predicted values with a representation of the cycle progression by a color gradient, b) compares the density of actual and predicted values. The calibration curves in c) assumes a normal distribution, where the mean and standard deviation are estimated from the 10th, 50th, and 90th percentile predictions. It depicts the proportion of values that fall within the predicted intervals defined by these quantiles, with the ideal diagonal line representing perfect calibration. The shaded area indicates the degree of miscalibration, denoted as  $A$ . Additionally, the points in this plot illustrate the observed proportions of actual values that fall within three specific intervals based on the quantiles: between the 10th and 50th, 50th and 90th, and 10th and 90th percentiles. d) illustrates the variability and central tendency of prediction intervals across cycles and e) provides a histogram of the quantiles as the prediction interval width between the 10th and 90th percentiles as a measure of sharpness. The dashed red line indicates sharpness as the mean interval width and shows the concentration of the predictive distributions.



Supplementary Figure 23: Comprehensive predictive performance and sensitivity assessment for  $M(P)_f$  on a selected sample from  $D_{NMC}$ . Plot a-c show the model's predictions for voltage drop, CE and  $Q_{dis}$ , respectively, alongside the actual measured values and associated uncertainty. Plots d), e), and f) detail the model's sensitivity to each predictive cycle, represented on a logarithmic scale, demonstrating how input variations affect the output. Plot g), h), and i) aggregate the sensitivity data across all given cycles, providing an overview of the model's input responsiveness throughout the cycling process.

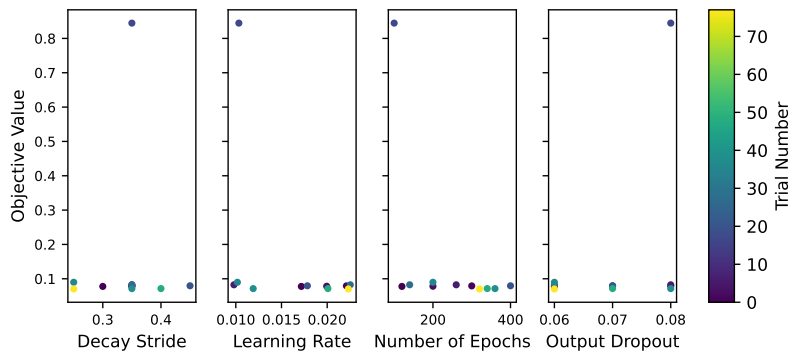


Supplementary Figure 24: Multi-head attention weight analysis of  $M(P)_f$  for a selected sample from  $D_{NMC}$ . The first four plots (a-d) represent the attention weights from separate heads for selected input cycles. The final plot shows the average attention weights across all heads, providing an overview of the model's focus distribution throughout the prediction process. This composite view illustrates how the model prioritizes different cycles to optimize prediction accuracy.

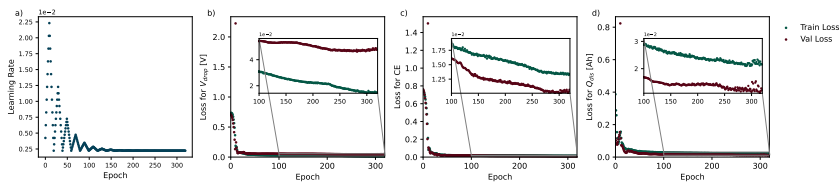


## 11 Performance of $M(P)_{Na}$ and $M(B)_{Na}$ on $D_{Na}$

The fine-tuning of both  $M(P)$  and  $M(B)$  for Na-ion batteries data, denoted as  $M(P)_{Na}$  and  $M(B)_{Na}$  respectively, followed the same strategy of adjusting the decoder's layer (Sec. 7). Similarly, this approach was chosen to be applied to novel materials and protocols in our custom batteries, which exhibit unique and varied degradation pathways. The performance of both models during the training and validation phases, with details on the optimal hyperparameters determined through Optuna, can be seen below in Supplementary Figure 26 to 29. The optimal parameters for  $M(P)_{Na}$  included a decay stride of 0.2677, a learning rate of 0.0116, and an output dropout of 0.0525 over 285 epochs. Correspondingly  $M(B)_{Na}$ , presented a decay stride of 0.25, a learning rate of 0.0223, an output dropout of 0.06, and 320 epochs.



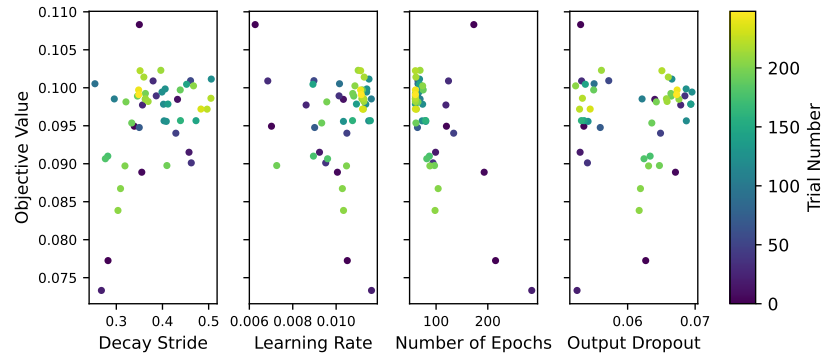
Supplementary Figure 26: Graphical representation of hyperparameter optimization using Optuna<sup>28</sup>. This slice plot delineates the multidimensional search space explored during the optimization process for the Model  $M(B)_{Na}$ . Each axis represents a distinct hyperparameter, illustrating the range of values explored.



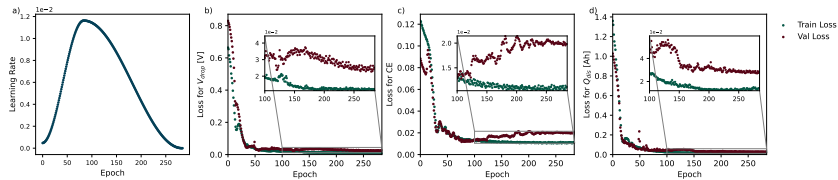
Supplementary Figure 27: Comprehensive model training and performance analysis for  $M(B)_{Na}$ : a) Learning rate dynamics, which shows the adaptive adjustment of learning rates over epochs using a cycle scheduler, b) Loss trends for tracing training and validation loss during voltage drop [V] c) Coulomb efficiency, and d) Discharge capacity [Ah].

Supplementary Table 4: Summary of the evaluation metrics for  $M(P)_{Na}$  and  $M(B)_{Na}$ , tested on 18 unseen coin cells ( $D_{Na}$ ). The evaluation used nine initial cycles of historical data\* to predict six cells cycled with C-rate protocols up to the 40th cycle and 12 samples cycled with CC-CV protocol up to the 140th cycle (shown in Supplementary Figure 30).

Metrics	$M(P)_{Na}$			$M(B)_{Na}$		
	Voltage drop [V]	CE	$Q_{dis}$ [Ah]	Voltage drop [V]	CE	$Q_{dis}$ [Ah]
<b>RMSE</b>	0.1197	0.1138	$11.7 \times 10^{-6}$	0.1106	0.1098	$7.65 \times 10^{-6}$
<b>MAPE</b>	24.8176	7.6430	222.1276	34.6403	7.4923	337.2994
<b>MAE</b>	0.0468	0.0451	$5.022 \times 10^{-6}$	0.0582	0.0390	$4.7 \times 10^{-6}$
<b>medAE</b>	0.0126	0.0137	$1.836 \times 10^{-6}$	0.0448	0.0108	$2.98 \times 10^{-6}$



Supplementary Figure 28: Graphical representation of hyperparameter optimization using Optuna<sup>28</sup> Algorithm: This slice plot delineates the multidimensional search space explored during the optimization process for Model  $M(P)_{Na}$ . Each axis represents a distinct hyperparameter, illustrating the range of values explored.

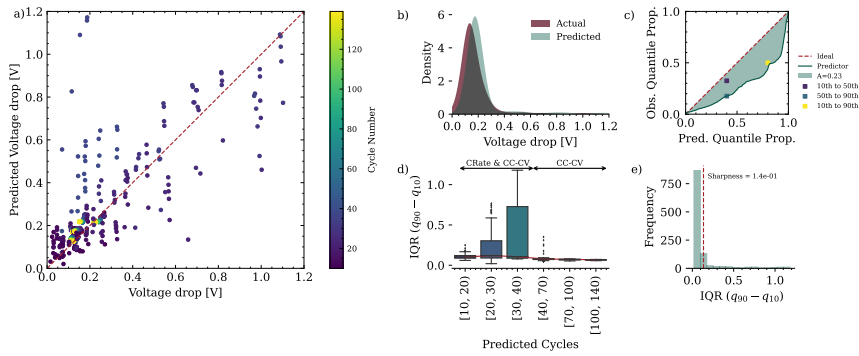


Supplementary Figure 29: Comprehensive model training and performance analysis for  $M(P)_{Na}$ : a) Learning rate dynamics, which shows the adaptive adjustment of learning rates over epochs using a one-cycle scheduler, b) Loss trends for tracing training and validation loss during voltage drop c) Coulomb efficiency, and d) Discharge capacity.

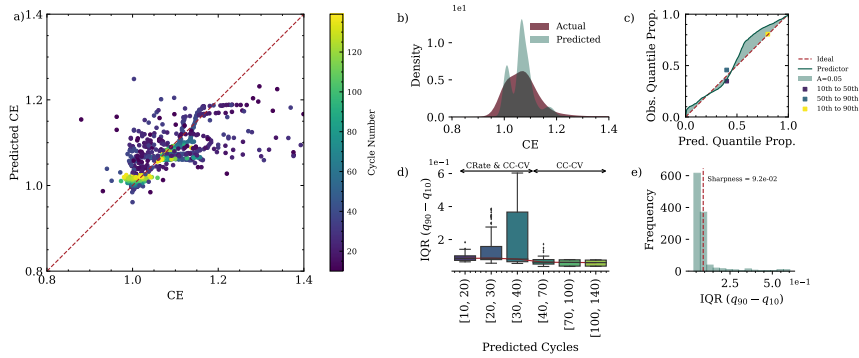
\*The number of initial cycles was chosen randomly to resemble practical scenarios with limited initial data. The user can specify any preferred number of initial cycles in the provided configuration file, which is detailed at <https://github.com/basf/ARCANA/blob/master/config/>

## 12 Evaluation of $D_{Na}$

Panel I

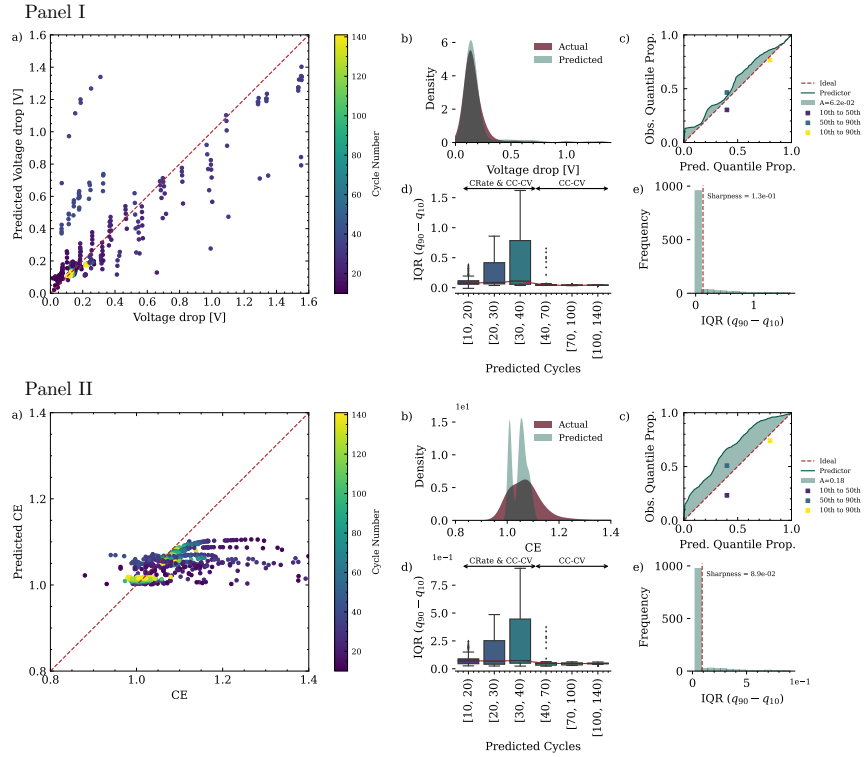


Panel II

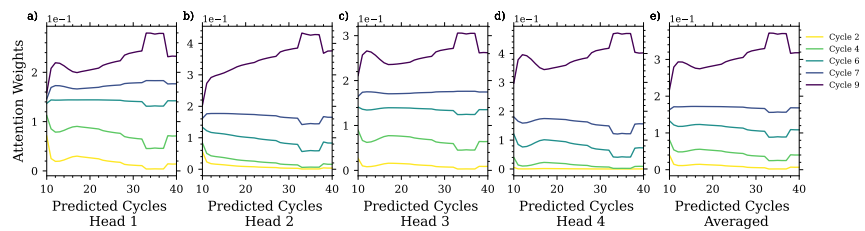


Supplementary Figure 30: Evaluation of  $M(B)_{Na}$  prediction for Voltage drop, Coulombic efficiency on  $D_{Na}$ . a) Shows the correlation between actual and predicted values with a representation of the cycle progression by a color gradient, b) compares the density of actual and predicted values. The calibration curves in c) assumes a normal distribution, where the mean and standard deviation are estimated from the 10th, 50th, and 90th percentile predictions. It depicts the proportion of values that fall within the predicted intervals defined by these quantiles, with the ideal diagonal line representing perfect calibration. The shaded area indicates the degree of miscalibration, denoted as  $A$ . Additionally, the points in this plot illustrate the observed proportions of actual values that fall within three specific intervals based on the quantiles: between the 10th and 50th, 50th and 90th, and 10th and 90th percentiles. d) illustrates the variability and central tendency of prediction intervals across cycles and e) provides a histogram of the quantiles as the prediction interval width between the 10th and 90th percentiles as a measure of sharpness. The dashed red line indicates sharpness as the mean interval width and shows the concentration of the predictive distributions.





Supplementary Figure 31: Evaluation of  $M(P)_{Na}$  prediction for Voltage drop, Coulombic efficiency on  $D_{Na}$ . a) Shows the correlation between actual and predicted values with a representation of the cycle progression by a color gradient, b) compares the density of actual and predicted values. The calibration curve in c) assumes a normal distribution, where the mean and standard deviation are estimated from the 10th, 50th, and 90th percentile predictions. It depicts the proportion of values that fall within the predicted intervals defined by these quantiles, with the ideal diagonal line representing perfect calibration. The shaded area indicates the degree of miscalibration, denoted as  $A$ . Additionally, the points in this plot illustrate the observed proportions of actual values that fall within three specific intervals based on the quantiles: between the 10th and 50th, 50th and 90th, and 10th and 90th percentiles. d) illustrates the variability and central tendency of prediction intervals across cycles, and e) provides a histogram of the quantiles as the prediction interval width between the 10th and 90th percentiles as a measure of sharpness. The dashed red line indicates sharpness as the mean interval width and shows the concentration of the predictive distributions.



Supplementary Figure 32: Multi-head attention weight analysis of  $M(P)_{Na}$  for a selected sample from  $D_{Na}$ . The first four plots (a-d) represent the attention weights from separate heads for selected input cycles. The final plot (e) shows the average attention weights across all heads, providing an overview of the model's focus distribution throughout the prediction process. This composite view illustrates how the model prioritizes different cycles to optimize prediction accuracy.

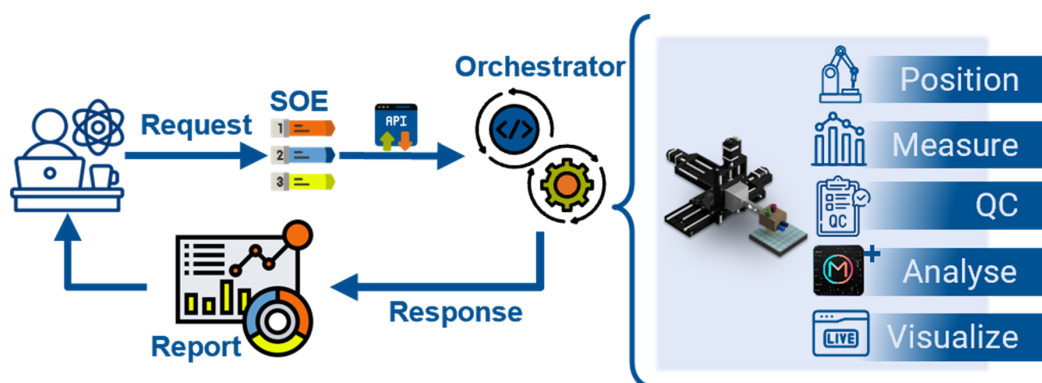
### Supplementary References

1. Severson, K. A. *et al.* Data-driven prediction of battery cycle life before capacity degradation. *Nat. Energy* **4**, 383–391 (2019).
2. Attia, P. M. *et al.* Closed-loop optimization of fast-charging protocols for batteries with machine learning. *Nature* **578**, 397–402 (2020).
3. Toyota Research Institute. Experimental data platform: Project Data-driven prediction of battery cycle life before capacity degradation. *data.matr.io*. Dataset: <https://data.matr.io/1/projects/5c48dd2bc625d700019f3204> (2021).
4. Toyota Research Institute. Experimental data platform: Project Closed-loop optimization of extreme fast charging for batteries using machine learning. *data.matr.io*. Dataset: <https://data.matr.io/1/projects/5d80e633f405260001c0b60a> (2019).
5. Strange, C., Li, S., Gilchrist, R. & Dos Reis, G. Elbows of internal resistance rise curves in Li-ion cells. *Energies* **14**, 1206 (2021).
6. Ibraheem, R., Strange, C. & dos Reis, G. Capacity and Internal Resistance of lithium-ion batteries: Full degradation curve prediction from Voltage response at constant Current at discharge. *J. Power Sources* **556**, 232477 (2023).
7. Strange, C., Li, S., Gilchrist, R. & Dos Reis, G. Synthetic IR data for the Attia et al. (2020) battery dataset. *datashare*. Dataset: <https://datashare.ed.ac.uk/handle/10283/3798> (2020).
8. Zhu, J. *et al.* Data-driven capacity estimation of commercial lithium-ion batteries from voltage relaxation. *Zenodo*. Dataset: <https://doi.org/10.5281/zenodo.6405084> (2022).
9. Zhu, J. *et al.* Data-driven capacity estimation of commercial lithium-ion batteries from voltage relaxation. *Nat. Commun.* **13**, 2261 (2022).
10. Zhang, B., Merker, L., Sanin, A. & Stein, H. S. Robotic cell assembly to accelerate battery research. *Digital Discovery* **1**, 755–762 (2022).
11. Zhang, Merker, Sanin & Stein. Cycling Data of 64 Cells manufactured by AutoBASS. Version 2. *Zenodo*. Dataset: <https://doi.org/10.5281/zenodo.7299473> (2022).
12. Merker, L. 2023 Commercial Coincell 45mAh. Version 1.0. *Zenodo*. Dataset: <https://doi.org/10.5281/zenodo.10102627> (2023).
13. Merker, L. InZePro InForm 300 Cycles CCCV after EOL. Version 1.0. *Zenodo*. Dataset: <https://doi.org/10.5281/zenodo.10102508> (2023).
14. Nuss, L., Merker, L., Zhang, B. & Stein, H. Formation and cycling data for Na-ion batteries from high-throughput synthesis, coating, and assembly. Version v1. *Zenodo*. Dataset: <https://doi.org/10.5281/zenodo.7981011> (2023).
15. CALCE: Center for Advanced Life Cycle Engineering. *University of Maryland*. Dataset: <https://calce.umd.edu/data> (2011).
16. He, W., Williard, N., Osterman, M. & Pecht, M. Prognostics of lithium-ion batteries based on Dempster–Shafer theory and the Bayesian Monte Carlo method. *J. Power Sources* **196**, 10314–10321 (2011).
17. Williard, N., He, W., Osterman, M. & Pecht, M. Comparative analysis of features for determining state of health in lithium-ion batteries. *Int. J. Progn. Health Manag.* **4** (2013).
18. Guo, J., Li, Z. & Pecht, M. A Bayesian approach for Li-Ion battery capacity fade modeling and cycles to failure prognostics. *J. Power Sources* **281**, 173–184 (2015).
19. Saha, B. & Goebel, K. NASA. *Prognostics Data Repository*. Dataset: <https://www.nasa.gov/content/prognostics-center-of-excellence-data-set-repository> (2007).
20. Dos Reis, G., Strange, C., Yadav, M. & Li, S. Lithium-ion battery data and where to find it. *Energy and AI* **5**, 100081 (2021).
21. Saxena, A. *et al.* Designing data-driven battery prognostic approaches for variable loading profiles: Some lessons learned. *European conference of prognostics and health management society*, 72–732 (2012).


22. Devie, A., Baure, G. & Dubarry, M. Intrinsic variability in the degradation of a batch of commercial 18650 lithium-ion cells. *Energies* **11**, 1031 (2018).
23. Sandia National Laboratories Grid Energy Storage Department. *Homepage of Battery Archive*. Dataset: <https://www.batteryarchive.org> (2021).
24. Preger, Y. *et al.* Degradation of commercial lithium-ion cells as a function of chemistry and cycling conditions. *J. Electrochem. Soc.* **167**, 120532 (2020).
25. Roman, D., Saxena, S., Robu, V., Pecht, M. & Flynn, D. Machine learning pipeline for battery state-of-health estimation. *Nat. Mach. Intell.* **3**, 447–456 (2021).
26. Tian, Y. *et al.* Capacity estimation of lithium-ion batteries based on optimized charging voltage section and virtual sample generation. *Appl. Energy* **332**, 120516 (2023).
27. Zhang, Y., Feng, X., Zhao, M. & Xiong, R. In-situ battery life prognostics amid mixed operation conditions using physics-driven machine learning. *J. Power Sources* **577**, 233246 (2023).
28. Akiba, T., Sano, S., Yanase, T., Ohta, T. & Koyama, M. Optuna: A Next-generation Hyperparameter Optimization Framework. *DLP-KDD '19*, 2623–2631 (2019).

## 4.5. Autonomous millimeter scale high throughput battery research system

### 4.5.1. Publication Details




---

<b>Title:</b>	"Autonomous millimeter scale high throughput battery research system"
<b>Journal:</b>	<i>Digital Discovery</i> * 2024
<b>Publisher:</b>	Royal Society of Chemistry
<b>Authors:</b>	<b>Rahmanian, Fuzhan</b> and Fuchs, Stefan and Zhang, Bojing and Fichtner, Maximilian and Stein, Helge Sören
<b>Status:</b>	Published: 21. March 2024
<b>DOI:</b>	<a href="https://doi.org/10.1039/D3DD00257H">https://doi.org/10.1039/D3DD00257H</a>
<b>Developed Software:</b>	 <a href="https://github.com/fuzhanrahmanian/MISCHBARES">https://github.com/fuzhanrahmanian/MISCHBARES</a>

---

\* For reprint permission refer to Section A.1

## Publication Content

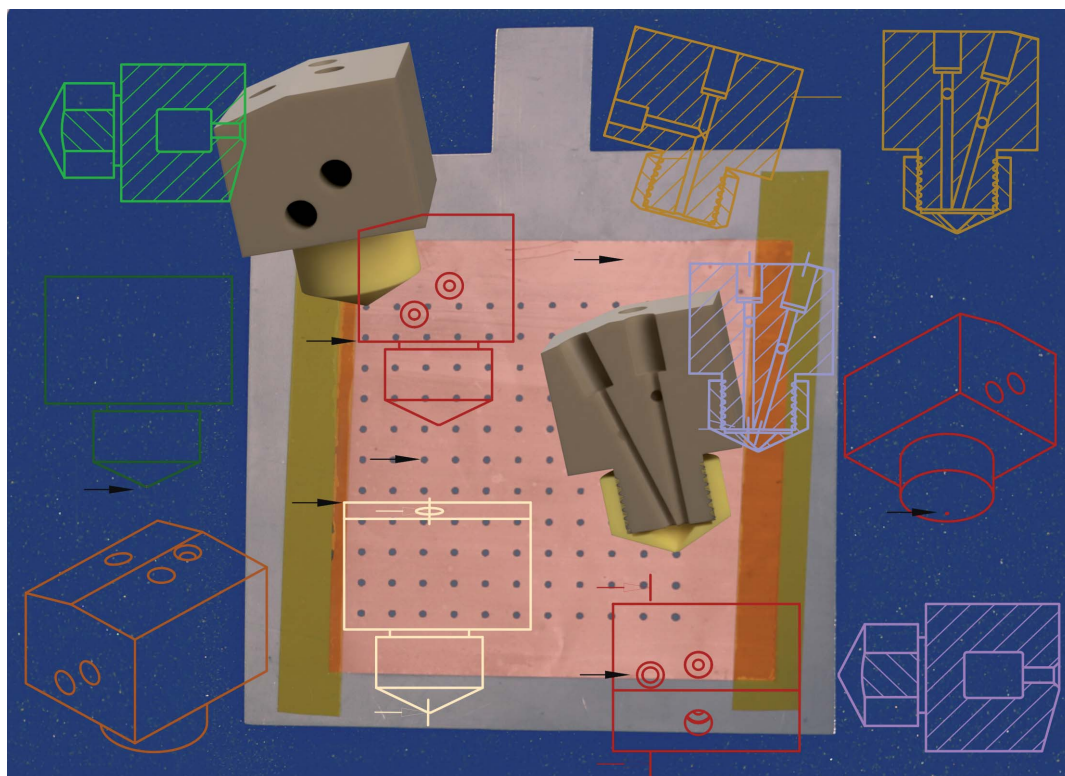
Designing trustworthy workflows for non-aqueous battery systems is a challenging task, for which Auto-MISCHBARES presents a reliable high-throughput electrochemical experimentation framework that mitigates the pitfalls of traditional approaches, which are often labor-intensive, time-consuming, and prone to human error. Auto-MISCHABRES integrates hardware, task orchestration, automated quality control, data analysis, database curation, and live visualization, thereby delivering reproducible results despite the potential for systemic problems that arise from miniaturization, evaporation, and salt formation. The system is designed with a granular control mechanism and establishes four hubs to facilitate orchestration for a variety of different configuration of electrochemical procedures. The ServerHub enables researchers to design, schedule and monitor experimental batches using a user-friendly web interface developed with HTML, CSS, and JavaScript. It is complemented by Flask, for a backend communication with the Python orchestrator that executes and manages experiments both sequentially and in parallel over an asynchronous web server for autonomous experimentation as an expansion to the earlier introduced HELAO framework. Throughout the process, a custom live Bokeh visualizer, deployed over Websocket, is used to deliver immediate visual feedback to the user. The DeviceHub consists of an open three-electrode cell setup connected to a motor, a syringe pumping system, and a multichannel potentiostat for the execution of electrochemical measurements. The MutliAnalyseHub performs two tasks, which are the monitoring of experiment quality for reliability and the real-time analysis of live data. Quality control is orchestrated asynchronously and is designed to perform computer-vision-aided drop detection, mandatory cleaning movements and automated contact detection of the electrode in order to minimize material disruption. Data analysis includes real-time processing of CV data as well as instantaneous report creation from raw and processed data using statistical and ML algorithms, all of which expand on the previously introduced MADAP analysis tool. The DataHub functions as the designed data management system, built with PostgreSQL for real-time storage of experimental raw and processed data, securing integrity, lineage, and accessibility in alignment with FAIR principles. In this publication, the engineered system is showcased in the initial cycle of a charging and discharging process for a screen-printed half-cell electrode. The system demonstrates

a high degree of reliability in outcomes not only on electrochemical levels but also across ex situ X-ray photoelectron spectroscopy (XPS) characterization. The agnostic nature of the proposed framework is distinctive within the battery research scientific community and makes it adaptable across organic and inorganic applications for the discovery of new materials.

### Individual Contributions

**Fuzhan Rahmanian** designed the PostgreSQL database, designed the Object Oriented Programming (OOP) schema for the application, implemented the code including the automated testing, the connection to the database, the quality control steps and expanded the HELAO automated workflow. **F.R.** designed and implemented the UI and its backend, curated the GitHub Repository and the documentation. **F.R.** expanded MADAP package for voltammetry analysis. B.Z. designed and 3D-printed the waste and camera holder, while H.S.S. prepared the screen printing mask. S.F. and **F.R.** calibrated the setup, performed the electrochemical experiment. S.F. performed XPS experiment and interpreted electrochemical and spectroscopic results, while **F.R.** plotted the results and assembled the paper.

## 4.5.2. Manuscript



Showcasing research from Fuzhan Rahmanian and Professor Helge Sören Stein from Technical University of Munich, Bavaria, Germany.

Autonomous millimeter scale high throughput battery research system

Millimeter-scale high-throughput battery research (MISCHBARES) on slurry-derived electrodes is herein integrated with data analysis, data management, and quality control for expedited knowledge generation. In-depth high-throughput XPS and XRF enable correlative spectroscopy across all states of charge (SOC). This research is enabled by the hierarchical experimental laboratory automation and orchestration framework (HELAO) and the Modular and Autonomous Data Analysis Platform (MADAP) which offer quality control gates and data lineage tracking.

As featured in:



See Fuzhan Rahmanian, Helge Sören Stein *et al.*, *Digital Discovery*, 2024, 3, 883.


 Cite this: *Digital Discovery*, 2024, 3, 883

## Autonomous millimeter scale high throughput battery research system†

 Fuzhan Rahmanian,<sup>ib</sup>\*<sup>abdef</sup> Stefan Fuchs,<sup>ab</sup> Bojing Zhang,<sup>abdef</sup> Maximilian Fichtner,<sup>ib</sup>\*<sup>ac</sup> and Helge Sören Stein<sup>\*abdef</sup>

Discoveries of novel electrolyte–electrode combinations require comprehensive structure–property–interface correlations. Herein, we present autonomous millimeter scale high-throughput battery research system (Auto-MISCHBARES) operated with an asynchronous web-based orchestration framework that integrates modular research instrumentation designed for autonomous electrochemical experimentation. The platform allows researchers to define a range of experiments with granular parameter control, start the process, and receive a live visualization of measurements through a web-based user interface. This paper presents a proof of concept for cathode electrolyte interphase (CEI) formation in lithium-ion batteries (LiBs) at various potentials, all controlled through Auto-MISCHBARES and correlating its high-throughput electrochemistry results with X-ray photoelectron spectroscopy (XPS) characterization. We believe quality control, complex data analysis, and management to be the missing puzzle pieces toward more complex workflow automation. Auto-MISCHBARES integrates automatic quality control for both hardware and software using AI enablers to ensure high reliability through an on-the-fly fidelity assessment of each experiment. In the presented case study, voltammetry measurements are handled through a modular platform capable of performing fully automated analysis, while data lineage is provided through relational data storage in adherence with Findable, Accessible, Interoperable, and Reusable (FAIR) guidelines, all in real-time. Thus, Auto-MISCHBARES represents a point of contact between the orchestration of automated instrumentation, quality control, real-time data analysis, and management, enabling reproducible and versatile workflows for the discovery of new materials, especially for batteries. We demonstrate this integrated workflow for reliable charging/discharging protocols.

 Received 31st December 2023  
 Accepted 15th March 2024

DOI: 10.1039/d3dd00257h

[rsc.li/digitaldiscovery](https://rsc.li/digitaldiscovery)

Automated quality control and data interpretation are the missing puzzle pieces towards prolonged walk-away-times in closed-loop experimentation.<sup>1</sup> These advances increase the efficiency and innovation of the research process by minimizing the need for human oversight and ensuring the generation of reliable, insightful data. Early demonstrations of closed-loop experiments included mostly error resilient measurement and facile data analysis, but the step towards complex and interrelated experimentation necessitates more robust data quality

assessment. The evolution of these automated experiments towards truly autonomous Material Acceleration Platforms (MAPs) requires integration of experimental processes, data management, and strategic decision-making<sup>2</sup> self-driving laboratories (SDLs).<sup>3,4</sup> Laboratories such as BEAR,<sup>5</sup> ARES,<sup>6</sup> Clio,<sup>7</sup> equipped with advanced frameworks are instrumental in boosting operational efficiency and research safety.<sup>8</sup> These technological leaps not only streamline experimental processes, but also enable scientists to undertake deeper and more intricate inquiries, accelerating discovery in various scientific domains.<sup>9,10</sup> Additionally, the integration of AI and machine learning (ML) allows for efficient exploration of complex chemical and material terrains.<sup>10,11</sup> SDLs, in particular, show the potential to accelerate research output by up to 30 times.<sup>9</sup> By automating and digitalizing processes, these systems increase experimental accuracy and walk away time.<sup>4</sup>

<sup>a</sup>Helmholtz Institute Ulm, Applied Electrochemistry, Helmholtzstr. 11, 89081 Ulm, Germany

<sup>b</sup>Karlsruhe Institute of Technology, Institute of Physical Chemistry, Fritz-Haber-Weg 2, 76131 Karlsruhe, Germany

<sup>c</sup>Karlsruhe Institute of Technology, Institute of Nanotechnology, 76021 Karlsruhe, Germany

<sup>d</sup>Technische Universität München, School of Natural Sciences, Department of Chemistry, Lichtenbergstr 4, 85748 Garching, Germany. E-mail: helge.stein@tum.de; fuzhan.rahmanian@tum.de

<sup>e</sup>Technische Universität München, Munich Data Science Institute, Walther-von-Dyck-Straße 10, 4, 85748 Garching, Germany

<sup>f</sup>Technische Universität München, Munich Institute for Robotic and Machine Intelligence, Georg-Brauchle-Ring 60-62, 80992 Munich, Germany

† Electronic supplementary information (ESI) available. See DOI: <https://doi.org/10.1039/d3dd00257h>

### 1 The challenge of multifidelity

There is a sprawl of MAPs in various fields<sup>12–14</sup> but its progress in non-aqueous battery applications has been hindered by unique challenges.<sup>15</sup> As a result, only a few established MAP efforts exist, chief among which is the Battery Interface Genome-Materials





## Digital Discovery

Acceleration Platform (BIG-MAP) initiative.<sup>16</sup> This complexity arises mainly from the special housing and safety measures necessary to conduct battery research and the vast chemical space required to optimize, for example, electrolytes, electrodes, design, and physical properties.<sup>17–19</sup> Significant efforts have been made to address each aspect; for instance, Dave *et al.*<sup>7</sup> developed an autonomous workflow to optimize the electrolyte formulation for a single salt and ternary solvent design at various ratios for non-aqueous battery systems by utilizing a robotic platform. At the interface level, the autonomous investigation of CEI and solid electrolyte interphase (SEI) within MAPs are not extensively explored on an experimental level.<sup>20–22</sup> This highlights the ongoing need for innovative approaches in battery studies, especially in understanding and optimizing the complex interactions at these interfaces,<sup>23,24</sup> which involve multiple and varied testing scenarios, such as the correlation of electrochemical and spectroscopy characterization. A challenge in developing a system capable of providing a multifaceted solution for the next generation of battery materials<sup>19</sup> is the integration of all the necessary devices within a single laboratory.<sup>25</sup> Herein, granular control across each step of the experimentation is crucial for achieving multifidelity. Additionally, due to variations arising from different samples, experimental correlation and device integration within a single lab become even more critical to ensure consistency and reliability of results, as it effectively minimizes discrepancies that might occur from diverse laboratory environments.

## 2 The challenge of designing an integrative database solution

To address the challenges of multi-device testing on a single sample, the development of a robust data management is essential.<sup>24,26–28</sup> This system must enable seamless integration and communication across various instruments and bridge physical and temporal gaps in experimental stages that often exist between disparate phases.<sup>29,30</sup> Such advancements are crucial in SDLs, where progress has been hindered by a lack of standardized and user-friendly software between laboratory instrumentation and intuitive operational guidelines.<sup>15</sup> Efficient data management and experimental planning enable rapid processing and interpretation of high dimensional data, which unravel physicochemical relations that surpass the analytical capacity of conventional approaches.<sup>1,31,32</sup> It also facilitates the incorporation of AI agents and Deep Learning (DL) tools, which can further accelerate the exploration of the chemical spaces and reduce recourse allocation.<sup>32–34</sup> This approach is in line with significant scientific efforts in chemistry<sup>35</sup> and in other domains,<sup>10</sup> which emphasize the importance of consistent data quality protocols and data acquisition methods, in compliance with FAIR data principles.<sup>36</sup>

## 3 AI enablers for reliable experimentation

In autonomous experimental setups, replicating burdensome human-intensive tasks, such as material sufficiency management or equipment cleaning, is challenging.<sup>2,37</sup> Simultaneously,

these ensure the reliability and fidelity of measurements and require rigorous validation for experimental accuracy and consideration of potential hardware and software flaws.<sup>38</sup> As proposed in recent studies,<sup>4,39,40</sup> the utilization of AI technology, such as ML and computer vision methods, can significantly improve system robustness, which is crucial to monitor parameter validity in real time.<sup>4</sup> The goal is to achieve data integrity and support AI planners in informed decision-making. This is particularly beneficial for non-aqueous battery systems experimentation in gloveboxes, where assembling and controlling multiple experiments present complexities that even with human intervention may prove challenging to manage effectively. The progress in adopting AI enablers, thus, signifies a transformative shift in scientific experimentation towards enhanced precision and reliability,<sup>39</sup> highlighted by the critical need to recognize and address the technical challenges in experiment-specific boundaries to ensure results are both comprehensible and reproducible.<sup>14,41</sup>

To advance the MAPs and overcome existing constraints of multifidelity, robust data management, and reliable and reproducible automated experimentation,<sup>9,10</sup> we introduce the Auto-MISCHBARES, an open-source framework designed for fully unsupervised operations. Building upon our earlier studies on asynchronous web-based frameworks,<sup>30</sup> it orchestrates live visualization of electrochemical measurements, quality control and user feedback, data provenance and analysis, thus enhancing the experimental processes. This platform features automated capabilities for conducting a variety of electrochemical experiments configured over a web user interface (UI), as showcased in our case study of the CEI formation on screen-printed battery electrodes. Auto-MISCHBARES performed sequential measurements using an open-cell setup<sup>42</sup> and characterized them using XPS under ultra-high vacuum conditions. The agnostic nature of our framework ensures its adaptability for diverse organic and inorganic materials. This platform not only can accelerate research but also facilitate the sharing of validated data, helping scientists in the efficient extraction and transfer of information within the community.<sup>17,43</sup>

## 4 Design and methodology

### 4.1 Framework overview

The Auto-MISCHBARES framework is developed by integrating four key Hubs overarching hardware and software of the experimental workflow. The DeviceHub encompasses a set of hardware that is responsible for the exact placement, dispensing, and measurement. The ServerHub ensures robust operations and communication workflow through orchestration and API design. The DataHub manages the database environment and is key for data integrity and accessibility. Lastly, the MultiAnalyticHub provides a wide spectrum of analytics, from statistical assessments to computer vision methods.<sup>46</sup> The integration of all the Hubs is the prerogative of acceleration in material development,<sup>15,47</sup> and therefore, by following this design philosophy, our Auto-MISCHBARES platform is able to perform fully autonomous electrochemical measurements tailored to study the formation of CEI and



monitor oxidation state changes in active materials at different stages of the experiment.

**4.1.1 DeviceHub.** In this study, the core of our DeviceHub is an electrochemical system known as SDC.<sup>42</sup> This setup is an open-cell miniaturized 3-electrode-cell construction comprising a gold reference electrode (RE) and a platinum counter electrode (CE), both positioned within a movable cell housing made from polytetrafluoroethylene (PTFE). This housing utilizes electrode spots on a planar substrate functioning as the working electrode (WE). The SDC is connected to a stepper motor ‡ and a multichannel potentiostat device §. Additionally, the DeviceHub encompasses a syringe pump system ¶, which is connected to this cell *via* an inlet. Our configuration allows for precise delivery of the desired electrolyte formulation, as well as enabling accurate positioning over the targeted measurement area on the WE substrate and the deposition of a single droplet of electrolyte. Upon contact of all three electrodes, the system is ready to execute the selected protocols (Fig. 1b, section setup). The placement of the SDC and measurement through the potentiostat are controlled by the ServerHub.

**4.1.2 ServerHub.** This platform is an advanced extension of our initial ServerHub presented in HELAO.<sup>30</sup> It is capable of executing experiments both sequentially and in parallel, and allows for the integration of an active learning decision-maker to orchestrate tasks across instruments. The complete workflow is illustrated in Fig. 1a. At the beginning, researchers configure experimental setups and schedule multiple, dynamic batches of experiments through a user-friendly and modular interface (ESI 1†). The UI is constructed using HTML, and CSS with dynamic functionalities implemented in Node.js and facilitates easy browsing with a diverse array of electrochemical protocols. This interaction layer is further enhanced by Flask,<sup>48</sup> a Python-based web framework, to streamline user engagement. Once single or multiple experimental batches are designed, the configurations are passed to the Python back-end, requiring no additional user intervention, and are translated to FastAPI requests. The central orchestrator will then efficiently schedule and manage high-throughput experimentation in an asynchronous manner. After the execution of all requested experimental batches, the operator receives a response from the orchestrator with a comprehensive report detailing all experimental steps, their timestamps, and outcomes.

**4.1.3 MultiAnalyticHub.** A key challenge in automation is maintaining the reliability of results, which is crucial for managing potential risks since a plethora of variables and parameters are prone to errors during experimentation.<sup>2</sup> These include tasks typically simple for humans, such as removing salt accumulation, replenishing depleted electrolyte bottles, ensuring electrical connection at the hardware level, and maintaining safe thresholds for measurement parameters at the software level. Failure to address these aspects could lead to

experimental inaccuracies and substantial time and resource wastage. Mitigation strategies are a crucial aspect in the realization of a truly autonomous laboratory.<sup>47</sup> Thus, our Multi-AnalyticHub is equipped to enhance the platform by implementing mechanisms for providing critical feedback through automated quality control (QC) and real-time analysis throughout the experimental stages (Fig. 1b, Section Quality Control & Analysis). This Hub aims to inform researchers of ongoing progress and potential failures and provide accurate, statistically driven analysis, increasing trustworthiness in high-throughput experimentation.

The initial QC assessment in our system is monitoring material sufficiency at the electrolyte exchange stage for each measurement. A key component of this process is the Droplet Detection routine, designed to verify proper flushing. This detection is implemented using the OpenCV library<sup>49</sup> for computer vision tasks and analyzes a video streams to detect the presence of a drop.<sup>50</sup> The algorithm selects a specific region of interest (ROI) in the video frame, converts this segment into grayscale, and applies a Gaussian blur to minimize noise. By continuously calculating the absolute difference between the initial frame and subsequent frames within the ROI, the system can detect motion. A non-zero sum in the thresholded image within this area indicates of a drop's presence. The selection of a ROI is motivated by two main reasons. The reduction of computation time by focusing on a small area of the output and the elimination of false positives that may arise due to motion detection in the background of the camera. Given that the SDC movement is motorized, and the material is flushed at a predefined position, the ROI is calibrated only during the setup phase and remains unchanged throughout the experimentation. In addition, visual feedback is provided on the monitor for user verification and oversight.

Once the electrolyte has been exchanged, a non-negligible chance persists of residual material remaining attached to the head of the SDC, which can lead to salt formation, crystallization, or inconsistencies in later measurements. We expanded our quality control protocol and incorporated a mandatory movement of the SDC head to a wiping pad, ensuring the removal of any leftover electrolytes. Following this preparation, the stepper motor positions the SDC head over the designated measurement area of the WE (Fig. 1b, section automated experiment).

Additional QC is implemented to control the movement of the SDC head precisely and ensure optimal electrical connectivity with the substrate in the coming measurement. This mechanism is designed to lower the SDC head gradually, performing the descent in small, constant steps. This approach secures each movement to stay within a defined threshold to prevent excessive force on the head. For stepwise monitoring of electrical potential, frequent control measurements are integrated with potentiostatic endpoints of the ServerHub. The voltage data is then used to determine successful contact with the substrate, indicated by a sharp decay in potential towards zero. If contact is not established within the initial steps, the routine initiates corrective measures. These include the controlled addition of electrolytes, periodic potential

‡ <https://www.owis.eu/en/>.

§ [https://www.metrohm.com/de\\_de/products/a/ut30/aut302n\\_s.html](https://www.metrohm.com/de_de/products/a/ut30/aut302n_s.html).

¶ <https://www.hamiltoncompany.com/laboratory-products/microlab-600/syringe-pump>.

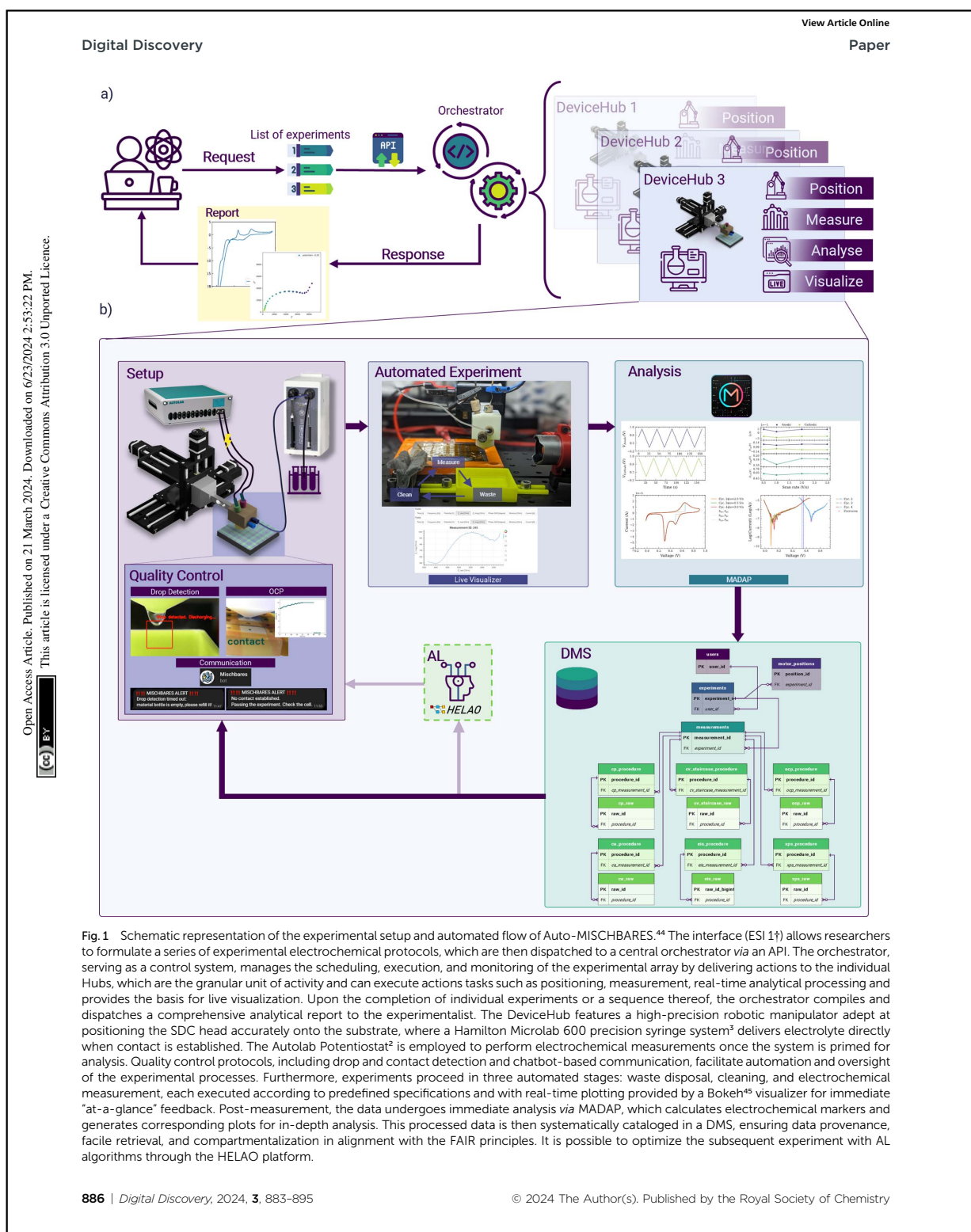
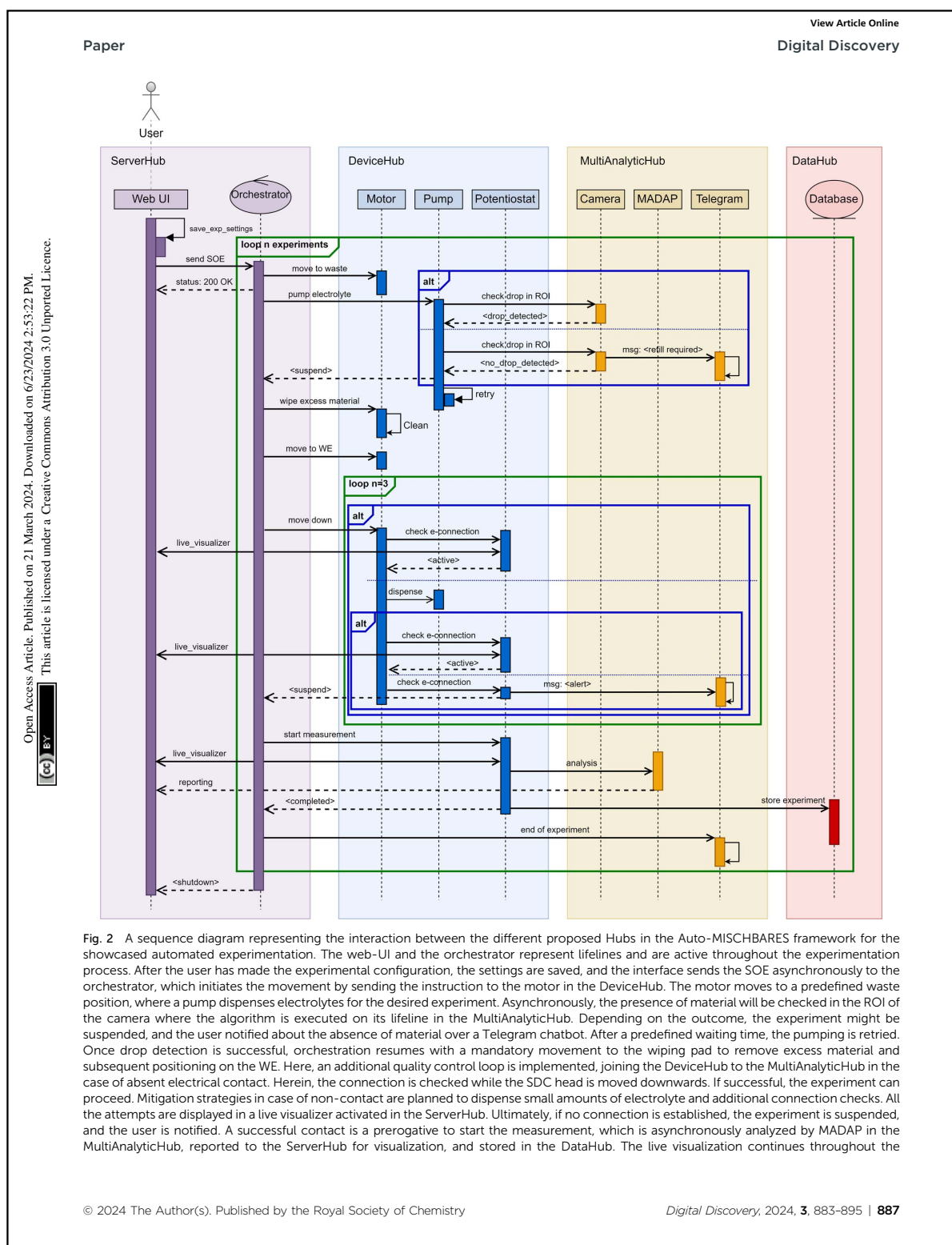


**Fig. 1** Schematic representation of the experimental setup and automated flow of Auto-MISCHBARES.<sup>44</sup> The interface (ESI 1†) allows researchers to formulate a series of experimental electrochemical protocols, which are then dispatched to a central orchestrator via an API. The orchestrator, serving as a control system, manages the scheduling, execution, and monitoring of the experimental array by delivering actions to the individual Hubs, which are the granular unit of activity and can execute actions tasks such as positioning, measurement, real-time analytical processing and provides the basis for live visualization. Upon the completion of individual experiments or a sequence thereof, the orchestrator compiles and dispatches a comprehensive analytical report to the experimentalist. The DeviceHub features a high-precision robotic manipulator adept at positioning the SDC head accurately onto the substrate, where a Hamilton Microlab 600 precision syringe system<sup>3</sup> delivers electrolyte directly when contact is established. The Autolab Potentiostat<sup>2</sup> is employed to perform electrochemical measurements once the system is primed for analysis. Quality control protocols, including drop and contact detection and chatbot-based communication, facilitate automation and oversight of the experimental processes. Furthermore, experiments proceed in three automated stages: waste disposal, cleaning, and electrochemical measurement, each executed according to predefined specifications and with real-time plotting provided by a Bokeh<sup>45</sup> visualizer for immediate “at-a-glance” feedback. Post-measurement, the data undergoes immediate analysis via MADAP, which calculates electrochemical markers and generates corresponding plots for in-depth analysis. This processed data is then systematically cataloged in a DMS, ensuring data provenance, facile retrieval, and compartmentalization in alignment with the FAIR principles. It is possible to optimize the subsequent experiment with AL algorithms through the HELAO platform.



## Digital Discovery

measurements, and emergency procedures in place for unresolved non-contact situations. Upon measurement initiation, an established safety threshold for experimental procedures prevents overshooting. Throughout the entire QC process, continuous feedback is provided with logging and the option of communication through a Telegram chatbot, which update the experimentalist at checkpoints and about potential failures, especially beneficial of walk-away experimentation.

Our previously designed modular and versatile data analysis framework, MADAP,<sup>51</sup> capable of analyzing a variety of electrochemical protocols, is additionally integrated into the Multi-AnalyticHub of our high-throughput automated workflow. It enables the real-time transformation of raw measurement into analyzed results for each experiment. The strength of this framework lies in its ability to simultaneously plot the raw and processed data (Fig. 1b, section analysis). The integration of this modular package was a facile solution for Auto-MISCHBARES to gain the ability to generate reports and summaries in compliance with FAIR principles, expanding the platform to include rapid assessment of experimental quality for valuable scientific insights.<sup>3,46</sup> Tailored to our case study, MADAP was expanded with voltammetry tests that include the statistically driven identification of parameters as, for instance, half-wave potential and current, peak-to-peak separation, oxidation and reduction peaks to include them in the report. Additional information about the expanded implementation can be found in ESI 5.†

**4.1.4 DataHub.** The provenance of data is central in drawing conclusions from raw experimental recordings.<sup>29,52,53</sup> This necessitates active tracking of acquisition and processing. To address the challenge of managing these complexities, our DMS implements a real-time approach in the context of the DataHub, which is backed by a locally hosted PostgreSQL database designed to dynamically handle meta, raw, and analyzed data. It consists of several interconnected tables that capture specific details of the proposed experiments. The *experiments* table forms the core of the database and stores essential metadata, such as material, date, and operator information (Fig. 1b, Section DMS). This is complemented by the *users* table, which details the researchers involved, ensuring traceability and accountability. The *motor-positions* table logs the specific operational data, such as precise motor positions of the SDC head, adding further detail to the experimental records. Each type of electrochemical measurement in the database features paired procedures and raw tables. The *procedure* tables encapsulate the unique parameters and settings of every measurement, while the *raw* tables record granular empirical data. Key metrics, provided by MADAP from the Multi-AnalyticHub and passed to HELAO in the ServerHub, support processing large data volumes through web server communication. Robust data integrity is ensured through primary and foreign keys, enabling complex queries that link procedures, raw data, and experimental metadata. Additionally, the

database incorporates sequences for auto-generating Unique Identifiers (UIDs), streamlining data entry and retrieval. This cohesive database system is designed to maintain the integrity, accessibility, usability, and interpretability<sup>54</sup> of experimental data by incorporating both FAIR principles<sup>36</sup> and atomicity, consistency, isolation, and durability (ACID) standards<sup>55</sup> for modern data management and reliable operational processing. Herein, the DataHub offers a unified platform for comprehensive multi-modal data analysis engineered to facilitate the correlation of electrochemical and spectroscopic tests.

The integration of the four key Hubs defines our robust Auto-MISCHBARES platform,<sup>44,50</sup> streamlining sequential experimentation through unified process control, scheduling, feedback, and advanced real-time data management, encompassing measurement, validation, and analysis. Herein, experiments are started in the ServerHub, which schedules and orchestrates the measuring step performed by the instruments in the DeviceHub. The procedure is controlled for its quality and analyzed for its outcome by the MultiAnalyticHub while the DataHub records all trackable data points. A detailed representation of the asynchronous interaction between these Hubs is depicted as a sequence diagram in Fig. 2. The modular design of Auto-MISCHBARES as an open-source Python framework and multiple unit-tests ensure ease of expansion and adaptability for users.

## 4.2 Experimental procedure

To showcase the efficacy of Auto-MISCHBARES, we investigate the formation of the CEI, as it is influenced significantly by the type of active material, the inactive components of the composite electrode, and the electrolyte formulation.<sup>56,57</sup> The presented electrochemical setup, SDC, eliminates the need for cell disassembly for *ex situ* measurements, thus minimizing the risk of mechanical alterations. To demonstrate the reliability and reproducibility of our proposed Auto-MISCHBARES framework, we investigate the evolution of CEI in lithium iron phosphate (LFP), a well-studied cathode material used in commercial batteries.<sup>58–60</sup> We used 1 M LiPF<sub>6</sub> solution in a mixture of ethylene carbonate (EC):ethyl methyl carbonate (EMC) in a 3 : 7 weight ratio as the electrolyte (E-lyte, Germany). The entire setup was maintained in a nitrogen-filled glovebox. It is important to note that electrolyte evaporation can occur due to the open-cell setup. This poses challenges for long-term cycling tests, however, it offers distinct advantages for a variety of short-term measurements, which would otherwise require extensive assembly, disassembly, and electrode post-treatment. We designed our high-throughput sequential experimentation protocol using cyclic voltammetry (CV) tests, which are stopped at different potentials during the second cycle to analyze features related to redox reactions and repeated the procedure two times. Our novel approach to cathode electrode preparation involves screen-printing onto the substrate in

measurement. Orchestration now considers the experiment complete, will notify the user, and will move to the next instance defined in the SOE. The process is repeated until the experimental list defined by the research is completed. The orchestrator will shut down all remaining active components, and details of inputs, outputs, and metadata will be saved in .hdf5 formatted file.





an open atmosphere due to the stability of the active material and slurry components. This method minimizes material usage and precisely defines the active material area. After preparation, the electrodes are transferred to the glovebox for further processing and analysis. For each experiment, the SDC head is positioned at the predefined measurement spot, where it dispenses a droplet of electrolyte and ensures electrical connection before performing CV. Upon completing a series of experiments, it is necessary to remove the excess  $\text{LiPF}_6$  salt residue, a byproduct of electrolyte evaporation, from the electrodes. This is achieved by depositing a droplet of propylene carbonate (PC) on each measurement spot, allowing it to soak for three minutes to dissolve the salt, and then aspirating it using the SDC head. This cleaning process is repeated three times. Once the cleaned samples are dried, they are transferred within the glovebox directly into the XPS's sample environment for *ex situ* analysis, preventing air exposure. The analysis aims to characterize the synthesized CEI at different potentials and identify the formation stages of its components. The CasaXPS software<sup>6†</sup> is utilized to evaluate the outcomes.

## 5 Results and discussions

### 5.1 Reproducibility towards electrode fabrication

In our setup, electrodes were fabricated through screen-printing to ensure reproducible dimensions and alignment on a predefined grid. This method effectively decouples the electrodes from the electrolyte spreading area, thereby minimizing cross-contamination risks associated with electrolyte dispersion on the substrate. Additionally, this technique significantly reduces

waste of active material. Unlike other coating methods such as doctor blading, which produce cut-out waste, screen-printing only coats the specific spots required for measurements.

The electrodes were coated as circular points with a 1.5 mm diameter, arranged in an  $11 \times 11$  square grid with each point spaced 4.9 mm apart. Details can be found in Section 4 of the ESI.<sup>†</sup> To evaluate the uniformity of the coating, these electrodes were analyzed using XRF. Fig. 3a illustrates the distribution of Fe signal intensity across the grid, with the colorbar reflecting the relative Fe content as determined by the integrated signal at each point. As a direct measurement of the active material mass on this type of coating is challenging, the Fe signal in XRF images was used as a proxy for estimating Fe distribution and the active material content. By weighing the Al-foil before and after coating and drying, an average active material mass of 0.0218 mg was calculated. The Fe count per second (CPS) is centered around a central peak, indicating an underlying normal distribution with a maximum spread of  $\pm 6.5\%$ , as depicted in Fig. 3c. Our two distinct sets of measurements are represented by red and blue markers in Fig. 3a. The color distribution across the grid indicates a uniform Fe coating, although some areas exhibit higher or lower concentrations. This is crucial for evaluating the consistency of the screen-printing process. The XRF spectrum of a representative coated point is shown in Fig. 3b and features Fe peaks at 6.41 keV and 7.06 keV. While the spectrum is primarily characterized by Fe, minor peaks for Cr and Ni indicate their subordinate presence. Additional elements including P and Al, with peaks at 2.02 keV and 20.19 keV respectively, are also identified. The peaks, with lower CPS, are detailed in ESI 3.<sup>†</sup> In the electrochemical

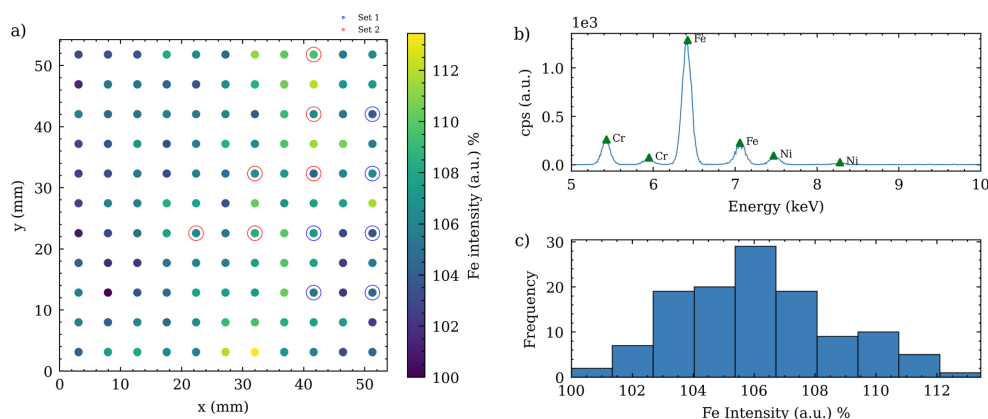


**Fig. 3** (a) Spatial distribution of the integrated relative Fe signal intensity from screen printed electrodes, as measured by XRF. The Fe signal is integrated over a circular area of 1.8 mm in diameter at each measurement point, with color coding indicating the intensity percentage. Set 1 and Set 2 refer to two different batches under which the electrodes were tested, showcasing potential variability in Fe distribution across the samples. (b) Averaged XRF spectrum representing cumulative signals from one of the screen-printed spots, highlighting characteristic X-ray peaks. Peaks are labeled with corresponding elemental symbols, with prominent feature for Fe observed at around 6.4 keV. Other elements such as Cr and Ni are represented at their respective energies, illustrating the composition of the samples. (c) Histogram representing the distribution of Fe intensity percentages across the measurement points. The distribution shows a rightward skew, with a predominant concentration of data points on the lower side of the Fe intensity scale. Despite the skew, the bulk of the data clusters around a central peak, suggesting an underlying normal distribution tendency with some deviations, possible due to variations in the screen-printing process or material heterogeneity.



## Digital Discovery

procedures, such as galvanostatic cycling, this data can be utilized for setting the correct current to achieve the desired C-rate during charging and discharging protocols. For CV, as employed in this study, the information is essential to normalize the obtained current response.

## 5.2 Reproducibility at electrochemical level

Electrochemical data that derived from the automated experiments orchestrated with Auto-MISCHBARES platform demonstrated high reliability, with no observable failures or hardware errors that could compromise the results. All the measurements are stored on-the-fly in our DMS. The CV profiles of LFP electrodes, cycled between 1.8 V and 4.7 V at a scan rate of  $5 \text{ mV s}^{-1}$  are presented for two identical experimental sets for comparison, as shown in Fig. 4a and b. The scan rate selected for our study was an order of magnitude higher than typically reported for battery electrodes.<sup>62</sup> This choice aimed to mitigate issues associated with electrolyte evaporation in our open setup. Such evaporation could disrupt electrical contact between the WE and the RE during measurement and increase salt concentrations in electrolyte.<sup>63</sup> However, these effects were minimized by using a fast scan rate and routine flushing of the SDC head with fresh electrolyte after each measurement. The high scan rate can cause the change of slope in current density for CV measurements.<sup>64</sup>

In both sets of experiments, anodic and cathodic peaks were observed at approximately 3.8 V and 3.15 V, respectively, with a characteristic pair of redox peaks around 3.47 V corresponding to the charge–discharge reaction of  $\text{Fe}^{2+}/\text{Fe}^{3+}$ . In the first set, a minor anodic peak at 4.4 V was also detected, the origin of which remains unclear but aligns with findings reported by

Chen *et al.*<sup>65</sup> Our observed peak values, including anodic ones at 3.7 V, cathodic ones at 3.25 V, and half-wave potentials of 3.4 V at a scan rate of  $0.1 \text{ mV s}^{-1}$ , closely match those documented in their study. It is also important to mention that the reference potential was calibrated against a 5 mM ferrocene solution prior to experimentation.

In the first set of experiments, a slight shift in anodic peaks was observed, while the cathodic peak potential remained constant. The slight increased peak to peak separation, suggests lower reversibility,<sup>66,67</sup> likely due to the higher scan rate<sup>62,64</sup> used in our measurements. However, the experiments were able to replicate features documented in related literature.<sup>65,66</sup> The growing asymmetry in peaks, observed as measurements progressed, can be attributed to increasing conductivity constrains,<sup>65</sup> a result of SEI growth at the CE and the RE, as these were not exchanged between measurements. In the second set of experiments, consistency was observed across all CV tests, with only minor variations in samples 4 and 5. The half-wave potential and peak separation showed a slight shift towards higher values. These changes in polarization might be partially attributed to the distance between the WE and the RE,<sup>68</sup> or to an uneven substrate. Despite these complexities, the overall results from the SDC demonstrated a high degree of reproducibility across both sets of experiments. The synthesized CEI outcomes from these data are suitable for further exploration using *ex situ* techniques.

## 5.3 Reproducibility at spectroscopic levels

Upon completing both sets of electrochemical experiments, the electrodes were rinsed with a PC solution, using SDC system to remove any residual dried electrolyte. After drying, an *ex situ*

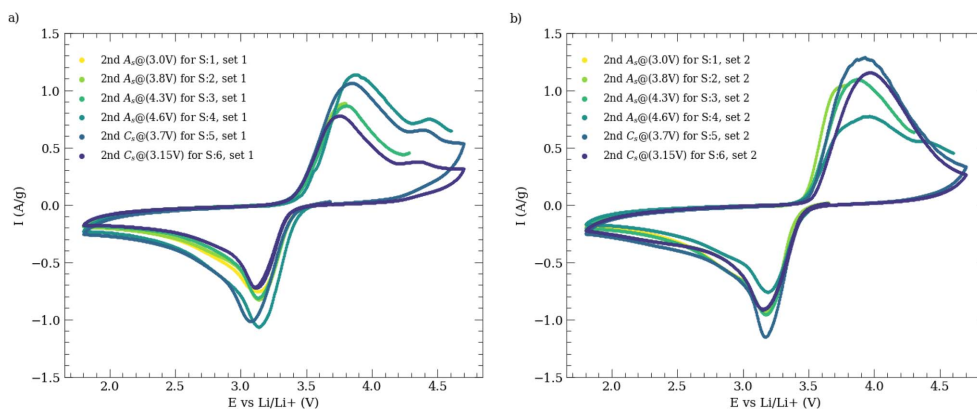


Fig. 4 Demonstration of the second cycle of CV profiles derived from high-throughput experimentation utilizing Auto-MISCHBARES. Experiments were applied within a voltage range between 1.8 V and 4.7 V at a scan rate of  $5 \text{ mV s}^{-1}$ , starting from the OPC in the anodic direction. The CV curves reveal distinct redox peaks and the anodic peaks align closely at approximately 3.8 V while the corresponding cathodic peaks are positioned near 3.15 V, indicating similar consistent electrochemical response with a high degree of overlap across all measurements. (a) illustrates the first set and (b) the second, with each set consisting of six different experiments. For comparative analysis, CV tests that conclude at the same stop potential between the two batches, are color-matched. The exact termination potentials, corresponding to either the anodic or cathodic directions, are denoted in the legend. The reported current density is normalized to the mass of LFP, determined by XRF measurements of the Fe signal as a proxy for the LFP content.

## Paper

View Article Online

Digital Discovery

XPS analysis was performed on the initial experimental set to evaluate the development of the CEI. This analysis identified various species and functional groups, as demonstrated in Fig. 5a across all panels, which presents the spectra from sample 1 (S1) of this set. The C=C peak, representative of the conductive carbon at the electrode surface, was selected as the reference with a relative concentration of 1. All subsequent signals are scaled and normalized to this benchmark.

Within the C 1s region (Fig. 5a, panel I), a variety of carbon-containing species were identified. Peaks at 284.3 eV and 284.8 eV correspond to  $sp^2$  (C=C) and  $sp^3$  (C-C) carbon bonds, respectively. Additional peaks at higher binding energy, such as 286.3 eV, 288.8 eV, and 290.7 eV, were assigned to C-O, carboxyl (O-C=O), and carbonates  $CO_3$  groups. In other samples of this set, a C=O signal was also detected near 287.8 eV (ESI 7 and 9†). These signals are complemented by corresponding peaks in the

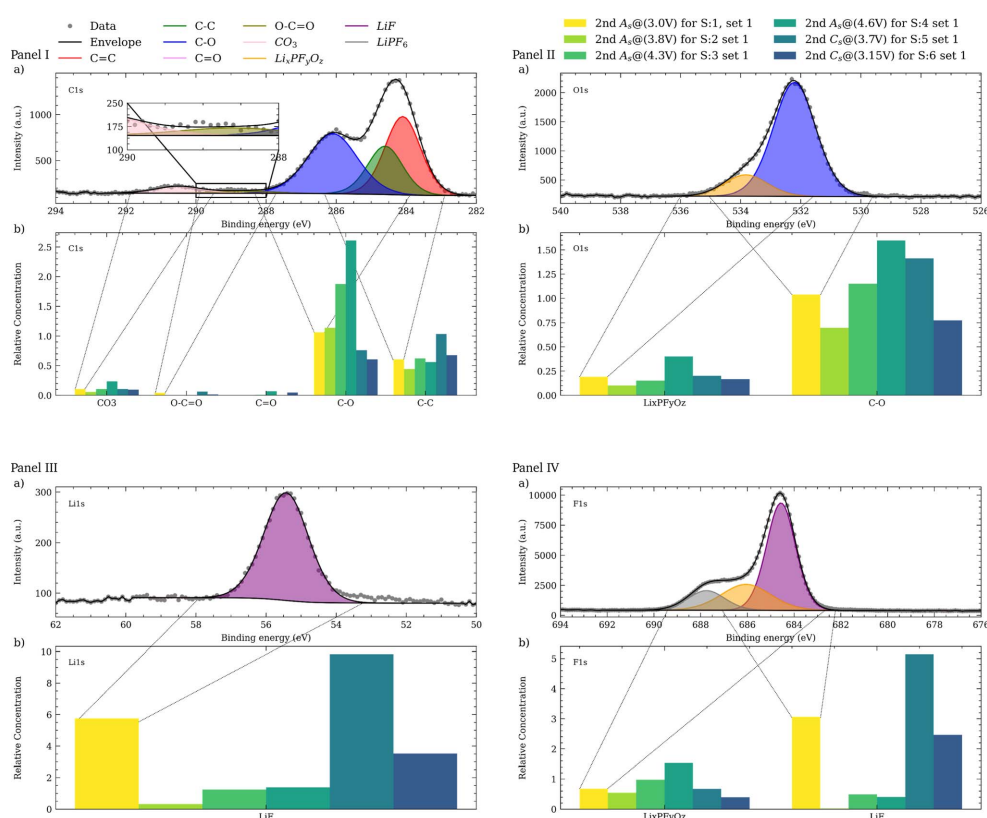


**Fig. 5** Characterization of the synthesized CEI from Auto-MISCHBARES on screen-printed electrode using *ex situ* XPS analysis. In all panels, (a) present the XPS spectra of CEI from sample 1 (S1) in the first experimental series, obtained during the second anodic scan at the stopping potential of 3 V from the CV test. These spectra reveal the diverse chemical composition of this layer, with peaks corresponding to various functional groups and compounds: (panel I) C 1s spectrum with multiple peaks indicative of carbon-based species, including C-C, C-O, and contributions from other carbon-oxygen groups. (Panel II) The O 1s spectrum with a peak for C-O bonds. (Panel III) The Li 1s region with presence of lithium-containing compounds depicted by LiF peak, originating from the decomposition of  $LiPF_6$ . (Panel IV) The F 1s region characterized by peaks associated with fluorinated compounds. Each chemical state identified is denoted by a distinct color in the spectra. The overlaid black line represents the envelope of the aggregated measured data, indicating the sum of contributions from all fitted peaks. The bottom bar charts (b) provide a comparative analysis of the evolution of XPS signals for various species, observed from the first set and aligned by sequence of appearance in the CV tests, illustrating the binding energy signatures of specific chemical states within the CEI with relative concentration at these regions. The C=C peak intensity is set as a reference with the relative concentration of 1, representing the conductive carbon additive at the electrode surface, with other species normalized to this reference. The relative concentration of C-O in the C 1s region shows a significant increase from sample 2 (S2) to sample 4 (S4), followed by a decrease in sample 5 (S5). In contrast, the LiF signal in the Li 1s and F 1s regions decreases up until S4 and then exhibits a sharp increase from S4 to S5. The behavior for  $Li_xPF_yO_z$  species in the O 1s and F 1s regions follows a similar pattern to that of the C-O group.





## Digital Discovery

View Article Online

Paper

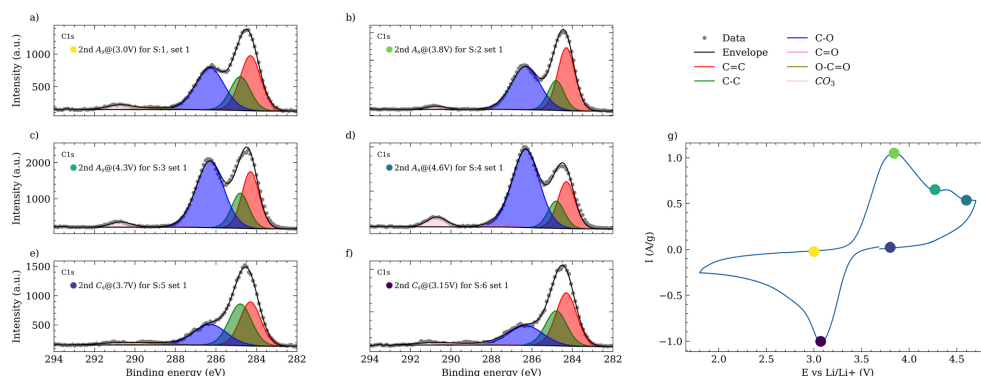


Fig. 6 Representation of the XPS spectra in the C 1s region for all samples from the first set of high-throughput experimentation (a–f). The key potentials at which measurements were paused during the second cycle of CV test are depicted in (g). During the anodic scan (a–d), an increase in the intensity of signals from organic species, such as C–O, is observed, indicative of the evolving composition of the CEI. During the cathodic scan (e and f), this intensity decreases significantly.

O 1s region, with a major contribution from C–O bonds, centered at 532.4 eV (Fig. 5a, panel II). In the F 1s spectrum (Fig. 5a, panel IV), the residuals from the LiPF<sub>6</sub> salt is discernible at 688.0 eV. The remaining salt from the rinsing process suggests a need for further investigation by utilizing EMC or dimethyl carbonate (DMC) to potentially enhance the efficiency of the washing procedure, due to their higher LiPF<sub>6</sub> and lower LiF solubility. In the O 1s region, fluorophosphates, as degradation products of LiPF<sub>6</sub> observed at 534.0 eV, with corresponding signals at 686.6 eV in the F 1s region. The signal for LiF, indicating the presence of fluorinated and lithiated species, is evident at 684.8 eV in the F 1s and 55.6 eV in the Li 1s region (Fig. 5a, panel III). The similarity between the C–O and Li<sub>x</sub>PF<sub>y</sub>O<sub>z</sub> compounds reflects the dynamic alterations of the CEI composition throughout the electrochemical cycling process.

Fig. 5b for all panels, illustrate the evolution of the XPS signals across all the samples of this series. During the anodic scan of the CV measurement, an increase in the intensity of signals from organic species, such as C–O is observed in both C 1s and O 1s regions. These signals are attributed to the decomposition products of the electrolyte and contribute to the formation of the outer layer of the CEI. Notably, the increase in these signals becomes apparent in S3, at 4.3 V, coinciding with the peak of the anodic feature and subsequent potential elevation, consistent with findings reported by Kühn *et al.*<sup>56</sup> In contrast, during the cathodic scan, the intensity of these species decreases significantly from 4.6 V to 3.7 V. This pattern further supported by Fig. 6, exhibiting the C 1s trends across all samples. The observed increase in organic species during the anodic scan is indicative of a thickening of the CEI, presumably due to electrolyte decomposition at elevated voltages, which is supported by several studies<sup>69–72</sup> and evidenced by the reduced LiF signal from S1 to S4 (Fig. 5b, panel IV). During discharge, the cathodic scan shows an increasing LiF signal, suggesting the reformation of LiF, along with a decrease in C–O species.<sup>73</sup>

At last, the XPS analysis validates the electrochemical data at every potential, pinpointing key regions within the CV profile. This correlation further enhances the integrity of our designed Auto-MISCHBARES workflow, contributing to the robustness and advancement of MAPs.

## 6 Conclusions

A critical question that arises with high-throughput platforms is whether they truly accelerate processes or inadvertently cause deceleration. Answering this, requires considering three key aspects: reliability, time efficiency, and reproducibility. Regarding reliability, Auto-MISCHBARES, represents a significant advancement in laboratory automation and scientific experimentation by integrating a comprehensive array of key components for robust, sequential experimentation. It covers a wide range of functionalities, from configuring and scheduling experiments to robust online control assessment, and provides real-time feedback on critical failures and experimental progress. Encompassing computer vision and statistical tools, the platform not only ensures the reliability of outcomes but also streamlines tasks to minimize researcher intervention and reduce human errors. Its real-time measurement capabilities, enable live visualization and can further optimize the workflow, from data acquisition to comprehensive analysis. The structured PostgreSQL database environment within the platform efficiently manages data formats, strengthen data correlation across multiple measurements and lays the ground for transfer learning. In our SDC system, the modifications to mechanical integrity are minimal as opposed to coin cell setups where disassembly can lead to the breaking of coatings at the edges of the electrodes, and sometimes even cause the coating to stick to the separator. Our SDC system is a more reliable and less intrusive approach to cell handling and is suitable for applications in electrochemical studies.



## Paper

View Article Online

Digital Discovery

To establish time efficiency, our hierarchical framework demonstrates significant advantages due to its uninterrupted operational capabilities, which minimize the need for manual cell exchanges. For instance, considering our study scenario where our substrate consists of 121 electrode spots, each requiring a one-hour CV test. In this case, our Auto-MISCHBARES platform, using the SDC head, would complete the measurements in 121 hours, with an additional 10 hours for rinsing, and moving for a total of 131 hours. In contrast, the traditional manual approach would require extra time for cell assembly and disassembly, which takes an experienced researcher an additional 24 hours. Assuming an 8 hour workday without breaks, the manual process would span several days. Additionally, considering the limitation of processing only about 10 coin cells simultaneously due to channel availability in the cycler, this manual approach could extend the duration even further. While the measurement times are similar between our platform and manual methods, our framework's ability to operate continuously substantially enhances the time efficiency. As demonstrated in our previous study,<sup>30</sup> the capability of our framework for parallelization across multiple SDCs as well as its integration with AL frameworks can further accelerate the process.

To address the final aspect of reproducibility, our platform proves validity in both electrode fabrication and electrochemical measurements. The use of screen-printing to create miniaturized, defined areas of measurement not only saves materials but also facilitates automated *ex situ* analysis. This is attributed to the precisely arranged grid of measurement positions established by the screen-printed mask on the substrate. Further enhancements in future studies can be achieved by integrating XRF measurement results into the platform, allowing for the identification of mask defects and the selection of points with minimal deviation, thus reducing issues related to electrode thickness variation. Such variations can also affect the distance between the WE and RE, potentially leading to deviations in measurements.<sup>64</sup> These challenges can be further minimized by directly coating onto the substrate holder and avoid the use of a bendable foil for electrode fabrication. The consistency of our high-throughput electrochemical protocols, along with their correlation with XPS results that align with findings in the literature, further underscore the reproducibility and fidelity of our system. Auto-MISCHBARES enables in-depth investigation into the synthesis of SEI/CEI, especially for post-lithium battery materials, an area that still holds vast potential for exploration. It should be noted that the proposed electrochemical experimentation setup is bound by the availability of the measurement devices and their licensed software. However, through the modularity and agnosticism of the platform, Auto-MISCHBARES can be expanded with minimal effort following the provided templates to include any laboratory device needed for any specific experimental scenario.

Integrating the comprehensive capabilities of our platform, we establish a trustworthy foundation with online analytical characterization, robust data fidelity and management systems. This integration facilitates the incorporation of ML and AL algorithms, enhancing decision-making and accelerating

material optimization. Our hierarchical web server framework, which has been previously integrated with AL, now allows for further integration with more complex experimental planning algorithms such as Chimera<sup>74</sup> and Griffyn.<sup>75</sup> Additionally, for future study, the inclusion of cutting-edge approaches such as large language modeling (LLM) can further assist researchers,<sup>13</sup> steering us towards the ultimate goal of a fully reliable material acceleration platforms. Our user-friendly framework, committed to digitalization and technological integration, represents a crucial step towards the development of fully autonomous laboratories, which can significantly expanding the scope of scientific exploration.

### Additional information

Additional information can be found in the ESI.†

### Data and code availability

Data, supporting the findings of this study, are available online at <https://doi.org/10.5281/zenodo.10444324>. The Auto-MISCHBARES framework<sup>44</sup> can be cloned from <https://github.com/fuzhanrahmanian/MISCHBARES>. In addition, videos recorded from our fully autonomous workflow<sup>50</sup> can be accessed at <https://doi.org/10.5281/zenodo.10445749>.

### Author contributions

F. R. conceived the experiments, design the data analysis MADAP and Auto-MISCHBARES software, developed the quality control protocols, validation tests, and user interface. H. S. S. prepared the mask for screen printing. B. Z. designed and printed the waste, wipe, and camera housing. S. F. prepared the electrode material and coated them onto the printed mask. F. R. and S. F. assisted in experimentation and S. F. characterized the samples by applying XPS. All authors reviewed the manuscript.

### Conflicts of interest

The authors declare no conflict of interest.

### Acknowledgements

This work contributes to TUM Battery, the Munich Data Science Institute, and the Munich Institute for Robotic and Machine Intelligence. This work contributes to the research performed at CELEST (Center for Electrochemical Energy Storage Ulm-Karlsruhe) and was partly funded by the German Research Foundation (DFG) under Project ID 390874152 (POLiS Cluster of Excellence). This project also received funding from the European Union's Horizon 2020 research and innovation program under grant agreement No. 957189. The project is part of BATTERY 2030+, the large-scale European research initiative for inventing sustainable batteries for the future, funded by European Union's Horizon 2020 research and innovation program under Grant Agreement No. 957213 (BIG-MAP). HSS



View Article Online

Digital Discovery

Paper

acknowledges funding from German Research Foundation (DFG) under Project ID 390776260 (eConversion Cluster of Excellence).

## Notes and references

- H. S. Stein, *Trends Chem.*, 2022, **4**, 682–684.
- E. Stach, B. DeCost, A. G. Kusne, J. Hatrick-Simpers, K. A. Brown, K. G. Reyes, J. Schrier, S. Billinge, T. Buonassisi, I. Foster, *et al.*, *Matter*, 2021, **4**, 2702–2726.
- L. M. Roch, F. Häse, C. Kreisbeck, T. Tamayo-Mendoza, L. P. Yunker, J. E. Hein and A. Aspuru-Guzik, *PLoS One*, 2020, **15**, e0229862.
- M. Seifrid, R. Pollice, A. Aguilar-Granda, Z. Morgan Chan, K. Hotta, C. T. Ser, J. Vestfrid, T. C. Wu and A. Aspuru-Guzik, *Acc. Chem. Res.*, 2022, **55**, 2454–2466.
- A. E. Gongora, B. Xu, W. Perry, C. Okoye, P. Riley, K. G. Reyes, E. F. Morgan and K. A. Brown, *Sci. Adv.*, 2020, **6**, eaazi1708.
- P. Nikolaev, D. Hooper, F. Webber, R. Rao, K. Decker, M. Krein, J. Poleski, R. Barto and B. Maruyama, *npj Comput. Mater.*, 2016, **2**, 1–6.
- A. Dave, J. Mitchell, S. Burke, H. Lin, J. Whitacre and V. Viswanathan, *Nat. Commun.*, 2022, **13**, 5454.
- Y. Shi, P. L. Prieto, T. Zepel, S. Grunert and J. E. Hein, *Acc. Chem. Res.*, 2021, **54**, 546–555.
- M. Abolhasani and E. Kumacheva, *Nat. Synth.*, 2023, **2**, 483–492.
- S. Ament, M. Amsler, D. R. Sutherland, M.-C. Chang, D. Guevarra, A. B. Connolly, J. M. Gregoire, M. O. Thompson, C. P. Gomes and R. B. van Dover, *Sci. Adv.*, 2021, **7**, eabg4930.
- R. Ramprasad, R. Batra, G. Pilania, A. Mannodi-Kanakkithodi and C. Kim, *npj Comput. Mater.*, 2017, **3**, 54.
- A. Vriza, H. Chan and J. Xu, *Chem. Mater.*, 2023, **35**, 3046–3056.
- Z. Zheng, O. Zhang, C. Borgs, J. T. Chayes and O. M. Yaghi, *J. Am. Chem. Soc.*, 2023, **145**, 18048–18062.
- I. M. Pendleton, G. Cattabriga, Z. Li, M. A. Najeeb, S. A. Friedler, A. J. Norquist, E. M. Chan and J. Schrier, *MRS Commun.*, 2019, **9**, 846–859.
- H. S. Stein, A. Sanin, F. Rahmanian, B. Zhang, M. Vogler, J. K. Flowers, L. Fischer, S. Fuchs, N. Choudhary and L. Schroeder, *Curr. Opin. Electrochem.*, 2022, **35**, 101053.
- J. Amici, P. Asinari, E. Ayerbe, P. Barboux, P. Bayle-Guillemaud, R. J. Behm, M. Bercebar, E. Berg, A. Bhowmik, S. Bodoardo, *et al.*, *Adv. Energy Mater.*, 2022, **12**, 2102785.
- C. Ling, *npj Comput. Mater.*, 2022, **8**, 33.
- L. Su, M. Ferrandon, J. A. Kowalski, J. T. Vaughney and F. R. Brushett, *J. Electrochem. Soc.*, 2014, **161**, A1905.
- S. Matsuda, K. Nishioka and S. Nakanishi, *Sci. Rep.*, 2019, **9**, 6211.
- D. Martín-Yerga, M. Kang and P. R. Unwin, *ChemElectroChem*, 2021, **8**, 4240–4251.
- S. Dieckhöfer, W. Schuhmann and E. Ventosa, *ChemElectroChem*, 2021, **8**, 3143–3149.
- K. Sliozberg, D. Schäfer, T. Erichsen, R. Meyer, C. Khare, A. Ludwig and W. Schuhmann, *ChemSusChem*, 2015, **8**, 1270–1278.
- C. Yada, C. E. Lee, D. Laughman, L. Hannah, H. Iba and B. E. Hayden, *J. Electrochem. Soc.*, 2015, **162**, A722.
- D. Rajagopal, A. Koeppe, M. Esmailpour, M. Selzer, W. Wenzel, H. Stein and B. Nestler, *Adv. Energy Mater.*, 2023, **13**, 2301985.
- S. G. Baird and T. D. Sparks, *Matter*, 2022, **5**, 4170–4178.
- R. Pollice, G. dos Passos Gomes, M. Aldeghi, R. J. Hickman, M. Krenn, C. Lavigne, M. Lindner-D'Addario, A. Nigam, C. T. Ser, Z. Yao, *et al.*, *Acc. Chem. Res.*, 2021, **54**, 849–860.
- I. E. Castelli, D. J. Arismendi-Arrieta, A. Bhowmik, I. Cekic-Laskovic, S. Clark, R. Dominko, E. Flores, J. Flowers, K. Ulvskov Frederiksen, J. Friis, *et al.*, *Batteries Supercaps*, 2021, **4**, 1803–1812.
- M. Vogler, J. Busk, H. Hajiyani, P. B. Jørgensen, N. Safaei, I. E. Castelli, F. F. Ramirez, J. Carlsson, G. Pizzi, S. Clark, *et al.*, *Matter*, 2023, **6**, 2647–2665.
- D. Guevarra, K. Kan, Y. Lai, R. J. Jones, L. Zhou, P. Donnelly, M. Richter, H. S. Stein and J. M. Gregoire, *Digital Discovery*, 2023, **2**, 1806–1812.
- F. Rahmanian, J. Flowers, D. Guevarra, M. Richter, M. Fichtner, P. Donnelly, J. M. Gregoire and H. S. Stein, *Adv. Mater. Interfaces*, 2022, **9**, 2101987.
- P. Raghavan, B. C. Haas, M. E. Ruos, J. Schleinitz, A. G. Doyle, S. E. Reisman, M. S. Sigman and C. W. Coley, *ACS Cent. Sci.*, 2023, **9**, 2196–2204.
- M. Krenn, R. Pollice, S. Y. Guo, M. Aldeghi, A. Cervera-Lierta, P. Friederich, G. dos Passos Gomes, F. Häse, A. Jinich, A. Nigam, *et al.*, *Nat. Rev. Phys.*, 2022, **4**, 1–9.
- A. Benayad, D. Diddens, A. Heuer, A. N. Krishnamoorthy, M. Maiti, F. L. Cras, M. Legallais, F. Rahmanian, Y. Shin, H. Stein, *et al.*, *Adv. Energy Mater.*, 2022, **12**, 2102678.
- F. Rahmanian, R. M. Lee, D. Linzner, K. Michel, L. Merker, B. B. Berkes, L. Nuss and H. S. Stein, *Attention towards chemistry agnostic and explainable battery lifetime prediction*, 2023.
- L. Pascasio, S. Rihm, A. Naseri, S. Mosbach, J. Akroyd and M. Kraft, *J. Chem. Inf. Model.*, 2023, **21**, 6569–6586.
- M. D. Wilkinson, M. Dumontier, I. J. Aalbersberg, G. Appleton, M. Axton, A. Baak, N. Blomberg, J.-W. Boiten, L. B. da Silva Santos, P. E. Bourne, *et al.*, *Sci. Data*, 2016, **3**, 1–9.
- S. Rohrbach, M. Šiaučiuolis, G. Chisholm, P.-A. Pirvan, M. Saleeb, S. H. M. Mehr, E. Trushina, A. I. Leonov, G. Keenan, A. Khan, *et al.*, *Science*, 2022, **377**, 172–180.
- M. Christensen, L. P. Yunker, P. Shiri, T. Zepel, P. L. Prieto, S. Grunert, F. Bork and J. E. Hein, *Chem. Sci.*, 2021, **12**, 15473–15490.
- P. Shiri, V. Lai, T. Zepel, D. Griffin, J. Reifman, S. Clark, S. Grunert, L. P. Yunker, S. Steiner, H. Situ, *et al.*, *Science*, 2021, **24**, 102176.
- S. Eppel, H. Xu, M. Bismuth and A. Aspuru-Guzik, *ACS Cent. Sci.*, 2020, **6**, 1743–1752.
- G. Smith and E. J. Dickinson, *Nat. Commun.*, 2022, **13**, 6832.

Open Access Article. Published on 21 March 2024. Downloaded on 6/23/2024 2:55:22 PM.  
This article is licensed under a Creative Commons Attribution 3.0 Unported Licence.



## Paper

- 42 S. Daboss, F. Rahmanian, H. S. Stein and C. Kranz, *Electrochem. Sci. Adv.*, 2022, **2**, e2100122.
- 43 B. Burger, P. M. Maffettone, V. V. Gusev, C. M. Aitchison, Y. Bai, X. Wang, X. Li, B. M. Alston, B. Li, R. Clowes, *et al.*, *Nature*, 2020, **583**, 237–241.
- 44 F. Rahmanian, *Auto-MISCHBARES*, 2023, <https://github.com/fuzhanrahmanian/MISCHBARES>.
- 45 Bokeh Development Team, *Bokeh: Python library for interactive visualization*, 2018.
- 46 S. Back, A. Aspuru-Guzik, M. Ceriotti, G. Gryn'ova, B. A. Grzybowski, G. H. Gu, J. E. Hein, K. Hippalgaonkar, R. Hormazabal, Y. Jung, *et al.*, *Digital Discovery*, 2024, **3**(1), 22–33.
- 47 P. M. Maffettone, P. Friederich, S. G. Baird, B. Blaiszik, K. A. Brown, S. I. Campbell, O. A. Cohen, R. L. Davis, I. T. Foster, N. Haghmoradi, *et al.*, *Digital Discovery*, 2023, **2**, 1644–1659.
- 48 M. Grinberg, *Flask web development: developing web applications with python*, O'Reilly Media, Inc., 2018.
- 49 G. Bradski, *Dr. Dobb's Journal of Software Tools*, 2000.
- 50 F. Rahmanian, *Auto-MISCHBARES: Tutorial & Demonstration*, 2023, DOI: [10.5281/zenodo.10445749](https://doi.org/10.5281/zenodo.10445749).
- 51 F. Rahmanian, *Modular and Autonomous Data Analysis Platform (MADAP)*, 2023, DOI: [10.5281/zenodo.10357192](https://doi.org/10.5281/zenodo.10357192).
- 52 C. Draxl and M. Scheffler, *J. Phys.: Mater.*, 2019, **2**, 036001.
- 53 M. Uhrin, S. P. Huber, J. Yu, N. Marzari and G. Pizzi, *Comput. Mater. Sci.*, 2021, **187**, 110086.
- 54 J. Medina, A. W. Ziaullah, H. Park, I. E. Castelli, A. Shaon, H. Bensmail and F. El-Mellouhi, *Matter*, 2022, **5**, 3614–3642.
- 55 T. Haerder and A. Reuter, *ACM computing surveys (CSUR)*, 1983, **15**, 287–317.
- 56 S. P. Kühn, K. Edström, M. Winter and I. Cekic-Laskovic, *Adv. Mater. Interfaces*, 2022, **9**, 2102078.
- 57 H. Wang, X. Li, F. Li, X. Liu, S. Yang and J. Ma, *Electrochem. Commun.*, 2021, **122**, 106870.
- 58 X. Chen, W. Shen, T. T. Vo, Z. Cao and A. Kapoor, *2012 10th International Power & Energy Conference (IPEC)*, 2012, pp. 230–235.
- 59 D. Anseán González, M. González Vega, J. C. Viera Pérez, J. C. Álvarez Álvarez, C. J. Blanco Viejo, V. García *et al.*, *Conference and Exhibition-2013 International Conference on New Concepts in Smart Cities: Fostering Public and Private Alliances, SmartMILE 2013*, 2013.
- 60 P. Ayuso, H. Beltran, J. Segarra-Tamarit and E. Pérez, *Math. Comput. Simulat.*, 2021, **183**, 97–115.
- 61 N. Fairley, V. Fernandez, M. Richard-Plouet, C. Guillot-Deudon, J. Walton, E. Smith, D. Flahaut, M. Greiner, M. Biesinger, S. Tougaard, *et al.*, *Appl. Surf. Sci. Adv.*, 2021, **5**, 100112.
- 62 M. Mao, B. Huang, Q. Li, C. Wang, Y.-B. He and F. Kang, *Nano Energy*, 2020, **78**, 105282.
- 63 Y. Pan, G. Wang and B. L. Lucht, *Electrochim. Acta*, 2016, **217**, 269–273.
- 64 J. Ming, M. Li, P. Kumar and L.-J. Li, *ACS Nano*, 2016, **10**, 6037–6044.
- 65 Z.-Y. Chen, H.-L. Zhu, Z. Wei, J.-L. Zhang and Q.-F. Li, *Trans. Nonferrous Met. Soc. China*, 2010, **20**, 614–618.
- 66 J. Hou, R. Girod, N. Nianias, T.-H. Shen, J. Fan and V. Tileli, *J. Electrochem. Soc.*, 2020, **167**, 110515.
- 67 L. T. N. Huynh, H. H. A. Nguyen, T. T. D. Tran, T. T. T. Nguyen, T. M. A. Nguyen, T. H. La, V. M. Tran, M. L. P. Le, *et al.*, *J. Nanomater.*, 2019, **2019**, 2464920.
- 68 N. Elgrishi, K. J. Rountree, B. D. McCarthy, E. S. Rountree, T. T. Eisenhart and J. L. Dempsey, *J. Chem. Educ.*, 2018, **95**, 197–206.
- 69 N. Mahne, S. E. Renfrew, B. D. McCloskey and S. A. Freunberger, *Angew. Chem., Int. Ed.*, 2018, **57**, 5529–5533.
- 70 R. Wang, X. Yu, J. Bai, H. Li, X. Huang, L. Chen and X. Yang, *J. Power Sources*, 2012, **218**, 113–118.
- 71 K. Tasaki, A. Goldberg, J.-J. Lian, M. Walker, A. Timmons and S. J. Harris, *J. Electrochem. Soc.*, 2009, **156**, A1019.
- 72 Z.-W. Yin, X.-X. Peng, J.-T. Li, C.-H. Shen, Y.-P. Deng, Z.-G. Wu, T. Zhang, Q.-B. Zhang, Y.-X. Mo, K. Wang, *et al.*, *ACS Appl. Mater. Interfaces*, 2019, **11**, 16214–16222.
- 73 Q. Li, Y. Wang, X. Wang, X. Sun, J.-N. Zhang, X. Yu and H. Li, *ACS Appl. Mater. Interfaces*, 2019, **12**, 2319–2326.
- 74 F. Häse, L. M. Roch and A. Aspuru-Guzik, *Chem. Sci.*, 2018, **9**, 7642–7655.
- 75 F. Häse, M. Aldeghi, R. J. Hickman, L. M. Roch and A. Aspuru-Guzik, *Applied Physics Reviews*, 2021, **8**, 031406.



### 4.5.3. Supporting Information

Electronic Supplementary Material (ESI) for Digital Discovery.  
This journal is © The Royal Society of Chemistry 2024

#### Autonomous Millimeter Scale High Throughput Battery Research System

Fuzhan Rahmanian<sup>1,2,4,5,6\*</sup>, Stefan Fuchs<sup>1,2</sup>, Bojing Zhang<sup>1,2,4,5,6</sup>, Maximilian Fichtner<sup>1,3</sup>, and Helge Sören Stein<sup>4,5,6\*</sup>

<sup>1</sup>Helmholtz Institute Ulm, Applied Electrochemistry, Helmholtzstr. 11, 89081 Ulm, Germany

<sup>2</sup>Karlsruhe Institute of Technology, Institute of Physical Chemistry, Fritz-Haber-Weg 2, 76131 Karlsruhe, Germany

<sup>3</sup>Karlsruhe Institute of Technology, Institute of Nanotechnology, , 76021 Karlsruhe, Germany

<sup>4</sup>Technische Universität München, School of Natural Sciences, Department of Chemistry Lichtenbergstr 4, 85748 Garching, Germany

<sup>5</sup>Technische Universität München, Munich Data Science Institute, Walther-von-Dyck-Straße 10, 4, 85748 Garching, Germany

<sup>6</sup>Technische Universität München, Munich Institute for Robotic and Machine Intelligence, Georg-Brauchle-Ring 60-62, 80992 Munich, Germany

\*corresponding author(s): Helge Sören Stein (helge.stein@tum.de),  
Fuzhan Rahmanian (fuzhan.rahmanian@tum.de)

**Supplementary Information**

## 1 Technology Stack

The autonomous millimeter scale high-throughput battery research system (Auto-MISCHBARES) project, accessible over GitHub at <https://github.com/fuzhanrahmanian/MISCHBARES>, is a Python-based web application developed on top of hierarchical autonomous laboratory automation and orchestration (HELAO)<sup>1</sup>, which uses FastAPI<sup>2</sup> and leverages asynchronous Uvicorn<sup>3</sup> as Asynchronous Server Gateway Interface (ASGI) for handling the flow of electrochemical experimentation. The logical representation of Auto-MISCHBARES is divided into Hubs, each dedicated to a specific task yet sharing a common codebase. Central is the ServerHub, which utilizes FastAPI<sup>2</sup> for task delegation and hosts user interfaces for experimental definition developed with Flask<sup>4</sup>, Node.js, HTML, and CSS for web-based interactions. It also encompasses a live visualizer build with `bokeh`<sup>5</sup> package leveraging WebSockets<sup>6</sup>. The DeviceHub manages connectors for the different devices and acts as an intermediary between the equipment and the ServerHub. It enables Ethernet connections to the Hamilton Pump system <https://www.hamiltoncompany.com/laboratory-products/microlab-600/syringe-pump> and COM serial port connections to the stepper motor <https://www.owis.eu/en/>. Both systems are controlled using the API and DLLs provided by the manufacturer. The Metrohm potentiostat [https://www.metrohm.com/de\\_de/products/a/ut30/aut302n\\_s.html](https://www.metrohm.com/de_de/products/a/ut30/aut302n_s.html) is controlled by the Autolab SDK and the Metrohm DLLs. All DLLs are imported using `pythonnet`<sup>7</sup>, allowing C# compiled code to be integrated. The DataHub utilizes `NumPy`<sup>8</sup> and `Pandas`<sup>9</sup> for data processing and connects to a local PostgreSQL database<sup>10</sup> via the `psycopg2`<sup>11</sup> database adapter. The MultiAnalyticHub utilizes a range of open-source packages, including `OpenCV`<sup>12</sup> for motion detection and Modular and Autonomous Data Analysis Platform (MADAP)<sup>13</sup> for electrochemical analysis, enhanced by `scikit-learn`<sup>14</sup> and `SciPy`<sup>15</sup> for statistical parameter computation. Extensive unit and functional testing is implemented with the `pytest` package<sup>16</sup>. Documentation is available at <https://fuzhanrahmanian.github.io/MISCHBARES/>.

## 2 Operational guidelines

Researchers interested in the usage of Auto-MISCHBARES must first configure the `main_config.py` file with the correct IP addresses for the devices, paths to the manufacturers' DLLs, detailed quality control settings if desired, provide admin user credentials, password, and address for a hosted PostgreSQL database<sup>10</sup>, and give the Telegram API and Chat ID as environmental variables. Python packages listed in the `requirements.txt` file should be installed within the desired environment, and the Web user interface (UI) (Fig. 1) can be started by executing the `app.py` file. This UI consists of a login portal and a configuration panel. The login section secures user access, requires credentials for system entry, and ensures experiment accountability. Users can define general settings in the main configuration panel, generate measurement grids, and manage experimental parameters across multiple batches. The settings allow for the specification of individual experiments and their parameters within each batch. Users can run the experiment, save and retrieve configurations which are written as JSON formatted files picked up by the Auto-MISCHBARES application once the experiment begins. The `main.py` file serves as the entry point for running experiments, controlling the start and shutdown of all involved actions and servers, and performing the configured sequence of experiments. After the initial movement of the Scanning Droplet Cell (SDC) head, quality control for material sufficiency will display the camera feed for movement detection. Following wiping, the live visualizer will asynchronously display the voltage until contact is established. Subsequently, the visualizer will also display the live measurement. If quality checks fail, the orchestrator will either suspend the experimentation or stop it completely, depending on the scenario. After each measurement, analysis is performed on the fly, and results and raw data are stored in their respective tables in the database. All records are decorated with a Unique Identifier (UID), and each experiment acts as the primary key for its performed measurements, which in turn serves as the primary key for the collected analysis and raw data. Reports of the analysis will be plotted and saved in the configured folders, and the logged-in researcher will be notified of the progress. This process will be repeated until all the defined sequences of the experiment are performed. Upon completion, servers are shut down automatically, and an additional `.hdf5` file will be logged with all the experimental run's input, output, and metadata. A live demonstrative run, including a detailed tutorial, can be found on YouTube at [https://www.youtube.com/watch?v=dMZ1WIy7i5s&ab\\_channel=FuzhanR](https://www.youtube.com/watch?v=dMZ1WIy7i5s&ab_channel=FuzhanR).

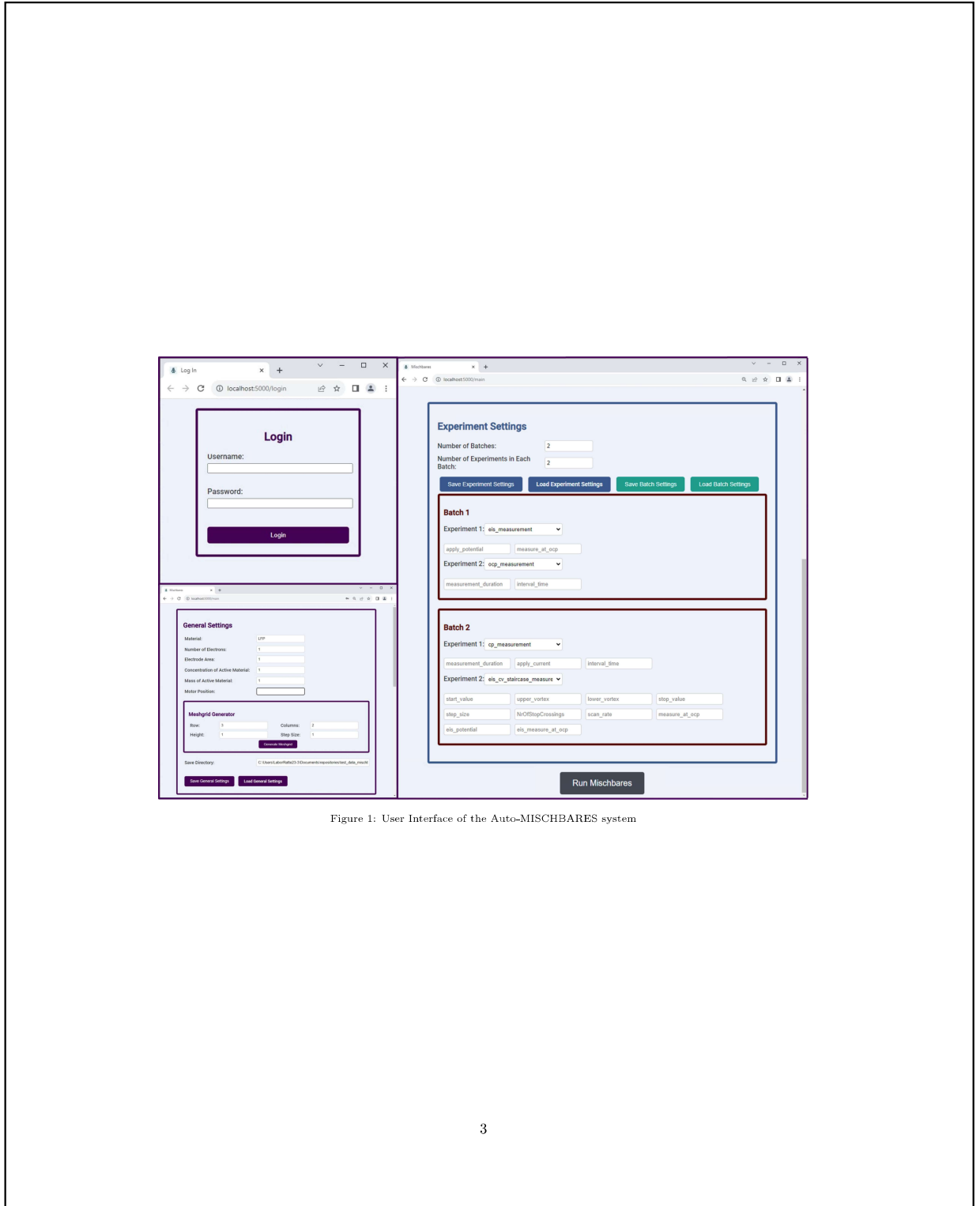


Figure 1: User Interface of the Auto-MISCHBARES system



### 3 XRF test measurement

X-ray Fluorescence (XRF) mapping was performed using a HORIBA XGF-900 micro X-ray Fluorescence Analytical Microscope ( $\mu$ -XRF, Horiba Scientific, Japan). The spectra were acquired using a Rh source with an energy of 50 kV and 100  $\mu$ m polycapillary optics without an energy filter. The XRF elemental maps depicted in Supp. 2 show the distributions of Fe, Cr, Mn, Ni, Al and P on the screen-printed LFP electrodes. Fe and P show their highest intensities as circular points of 1.5 mm diameter in a 11x11 grid with a spacing of 4.9 mm correlating to the screen-printed LFP electrodes. Here, P is exclusively observed on these spots, while Fe can also be observed at a low intensity on the space surrounding that area. Cr, Mn, Ni, Al can be observed on the space surrounding the circular points. This area corresponds to the exposed Al-foil and Cr, Mn, Ni and the Fe observed, are related to impurities from the machining process of the foil as these are common components of stainless steel.

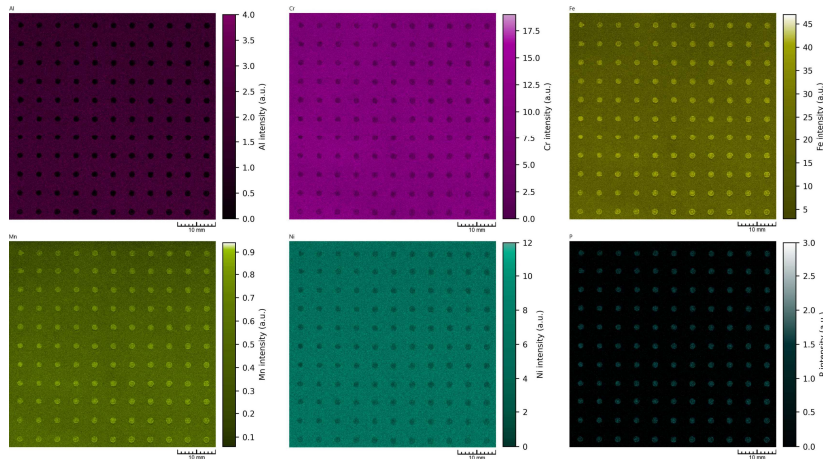


Figure 2: XRF elemental distribution maps of the screen-printed LFP electrodes showing the distribution of Al, Cr, Fe, Mn, Ni, and P. Bright colors show high concentrations, while dark colors show lower concentrations. The coated points can be observed as circular spots in the elemental maps, where the presence of overlying active material reduces the background to negligible levels. Notably, the spatial distribution of Mn and Fe possess comparable patterns, which can be explained due to their comparable ionic radii and chemical affinities. Despite this similarity, the signal intensity of Mn is significantly lower compared to Fe, which indicates different concentration levels within the sample. Subtle differences in their spatial distribution may relate to the manufacturing process.

## 4 Electrode production

The screen printing mask was prepared by applying the mask emulsion (FLX Screen hybrid-fotoemulsion) onto a 43T/110 silk net mesh, subsequently drying it in a dark room, and then hardening it through exposure to ultraviolet (UV) light. Circular holes were imprinted onto the mask to serve as electrodes.

### 4.1 Preparation of the LFP electrodes

For the fabrication of the cathode working electrode, a homogeneous slurry was prepared. This slurry comprised LFP, Carbon Black, and Carboxymethylcellulose (CMC, Sigma-Aldrich, medium viscosity) as a binder, in a weight ratio of 8.5 : 1 : 0.5, respectively. Milli-Q water (18.2 M $\Omega$ cm) was utilized as the solvent. The mixture was subjected to a two-cycle blending process in a Planetary Centrifugal Mixer (Thinky, ARE250), with each cycle consisting of a mixing phase at 1500 rpm for 10 minutes and a defoaming phase at 400 rpm for 1 minute. Subsequently, the Aluminum foil, employed as the current collector, was etched in a 1 M KOH solution for a minute to enhance surface roughness, thereby



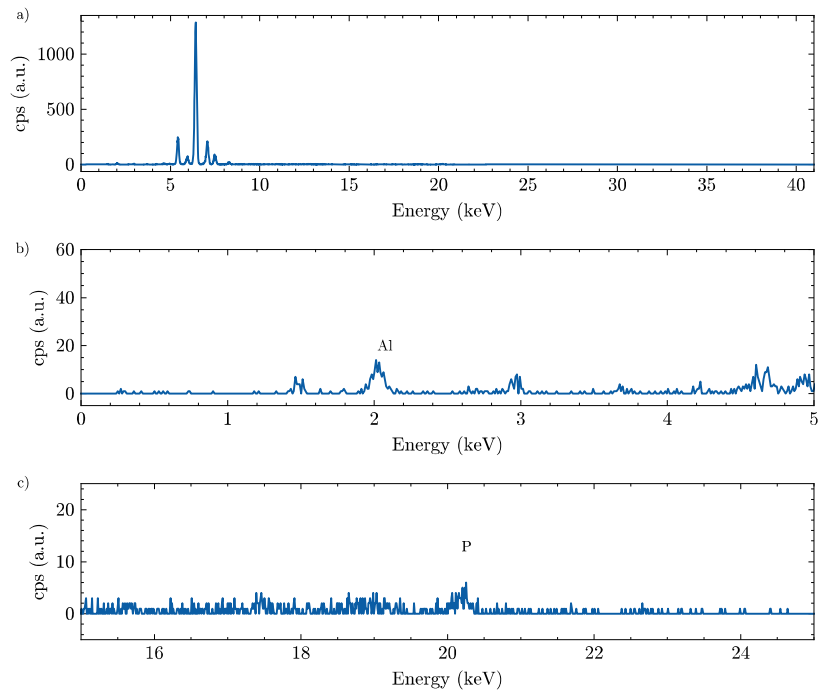


Figure 3: Averaged XRF spectrum representing cumulative signals from one of the screen-printed spots, highlighting characteristic X-ray peaks. a) Showing the whole spectral region, b) inset highlighting the minor contribution of Al and c) P signals.

augmenting adhesion and reducing slurry dispersion. Post-etching, the foil was thoroughly rinsed with distilled water to eliminate residual hydroxides. The prepared slurry was then uniformly screen-printed onto the Aluminum foil. The electrodes were subsequently dried at atmospheric pressure, at a temperature of 140 °C for 12 hours. After the screen-printing procedure, the electrode thickness was measured to be  $0.008 \pm 0.002$  mm. This measurement was obtained using a digital thickness gauge at ten different points across the electrode surface to account for potential variability in thickness.

## 5 MADAP analysis

Our analysis package, MADAP, is further expanded with voltammetry tests, integrating it into our Auto-MISCHBARES framework to facilitate the on-the-fly characterization capabilities (Fig. 4). In our case study, we illustrate the application of the cyclic voltammetry (CV) class from MADAP's voltammetry module for the real-time analysis of the electrochemical data. The class initiates the process by identifying forward and backward scans and automatically labeling cycle numbers, irrespective of their starting points, to enable accurate visualization of the electrochemical process (see `_find_fwd_bwd_scans` and `_identify_cycles`). The module further utilizes the `find_peaks` method from the `scipy.signal` library to locate the peaks in both cathodic and anodic directions and store this information for subsequent analysis (see `_find_peak_currents`). This includes calculating peak-to-peak separation as the absolute distance between the cathodic and anodic peak voltages. Additionally, the half-wave potential is determined by averaging the voltages of corresponding peaks, subsequently used for finding a linear fit with `numpy.polyfit`, from which the half-wave current is derived (see `_calculate_E_half`). The module extends its analysis to compute overpotential, as all the requisite parameters are now available (see `_find_overpotential`). For reactions considered reversible, it calculates the diffusion coefficients, defaulting to a standard temperature of 298 K unless otherwise specified, utilizing the Randles-Sevcik equation to elucidate electrochemical reaction kinetics<sup>17</sup> (see `_calculate_diffusion_coefficient`). This class also quantifies peak currents by identifying the linear representation of the capacitive region through a windowed linear fit, with the fit's quality evaluated by the coefficient of determination (r-squared) value. This approach determines the height of the peak currents relative to this baseline for both cathodic and anodic sweeps (see `_find_height_of_cathodic_peak_current` and `_find_height_of_anodic_peak_current`). Although not the primary focus of our study, the module provides insights into Tafel plot parameters and corrosion point (see `_find_tafel_region` and `_calculate_corrosion_point`). It can generate up to five types of plots, including E-t, I-t, peak parameters versus scan rates, I-V, and Tafel plot, demonstrating its robustness in visual data representation (see `plot`). Finally, the class supports the generation of detailed reports, encapsulating both raw data and analyzed results in CSV and JSON formatted files, respectively (see `save_data`). Additional documentation about this package and the code details can be found in <https://pypi.org/project/MADAP/> and <https://fuzhanrahmanian.github.io/MADAP/> and in GitHub<sup>18</sup>.

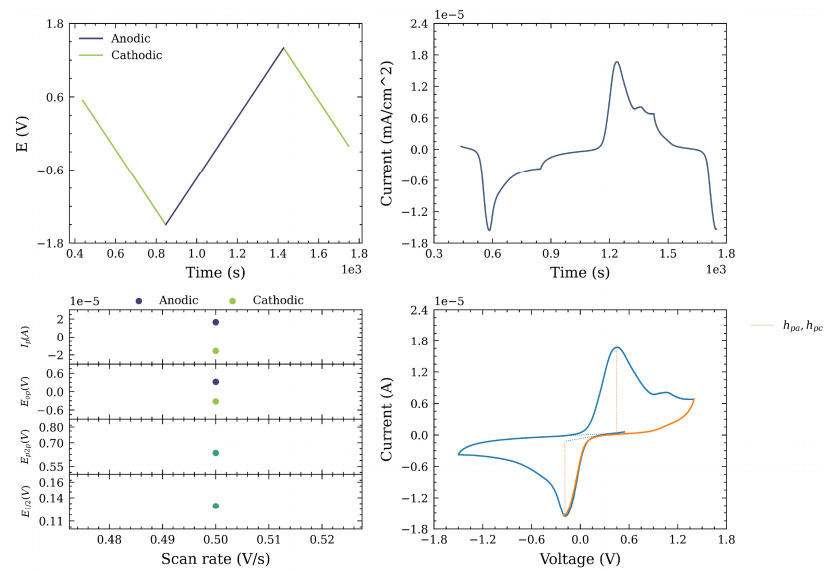


Figure 4: Visualization showcase of sample 6 from set 1, measured with Auto-MISCHBARES and analyzed through MADAP during CV test. This analysis delineates parameters such as anodic and cathodic peaks and half-wave information alongside capacitive and Faradaic current components derived from this package<sup>18</sup>.

## 6 XPS

X-ray photoelectron spectra were recorded under high vacuum conditions using a near-ambient pressure x-ray photoelectron spectroscopy (NAP-XPS) system EnviroESCA from Specs equipped with an Al-K $\alpha$  source (1486.71 eV) operated at 15 kV, 43 W (3 mA emission) and a Phoibos 150 NAP hemispherical analyzer. The base pressure was  $1 \times 10^{-7}$  mbar in the analysis chamber and  $1 \times 10^{-9}$  mbar in the analyzer section. This NAP-XPS is part of the Platform for accelerated electrochemical energy storage Research (PLACES/R) at Helmholtz Institute Ulm<sup>19</sup>. To avoid contact with air, the sample environment of the NAP-XPS is directly connected to the glovebox in which the electrochemical measurements were performed. High-resolution spectra were recorded using a pass energy of 30 eV. Peak fitting was performed with CasaXPS version 2.3.24PR1.0 using a Shirley type background and 70% Gaussian and 30% Lorentzian profiles<sup>20</sup>.

### 6.1 Spectra

In the following, the XPS spectra for the remaining samples 2 to 6 of the first experimental set are listed.

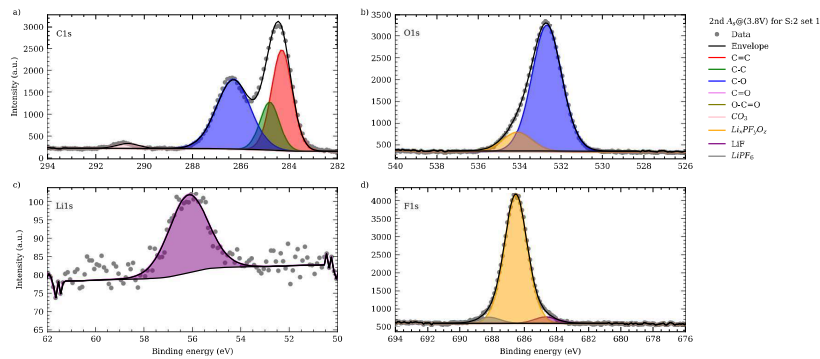


Figure 5: Schematic of X-ray photoelectron spectroscopy (XPS) spectra of the synthesized cathode electrolyte interphase (CEI) on sample 2 from the first set of experiments, captured during the second anodic scan in CV test with a stopping potential value of 3.8 V. This figure illustrates the diverse chemical composition of this layer with peaks corresponding to various functional groups and species: a) The C1s region demonstrates multiple peaks indicative of carbon-based species, b) the O1s region. c) The Li1s region shows the presence of lithium-containing compounds, d) the F1s region is characterized by peaks associated with fluorinated species. Each chemical state identified is denoted by a distinct color in the spectra. The overlaid black line represents the envelope of the aggregated measured data, indicating the sum of contributions from all fitted peaks.

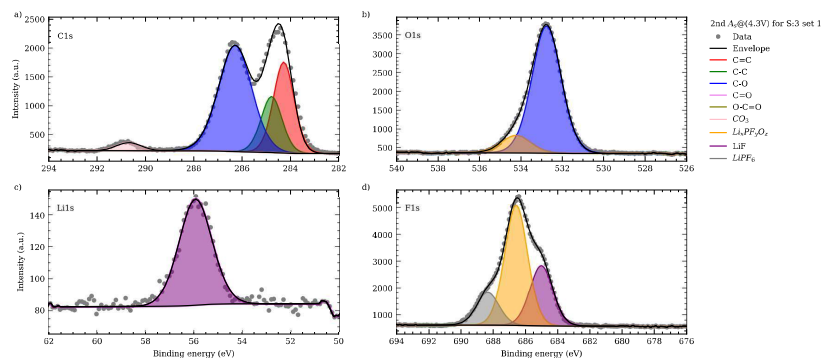


Figure 6: Schematic of XPS spectra of the synthesized CEI on sample 3 from the first set of experiments, captured during the second anodic scan in CV test with a stopping potential value of 4.3 V. This figure illustrates the diverse chemical composition of this layer with peaks corresponding to various functional groups and species: a) The C1s region demonstrates multiple peaks indicative of carbon-based species, b) the O1s region, c) The Li1s region shows the presence of lithium-containing compounds, d) the F1s region is characterized by peaks associated with fluorinated species. Each chemical state identified is denoted by a distinct color in the spectra. The overlaid black line represents the envelope of the aggregated measured data, indicating the sum of contributions from all fitted peaks.

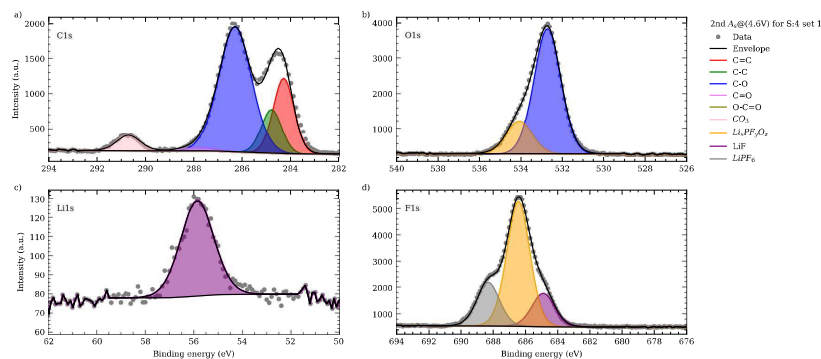


Figure 7: Schematic of XPS spectra of the synthesized CEI on sample 4 from the first set of experiments, captured during the second anodic scan in CV test with a stopping potential value of 4.6 V. This figure illustrates the diverse chemical composition of this layer with peaks corresponding to various functional groups and species: a) The C1s region demonstrates multiple peaks indicative of carbon-based species, b) the O1s region, c) The Li1s region shows the presence of lithium-containing compounds, d) the F1s region is characterized by peaks associated with fluorinated species. Each chemical state identified is denoted by a distinct color in the spectra. The overlaid black line represents the envelope of the aggregated measured data, indicating the sum of contributions from all fitted peaks.

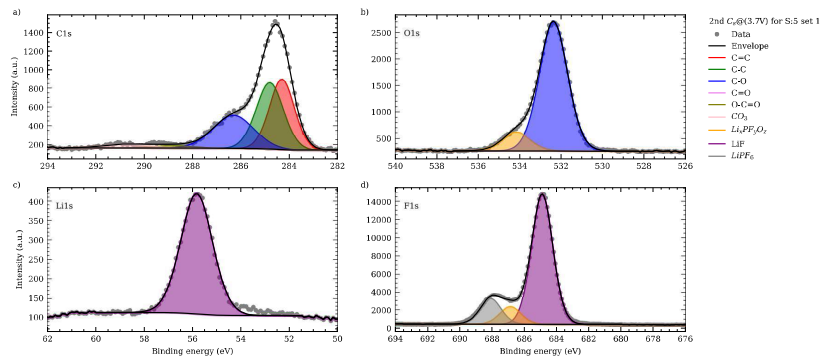


Figure 8: Schematic of XPS spectra of the synthesized CEI on sample 5 from the first set of experiments, captured during the second anodic scan in CV test with a stopping potential value of 3.7 V. This figure illustrates the diverse chemical composition of this layer with peaks corresponding to various functional groups and species: a) The C1s region demonstrates multiple peaks indicative of carbon-based species. b) the O1s region. c) The Li1s region shows the presence of lithium-containing compounds. d) the F1s region is characterized by peaks associated with fluorinated species. Each chemical state identified is denoted by a distinct color in the spectra. The overlaid black line represents the envelope of the aggregated measured data, indicating the sum of contributions from all fitted peaks.

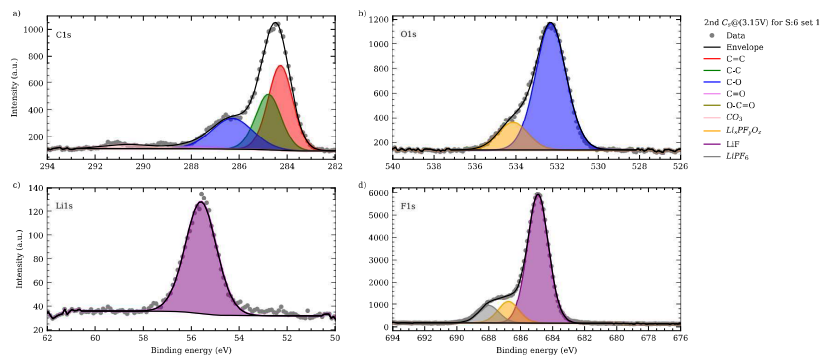


Figure 9: Schematic of XPS spectra of the synthesized CEI on sample 6 from the first set of experiments, captured during the second anodic scan in CV test with a stopping potential value of 3.15 V. This figure illustrates the diverse chemical composition of this layer with peaks corresponding to various functional groups and species: a) The C1s region demonstrates multiple peaks indicative of carbon-based species. b) the O1s region. c) The Li1s region shows the presence of lithium-containing compounds. d) the F1s region is characterized by peaks associated with fluorinated species. Each chemical state identified is denoted by a distinct color in the spectra. The overlaid black line represents the envelope of the aggregated measured data, indicating the sum of contributions from all fitted peaks.

Table 1: To evaluate the fit quality of XPS data, two metrics, namely Residual Standard Deviation (RSD) and Goodness of Fit, are provided for every spectral region across all samples.

Sample	Region	Goodness of Fit	Residual STD
S:1, set 1	C1s	239.208	0.854
	O1s	320.822	1.079
	F1s	1505.901	2.661
	Li1s	416.715	1.534
S:2, set 1	C1s	990.612	2.094
	O1s	329.004	0.810
	F1s	448.093	0.883
	Li1s	214.526	0.794
S:3, set 1	C1s	1128.550	2.351
	O1s	419.031	1.134
	F1s	847.567	1.325
	Li1s	243.398	0.854
S:4, set 1	C1s	761.609	1.998
	O1s	441.226	1.243
	F1s	614.448	1.081
	Li1s	195.243	0.823
S:5, set 1	C1s	303.729	1.064
	O1s	413.421	1.241
	F1s	1926.761	3.194
	Li1s	543.616	1.778
S:6, set 1	C1s	271.224	1.089
	O1s	313.175	1.175
	F1s	735.157	2.029
	Li1s	227.720	1.163

## References

- [1] F. Rahmadian, J. Flowers, D. Guevarra, M. Richter, M. Fichtner, P. Donnelly, J. M. Gregoire and H. S. Stein, *Advanced Materials Interfaces*, 2022, **9**, 2101987.
- [2] S. Ramírez, *FastAPI*, <https://github.com/tiangolo/fastapi>.
- [3] T. Christie, *Uvicorn*, <https://github.com/encode/uvicorn>.
- [4] M. Grinberg, *Flask web development: developing web applications with python*, " O'Reilly Media, Inc.", 2018.
- [5] Bokeh Development Team, *Bokeh: Python library for interactive visualization*, 2018.
- [6] *WebSockets*, <https://github.com/python-websockets/websockets/tree/main>.
- [7] *pythonnet - Python.NET*, <https://github.com/pythonnet/pythonnet>.
- [8] C. R. Harris, K. J. Millman, S. J. van der Walt, R. Gommers, P. Virtanen, D. Cournapeau, E. Wieser, J. Taylor, S. Berg, N. J. Smith, R. Kern, M. Picus, S. Hoyer, M. H. van Kerkwijk, M. Brett, A. Haldane, J. F. del Río, M. Wiebe, P. Peterson, P. Gérard-Marchant, K. Sheppard, T. Reddy, W. Weckesser, H. Abbasi, C. Gohlke and T. E. Oliphant, *Nature*, 2020, **585**, 357–362.
- [9] W. McKinney *et al.*, Proceedings of the 9th Python in Science Conference, 2010. pp. 51–56.
- [10] *pgAdmin*, <https://www.pgadmin.org/>.
- [11] F. Di Gregorio, *psycopg2 - Python-PostgreSQL Database Adapter*, <https://github.com/psycopg/psycopg2>.
- [12] G. Bradski, *Dr. Dobbs's Journal of Software Tools*, 2000, –.
- [13] F. Rahmadian, *MADAP*, <https://github.com/fuzhanrahmadian/MADAP>.
- [14] F. Pedregosa, G. Varoquaux, A. Gramfort, V. Michel, B. Thirion, O. Grisel, M. Blondel, P. Prettenhofer, R. Weiss, V. Dubourg, J. Vanderplas, A. Passos, D. Cournapeau, M. Brucher, M. Perrot and E. Duchesnay, *Journal of Machine Learning Research*, 2011, **12**, 2825–2830.
- [15] P. Virtanen, R. Gommers, T. E. Oliphant, M. Haberland, T. Reddy, D. Cournapeau, E. Burovski, P. Peterson, W. Weckesser, J. Bright, S. J. van der Walt, M. Brett, J. Wilson, K. J. Millman, N. Mayorov, A. R. J. Nelson, E. Jones, R. Kern, E. Larson, C. J. Carey, Í. Polat, Y. Feng, E. W. Moore, J. VanderPlas, D. Laxalde, J. Perktold, R. Cimrman, I. Henriksen, E. A. Quintero, C. R. Harris, A. M. Archibald, A. H. Ribeiro, F. Pedregosa, P. van Mulbregt and SciPy 1.0 Contributors, *Nature Methods*, 2020, **17**, 261–272.
- [16] H. Krekel, B. Oliveira, R. Pfannschmidt, F. Bruynooghe, B. Laughner and F. Bruhin, *pytest x.y*, 2004, <https://github.com/pytest-dev/pytest>.
- [17] A. J. Bard, L. R. Faulkner and H. S. White, *Electrochemical methods: fundamentals and applications*, John Wiley & Sons, 2022.
- [18] F. Rahmadian, *Modular and Autonomous Data Analysis Platform (MADAP)*”, 2023, <https://doi.org/10.5281/zenodo.10357192>.
- [19] H. S. Stein, A. Sanin, F. Rahmadian, B. Zhang, M. Vogler, J. K. Flowers, L. Fischer, S. Fuchs, N. Choudhary and L. Schroeder, *Current Opinion in Electrochemistry*, 2022, **35**, 101053.
- [20] N. Fairley, V. Fernandez, M. Richard-Plouet, C. Guillot-Deudon, J. Walton, E. Smith, D. Flahaut, M. Greiner, M. Biesinger, S. Tougaard *et al.*, *Applied Surface Science Advances*, 2021, **5**, 100112.





*“We must develop a comprehensive and globally shared view of how technology is affecting our lives and reshaping our economic, social, cultural, and human environments. There has never been a time of greater promise, or greater peril.”*  
— Klaus Schwab

## 5. Conclusion and Outlook

This chapter expounds the conclusive thoughts and realizations of the presented dissertation, along with a perspective on the future of this field and an additional personal viewpoint on the ethical considerations involved in the development of AI tools.

### 5.1. In aid of digital intelligence

This dissertation introduces an ensemble of digitalization tools and enablers from interdisciplinary domains, such as informatics, data analytics, and artificial intelligence, designed for developing reliable Materials Acceleration Platforms. It elucidates how the strategic integration of these tools advances the functionality and efficiency of these frameworks and enables digitizable knowledge creation in machine-readable formats. The endeavors begin with the implementation and demonstration of a high-throughput orchestration platform, HELAO, designed to enable modular autonomous feedback loops for experimental processes. This framework utilizes FastAPI for communication across distributed hardware and software laboratory systems, which facilitates system interoperability and broadens the principles of the Internet of Things to scientific research. This closed-loop architecture also incorporates machine learning algorithms to dynamically optimize experimental parameters through an iterative process and further supports parallelization and multi-threading. Additionally, it adheres to research data management standards by documenting every step of the experimental processes, including inputs, outputs, and metadata. A simulated example illustrates how the framework accelerates insight generation and achieves a reduced “time to solution”.

The project then elaborates on the deployment of an open-source analysis software package, MADAP, tailored for electrochemical tests. Its architecture, developed with an abstract design and enhanced by a variety of data-driven algorithms, provides a modular and versatile framework. The software maintains transparency throughout

operational stages, from initial execution to modeling and fitting, and, in compliance with the FAIR data principle, it records all these steps and configurations. Additionally, MADAP delivers immediate analytical insights for researchers by providing comprehensive visualizations through a user-friendly interface design. The dissertation advances the discourse on factors in efficient modeling and enhances their explainability through two applications. On one hand, the one-shot active learning pipeline illustrates the role of rich prior knowledge in optimizing learning processes and the interpretability of polynomial models for insightful decision-making; on the other hand, ARCANA, a highly regularized deep sequence-to-sequence framework, represents its unique architectural design through a high level of explainability, generalization, and transparency. It validates the framework's robustness with bespoke, customized model elements and provides local explainability through attention scores. The model further quantifies prediction uncertainty and analyses the impact of input variability on predicting battery lifetime parameters. Its capability for multi-output prediction further elucidates its rationale for decision-making. This framework's versatile and adaptable design remains agnostic across various applications, and its modular architecture supports various operational modes, including training, tuning, predicting, and fine-tuning. This pipeline, deployed as a Python package and grounded in FAIR principles, accelerates the testing process, is especially beneficial for lengthy cycling procedures, and enhances optimization capabilities through active learning and real-time monitoring. The model highlights the significance of data-centric approaches by evaluating the impact of data size and quality on predictions and validating the applications' utility and fidelity.

Lastly, the Auto-MISCHBARES framework is presented, which integrates various developed tools alongside two additional components, namely a data infrastructure utilizing a locally hosted PostgreSQL database for data management and storage, and quality control protocols for validating experimental steps. This framework allows users to conduct numerous experimental procedures through a modular web interface. Additional functionalities, such as a live visualizer and chatbot, enable researchers to monitor intermediate measurements in real-time and stay informed throughout a fully autonomous experimentation process. The framework's functionality is demonstrated using a miniaturized scanning droplet cell setup for electrochemical experiments. This downsampled setup minimizes material usage and further accelerates data

generation through high-throughput experimental settings. Auto-MISCHBARES demonstrates reliability, reproducibility, and autonomy, making it suitable for autonomous platforms.

Conclusively, revisiting the research question outlined at the outset of this dissertation, whether the integration of AI technology and informatics tools can accelerate insights in battery-related studies, the response is unequivocally affirmative. The effective deployment of these tools can accelerate the discovery and understanding in this field. However, achieving such acceleration is contingent upon maintaining transparency at various levels of granularity. This includes functional transparency, which describes the underlying mechanisms of algorithms, structural transparency, detailing the execution processes of each algorithm, and run transparency, which requires a thorough grasp of how the system integrates and interacts with various elements. All frameworks developed within this thesis adhere to these transparency standards. Beyond these principles, these systems, in particular ARCANA and Auto-MISCHBARES, provide the groundwork for explainability and interpretability to elucidate the processes and reasoning behind decisions. Offering holistic explanations and localized insights becomes essential where decisions originate solely from automated processes, which might otherwise promote automation bias, the presumption of correctness based on perceived objectivity. Additionally, the commitment to democratizing AI and ensuring ethical practices in technology deployment is emphasized by the open-source availability of all project deliverables, covering both software and data.

The suite of tools has proven indispensable in designing a robust Materials Acceleration Platform and positions it at the forefront of self-driving laboratory realization. Its broad applicability extends from small-scale laboratory settings to expansive manufacturing facilities, suggesting insights across various scales. Many material systems remain unexplored; strategically deploying these tools can unlock their potential and accelerate breakthroughs in scientific discoveries. It can be therefore concluded that the reliance on digital tools and frameworks is beneficial for advancing energy storage technology and offering more defined strategies for green energy solutions, an intertwining that can and will sustain the ecological responsibility of the scientific community.

## 5.2. Perspectives on scalable efforts

Looking back to the beginning of this work, it is now clear that the success of next-generation batteries fundamentally depends on the dimensions of "time" and "data availability." The most influential factor will be the strategic integration and utilization of AI enablers within the architectural framework of acceleration platforms, which must comply with the FAIR principles. In the near term, the focus will be on expanding MAPs for battery materials optimization methodologies through improved explainability and integration of large language models i.e., GTPs, that will assist researchers as co-scientists in a variety of tasks spanning from reporting to documentation or code execution and advanced literature research.

In addition, the emerging Digital Twin technology will allow for the real-time diagnostic of equipment performance and the optimization of battery chemistries and protocols. The path forward also involves a concerted effort towards standardization, interoperability, and interchangeability where digitally mirrored components and physical systems interact seamlessly, with the goal of overcoming the physicochemical barriers of battery optimization. The information flow from all data creators will be exposed to advanced AI toolkits, allowing the resulting model predictions to be continuously updated and the learning processes to be dynamically adapted. These innovations draw a future where AI not only speeds up material discovery but also ensures sustainability and precision in production, closing the loop from material discovery to commercialization. The holistic integration of these digital systems and their AI-assisted software will allow for the predictive modeling of battery life cycles and behaviors, ensuring that every aspect of production is enhanced and aligned with the demands of modern energy solutions.

## 5.3. Ethics for the present and the future

In the past century, scientists awakened the power of the atom, and this century is turning out to be the one in which scientists are awakening the power of AI. Increasingly, it appears inevitable that we will develop a General Artificial Intelligence possessing the sophistication necessary to transcend its initial programming and operational confines to tackle challenges not envisioned by either the designers or

the users. The digital timescale is accelerating, surpassing the gradual biological evolution that has carried humanity to and on the moon during mere slivers of our 250,000 existential generations. Today, central processing units operate at gigahertz speeds, overtaking the limits of the natural plasticity of the remarkable biology of our brain. Shortly, AI may not only complement but assume distinct social roles, necessitating new standards in design for transparency, predictability, and ethical alignment. Sufficiently general AI algorithms will evolve beyond predictable environments, necessitating adaptation to ensure safety and to embed ethical considerations. The objectives we set for AI, the parameters within which it seeks optimization, and, conclusively, acceleration, must reflect ethical values that align with our deepest moral convictions as an evolved species. In other words, the superintelligence that humanity is assembling, beyond the singularity, should be capable of *superethics*, an advanced form of ethical reasoning consistent within current frameworks and adaptable to unforeseen contexts. Our current and future ethical standards should be incorporated into today's designs, steering AI through present-day challenges and future scenarios along our shared trajectory. In the context of MAPs and automation, this means considering data privacy and intellectual property rights amidst extensive data sharing and biases in AI algorithms that may influence experimental outcomes and material properties. Concurrently, a pressing societal urgency in addressing global climatic challenges relies on an accelerated process that goes from scientific discovery to commercialization. Finding the safety and ethical balance is an endeavor that adds another layer of complexity to the possibly most significant human achievement represented by general Artificial Intelligence. Nick Bostrom, contemporary philosopher and founder of the Future of Humanity Institute at Oxford University, can be quoted saying, 'Machine intelligence is the last invention that humanity will ever need to make' in a warning of the fading control of humanity over scientific discovery. Facing the reality that machines may soon surpass human capabilities in cognitive speed, trust, and intelligence, our ethical expectations and standards should rise, and AI should not merely replicate human decency but achieve, instead, unreached levels of excellence.

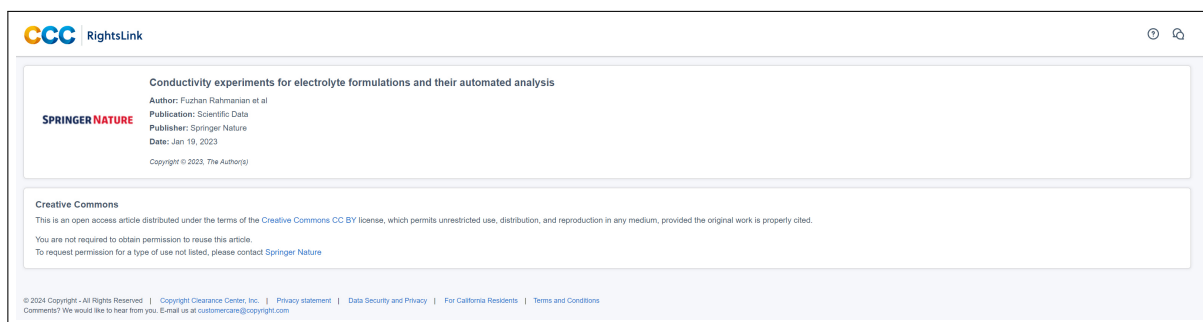


# A. Appendix

## A.1. Licenses and Reprint permissions

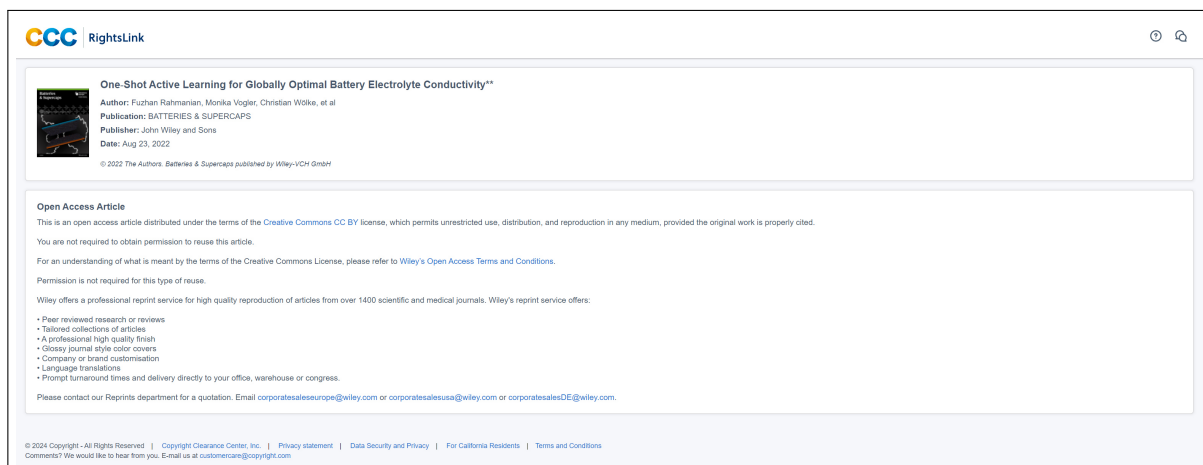
This section outlines the licenses and reprint permissions granted by the journals for the publications accessory of the present dissertation in compliance with the respective copyright policies.

### Conductivity experiments for electrolyte formulations and their automated analysis



The screenshot shows a RightsLink interface for the article "Conductivity experiments for electrolyte formulations and their automated analysis". The author is Fuzhan Rahmanian et al., published in Scientific Data by Springer Nature on Jan 19, 2023. It is a Creative Commons CC BY licensed work. The page includes a copyright notice for 2024 and contact information for Springer Nature.

### One-Shot Active Learning for Globally Optimal Battery Electrolyte Conductivity



The screenshot shows a RightsLink interface for the article "One-Shot Active Learning for Globally Optimal Battery Electrolyte Conductivity". The authors are Fuzhan Rahmanian, Monika Vogler, and Christian Wolke, et al., published in BATTERIES & SUPERCAPS by John Wiley and Sons on Aug 23, 2022. It is an Open Access Article under a Creative Commons CC BY license. The page lists various reprint services offered by Wiley, such as peer-reviewed research, tailored collections, and professional high-quality finishes. It includes a copyright notice for 2024 and contact information for Wiley's Reprints department.



## Enabling Modular Autonomous Feedback-Loops in Materials Science through Hierarchical Experimental Laboratory Automation and Orchestration

5/2/24, 10:43 PM		RightsLink Printable License	
JOHN WILEY AND SONS LICENSE TERMS AND CONDITIONS			
May 02, 2024			
<hr/> <p>This Agreement between Technical University of Munich -- Fuzhan Rahmanian ("You") and John Wiley and Sons ("John Wiley and Sons") consists of your license details and the terms and conditions provided by John Wiley and Sons and Copyright Clearance Center.</p>			
License Number	5780961421176		
License date	May 02, 2024		
Licensed Content Publisher	John Wiley and Sons		
Licensed Content Publication	Advanced Materials Interfaces		
Licensed Content Title	Enabling Modular Autonomous Feedback-Loops in Materials Science through Hierarchical Experimental Laboratory Automation and Orchestration		
Licensed Content Author	Fuzhan Rahmanian, Jackson Flowers, Dan Guevarra, et al		
<a href="https://s100.copyright.com/AppDispatchServlet">https://s100.copyright.com/AppDispatchServlet</a>		1/8	
5/2/24, 10:43 PM		RightsLink Printable License	
Licensed Content Date	Jan 6, 2022		
Licensed Content Volume	9		
Licensed Content Issue	8		
Licensed Content Pages	8		
Type of use	Dissertation/Thesis		
Requestor type	Author of this Wiley article		
Format	Print and electronic		
Portion	Full article		
Will you be translating?	No		
Title of new work	Design and Implementation of Enablers in Material Acceleration Platforms for Battery Research		
Institution name	Technical University Munich - TUM		
<a href="https://s100.copyright.com/AppDispatchServlet">https://s100.copyright.com/AppDispatchServlet</a>		2/8	

5/2/24, 10:43 PM RightsLink Printable License

Expected presentation date	May 2024
Requestor Location	Technical University of Munich Baaderstr. 82 München, 80469 Germany Attn: Technical University of Munich
Publisher Tax ID	EU826007151
Total	0.00 EUR

Terms and Conditions

TERMS AND CONDITIONS

This copyrighted material is owned by or exclusively licensed to John Wiley & Sons, Inc. or one of its group companies (each a "Wiley Company") or handled on behalf of a society with which a Wiley Company has exclusive publishing rights in relation to a particular work (collectively "WILEY"). By clicking "accept" in connection with completing this licensing transaction, you agree that the following terms and conditions apply to this transaction (along with the billing and payment terms and conditions established by the Copyright Clearance Center Inc., ("CCC's Billing and Payment terms and conditions"), at the time that you opened your RightsLink account (these are available at any time at <http://myaccount.copyright.com>).

**Terms and Conditions**

- The materials you have requested permission to reproduce or reuse (the "Wiley Materials") are protected by copyright.

https://s100.copyright.com/AppDispatchServlet 3/8

---

5/2/24, 10:43 PM RightsLink Printable License

- You are hereby granted a personal, non-exclusive, non-sub licensable (on a stand-alone basis), non-transferable, worldwide, limited license ~~to reproduce the Wiley Materials for the purpose specified in the licensing process.~~ This license, **and any CONTENT (PDF or image file) purchased as part of your order**, is for a one-time use only and limited to any maximum distribution number specified in the license. The first instance of republication or reuse granted by this license must be completed within two years of the date of the grant of this license (although copies prepared before the end date may be distributed thereafter). The Wiley Materials shall not be used in any other manner or for any other purpose, beyond what is granted in the license. Permission is granted subject to an appropriate acknowledgement given to the author, title of the material/book/journal and the publisher. You shall also duplicate the copyright notice that appears in the Wiley publication in your use of the Wiley Material. Permission is also granted on the understanding that nowhere in the text is a previously published source acknowledged for all or part of this Wiley Material. Any third party content is expressly excluded from this permission.
- With respect to the Wiley Materials, all rights are reserved. Except as expressly granted by the terms of the license, no part of the Wiley Materials may be copied, modified, adapted (except for minor reformatting required by the new Publication), translated, reproduced, transferred or distributed, in any form or by any means, and no derivative works may be made based on the Wiley Materials without the prior permission of the respective copyright owner. **For STM Signatory Publishers clearing permission under the terms of the STM Permissions Guidelines only, the terms of the license are extended to include subsequent editions and for editions in other languages, provided such editions are for the work as a whole in situ and does not involve the separate exploitation of the permitted figures or extracts.** You may not alter, remove or suppress in any manner any copyright, trademark or other notices displayed by the Wiley Materials. You may not license, rent, sell, loan, lease, pledge, offer as security, transfer or assign the Wiley Materials on a stand-alone basis, or any of the rights granted to you hereunder to any other person.
- The Wiley Materials and all of the intellectual property rights therein shall at all times remain the exclusive property of John Wiley & Sons Inc, the Wiley Companies, or their respective licensors, and your interest therein is only that of having possession of and the right to reproduce the Wiley Materials pursuant to Section 2 herein during the continuance of this Agreement. You agree that you own no right, title or interest in or to the Wiley Materials or any of the intellectual property rights therein. You shall have no rights hereunder other than the license as provided for above in Section 2. No right, license or interest to any trademark, trade

https://s100.copyright.com/AppDispatchServlet 4/8

<p>5/2/24, 10:43 PM</p> <p>name, service mark or other branding ("Marks") of WILEY or its licensors is granted hereunder, and you agree that you shall not assert any such right, license or interest with respect thereto</p> <ul style="list-style-type: none"> <li>• NEITHER WILEY NOR ITS LICENSORS MAKES ANY WARRANTY OR REPRESENTATION OF ANY KIND TO YOU OR ANY THIRD PARTY, EXPRESS, IMPLIED OR STATUTORY, WITH RESPECT TO THE MATERIALS OR THE ACCURACY OF ANY INFORMATION CONTAINED IN THE MATERIALS, INCLUDING, WITHOUT LIMITATION, ANY IMPLIED WARRANTY OF MERCHANTABILITY, ACCURACY, SATISFACTORY QUALITY, FITNESS FOR A PARTICULAR PURPOSE, USABILITY, INTEGRATION OR NON-INFRINGEMENT AND ALL SUCH WARRANTIES ARE HEREBY EXCLUDED BY WILEY AND ITS LICENSORS AND WAIVED BY YOU.</li> <li>• WILEY shall have the right to terminate this Agreement immediately upon breach of this Agreement by you.</li> <li>• You shall indemnify, defend and hold harmless WILEY, its Licensors and their respective directors, officers, agents and employees, from and against any actual or threatened claims, demands, causes of action or proceedings arising from any breach of this Agreement by you.</li> <li>• IN NO EVENT SHALL WILEY OR ITS LICENSORS BE LIABLE TO YOU OR ANY OTHER PARTY OR ANY OTHER PERSON OR ENTITY FOR ANY SPECIAL, CONSEQUENTIAL, INCIDENTAL, INDIRECT, EXEMPLARY OR PUNITIVE DAMAGES, HOWEVER CAUSED, ARISING OUT OF OR IN CONNECTION WITH THE DOWNLOADING, PROVISIONING, VIEWING OR USE OF THE MATERIALS REGARDLESS OF THE FORM OF ACTION, WHETHER FOR BREACH OF CONTRACT, BREACH OF WARRANTY, TORT, NEGLIGENCE, INFRINGEMENT OR OTHERWISE (INCLUDING, WITHOUT LIMITATION, DAMAGES BASED ON LOSS OF PROFITS, DATA, FILES, USE, BUSINESS OPPORTUNITY OR CLAIMS OF THIRD PARTIES), AND WHETHER OR NOT THE PARTY HAS BEEN ADVISED OF THE POSSIBILITY OF SUCH DAMAGES. THIS LIMITATION SHALL APPLY NOTWITHSTANDING ANY FAILURE OF ESSENTIAL PURPOSE OF ANY LIMITED REMEDY PROVIDED HEREIN.</li> <li>• Should any provision of this Agreement be held by a court of competent jurisdiction to be illegal, invalid, or unenforceable, that provision shall be deemed amended to achieve as nearly as possible the same economic effect as the original provision,</li> </ul> <p><a href="https://s100.copyright.com/AppDispatchServlet">https://s100.copyright.com/AppDispatchServlet</a></p>	<p>RightsLink Printable License</p> <p>58</p>
<p>5/2/24, 10:43 PM</p> <p>and the legality, validity and enforceability of the remaining provisions of this Agreement shall not be affected or impaired thereby.</p> <ul style="list-style-type: none"> <li>• The failure of either party to enforce any term or condition of this Agreement shall not constitute a waiver of either party's right to enforce each and every term and condition of this Agreement. No breach under this agreement shall be deemed waived or excused by either party unless such waiver or consent is in writing signed by the party granting such waiver or consent. The waiver by or consent of a party to a breach of any provision of this Agreement shall not operate or be construed as a waiver of or consent to any other or subsequent breach by such other party.</li> <li>• This Agreement may not be assigned (including by operation of law or otherwise) by you without WILEY's prior written consent.</li> <li>• Any fee required for this permission shall be non-refundable after thirty (30) days from receipt by the CCC.</li> <li>• These terms and conditions together with CCC's Billing and Payment terms and conditions (which are incorporated herein) form the entire agreement between you and WILEY concerning this licensing transaction and (in the absence of fraud) supersedes all prior agreements and representations of the parties, oral or written. This Agreement may not be amended except in writing signed by both parties. This Agreement shall be binding upon and inure to the benefit of the parties' successors, legal representatives, and authorized assigns.</li> <li>• In the event of any conflict between your obligations established by these terms and conditions and those established by CCC's Billing and Payment terms and conditions, these terms and conditions shall prevail.</li> <li>• WILEY expressly reserves all rights not specifically granted in the combination of (i) the license details provided by you and accepted in the course of this licensing transaction, (ii) these terms and conditions and (iii) CCC's Billing and Payment terms and conditions.</li> <li>• This Agreement will be void if the Type of Use, Format, Circulation, or Requestor Type was misrepresented during the licensing process.</li> <li>• This Agreement shall be governed by and construed in accordance with the laws of the State of New York, USA, without regards to such state's conflict of law rules. Any legal action, suit or proceeding arising out of or relating to these Terms and Conditions or the breach thereof shall be instituted in a court of competent</li> </ul> <p><a href="https://s100.copyright.com/AppDispatchServlet">https://s100.copyright.com/AppDispatchServlet</a></p>	<p>RightsLink Printable License</p> <p>68</p>

5/2/24, 10:43 PM RightsLink Printable License

jurisdiction in New York County in the State of New York in the United States of America and each party hereby consents and submits to the personal jurisdiction of such court, waives any objection to venue in such court and consents to service of process by registered or certified mail, return receipt requested, at the last known address of such party.

**WILEY OPEN ACCESS TERMS AND CONDITIONS**

Wiley Publishes Open Access Articles in fully Open Access Journals and in Subscription journals offering Online Open. Although most of the fully Open Access journals publish open access articles under the terms of the Creative Commons Attribution (CC BY) License only, the subscription journals and a few of the Open Access Journals offer a choice of Creative Commons Licenses. The license type is clearly identified on the article.

**The Creative Commons Attribution License**

The [Creative Commons Attribution License \(CC-BY\)](#) allows users to copy, distribute and transmit an article, adapt the article and make commercial use of the article. The CC-BY license permits commercial and non-

**Creative Commons Attribution Non-Commercial License**

The [Creative Commons Attribution Non-Commercial \(CC-BY-NC\) License](#) permits use, distribution and reproduction in any medium, provided the original work is properly cited and is not used for commercial purposes.(see below)

**Creative Commons Attribution-Non-Commercial-NoDerivs License**

The [Creative Commons Attribution Non-Commercial-NoDerivs License \(CC-BY-NC-ND\)](#) permits use, distribution and reproduction in any medium, provided the original work is properly cited, is not used for commercial purposes and no modifications or adaptations are made. (see below)

**Use by commercial "for-profit" organizations**

Use of Wiley Open Access articles for commercial, promotional, or marketing purposes requires further explicit permission from Wiley and will be subject to a fee.

Further details can be found on Wiley Online Library  
<http://olabout.wiley.com/WileyCDA/Section/id-410895.html>

https://s100.copyright.com/AppDispatchServlet 7/8

5/2/24, 10:43 PM RightsLink Printable License

**Other Terms and Conditions:**

**v1.10 Last updated September 2015**

Questions? [customercare@copyright.com](mailto:customercare@copyright.com).

---

https://s100.copyright.com/AppDispatchServlet 8/8

## Attention towards chemistry agnostic and explainable battery lifetime prediction

CCC RightsLink Ⓞ 🔍

**Attention towards chemistry agnostic and explainable battery lifetime prediction**  
Author: Fuzhan Rahmanian et al.  
Publication:npj Computational Materials  
Publisher: Springer Nature  
Date: May 10, 2024  
Copyright © 2024, The Author(s)

**Creative Commons**  
This is an open access article distributed under the terms of the Creative Commons CC BY license, which permits unrestricted use, distribution, and reproduction in any medium, provided the original work is properly cited.  
You are not required to obtain permission to reuse this article.  
To request permission for a type of use not listed, please contact Springer Nature

## Autonomous millimeter scale high throughput battery research system

✕

**Autonomous millimeter scale high throughput battery research system**

F. Rahmanian, S. Fuchs, B. Zhang, M. Fichtner and H. S. Stein, *Digital Discovery*, 2024, Advance Article, DOI: 10.1039/D3DD00257H

This article is licensed under a [Creative Commons Attribution 3.0 Unported Licence](#). **You can use material from this article in other publications without requesting further permissions** from the RSC, provided that the correct acknowledgement is given.

# List of Figures \*

- 1.1. Comparative overview of material design strategies, namely direct and inverse approaches. In the direct approach, experiments include the entire range of possible combinations of materials A and B through HTE or manual experimentation. This process segregates regions based on a prior search into physically infeasible areas (inaccessible) and previously explored (quantified) regions, while also identifying unmeasured (under exploration) and unknown (uncharted) ones. Here, the combinations of each material with their known ACS, are explored for a potential functionality  $P(ACS)$ . In contrast, the inverse strategy reverses the sequence by estimating the target functionality,  $P(ACS)$ , and guides the search toward optimal ACS combinations in fewer steps. This approach is illustrated in a contour plot, where the estimated functionality is derived from the quantified ACS data from the lower grid space, and the measurements are directed to compounds with predicted maximized functionality<sup>53</sup>. Such a strategy enables a more efficient, targeted exploration and can accelerate the discovery of novel materials. . . . . 6

\* All Figures were created with BioRender.com

- 1.2. Schematic representation of MAPs. The process begins by collecting prior knowledge, such as empirical data, literature reviews, and statistical analyses of previous experiments. This information is then used by the scientist to formulate a hypothesis for a research question. Following this step, the MAPs carry out an iterative high-throughput experiment using a closed-loop feedback mechanism that integrates the robotic experimentation platform, real-time analysis, and AI/ML-driven algorithms to optimize experimental parameters and plan the subsequent run. This iterative process is orchestrated by web interfaces that communicate between devices and servers at every stage to accelerate data transfer. Every phase, from setup and preparation to characterization, is stored in a unified data repository and is documented in reports that adhere to FAIR data principles. . . . . 9
- 1.3. An overview of the data and information flow across various domains in the BIG-MAP project<sup>196</sup>. It showcases the integration of experimental workflows, computational tools, and data-driven strategies within a unified and shared data infrastructure. Herein, standardized protocols and ontologies, together with public repositories, ensure data exchange and interoperability across theoretical, experimental, and AI-driven domains. The commitment to FAIR principles<sup>187</sup> is further reinforced by the open-source publication of data in the cloud and the collection of tools and developed software within the BIG-MAP registry<sup>199</sup> to allow for efficient collaboration among project partners. Applications such as SDLabs, HELAO, and tomato for experimental design and laboratory automation are curated, along with computational resources such as the SEI Modeler and Quantum Espresso. Other applications, including PRISMA and EVA, are designed for spectral characterization and electrochemical analysis. The BIG-MAP project is a collaborative platform that aims to unravel the complexities of batteries from materials development to end-use applications to ultimately accelerate and advance the frontiers of energy storage technology. . . . . 18





---

<p>2.1. Design of enablers and tools for a reliable materials acceleration platform for battery-related studies engineered for the fulfillment of this thesis’ objectives and achieved through the integration of various building blocks. These include the development of hardware components for the experimental setup (SDC), the design of an asynchronous Python-based web interface for orchestrating sequential or parallel experiments for orchestration (HELAO), the implementation of a real-time quality control mechanism, the development of a data analysis package (MADAP), the design of a FAIR-based data management system, a user-friendly interface, and two AI-based frameworks. In particular, an ML pipeline for active learning applications and a DL pipeline for predicting high-dimensional scenarios such as battery lifetime (AR-CANA). Together, these tools contribute to an advanced intelligent acceleration platform (Auto-MISCHBARES). . . . .</p>	<p>24</p>
<p>3.1. Schematic representation of concurrent multithreading system, where the non-blocking execution of tasks is achieved through parallelism across multiple CPU cores and concurrency within threads. Here, each horizontal lane represents a single thread running in parallel with others. Threads 1 and 2 illustrate the concurrent execution of a sequence of experimental tasks in separate setups. Thread 3 manages real-time auto-inspection and dynamic data management tasks, and Thread 4 maintains a live visualization throughout the operation. This depiction exemplifies the two different types of executions applicable in the design of laboratory automation frameworks. . . . .</p>	<p>29</p>
<p>3.2. An asynchronous event-driven execution framework, where multiple tasks submit requests to an event queue. A single-threaded, non-blocking event loop processes these requests and orchestrates the execution flow by scheduling and delegating events in the queue and registering callbacks without awaiting operation completion. Once operations are finished, the registered callbacks will be triggered, and the event loop will continue to process new requests. Completed responses are asynchronously returned to the tasks. . . . .</p>	<p>30</p>

- 3.3. Illustration of the API communication process and endpoint configuration in the FastAPI framework, showcased at an exemplary function, which contains the components of an API request and its corresponding validation mechanism. The provided code snippet shows a FastAPI POST decorator that defines an asynchronous endpoint. This request includes `experiment_id` as the path parameter for unique experiment identification and the query parameter `experiment_type`. Additionally, this example illustrates the request header, `scientists_username`, implemented for tracking and authentication. The `Experiment` class, which inherits from the `BaseModel` module of the Pydantic package, defines the schema of the request body, with attributes such as `description`, `duration`, and `voltage`. This is used to validate the type of the incoming request. . . . . 32
- 3.4. Overview of RDM lifecycle. This diagram illustrates the sequential phases of RDM, beginning with Project Planning, where strategies for data management and compliance with FAIR principles<sup>187</sup> are established. It progresses through Data Acquisition and Preprocessing to create and structure the planned databases and assure data quality. The next phase continues with the Analysis and Prediction, where AI, ML, and statistical algorithms are applied, and code developments are supported by version control systems. In the following phase, data sharing is achieved through visualization tools such as Matplotlib and Plotly<sup>234</sup> and results are shared via interactive web UIs or GUIs. The cycle is completed with the Access and Reuse of data across local storage or cloud-based repositories such as Zenodo<sup>235</sup> to facilitate its extended use and impact. . . . . 34

- 3.5. A feedback loop for high-throughput experimentation. The schematic illustrates a closed-loop system, initiating with a randomly selected trial from a predefined list of experiments. The automated sequential process includes testing, measurement, and data analysis to derive the experiment’s FOM that is then incorporated into an AL framework; here, the data of the completed experiment is added to the training dataset and is simultaneously removed from the testing queue. The selected ML model, represented here by a RF regressor, is retrained with the updated dataset and proceeds to predict the FOM for the remaining unsampled trials, accompanied by an estimated mean ( $\mu$ ) and standard deviation ( $\sigma$ ). Following this prediction, an acquisition function, represented here by an upper confidence bound heuristic, is applied to acquire these predictions to target areas of the greatest model uncertainty. This function balances between explorative and exploitative strategies via a tunable parameter,  $\lambda$ . The experiment that maximizes the acquisition function’s criteria is thus selected for the subsequent execution, with its parameters sent to the devices. This iterative feedback loop perpetuates until a predefined experimental budget is reached or the optimal solution within the search space is empirically determined. . . . . 41
- 3.6. Estimation of prediction interval using the jackknife+ method. The series of panels enclosed in the yellow frame represents the model evaluations ( $M_1, \dots, M_{17}, \dots, M_{25}, \dots$ ), with each model trained on subsets of the data excluding one observation ( $X_{-i}$ ) in successive LOO iterations to calculate the corresponding conformity score from the residual error. The process loops across the entire training dataset. The rightmost panel combines all these evaluations, utilizing the empirical quantiles of the conformity scores to establish the prediction interval for new observations, depicted as a shaded area. This provides a reliable measure of uncertainty for future predictions. . . . . 43

- 3.7. The schematic illustration of common neural network activation functions and their derivatives. a) represents the sigmoid activation function, which maps input to values between 0 and 1, and its derivative, which is maximal at the function's inflection point, indicating maximum input sensitivity. b) depicts the tanh function, which produces outputs ranging from  $-1$  to  $1$ , with its derivative reaching its highest absolute value at the origin. c) presents the Leaky ReLU activation function, which prevents gradient vanishing during backpropagation for negative inputs by allowing a small and non-zero gradient. The derivative of this function maintains a constant positive slope for negative inputs and a slope of one for positive ones. . . . . 45
- 3.8. Schematic of an RNN. The circuit diagram on the left illustrates the compact cyclic architecture of an RNN in which the hidden state  $h$ , is recurrently updated based on the current input ( $x$ ) and the previous states. This update process is parameterized by weight matrices  $U$  and  $W$ , for input-to-hidden and hidden-to-hidden connections, respectively. The graph on the right side depicts the unfolded RNN across multiple time steps, detailing the processing of input sequences. At each time step  $t$ , the hidden state is updated by applying a tanh activation function to the weighted sum of the input  $x^{(t)}$  and the previous hidden state  $h^{(t-1)}$ . The output  $y^{(t)}$  at this time step is then calculated from the hidden state through another transformation involving the weight matrix  $V$ , which connects this state to the output. This unfolded computational graph demonstrates how RNN captures temporal dependencies within sequences. . . . . 46

- 3.9. Schematic representation of an LSTM unit during the t-th time step. This structure illustrates the information flow from the input vector  $(x^{(t)})$ , the previous hidden state  $(h^{(t-1)})$ , and the cell state  $(s^{(t-1)})$  through various gates: the forget  $f^{(t)}$ , input  $g^{(t)}q^{(t)}$ , and output gate  $o^{(t)}$ . Each gate executes a pointwise operation that combines  $x^{(t)}$ ,  $h^{(t-1)}$ , and their corresponding weights with their bias, subsequently passing through a non-linear activation function. The forget gate calculates the amount of short-term information remembered from  $h^{(t-1)}$  in the long-term memory  $s^{(t-1)}$  while ignoring the rest. The input gate consists of two sections that decide both the quantity of short-term information to be acquired and its proportion to be stored in the long-term memory. The combination of these two gates results in a state update, which is the new long-term memory,  $s^{(t)}$ . Lastly, the information from the output gate is multiplied by the transformed updated cell state, resulting in a new hidden state,  $h^{(t)}$ . . . . . 49
  
- 3.10. The electrochemical process of a rechargeable Li-ion battery during charging and discharging cycles is illustrated by the "rocking chair" model. The anode consists of a graphite-based composite on a copper current collector, and the cathode comprises LFP on an aluminum foil. The direction of electron and lithium-ion flow is indicated by the orange and blue arrows for charge and discharge. Lithium ions are transferred during charging from the cathode to the anode across the electrolyte and intercalate into the graphite layers. This is accompanied by the flow of electrons through the external circuit, resulting in a reduction reaction within the anode to balance the charge. Reversely, the discharge process involves the deintercalation of lithium ions from the graphite layers at the anode, whereby they flow back through the electrolyte and towards the cathode, with electrons traveling through the external circuit to the aluminum sheet, thus delivering electric energy. Crystal structures of LFP,  $FePO_4$ , and graphite were obtained from the Materials Project<sup>66</sup>. . . . . 54

3.11. Schematic representation of Nyquist plot illustrating the impedance characteristics of a Randles ECM over a wide range of frequencies. The circuit elements consist of the solution resistance  $R_s$ , which is positioned at the highest frequency and intercepts on the real axis, representing the ionic transport resistance of the electrolyte. The charge transfer resistance,  $R_{ct}$ , is indicative of the kinetic barriers at the electrode-electrolyte interface, and the capacitance,  $C_{dl}$ , is representative of the accumulated charge in the electrode’s double layer. All these charge transfer-controlled features can be observed in the semicircle in the Nyquist plot. The total impedance at low-frequency intercept on the real axis is the sum of  $R_s$  and  $R_{ct}$ . The line at a  $45^\circ$  angle is indicative of a Warburg impedance  $Z_w$ , which models the mass transfer limitations, such as the diffusion of lithium ions in the electrolyte. It is important to note that in non-ideal systems, variations in electrolyte properties and electrode surface conditions result in deviations from ideal capacitive behavior. These deviations can be modeled by a constant phase element, which alters the representation of the Nyquist plot from ideal behavior<sup>281</sup>. . . . . 56

3.12. Schematic presentation of a voltammogram obtained from a CV test. The graph illustrates a curve obtained during a potential sweep, including anodic and cathodic scans, that recorded the current responses. In the forward pass, an oxidation reaction occurs, followed by the double layer’s charging and an anodic peak( $E_{pa}$ ,  $I_{pa}$ ). During the backward scan, the oxidized species are reduced, resulting in a cathodic peak ( $E_{pc}$ ,  $I_{pc}$ ). The peaks provide further insights into the reversibility of the electrochemical system. . . . . 58



# Abbreviations

**ACID** atomicity, consistency, isolation, and durability.

**ACS** atomic fingerprint, composition, and structure.

**AFLOW** Automatic-FLOW.

**AI** Artificial Intelligence.

**AL** Active Learning.

**AMANDA** Autonomous Materials and Device Application Platform.

**ANNs** Artificial Neural Networks.

**API** Application Programming Interface.

**ARCANA** Attention-based ReCurrent Algorithm for Neural Analysis.

**ARES** Autonomous Research System.

**ASGI** Asynchronous Server Gateway Interface.

**Auto-MISCHBARES** autonomous millimeter scale high-throughput battery research system.

**BattINFO** Battery interface ontology.

**BayBE** Bayesian Back End.

**BEAR** Bayesian experimental autonomous researcher.

**BIG-MAP** Battery Interface Genome – Materials Acceleration Platform.

**BMS** battery management systems.

**BO** Bayesian Optimization.



**BPTT** backward propagation through time.

**CAMEO** closed-loop, autonomous system for materials exploration and optimization.

**CE** coulombic efficiency.

**CEI** cathode electrolyte interphase.

**ChASM** Chemical Assembly.

**CLO** closed-loop optimization.

**CMS** Combinatorial Materials Sciences.

**CNN** Convolutional Neural Network.

**CNTs** carbon nanotubes.

**CPUs** Central Processing Units.

**CRUD** Create, Read, Update, Delete.

**CSD** Cambridge Structural Database.

**CV** cyclic voltammetry.

**DL** Deep Learning.

**DMPs** data management plans.

**DMS** Data Management System.

**DoE** Design of Experiments.

**EaaS** Experiment-as-a-Service.

**EC** ethylene carbonate.

**ECM** equivalent circuit model.

**EIS** Electrochemical Impedance Spectroscopy.

- EMMC** European Materials Modelling Council.
- EMMO** European Materials Modelling Ontology.
- ESCALATE** Experiment Specification, Capture and Laboratory Automation Technology.
- ESS** energy storage solutions.
- FAIR** Findable, Accessible, Interoperable, and Reusable.
- FFNNs** feed-forward neural networks.
- FOM** figure-of-merit.
- GANs** Generative Adversarial Networks.
- GAs** genetic algorithms.
- GIL** Global Interpreter Lock.
- GPUs** Graphics Processing Units.
- GRU** Gated Recurrent Units.
- GUI** graphical user interface.
- HELAO** hierarchical autonomous laboratory automation and orchestration.
- HGP** Human Genome Project.
- HTE** High-Throughput Experimentation.
- I/O** Input/Output.
- ICSD** Inorganic Crystal Structure Database.
- i.i.d.** independent and identically distributed.
- Leaky ReLU** leaky rectified linear unit.
- LFP** lithium iron phosphate.

**LIBs** Lithium-ion batteries.

**LiBs** Lithium-ion batteries.

**LiPF<sub>6</sub>** lithium hexafluorophosphate.

**LLMs** Large Language Models.

**LOO** leave-one-out.

**LSTM** long short term memory.

**MADAP** Modular and Autonomous Data Analysis Platform.

**MAOS** Materials Acceleration Operation System.

**MAPs** Materials Acceleration Platforms.

**MGI** Material Genome Initiative.

**ML** machine learning.

**MSE** mean square error.

**NLP** Natural Languages Processing.

**NOMAD** Novel Materials Discovery.

**OOP** Object Oriented Programming.

**OQMD** Open Quantum Materials Database.

**PC** propylene carbonate.

**QRL** quality, reliability, and life.

**RAPID** Robot-Accelerated Perovskite Investigation and Discovery.

**RDBMS** relational database management system.

**RDM** Research Data Management.

**REST** Representational State Transfer.

**RF** random forest.

**RL** reinforcement learning.

**RMSE** root mean squared error.

**RNN** Recurrent Neural Network.

**SDC** Scanning Droplet Cell.

**SDLs** Self-Driving Laboratories.

**SEI** solid electrolyte interphase.

**Seq-to-Seq** sequence-to-sequence.

**SoH** State of Health.

**tanh** hyperbolic tangent.

**TDD** test-driven development.

**TRL** Technology Readiness Level.

**UI** User Interface.

**UUIDs** Universally Unique Identifiers.

**VAE** variational autoencoder.

**VR** virtual reality.

**w.r.t.** with respect to.

**XPS** X-ray photoelectron spectroscopy.



# Bibliography

- [1] X.-D. Xiang and I. Takeuchi. *Combinatorial Materials Synthesis*. 1st ed. CRC Press, Aug. 2003. ISBN: 9780203912737. DOI: [10.1201/9780203912737](https://doi.org/10.1201/9780203912737).
- [2] M. Fichtner. “Recent Research and Progress in Batteries for Electric Vehicles”. In: *Batteries & Supercaps* 5.2 (Oct. 2021), e202100224. ISSN: 2566-6223. DOI: [10.1002/batt.202100224](https://doi.org/10.1002/batt.202100224).
- [3] P. Kirkpatrick and C. Ellis. “Chemical space”. In: *Nature* 432.7019 (Dec. 2004), pp. 823–823. ISSN: 1476-4687. DOI: [10.1038/432823a](https://doi.org/10.1038/432823a).
- [4] K. L. M. Drew, H. Baiman, P. Khwaounjoo, B. Yu, and J. Reynisson. “Size estimation of chemical space: how big is it?” In: *Journal of Pharmacy and Pharmacology* 64.4 (Dec. 2011), pp. 490–495. ISSN: 0022-3573. DOI: [10.1111/j.2042-7158.2011.01424.x](https://doi.org/10.1111/j.2042-7158.2011.01424.x).
- [5] A. Bhowmik, I. Castelli, J. M. García-Lastra, P. B. Jørgensen, O. Winther, and T. Vegge. “A perspective on inverse design of battery interphases using multi-scale modelling, experiments and generative deep learning”. In: *Energy Storage Materials* 21 (Sept. 2019), pp. 446–456. ISSN: 2405-8297. DOI: [10.1016/j.ensm.2019.06.011](https://doi.org/10.1016/j.ensm.2019.06.011).
- [6] L. Su, M. Ferrandon, J. A. Kowalski, J. T. Vaughey, and F. R. Brushett. “Electrolyte Development for Non-Aqueous Redox Flow Batteries Using a High-Throughput Screening Platform”. In: *Journal of The Electrochemical Society* 161.12 (Sept. 2014), A1905–A1914. ISSN: 1945-7111. DOI: [10.1149/2.0811412jes](https://doi.org/10.1149/2.0811412jes).
- [7] S. Matsuda, K. Nishioka, and S. Nakanishi. “High-throughput combinatorial screening of multi-component electrolyte additives to improve the performance of Li metal secondary batteries”. In: *Scientific Reports* 9.1 (Apr. 2019), p. 6211. ISSN: 2045-2322. DOI: [10.1038/s41598-019-42766-x](https://doi.org/10.1038/s41598-019-42766-x).
- [8] I. Takeuchi, J. Lauterbach, and M. J. Fasolka. “Combinatorial materials synthesis”. In: *Materials Today* 8.10 (Oct. 2005), pp. 18–26. ISSN: 1369-7021. DOI: [10.1016/s1369-7021\(05\)71121-4](https://doi.org/10.1016/s1369-7021(05)71121-4).

- [9] B. Rohr, H. S. Stein, D. Guevarra, Y. Wang, J. A. Haber, M. Aykol, S. K. Suram, and J. M. Gregoire. "Benchmarking the acceleration of materials discovery by sequential learning". In: *Chemical Science* 11.10 (Jan. 2020), pp. 2696–2706. ISSN: 2041-6539. DOI: [10.1039/c9sc05999g](https://doi.org/10.1039/c9sc05999g).
- [10] J. Amici, P. Asinari, E. Ayerbe, P. Barboux, P. Bayle-Guillemaud, R. J. Behm, M. Bercibar, E. Berg, A. Bhowmik, S. Bodoardo, I. E. Castelli, I. Cekic-Laskovic, R. Christensen, S. Clark, R. Diehm, R. Dominko, M. Fichtner, A. A. Franco, A. Grimaud, N. Guillet, M. Hahlin, S. Hartmann, V. Heiries, K. Hermansson, A. Heuer, S. Jana, L. Jabbour, J. Kallo, A. Latz, H. Lorrman, O. M. Løvvik, S. Lyonnard, M. Meeus, E. Paillard, S. Perraud, T. Placke, C. Punckt, O. Raccurt, J. Ruhland, E. Sheridan, H. Stein, J.-M. Tarascon, V. Trapp, T. Vegge, M. Weil, W. Wenzel, M. Winter, A. Wolf, and K. Edström. "A Roadmap for Transforming Research to Invent the Batteries of the Future Designed within the European Large Scale Research Initiative BATTERY 2030+". In: *Advanced Energy Materials* 12.17 (Jan. 2022), p. 2102785. ISSN: 1614-6840. DOI: [10.1002/aenm.202102785](https://doi.org/10.1002/aenm.202102785).
- [11] M. Gauthier, T. J. Carney, A. Grimaud, L. Giordano, N. Pour, H.-H. Chang, D. Fenning, S. Lux, O. Paschos, C. Bauer, F. Maglia, S. Lupart, P. Lamp, and Y. Shao-horn. "Electrode–Electrolyte Interface in Li-Ion Batteries: Current Understanding and New Insights". In: *The Journal of Physical Chemistry Letters* 6.22 (Nov. 2015), pp. 4653–4672. ISSN: 1948-7185. DOI: [10.1021/acs.jpcllett.5b01727](https://doi.org/10.1021/acs.jpcllett.5b01727).
- [12] M. Winter. "The Solid Electrolyte Interphase – The Most Important and the Least Understood Solid Electrolyte in Rechargeable Li Batteries". In: *Zeitschrift für Physikalische Chemie* 223.10-11 (Dec. 2009), pp. 1395–1406. ISSN: 0942-9352. DOI: [10.1524/zpch.2009.6086](https://doi.org/10.1524/zpch.2009.6086).
- [13] A. Benayad, D. Diddens, A. Heuer, A. N. Krishnamoorthy, M. Maiti, F. L. Cras, M. Legallais, F. Rahmanian, Y. Shin, H. Stein, M. Winter, C. Wölke, P. Yan, and I. Cekic-Laskovic. "High-Throughput Experimentation and Computational Freeway Lanes for Accelerated Battery Electrolyte and Interface Development Research". In: *Advanced Energy Materials* 12.17 (Nov. 2021), p. 2102678. ISSN: 1614-6840. DOI: [10.1002/aenm.202102678](https://doi.org/10.1002/aenm.202102678).

- [14] K. A. Severson, P. M. Attia, N. Jin, N. Perkins, B. Jiang, Z. Yang, M. H. Chen, M. Aykol, P. K. Herring, D. Fraggedakis, M. Z. Bazant, S. J. Harris, W. C. Chueh, and R. D. Braatz. “Data-driven prediction of battery cycle life before capacity degradation”. In: *Nature Energy* 4.5 (Mar. 2019), pp. 383–391. ISSN: 2058-7546. DOI: [10.1038/s41560-019-0356-8](https://doi.org/10.1038/s41560-019-0356-8).
- [15] A. Bhowmik, M. Berecibar, M. Casas-Cabanas, G. Csányi, R. Dominko, K. Hermansson, M. R. Palacín, H. Stein, and T. Vegge. “Implications of the BATTERY 2030+ AI-Assisted Toolkit on Future Low-TRL Battery Discoveries and Chemistries”. In: *Advanced Energy Materials* 12.17 (Nov. 2021), p. 2102698. ISSN: 1614-6840. DOI: [10.1002/aenm.202102698](https://doi.org/10.1002/aenm.202102698).
- [16] H. S. Stein, A. Sanin, F. Rahmanian, B. Zhang, M. Vogler, J. K. Flowers, L. Fischer, S. Fuchs, N. Choudhary, and L. Schroeder. “From materials discovery to system optimization by integrating combinatorial electrochemistry and data science”. In: *Current Opinion in Electrochemistry* 35 (Oct. 2022), p. 101053. ISSN: 2451-9103. DOI: [10.1016/j.coelec.2022.101053](https://doi.org/10.1016/j.coelec.2022.101053). URL: <https://www.sciencedirect.com/science/article/abs/pii/S2451910322001181>.
- [17] H. S. Stein and J. M. Gregoire. “Progress and prospects for accelerating materials science with automated and autonomous workflows”. In: *Chemical Science* 10.42 (Sept. 2019), pp. 9640–9649. ISSN: 2041-6539. DOI: [10.1039/c9sc03766g](https://doi.org/10.1039/c9sc03766g).
- [18] A. Aspuru-Guzik and K. Persson. *Materials Acceleration Platform: Accelerating Advanced Energy Materials Discovery by Integrating High-Throughput Methods and Artificial Intelligence*. 2018. URL: <http://nrs.harvard.edu/urn-3:HUL.InstRepos:35164974> (visited on 05/05/2024).
- [19] M. M. Flores-Leonar, L. M. Mejia-Mendoza, A. Aguilar-Granda, B. Sanchez-Lengeling, H. Tribukait, C. Amador-Bedolla, and A. Aspuru-Guzik. “Materials Acceleration Platforms: On the way to autonomous experimentation”. In: *Current Opinion in Green and Sustainable Chemistry* 25 (Oct. 2020), p. 100370. ISSN: 2452-2236. DOI: [10.1016/j.cogsc.2020.100370](https://doi.org/10.1016/j.cogsc.2020.100370).
- [20] M. Fichtner, K. Edström, E. Ayerbe, M. Berecibar, A. Bhowmik, I. Castelli, S. Clark, R. Dominko, M. Erakca, A. Franco, A. Grimaud, B. Horstmann, A. Latz, H. Lorrmann, M. Meeus, R. Narayan, F. Pammer, J. Ruhland, H. Stein, T. Vegge, and M. Weil. “Rechargeable Batteries of the Future—The State of the



- Art from a BATTERY 2030+ Perspective". In: *Advanced Energy Materials* 12.17 (Dec. 2021), p. 2102904. ISSN: 1614-6840. DOI: [10.1002/aenm.202102904](https://doi.org/10.1002/aenm.202102904).
- [21] S. Sripad and V. Viswanathan. "Performance Metrics Required of Next-Generation Batteries to Make a Practical Electric Semi Truck". In: *ACS Energy Letters* 2.7 (June 2017), pp. 1669–1673. ISSN: 2380-8195. DOI: [10.1021/acsenergylett.7b00432](https://doi.org/10.1021/acsenergylett.7b00432).
- [22] T. S. Kuhn and D. Hawkins. "The Structure of Scientific Revolutions". In: *American Journal of Physics* 31.7 (July 1963), pp. 554–555. ISSN: 1943-2909. DOI: [10.1119/1.1969660](https://doi.org/10.1119/1.1969660).
- [23] J. J. De Pablo, B. Jones, C. L. Kovacs, V. Ozolins, and A. P. Ramirez. "The Materials Genome Initiative, the interplay of experiment, theory and computation". In: *Current Opinion in Solid State and Materials Science* 18.2 (Apr. 2014), pp. 99–117. ISSN: 1359-0286. DOI: [10.1016/j.cossms.2014.02.003](https://doi.org/10.1016/j.cossms.2014.02.003).
- [24] E. O. Pyzer-Knapp, J. W. Pitera, P. W. J. Staar, S. Takeda, T. Laino, D. P. Sanders, J. Sexton, J. R. Smith, and A. Curioni. "Accelerating materials discovery using artificial intelligence, high performance computing and robotics". In: *npj Computational Materials* 8.1 (Apr. 2022), p. 84. ISSN: 2057-3960. DOI: [10.1038/s41524-022-00765-z](https://doi.org/10.1038/s41524-022-00765-z).
- [25] R. Hoogenboom, M. A. R. Meier, and U. S. Schubert. "Combinatorial Methods, Automated Synthesis and High-Throughput Screening in Polymer Research: Past and Present". In: *Macromolecular Rapid Communications* 24.1 (Jan. 2003), pp. 15–32. ISSN: 1521-3927. DOI: [10.1002/marc.200390013](https://doi.org/10.1002/marc.200390013).
- [26] W. F. Maier, K. Stoewe, and S. Sieg. "Combinatorial and High-Throughput Materials Science". In: *Angewandte Chemie International Edition* 46.32 (Aug. 2007), pp. 6016–6067. ISSN: 1521-3773. DOI: [10.1002/anie.200603675](https://doi.org/10.1002/anie.200603675).
- [27] Y. Xu, X. Liu, X. Cao, C. Huang, E. Liu, S. Qian, X. Liu, Y. Wu, F. Dong, C.-W. Qiu, J. Qiu, K. Hua, W. Su, J. Wu, H. Xu, Y. Han, C. Fu, Z. Yin, M. Liu, R. Roepman, S. Dietmann, M. Virta, F. Kengara, Z. Zhang, L. Zhang, T. Zhao, J. Dai, J. Yang, L. Lan, M. Luo, Z. Liu, T. An, B. Zhang, X. He, S. Cong, X. Liu, W. Zhang, J. P. Lewis, J. M. Tiedje, Q. Wang, Z. An, F. Wang, L. Zhang, T. Huang, C. Lu, Z. Cai, F. Wang, and J. Zhang. "Artificial intelligence: A

- powerful paradigm for scientific research". In: *The Innovation* 2.4 (Nov. 2021), p. 100179. ISSN: 2666-6758. DOI: [10.1016/j.xinn.2021.100179](https://doi.org/10.1016/j.xinn.2021.100179).
- [28] H. Stein, M. Suta, and J. George. "Die Materialsynthesemaschine". In: *Nachrichten aus der Chemie* 68.12 (Dec. 2020), pp. 66–69. ISSN: 1868-0054. DOI: [10.1002/nadc.20204096061](https://doi.org/10.1002/nadc.20204096061).
- [29] A. M. Turing. "Computing Machinery and Intelligence". In: *Mind* LIX.236 (Oct. 1950), pp. 433–460. ISSN: 0026-4423. DOI: [10.1093/mind/lix.236.433](https://doi.org/10.1093/mind/lix.236.433).
- [30] G. Moore. "Progress in digital integrated electronics". In: *International Electron Devices Meeting* (1975). URL: [https://www.eng.auburn.edu/users/agrawvd/COURSE/E7770\\_Spr07/READ/Gordon\\_Moore\\_1975\\_Speech.pdf](https://www.eng.auburn.edu/users/agrawvd/COURSE/E7770_Spr07/READ/Gordon_Moore_1975_Speech.pdf) (visited on 05/05/2024).
- [31] R. Rojas. "Konrad Zuse's Legacy: The Architecture of the Z1 and Z3". In: *IEEE Annals of the History of Computing* 19.2 (Apr. 1997), pp. 5–16. ISSN: 1058-6180. DOI: [10.1109/85.586067](https://doi.org/10.1109/85.586067).
- [32] M. Campbell-Kelly, W. F. Aspray, J. R. Yost, H. Tinn, and G. C. Diaz. *Computer A History Of The Information Machine. A history of the information machine*. Ed. by W. Aspray, J. R. Yost, G. C. Díaz, and H. Tinn. Fourth edition. Includes bibliographical references and index. New York, NY: Routledge, June 2023. 1 p. ISBN: 1000878724.
- [33] D. A. Boiko, R. MacKnight, B. Kline, and G. Gomes. "Autonomous chemical research with large language models". In: *Nature* 624.7992 (Dec. 2023), pp. 570–578. ISSN: 1476-4687. DOI: [10.1038/s41586-023-06792-0](https://doi.org/10.1038/s41586-023-06792-0).
- [34] G. Bell, T. Hey, and A. Szalay. "Beyond the Data Deluge". In: *Science* 323.5919 (Mar. 2009), pp. 1297–1298. ISSN: 1095-9203. DOI: [10.1126/science.1170411](https://doi.org/10.1126/science.1170411).
- [35] T. Hey, S. Tansley, K. Tolle, and J. Gray. *The Fourth Paradigm: Data-Intensive Scientific Discovery*. Microsoft Research, Oct. 2009. ISBN: 978-0-9825442-0-4. URL: <https://www.microsoft.com/en-us/research/publication/fourth-paradigm-data-intensive-scientific-discovery/>.
- [36] J. J. Hanak. "The 'multiple-sample concept' in materials research: Synthesis, compositional analysis and testing of entire multicomponent systems". In: *Journal of Materials Science* 5.11 (Nov. 1970), pp. 964–971. ISSN: 1573-4803. DOI: [10.1007/bf00558177](https://doi.org/10.1007/bf00558177).

- [37] E. M. Gordon, R. W. Barrett, W. J. Dower, S. P. Fodor, and M. A. Gallop. “Applications of Combinatorial Technologies to Drug Discovery. 2. Combinatorial Organic Synthesis, Library Screening Strategies, and Future Directions”. In: *Journal of Medicinal Chemistry* 37.10 (May 1994), pp. 1385–1401. ISSN: 1520-4804. DOI: [10.1021/jm00036a001](https://doi.org/10.1021/jm00036a001).
- [38] X.-D. Xiang, X. Sun, G. Briceno, Y. Lou, K.-A. Wang, H. Chang, W. G. Wallace-Freedman, S.-W. Chen, and P. G. Schultz. “A Combinatorial Approach to Materials Discovery”. In: *Science* 268.5218 (June 1995), pp. 1738–1740. ISSN: 1095-9203. DOI: [10.1126/science.268.5218.1738](https://doi.org/10.1126/science.268.5218.1738).
- [39] E. Danielson, J. Golden, E. McFarland, C. Reaves, W. Weinberg, and X. D. Wu. “A combinatorial approach to the discovery and optimization of luminescent materials”. In: *Nature* 389.6654 (Oct. 1997), pp. 944–948. ISSN: 1476-4687. DOI: [10.1038/40099](https://doi.org/10.1038/40099).
- [40] J. Noh, J. Kim, H. S. Stein, B. Sanchez-Lengeling, J. M. Gregoire, A. Aspuru-Guzik, and Y. Jung. “Inverse Design of Solid-State Materials via a Continuous Representation”. In: *Matter* 1.5 (Nov. 2019), pp. 1370–1384. ISSN: 2590-2385. DOI: [10.1016/j.matt.2019.08.017](https://doi.org/10.1016/j.matt.2019.08.017).
- [41] S. Leonelli. *Scientific Research and Big Data*. Ed. by S. E. of Philosophy. Stanford Encyclopedia of Philosophy. Stanford Encyclopedia of Philosophy. May 2020. URL: <https://plato.stanford.edu/entries/science-big-data/> (visited on 05/06/2024).
- [42] L. Himanen, A. Geurts, A. Foster, and P. Rinke. “Data-driven materials science: status, challenges, and perspectives”. In: *Advanced Science* 6.21 (Sept. 2019), p. 1900808. ISSN: 2198-3844. DOI: [10.1002/advs.201900808](https://doi.org/10.1002/advs.201900808). arXiv: [1907.05644](https://arxiv.org/abs/1907.05644).
- [43] G. E. Hinton, S. Osindero, and Y. Teh. “A Fast Learning Algorithm for Deep Belief Nets”. In: *Neural Computation* 18.7 (July 2006), pp. 1527–1554. ISSN: 1530-888X. DOI: [10.1162/neco.2006.18.7.1527](https://doi.org/10.1162/neco.2006.18.7.1527).
- [44] R. Batra, L. Song, and R. Ramprasad. “Emerging materials intelligence ecosystems propelled by machine learning”. In: *Nature Reviews Materials* 6.8 (Nov. 2020), pp. 655–678. ISSN: 2058-8437. DOI: [10.1038/s41578-020-00255-y](https://doi.org/10.1038/s41578-020-00255-y).

- [45] A. Agrawal and A. Choudhary. “Perspective: Materials informatics and big data: Realization of the ‘fourth paradigm’ of science in materials science”. In: *APL Materials* 4.5 (Apr. 2016), p. 053208. ISSN: 2166-532X. DOI: [10.1063/1.4946894](https://doi.org/10.1063/1.4946894).
- [46] K. Alberi, M. Nardelli, A. Zakutayev, L. Mitas, S. Curtarolo, A. Jain, M. Fornari, N. Marzari, I. Takeuchi, M. L. Green, M. Kanatzidis, M. Toney, S. Butenko, B. Meredig, S. Lany, U. Kattner, A. Davydov, E. Toberer, V. Stevanović, A. Walsh, N. Park, A. Aspuru-Guzik, D. P. Tabor, J. Nelson, J. Murphy, A. Setlur, J. Gregoire, H. Li, R. Xiao, A. Ludwig, L. W. Martin, A. Rappe, S. Wei, and J. Perkins. “The 2019 materials by design roadmap”. In: *Journal of Physics D: Applied Physics* 52.1 (Oct. 2018), p. 013001. ISSN: 1361-6463. DOI: [10.1088/1361-6463/aad926](https://doi.org/10.1088/1361-6463/aad926).
- [47] J. Wei, X. Chu, X.-Y. Sun, K. Xu, H.-X. Deng, J. Chen, Z. Wei, and M. Lei. “Machine learning in materials science”. In: *InfoMat* 1.3 (Sept. 2019), pp. 338–358. ISSN: 2567-3165. DOI: [10.1002/inf2.12028](https://doi.org/10.1002/inf2.12028).
- [48] R. Pollice, G. dos Passos Gomes, M. Aldeghi, R. J. Hickman, M. Krenn, C. Lavigne, M. Lindner-D’Addario, A. Nigam, C. T. Ser, Z. Yao, and A. Aspuru-Guzik. “Data-Driven Strategies for Accelerated Materials Design”. In: *Accounts of Chemical Research* 54.4 (Feb. 2021), pp. 849–860. ISSN: 1520-4898. DOI: [10.1021/acs.accounts.0c00785](https://doi.org/10.1021/acs.accounts.0c00785).
- [49] H. Wang, T. Fu, Y. Du, W. Gao, K. Huang, Z. Liu, P. Chandak, S. Liu, P. Van Katwyk, A. Deac, A. Anandkumar, K. Bergen, C. P. Gomes, S. Ho, P. Kohli, J. Lasenby, J. Leskovec, T.-Y. Liu, A. Manrai, D. Marks, B. Ramsundar, L. Song, J. Sun, J. Tang, P. Veličković, M. Welling, L. Zhang, C. W. Coley, Y. Bengio, and M. Zitnik. “Scientific discovery in the age of artificial intelligence”. In: *Nature* 620.7972 (Aug. 2023), pp. 47–60. ISSN: 1476-4687. DOI: [10.1038/s41586-023-06221-2](https://doi.org/10.1038/s41586-023-06221-2).
- [50] M. Umehara, H. S. Stein, D. Guevarra, P. F. Newhouse, D. A. Boyd, and J. M. Gregoire. “Analyzing machine learning models to accelerate generation of fundamental materials insights”. In: *npj Computational Materials* 5.1 (Mar. 2019), p. 34. ISSN: 2057-3960. DOI: [10.1038/s41524-019-0172-5](https://doi.org/10.1038/s41524-019-0172-5).

- [51] A. Franceschetti and A. Zunger. “The inverse band-structure problem of finding an atomic configuration with given electronic properties”. In: *Nature* 402.6757 (Nov. 1999), pp. 60–63. ISSN: 1476-4687. DOI: [10.1038/46995](https://doi.org/10.1038/46995).
- [52] J. Peng, D. Schwalbe-Koda, K. Akkiraju, T. Xie, L. Giordano, Y. Yu, C. J. Eom, J. R. Lunger, D. J. Zheng, R. R. Rao, S. Muiy, J. C. Grossman, K. Reuter, R. Gómez-Bombarelli, and Y. Shao-Horn. “Human-and machine-centred designs of molecules and materials for sustainability and decarbonization”. In: *Nature Reviews Materials* 7.12 (Aug. 2022), pp. 991–1009. ISSN: 2058-8437. DOI: [10.1038/s41578-022-00466-5](https://doi.org/10.1038/s41578-022-00466-5).
- [53] A. Zunger. “Inverse design in search of materials with target functionalities”. In: *Nature Reviews Chemistry* 2.4 (Mar. 2018), p. 0121. ISSN: 2397-3358. DOI: [10.1038/s41570-018-0121](https://doi.org/10.1038/s41570-018-0121).
- [54] P. C. Sabatier. “Past and future of inverse problems”. In: *Journal of Mathematical Physics* 41.6 (June 2000), pp. 4082–4124. ISSN: 1089-7658. DOI: [10.1063/1.533336](https://doi.org/10.1063/1.533336).
- [55] J. Wang, Y. Wang, and Y. Chen. “Inverse Design of Materials by Machine Learning”. In: *Materials* 15.5 (Feb. 2022), p. 1811. ISSN: 1996-1944. DOI: [10.3390/ma15051811](https://doi.org/10.3390/ma15051811).
- [56] K. T. Schütt, S. Chmiela, O. A. Von Lilienfeld, A. Tkatchenko, K. Tsuda, and K.-R. Müller. *Machine Learning Meets Quantum Physics*. Springer International Publishing, 2020. ISBN: 9783030402457. DOI: [10.1007/978-3-030-40245-7](https://doi.org/10.1007/978-3-030-40245-7). arXiv: [1903.03516](https://arxiv.org/abs/1903.03516).
- [57] Y. Xu, J. Ge, and C.-W. Ju. “Machine Learning in Energy Chemistry: Introduction, Challenge and Perspective”. In: *Energy Advances* 2.7 (Apr. 2023), pp. 896–921. ISSN: 2753-1457. DOI: [10.1039/d3ya00057e](https://doi.org/10.1039/d3ya00057e).
- [58] A. Kadurin, S. Nikolenko, K. Khrabrov, A. Aliper, and A. Zhavoronkov. “druGAN: An Advanced Generative Adversarial Autoencoder Model for de Novo Generation of New Molecules with Desired Molecular Properties in Silico”. In: *Molecular Pharmaceutics* 14.9 (Aug. 2017), pp. 3098–3104. ISSN: 1543-8392. DOI: [10.1021/acs.molpharmaceut.7b00346](https://doi.org/10.1021/acs.molpharmaceut.7b00346).

- [59] M. H. S. Segler, M. Preuss, and M. Waller. "Planning chemical syntheses with deep neural networks and symbolic AI". In: *Nature* 555.7698 (Mar. 2018), pp. 604–610. ISSN: 1476-4687. DOI: [10.1038/nature25978](https://doi.org/10.1038/nature25978). arXiv: [1708.04202](https://arxiv.org/abs/1708.04202).
- [60] Z. Zhou, X. Li, and R. Zare. "Optimizing Chemical Reactions with Deep Reinforcement Learning". In: *ACS Central Science* 3.12 (Dec. 2017), pp. 1337–1344. ISSN: 2374-7951. DOI: [10.1021/acscentsci.7b00492](https://doi.org/10.1021/acscentsci.7b00492).
- [61] R. Gómez-Bombarelli, J. N. Wei, D. Duvenaud, J. M. Hernández-Lobato, B. Sánchez-Lengeling, D. Sheberla, J. Aguilera-Iparraguirre, T. D. Hirzel, R. P. Adams, and A. Aspuru-Guzik. "Automatic Chemical Design Using a Data-Driven Continuous Representation of Molecules". In: *ACS Central Science* 4.2 (Jan. 2018), pp. 268–276. ISSN: 2374-7951. DOI: [10.1021/acscentsci.7b00572](https://doi.org/10.1021/acscentsci.7b00572). arXiv: [1610.02415](https://arxiv.org/abs/1610.02415).
- [62] E. S. Lander, L. M. Linton, B. Birren, et al. "Initial sequencing and analysis of the human genome". en. In: *Nature* 409.6822 (Feb. 2001), pp. 860–921. ISSN: 1476-4687. DOI: [10.1038/35057062](https://doi.org/10.1038/35057062).
- [63] I. H. G. S. Consortium. "Finishing the euchromatic sequence of the human genome". In: *Nature* 431.7011 (Oct. 2004), pp. 931–945. ISSN: 1476-4687. DOI: [10.1038/nature03001](https://doi.org/10.1038/nature03001).
- [64] J. C. Venter, M. D. Adams, E. W. Myers, et al. "The Sequence of the Human Genome". In: *Science* 291.5507 (Feb. 2001), pp. 1304–1351. ISSN: 1095-9203. DOI: [10.1126/science.1058040](https://doi.org/10.1126/science.1058040).
- [65] C. Suh, C. Fare, J. A. Warren, and E. O. Pyzer-Knapp. "Evolving the Materials Genome: How Machine Learning Is Fueling the Next Generation of Materials Discovery". In: *Annual Review of Materials Research* 50.1 (July 2020), pp. 1–25. ISSN: 1545-4118. DOI: [10.1146/annurev-matsci-082019-105100](https://doi.org/10.1146/annurev-matsci-082019-105100).
- [66] A. Jain, S. P. Ong, G. Hautier, W. Chen, W. D. Richards, S. Dacek, S. Cholia, D. Gunter, D. Skinner, G. Ceder, and K. A. Persson. "Commentary: The Materials Project: A materials genome approach to accelerating materials innovation". In: *APL Materials* 1.1 (July 2013). ISSN: 2166-532X. DOI: [10.1063/1.4812323](https://doi.org/10.1063/1.4812323).



- [67] S. Curtarolo, W. Setyawan, G. Hart, M. Jahnátek, R. Chepulskii, R. H. Taylor, S. Wang, J. Xue, K. Yang, O. Levy, M. Mehl, H. Stokes, D. Demchenko, and D. Morgan. “AFLOW: An automatic framework for high-throughput materials discovery”. In: *Computational Materials Science* 58 (June 2012), pp. 218–226. ISSN: 0927-0256. DOI: [10.1016/j.commatsci.2012.02.005](https://doi.org/10.1016/j.commatsci.2012.02.005). arXiv: [1308.5715](https://arxiv.org/abs/1308.5715).
- [68] S. Curtarolo, W. Setyawan, S. Wang, J. Xue, K. Yang, R. H. Taylor, L. J. Nelson, G. L. Hart, S. Sanvito, M. Buongiorno-Nardelli, N. Mingo, and O. Levy. “AFLOWLIB.ORG: A distributed materials properties repository from high-throughput ab initio calculations”. In: *Computational Materials Science* 58 (June 2012), pp. 227–235. ISSN: 0927-0256. DOI: [10.1016/j.commatsci.2012.02.002](https://doi.org/10.1016/j.commatsci.2012.02.002).
- [69] *Materials Genome Initiative for Global Competitiveness*. National Science and Technology Council (NSTC), June 2011. URL: <https://www.mgi.gov> (visited on 05/05/2024).
- [70] A. White. “The Materials Genome Initiative: One year on”. In: *MRS Bulletin* 37.8 (Aug. 2012), pp. 715–716. ISSN: 1938-1425. DOI: [10.1557/mrs.2012.194](https://doi.org/10.1557/mrs.2012.194).
- [71] C. Wadia. *New Commitments Support Administration’s Materials Genome Initiative*. 2012. URL: <https://obamawhitehouse.archives.gov/blog/2012/05/14/new-commitments-support-administration-s-materials-genome-initiative> (visited on 05/05/2024).
- [72] J. E. Saal, S. Kirklin, M. Aykol, B. Meredig, and C. Wolverton. “Materials Design and Discovery with High-Throughput Density Functional Theory: The Open Quantum Materials Database (OQMD)”. In: *JOM* 65.11 (Sept. 2013), pp. 1501–1509. ISSN: 1543-1851. DOI: [10.1007/s11837-013-0755-4](https://doi.org/10.1007/s11837-013-0755-4).
- [73] A. Ludwig. “Discovery of new materials using combinatorial synthesis and high-throughput characterization of thin-film materials libraries combined with computational methods”. In: *npj Computational Materials* 5.1 (July 2019), p. 70. ISSN: 2057-3960. DOI: [10.1038/s41524-019-0205-0](https://doi.org/10.1038/s41524-019-0205-0).
- [74] R. Zarnetta, P. J. S. Buenconsejo, A. Savan, S. Thienhaus, and A. Ludwig. “High-throughput study of martensitic transformations in the complete Ti–Ni–Cu system”. In: *Intermetallics* 26 (July 2012), pp. 98–109. ISSN: 0966-9795. DOI: [10.1016/j.intermet.2012.03.044](https://doi.org/10.1016/j.intermet.2012.03.044).

- [75] B. Sanchez-Lengeling and A. Aspuru-Guzik. “Inverse molecular design using machine learning: Generative models for matter engineering”. In: *Science* 361.6400 (July 2018), pp. 360–365. ISSN: 1095-9203. DOI: [10.1126/science.aat2663](https://doi.org/10.1126/science.aat2663).
- [76] C. Houben and A. A. Lapkin. “Automatic discovery and optimization of chemical processes”. In: *Current Opinion in Chemical Engineering* 9 (Aug. 2015), pp. 1–7. ISSN: 2211-3398. DOI: [10.1016/j.coche.2015.07.001](https://doi.org/10.1016/j.coche.2015.07.001).
- [77] C. W. Coley, N. S. Eyke, and K. F. Jensen. “Autonomous Discovery in the Chemical Sciences Part I: Progress”. In: *Angewandte Chemie International Edition* 59.51 (June 2020), pp. 22858–22893. ISSN: 1521-3773. DOI: [10.1002/anie.201909987](https://doi.org/10.1002/anie.201909987). arXiv: [2003.13754](https://arxiv.org/abs/2003.13754).
- [78] E. Stach, B. DeCost, A. G. Kusne, J. Hattrick-Simpers, K. A. Brown, K. G. Reyes, J. Schrier, S. Billinge, T. Buonassisi, I. Foster, C. P. Gomes, J. M. Gregoire, A. Mehta, J. Montoya, E. Olivetti, C. Park, E. Rotenberg, S. K. Saikin, S. Smullin, V. Stanev, and B. Maruyama. “Autonomous experimentation systems for materials development: A community perspective”. In: *Matter* 4.9 (Sept. 2021), pp. 2702–2726. ISSN: 2590-2385. DOI: [10.1016/j.matt.2021.06.036](https://doi.org/10.1016/j.matt.2021.06.036).
- [79] F. Rose, C. Toher, E. Gossett, C. Oses, M. B. Nardelli, M. Fornari, and S. Curtarolo. “AFLUX: The LUX materials search API for the AFLOW data repositories”. In: *Computational Materials Science* 137 (Sept. 2017), pp. 362–370. ISSN: 0927-0256. DOI: [10.1016/j.commatsci.2017.04.036](https://doi.org/10.1016/j.commatsci.2017.04.036). arXiv: [1612.05130](https://arxiv.org/abs/1612.05130).
- [80] R. H. Taylor, F. Rose, C. Toher, O. Levy, K. Yang, M. Buongiorno Nardelli, and S. Curtarolo. “A RESTful API for exchanging materials data in the AFLOWLIB.org consortium”. In: *Computational Materials Science* 93 (Oct. 2014), pp. 178–192. ISSN: 0927-0256. DOI: [10.1016/j.commatsci.2014.05.014](https://doi.org/10.1016/j.commatsci.2014.05.014).
- [81] M. Christensen, L. Yunker, P. Shiri, T. Zepel, P. L. Prieto, S. Grunert, F. Bork, and J. Hein. “Automation isn’t automatic”. In: *Chemical Science* 12.47 (Oct. 2021), pp. 15473–15490. ISSN: 2041-6539. DOI: [10.1039/d1sc04588a](https://doi.org/10.1039/d1sc04588a).
- [82] R. B. Canty, B. A. Koscher, M. A. McDonald, and K. F. Jensen. “Integrating Autonomy into Automated Research Platforms”. In: *Digital Discovery* 2.5 (Sept. 2023), pp. 1259–1268. ISSN: 2635-098X. DOI: [10.1039/d3dd00135k](https://doi.org/10.1039/d3dd00135k).



- [83] M. Aykol, J. Hummelshøj, A. Anapolsky, K. Aoyagi, M. Bazant, T. Bligaard, R. Braatz, S. Broderick, D. A. Cogswell, J. Dagdelen, W. Drisdell, E. R. García, K. Garikipati, V. Gavini, W. E. Gent, L. Giordano, C. P. Gomes, R. Gómez-Bombarelli, C. Gopal, J. Gregoire, J. Grossman, P. K. Herring, L. Hung, T. Jaramillo, L. A. King, H.-K. Kwon, R. Maekawa, A. Minor, J. H. Montoya, T. Mueller, C. Ophus, K. Rajan, R. Ramprasad, B. A. Rohr, D. Schweigert, Y. Shao-horn, Y. Suga, S. Suram, V. Viswanathan, J. Whitacre, A. Willard, O. Wodo, C. Wolverton, and B. Storey. “The Materials Research Platform: Defining the Requirements from User Stories”. In: *Matter* 1.6 (6 Dec. 2019), pp. 1433–1438. ISSN: 2590-2385. DOI: [10.1016/j.matt.2019.10.024](https://doi.org/10.1016/j.matt.2019.10.024).
- [84] J. M. Gregoire, L. Zhou, and J. A. Haber. “Combinatorial synthesis for AI-driven materials discovery”. In: *Nature Synthesis* 2.6 (Mar. 2023), pp. 493–504. ISSN: 2731-0582. DOI: [10.1038/s44160-023-00251-4](https://doi.org/10.1038/s44160-023-00251-4).
- [85] A. Henson, P. Gromski, and L. Cronin. “Designing Algorithms To Aid Discovery by Chemical Robots”. In: *ACS Central Science* 4.7 (July 2018), pp. 793–804. ISSN: 2374-7951. DOI: [10.1021/acscentsci.8b00176](https://doi.org/10.1021/acscentsci.8b00176).
- [86] S. Kong, D. Guevarra, C. P. Gomes, and J. Gregoire. “Materials Representation and Transfer Learning for Multi-Property Prediction”. In: *Applied Physics Reviews* 8.2 (June 2021). ISSN: 1931-9401. DOI: [10.1063/5.0047066](https://doi.org/10.1063/5.0047066). arXiv: [2106.02225](https://arxiv.org/abs/2106.02225).
- [87] H. Stein. “Advancing data-driven chemistry by beating benchmarks”. In: *Trends in Chemistry* 4.8 (Aug. 2022), pp. 682–684. ISSN: 2589-5974. DOI: [10.1016/j.trechm.2022.05.003](https://doi.org/10.1016/j.trechm.2022.05.003).
- [88] Y. Shi, P. L. Prieto, T. Zepel, S. Grunert, and J. Hein. “Automated Experimentation Powers Data Science in Chemistry”. In: *Accounts of Chemical Research* 54.3 (Jan. 2021), pp. 546–555. ISSN: 1520-4898. DOI: [10.1021/acs.accounts.0c00736](https://doi.org/10.1021/acs.accounts.0c00736).
- [89] E. Soedarmadji, H. Stein, S. Suram, D. Guevarra, and J. Gregoire. “Tracking materials science data lineage to manage millions of materials experiments and analyses”. In: *npj Computational Materials* 5.1 (79 July 2019), p. 79. ISSN: 2057-3960. DOI: [10.1038/s41524-019-0216-x](https://doi.org/10.1038/s41524-019-0216-x).

- [90] F. Häse, L. M. Roch, and A. Aspuru-Guzik. "Next-Generation Experimentation with Self-Driving Laboratories". In: *Trends in Chemistry* 1.3 (June 2019), pp. 282–291. ISSN: 2589-5974. DOI: [10.1016/j.trechm.2019.02.007](https://doi.org/10.1016/j.trechm.2019.02.007).
- [91] J. Li, Y. Tu, R. Liu, Y. Lu, and X. Zhu. "Toward 'On-Demand' Materials Synthesis and Scientific Discovery through Intelligent Robots". In: *Advance Science* 7.7 (Feb. 2020), p. 1901957. ISSN: 2198-3844. DOI: [10.1002/advs.201901957](https://doi.org/10.1002/advs.201901957).
- [92] F. Delgado-Licona and M. Abolhasani. "Research Acceleration in Self-Driving Labs: Technological Roadmap toward Accelerated Materials and Molecular Discovery". In: *Advanced Intelligent Systems* 5.4 (Dec. 2022), p. 2200331. ISSN: 2640-4567. DOI: [10.1002/aisy.202200331](https://doi.org/10.1002/aisy.202200331).
- [93] D. Xue, P. V. Balachandran, J. Hogden, J. Theiler, D. Xue, and T. Lookman. "Accelerated search for materials with targeted properties by adaptive design". In: *Nature Communications* 7.1 (Apr. 2016), pp. 1–9. ISSN: 2041-1723. DOI: [10.1038/ncomms11241](https://doi.org/10.1038/ncomms11241).
- [94] P. Nikolaev, D. Hooper, F. Webber, R. Rao, K. Decker, M. P. Krein, J. Poleski, R. R. Barto, and B. Maruyama. "Autonomy in materials research: a case study in carbon nanotube growth". In: *npj Computational Materials* 2.16031 (Oct. 2016), pp. 1–6. ISSN: 2057-3960. DOI: [10.1038/NPJCOMPUMATS.2016.31](https://doi.org/10.1038/NPJCOMPUMATS.2016.31).
- [95] S. Steiner, J. Wolf, S. Glatzel, A. Andreou, J. M. Granda, G. Keenan, T. Hinkley, G. Aragon-Camarasa, P. J. Kitson, D. Angelone, and L. Cronin. "Organic synthesis in a modular robotic system driven by a chemical programming language". In: *Science* 363.6423 (Jan. 2019), eaav2211. ISSN: 1095-9203. DOI: [10.1126/science.aav2211](https://doi.org/10.1126/science.aav2211).
- [96] F. Häse, L. M. Roch, and A. Aspuru-Guzik. "Chimera: enabling hierarchy based multi-objective optimization for self-driving laboratories". In: *Chemical Science* 9.39 (Aug. 2018), pp. 7642–7655. ISSN: 2041-6539. DOI: [10.1039/c8sc02239a](https://doi.org/10.1039/c8sc02239a).
- [97] F. Häse, L. M. Roch, C. Kreisbeck, and A. Aspuru-Guzik. "Phoenix: A Bayesian Optimizer for Chemistry". In: *ACS Central Science* 4.9 (Aug. 2018), pp. 1134–1145. ISSN: 2374-7951. DOI: [10.1021/acscentsci.8b00307](https://doi.org/10.1021/acscentsci.8b00307).
- [98] D. R. Jones. "A Taxonomy of Global Optimization Methods Based on Response Surfaces". In: *Journal of Global Optimization* 21.4 (Dec. 2001), pp. 345–383. ISSN: 0925-5001. DOI: [10.1023/a:1012771025575](https://doi.org/10.1023/a:1012771025575).

- [99] L. Roch, F. Häse, C. Kreisbeck, T. Tamayo-Mendoza, L. Yunker, J. Hein, and A. Aspuru-Guzik. “ChemOS: Orchestrating autonomous experimentation”. In: *Science Robotics* 3.19 (June 2018), eaat5559. ISSN: 2470-9476. DOI: [10.1126/scirobotics.aat5559](https://doi.org/10.1126/scirobotics.aat5559).
- [100] L. Roch, F. Häse, C. Kreisbeck, T. Tamayo-Mendoza, L. Yunker, J. Hein, and A. Aspuru-Guzik. “ChemOS: An orchestration software to democratize autonomous discovery”. In: *PLOS ONE* 15.4 (Apr. 2020). Ed. by J. Hu, e0229862. ISSN: 1932-6203. DOI: [10.1371/journal.pone.0229862](https://doi.org/10.1371/journal.pone.0229862).
- [101] M. Christensen, L. P. Yunker, F. Adedeji, F. Häse, L. M. Roch, T. Gensch, G. dos Passos Gomes, T. Zepel, M. S. Sigman, A. Aspuru-Guzik, et al. “Data-science driven autonomous process optimization”. In: *Communications Chemistry* 4.1 (Aug. 2021), p. 112. ISSN: 2399-3669. DOI: [10.1038/s42004-021-00550-x](https://doi.org/10.1038/s42004-021-00550-x).
- [102] M. Seifrid, R. Pollice, A. Aguilar-Granda, Z. M. Chan, K. Hotta, C. T. Ser, J. Vestfrid, T. C. Wu, and A. Aspuru-Guzik. “Autonomous Chemical Experiments: Challenges and Perspectives on Establishing a Self-Driving Lab”. In: *Accounts of Chemical Research* 55.17 (Aug. 2022), pp. 2454–2466. ISSN: 1520-4898. DOI: [10.1021/acs.accounts.2c00220](https://doi.org/10.1021/acs.accounts.2c00220).
- [103] F. Häse, M. Aldeghi, R. J. Hickman, L. M. Roch, and A. Aspuru-Guzik. “Gryffin: An algorithm for Bayesian optimization of categorical variables informed by expert knowledge”. In: *Applied Physics Reviews* 8.3 (July 2021). ISSN: 1931-9401. DOI: [10.1063/5.0048164](https://doi.org/10.1063/5.0048164). arXiv: [2003.12127](https://arxiv.org/abs/2003.12127).
- [104] M. Aldeghi, F. Häse, R. J. Hickman, I. Tambllyn, and A. Aspuru-Guzik. “Golem: an algorithm for robust experiment and process optimization”. In: *Chemical Science* 12.44 (Oct. 2021), pp. 14792–14807. ISSN: 2041-6539. DOI: [10.1039/d1sc01545a](https://doi.org/10.1039/d1sc01545a). arXiv: [2103.03716](https://arxiv.org/abs/2103.03716).
- [105] R. J. Hickman, F. Häse, L. M. Roch, and A. Aspuru-Guzik. *Gemini: Dynamic Bias Correction for Autonomous Experimentation and Molecular Simulation*. Mar. 2021. DOI: [10.48550/arXiv.2103.03391](https://doi.org/10.48550/arXiv.2103.03391). arXiv: [2103.03391](https://arxiv.org/abs/2103.03391). (Visited on 05/05/2024).
- [106] H. Beyer and B. Sendhoff. “Robust optimization – A comprehensive survey”. In: *Computer Methods in Applied Mechanics and Engineering* 196.33-34 (July 2007), pp. 3190–3218. ISSN: 0045-7825. DOI: [10.1016/j.cma.2007.03.003](https://doi.org/10.1016/j.cma.2007.03.003).

- [107] T. W. Edgar and T. R. Rice. “Experiment as a service”. In: (Apr. 2017), pp. 1–6. DOI: [10.1109/ths.2017.7943470](https://doi.org/10.1109/ths.2017.7943470).
- [108] J. Wagner, C. Berger, X. Du, T. Stubhan, J. Hauch, and C. Brabec. “The evolution of Materials Acceleration Platforms: toward the laboratory of the future with AMANDA”. In: *Journal of Materials Science* 56.29 (July 2021), pp. 16422–16446. ISSN: 1573-4803. DOI: [10.1007/s10853-021-06281-7](https://doi.org/10.1007/s10853-021-06281-7). arXiv: [2104.07455](https://arxiv.org/abs/2104.07455).
- [109] B. P. MacLeod, F. G. Parlane, T. D. Morrissey, F. Häse, L. M. Roch, K. E. Dettelbach, R. Moreira, L. P. Yunker, M. B. Rooney, J. R. Deeth, et al. “Self-driving laboratory for accelerated discovery of thin-film materials”. In: *Science Advances* 6.20 (May 2020), eaaz8867. ISSN: 2375-2548. DOI: [10.1126/sciadv.aaz8867](https://doi.org/10.1126/sciadv.aaz8867). arXiv: [1906.05398](https://arxiv.org/abs/1906.05398).
- [110] S. Langner, F. Häse, J. D. Perea, T. Stubhan, J. Hauch, L. M. Roch, T. Heumueller, A. Aspuru-Guzik, and C. J. Brabec. “Beyond Ternary OPV: High-Throughput Experimentation and Self-Driving Laboratories Optimize Multicomponent Systems”. In: *Advanced Materials* 32.14 (Feb. 2020), p. 1907801. ISSN: 1521-4095. DOI: [10.1002/adma.201907801](https://doi.org/10.1002/adma.201907801). arXiv: [1909.03511](https://arxiv.org/abs/1909.03511).
- [111] I. M. Pendleton, G. Cattabriga, Z. Li, M. A. Najeeb, S. A. Friedler, A. J. Norquist, E. M. Chan, and J. Schrier. “Experiment Specification, Capture and Laboratory Automation Technology (ESCALATE): a software pipeline for automated chemical experimentation and data management”. In: *MRS Communications* 9.3 (Sept. 2019), pp. 846–859. ISSN: 2159-6867. DOI: [10.1557/mrc.2019.72](https://doi.org/10.1557/mrc.2019.72).
- [112] Z. Li, M. A. Najeeb, L. Alves, A. Z. Sherman, V. Shekar, P. Cruz Parrilla, I. M. Pendleton, W. Wang, P. W. Nega, M. Zeller, et al. “Robot-Accelerated Perovskite Investigation and Discovery”. In: *Chemistry of Materials* 32.13 (June 2020), pp. 5650–5663. ISSN: 1520-5002. DOI: [10.1021/acs.chemmater.0c01153](https://doi.org/10.1021/acs.chemmater.0c01153).
- [113] B. J. Shields, J. Stevens, J. Li, M. Parasram, F. Damani, J. I. M. Alvarado, J. M. Janey, R. P. Adams, and A. G. Doyle. “Bayesian reaction optimization as a tool for chemical synthesis”. In: *Nature* 590.7844 (Feb. 2021), pp. 89–96. ISSN: 1476-4687. DOI: [10.1038/s41586-021-03213-y](https://doi.org/10.1038/s41586-021-03213-y).
- [114] Q. Liang, A. E. Gongora, Z. Ren, A. Tiihonen, Z. Liu, S. Sun, J. R. Deneault, D. Bash, F. Mekki-Berrada, S. A. Khan, K. Hippalgaonkar, B. Maruyama, K. A. Brown, J. W. F. Iii, and T. Buonassisi. “Benchmarking the performance

- of Bayesian optimization across multiple experimental materials science domains". In: *npj Computational Materials* 7.1 (Nov. 2021), p. 188. ISSN: 2057-3960. DOI: [10.1038/s41524-021-00656-9](https://doi.org/10.1038/s41524-021-00656-9). arXiv: [2106.01309](https://arxiv.org/abs/2106.01309).
- [115] A. E. Gongora, B. Xu, W. Perry, C. Okoye, P. F. Riley, K. G. Reyes, E. Morgan, and K. A. Brown. "A Bayesian experimental autonomous researcher for mechanical design". In: *Science Advances* 6.15 (Apr. 2020), eaaz1708. ISSN: 2375-2548. DOI: [10.1126/sciadv.aaz1708](https://doi.org/10.1126/sciadv.aaz1708).
- [116] A. Kusne, A. Kusne, H. Yu, C. Wu, H. Zhang, J. Hattrick-Simpers, B. L. DeCost, S. Sarker, C. Oses, C. Toher, S. Curtarolo, A. V. Davydov, R. Agarwal, L. Bendersky, M. Li, A. Mehta, and I. Takeuchi. "On-the-fly closed-loop materials discovery via Bayesian active learning". In: *Nature Communications* 11.1 (Nov. 2020), p. 5966. ISSN: 2041-1723. DOI: [10.1038/s41467-020-19597-w](https://doi.org/10.1038/s41467-020-19597-w).
- [117] B. Burger, P. M. Maffettone, V. Gusev, C. M. Aitchison, Y. Bai, X.-y. Wang, X. Li, B. M. Alston, B. Li, R. Clowes, N. Rankin, B. Harris, R. S. Sprick, and A. Cooper. "A mobile robotic chemist". In: *Nature* 583.7815 (July 2020), pp. 237–241. ISSN: 1476-4687. DOI: [10.1038/s41586-020-2442-2](https://doi.org/10.1038/s41586-020-2442-2).
- [118] J. R. Deneault, J. Chang, J. I. Myung, D. Hooper, A. Armstrong, M. Pitt, and B. Maruyama. "Toward autonomous additive manufacturing: Bayesian optimization on a 3D printer". In: *MRS Bulletin* 46.7 (Apr. 2021), pp. 566–575. ISSN: 1938-1425. DOI: [10.1557/s43577-021-00051-1](https://doi.org/10.1557/s43577-021-00051-1).
- [119] D. Reker, E. A. Hoyt, G. J. Bernardes, and T. Rodrigues. "Adaptive Optimization of Chemical Reactions with Minimal Experimental Information". In: *Cell Reports Physical Science* 1.11 (Nov. 2020), p. 100247. ISSN: 2666-3864. DOI: [10.1016/j.xcrp.2020.100247](https://doi.org/10.1016/j.xcrp.2020.100247).
- [120] R. W. Epps, M. Bowen, A. A. Volk, K. Abdel-latif, S. Han, K. G. Reyes, A. Amassian, and M. Abolhasani. "Artificial Chemist: An Autonomous Quantum Dot Synthesis Bot". In: *Advanced Materials* 32.30 (June 2020), p. 2001626. ISSN: 1521-4095. DOI: [10.1002/adma.202001626](https://doi.org/10.1002/adma.202001626).
- [121] P. Fantke, C. Cinquemani, P. Yaseneva, J. D. Mello, H. Schwabe, B. Ebeling, and A. Lapkin. "Transition to sustainable chemistry through digitalization". In: *Chem* 7.11 (Nov. 2021), pp. 2866–2882. ISSN: 2451-9294. DOI: [10.1016/j.chempr.2021.09.012](https://doi.org/10.1016/j.chempr.2021.09.012).

- [122] H. Adamu, S. I. Abba, P. B. Anyin, Y. Sani, and M. Qamar. “Artificial intelligence-navigated development of high-performance electrochemical energy storage systems through feature engineering of multiple descriptor families of materials”. In: *Energy Advances* 2.5 (Apr. 2023), pp. 615–645. ISSN: 2753-1457. DOI: [10.1039/d3ya00104k](https://doi.org/10.1039/d3ya00104k).
- [123] Y. Liu, B. Guo, X. Zou, Y. Li, and S. Shi. “Machine learning assisted materials design and discovery for rechargeable batteries”. In: *Energy Storage Materials* 31 (Oct. 2020), pp. 434–450. ISSN: 2405-8297. DOI: [10.1016/j.ensm.2020.06.033](https://doi.org/10.1016/j.ensm.2020.06.033).
- [124] P. Liu, B. Guo, T. An, F. Hui, G. Zhu, C.-C. Jiang, and X. Jiang. “High throughput materials research and development for lithium ion batteries”. In: *Journal of Materiomics* 3.3 (Sept. 2017), pp. 202–208. ISSN: 2352-8478. DOI: [10.1016/j.jmat.2017.07.004](https://doi.org/10.1016/j.jmat.2017.07.004).
- [125] D. Atkins, E. Ayerbe, A. Benayad, F. G. Capone, E. Capria, I. E. Castelli, I. Cekic-Laskovic, R. Ciria, L. Dudy, K. Edström, M. R. Johnson, H. Li, J. M. G. Lastra, M. L. De Souza, V. Meunier, M. Morcrette, H. Reichert, P. Simon, J.-P. Rueff, J. Sottmann, W. Wenzel, and A. Grimaud. “Understanding Battery Interfaces by Combined Characterization and Simulation Approaches: Challenges and Perspectives”. In: *Advanced Energy Materials* 12.17 (Dec. 2021), p. 2102687. ISSN: 1614-6840. DOI: [10.1002/aenm.202102687](https://doi.org/10.1002/aenm.202102687).
- [126] V. Ramadesigan, P. W. C. Northrop, S. De, S. Santhanagopalan, R. D. Braatz, and V. R. Subramanian. “Modeling and Simulation of Lithium-Ion Batteries from a Systems Engineering Perspective”. In: *Journal of The Electrochemical Society* 159.3 (Mar. 2012), R31–R45. ISSN: 1945-7111. DOI: [10.1149/2.018203jes](https://doi.org/10.1149/2.018203jes).
- [127] J. Peng, J. Meng, D. Chen, H. Liu, S. Hao, X. Sui, and X. Du. “A Review of Lithium-Ion Battery Capacity Estimation Methods for Onboard Battery Management Systems: Recent Progress and Perspectives”. In: *Batteries* 8.11 (Nov. 2022), p. 229. ISSN: 2313-0105. DOI: [10.3390/batteries8110229](https://doi.org/10.3390/batteries8110229).
- [128] B. P. MacLeod, F. G. L. Parlane, C. C. Rupnow, K. E. Dettelbach, M. S. Elliott, T. D. Morrissey, T. H. Haley, O. Proskurin, M. B. Rooney, N. Taherimakhsousi, D. J. Dvorak, H. N. Chiu, C. E. B. Waizenegger, K. Ocean, M. Mokhtari, and C. P. Berlinguette. “A self-driving laboratory advances the Pareto front for



- material properties". In: *Nature Communications* 13.1 (Feb. 2022), p. 995. ISSN: 2041-1723. DOI: [10.1038/s41467-022-28580-6](https://doi.org/10.1038/s41467-022-28580-6).
- [129] J. Schaarschmidt, J. Yuan, T. Strunk, I. Kondov, S. P. Huber, G. Pizzi, L. Kahle, F. T. Bölle, I. E. Castelli, T. Vegge, F. Hanke, T. Hickel, J. Neugebauer, C. R. C. Rêgo, and W. Wenzel. "Workflow Engineering in Materials Design within the BATTERY 2030+ Project". In: *Advanced Energy Materials* 12.17 (Dec. 2021), p. 2102638. ISSN: 1614-6840. DOI: [10.1002/aenm.202102638](https://doi.org/10.1002/aenm.202102638).
- [130] M. S. Lipu, M. Hannan, T. F. Karim, A. Hussain, M. Saad, A. Ayob, M. S. Miah, and T. Mahlia. "Intelligent algorithms and control strategies for battery management system in electric vehicles: Progress, challenges and future outlook". In: *Journal of Cleaner Production* 292 (Apr. 2021), p. 126044. ISSN: 0959-6526. DOI: [10.1016/j.jclepro.2021.126044](https://doi.org/10.1016/j.jclepro.2021.126044).
- [131] Z. Yao, Y. Lum, A. Johnston, L. M. Mejia-Mendoza, X. Zhou, Y. Wen, A. Aspuru-Guzik, E. H. Sargent, and Z. W. Seh. "Machine learning for a sustainable energy future". In: *Nature Reviews Materials* 8.3 (Oct. 2022), pp. 202–215. ISSN: 2058-8437. DOI: [10.1038/s41578-022-00490-5](https://doi.org/10.1038/s41578-022-00490-5). arXiv: [2210.10391](https://arxiv.org/abs/2210.10391).
- [132] E. Ayerbe, M. Bercibar, S. Clark, A. A. Franco, and J. Ruhland. "Digitalization of Battery Manufacturing: Current Status, Challenges, and Opportunities". In: *Advanced Energy Materials* 12.17 (Dec. 2021), p. 2102696. ISSN: 1614-6840. DOI: [10.1002/aenm.202102696](https://doi.org/10.1002/aenm.202102696).
- [133] L. Cheng, R. S. Assary, X. Qu, A. Jain, S. P. Ong, N. N. Rajput, K. Persson, and L. A. Curtiss. "Accelerating Electrolyte Discovery for Energy Storage with High-Throughput Screening". In: *The Journal of Physical Chemistry Letters* 6.2 (Jan. 2015), pp. 283–291. ISSN: 1948-7185. DOI: [10.1021/jz502319n](https://doi.org/10.1021/jz502319n).
- [134] X. Qu, A. Jain, N. N. Rajput, L. Cheng, Y. Zhang, S. P. Ong, M. Brafman, E. Maginn, L. A. Curtiss, and K. A. Persson. "The Electrolyte Genome project: A big data approach in battery materials discovery". In: *Computational Materials Science* 103 (June 2015), pp. 56–67. ISSN: 0927-0256. DOI: [10.1016/j.commat.2015.02.050](https://doi.org/10.1016/j.commat.2015.02.050).
- [135] R. Dmello, J. D. Milshtein, F. R. Brushett, and K. C. Smith. "Cost-driven materials selection criteria for redox flow battery electrolytes". In: *Journal of*

- Power Sources* 330 (Oct. 2016), pp. 261–272. ISSN: 0378-7753. DOI: [10.1016/j.jpowsour.2016.08.129](https://doi.org/10.1016/j.jpowsour.2016.08.129).
- [136] T. Vegge, J.-M. Tarascon, and K. Edström. “Toward Better and Smarter Batteries by Combining AI with Multisensory and Self-Healing Approaches”. In: *Advanced Energy Materials* 11.23 (Apr. 2021), p. 2100362. ISSN: 1614-6840. DOI: [10.1002/aenm.202100362](https://doi.org/10.1002/aenm.202100362).
- [137] J. F. Whitacre, J. Mitchell, A. Dave, W. Wu, S. Burke, and V. Viswanathan. “An Autonomous Electrochemical Test Stand for Machine Learning Informed Electrolyte Optimization”. In: *Journal of The Electrochemical Society* 166.16 (Oct. 2019), A4181–A4187. ISSN: 1945-7111. DOI: [10.1149/2.0521916jes](https://doi.org/10.1149/2.0521916jes).
- [138] A. Dave, J. M. Mitchell, K. Kandasamy, S. Burke, B. Paria, B. Póczos, J. Whitacre, and V. Viswanathan. “Autonomous Discovery of Battery Electrolytes with Robotic Experimentation and Machine Learning”. In: *Cell Reports Physical Science* 1.12 (Dec. 2020), p. 100264. ISSN: 2666-3864. DOI: [10.1016/j.xcrp.2020.100264](https://doi.org/10.1016/j.xcrp.2020.100264). arXiv: [2001.09938](https://arxiv.org/abs/2001.09938).
- [139] K. Kandasamy, K. R. Vysyaraju, W. Neiswanger, B. Paria, C. R. Collins, J. Schneider, B. Poczos, and E. P. Xing. “Tuning hyperparameters without grad students: scalable and robust Bayesian optimisation with dragonfly”. In: *J. Mach. Learn. Res.* 21.1 (Jan. 2020). ISSN: 1532-4435. DOI: [10.5555/3455716.3455797](https://doi.org/10.5555/3455716.3455797).
- [140] A. Dave, J. Mitchell, S. Burke, H. Lin, J. Whitacre, and V. Viswanathan. “Autonomous optimization of nonaqueous battery electrolytes via robotic experimentation and machine learning”. In: *Nature Communications* 13.5454 (1 Sept. 27, 2022). DOI: [10.1038/s41467-022-32938-1](https://doi.org/10.1038/s41467-022-32938-1).
- [141] K. Sliozberg, D. Schäfer, T. Erichsen, R. Meyer, C. Khare, A. Ludwig, and W. Schuhmann. “High-Throughput Screening of Thin-Film Semiconductor Material Libraries I: System Development and Case Study for Ti-W-O”. In: *ChemSusChem* 8.7 (Feb. 2015), pp. 1270–1278. ISSN: 1864-564X. DOI: [10.1002/cssc.201402917](https://doi.org/10.1002/cssc.201402917).
- [142] R. Meyer, K. Sliozberg, C. Khare, W. Schuhmann, and A. Ludwig. “High-Throughput Screening of Thin-Film Semiconductor Material Libraries II: Char-



- acterization of Fe-W-O Libraries". In: *ChemSusChem* 8.7 (Feb. 2015), pp. 1279–1285. ISSN: 1864-564X. DOI: [10.1002/cssc.201402918](https://doi.org/10.1002/cssc.201402918).
- [143] H. S. Stein, D. Guevarra, A. Shinde, R. J. Jones, J. M. Gregoire, and J. A. Haber. "Functional mapping reveals mechanistic clusters for OER catalysis across (Cu–Mn–Ta–Co–Sn–Fe)Ox composition and pH space". In: *Materials Horizons* 6.6 (Mar. 2019), pp. 1251–1258. ISSN: 2051-6355. DOI: [10.1039/c8mh01641k](https://doi.org/10.1039/c8mh01641k). URL: <https://pubs.rsc.org/en/content/articlelanding/2019/mh/c8mh01641k>.
- [144] D. Muñoz-Torrero, C. Santana Santos, E. García-Quismondo, S. Dieckhöfer, T. Erichsen, J. Palma, W. Schuhmann, and E. Ventosa. "The redox mediated – scanning droplet cell system for evaluation of the solid electrolyte interphase in Li-ion batteries". In: *RSC Advances* 13.23 (May 2023), pp. 15521–15530. ISSN: 2046-2069. DOI: [10.1039/d3ra00631j](https://doi.org/10.1039/d3ra00631j).
- [145] N. Aspern, G. Röschenthaler, M. Winter, M. Winter, and I. Cekic-Laskovic. "Fluorine and Lithium: Ideal Partners for High-Performance Rechargeable Battery Electrolytes." In: *Angewandte Chemie International Edition* 58.45 (July 2019), pp. 15978–16000. ISSN: 1521-3773. DOI: [10.1002/anie.201901381](https://doi.org/10.1002/anie.201901381).
- [146] S. Daboss, F. Rahmanian, H. S. Stein, and C. Kranz. "The potential of scanning electrochemical probe microscopy and scanning droplet cells in battery research". In: *Electrochemical Science Advances* 2.4 (Aug. 2021), e2100122. ISSN: 2698-5977. DOI: [10.1002/elsa.202100122](https://doi.org/10.1002/elsa.202100122).
- [147] M. Abolhasani and E. Kumacheva. "The rise of self-driving labs in chemical and materials sciences". In: *Nature Synthesis* 2.6 (Jan. 2023), pp. 483–492. ISSN: 2731-0582. DOI: [10.1038/s44160-022-00231-0](https://doi.org/10.1038/s44160-022-00231-0).
- [148] K. Xu. "Interfaces and interphases in batteries". In: *Journal of Power Sources* 559 (Mar. 2023), p. 232652. ISSN: 0378-7753. DOI: [10.1016/j.jpowsour.2023.232652](https://doi.org/10.1016/j.jpowsour.2023.232652).
- [149] R. Narayan, C. Laberty-Robert, J. Pelta, J.-m. Tarascon, and R. Dominko. "Self-Healing: An Emerging Technology for Next-Generation Smart Batteries". In: *Advanced Energy Materials* 12.17 (Oct. 2021), p. 2102652. ISSN: 1614-6840. DOI: [10.1002/aenm.202102652](https://doi.org/10.1002/aenm.202102652).

- [150] A. Y. S. Eng, C. B. Soni, Y. Lum, E. Khoo, Z. Yao, S. K. Vineeth, V. Kumar, J. Lu, C. S. Johnson, C. Wolverton, and Z. W. Seh. "Theory-guided experimental design in battery materials research". In: *Science Advances* 8.19 (May 2022), eabm2422. ISSN: 2375-2548. DOI: [10.1126/sciadv.abm2422](https://doi.org/10.1126/sciadv.abm2422).
- [151] I. Goodfellow, J. Pouget-Abadie, M. Mirza, B. Xu, D. Warde-Farley, S. Ozair, A. Courville, and Y. Bengio. "Generative Adversarial Nets". In: *Advances in Neural Information Processing Systems*. Ed. by Z. Ghahramani, M. Welling, C. Cortes, N. Lawrence, and K. Weinberger. Vol. 27. Curran Associates, Inc., 2014. URL: [https://proceedings.neurips.cc/paper\\_files/paper/2014/file/5ca3e9b122f61f8f06494c97b1afccf3-Paper.pdf](https://proceedings.neurips.cc/paper_files/paper/2014/file/5ca3e9b122f61f8f06494c97b1afccf3-Paper.pdf).
- [152] Z. Hu, Z. Yang, R. Salakhutdinov, and E. P. Xing. *On Unifying Deep Generative Models*. July 2017. DOI: [10.48550/arXiv.1706.00550](https://doi.org/10.48550/arXiv.1706.00550). arXiv: 1706.00550.
- [153] D. Hafner, D. Tran, T. Lillicrap, A. Irpan, and J. Davidson. *Noise Contrastive Priors for Functional Uncertainty*. July 2019. DOI: [10.48550/ARXIV.1807.09289](https://doi.org/10.48550/ARXIV.1807.09289). (Visited on 05/05/2024).
- [154] B. Lakshminarayanan, A. Pritzel, and C. Blundell. "Simple and Scalable Predictive Uncertainty Estimation using Deep Ensembles". In: *Advances in Neural Information Processing Systems*. Ed. by I. Guyon, U. V. Luxburg, S. Bengio, H. Wallach, R. Fergus, S. Vishwanathan, and R. Garnett. Vol. 30. Curran Associates, Inc., Dec. 2017. URL: [https://proceedings.neurips.cc/paper\\_files/paper/2017/file/9ef2ed4b7fd2c810847ffa5fa85bce38-Paper.pdf](https://proceedings.neurips.cc/paper_files/paper/2017/file/9ef2ed4b7fd2c810847ffa5fa85bce38-Paper.pdf).
- [155] D. Rajagopal, A. Koeppe, M. Esmailpour, M. Selzer, W. Wenzel, H. Stein, and B. Nestler. "Data-Driven Virtual Material Analysis and Synthesis for Solid Electrolyte Interphases". In: *Advanced Energy Materials* 13.40 (Sept. 2023), p. 2301985. ISSN: 1614-6840. DOI: [10.1002/aenm.202301985](https://doi.org/10.1002/aenm.202301985).
- [156] H. Stein, D. Guevarra, P. Newhouse, E. Soedarmadji, and J. M. Gregoire. "Machine learning of optical properties of materials – predicting spectra from images and images from spectra". In: *Chemical Science* 10.1 (Oct. 2018), pp. 47–55. ISSN: 2041-6539. DOI: [10.1039/c8sc03077d](https://doi.org/10.1039/c8sc03077d).
- [157] Z. Deng, V. Kumar, F. T. Bölle, F. Caro, A. A. Franco, I. E. Castelli, P. Canepa, and Z. W. Seh. "Towards autonomous high-throughput multiscale modelling

- of battery interfaces". In: *Energy & Environmental Science* 15.2 (Dec. 2021), pp. 579–594. ISSN: 1754-5706. DOI: [10.1039/d1ee02324a](https://doi.org/10.1039/d1ee02324a).
- [158] Y. Lyu, Y.-l. Liu, T. Cheng, and B. Guo. "High-throughput characterization methods for lithium batteries". In: *Journal of Materiomics* 3.3 (Sept. 2017), pp. 221–229. ISSN: 2352-8478. DOI: [10.1016/j.jmat.2017.08.001](https://doi.org/10.1016/j.jmat.2017.08.001).
- [159] P. M. Attia, A. Bills, F. Planella, P. Dechent, G. dos Reis, M. Dubarry, P. Gasper, R. Gilchrist, S. Greenbank, D. Howey, O. Liu, E. Khoo, Y. Preger, A. Soni, S. Sripad, A. Stefanopoulou, and V. Sulzer. "Review—'Knees' in Lithium-Ion Battery Aging Trajectories". In: *Journal of The Electrochemical Society* 169.6 (June 2022), p. 060517. ISSN: 1945-7111. DOI: [10.1149/1945-7111/ac6d13](https://doi.org/10.1149/1945-7111/ac6d13). arXiv: [2201.02891](https://arxiv.org/abs/2201.02891).
- [160] X. Liu, L. Zhang, H. Yu, J. Wang, J. Li, K. Yang, Y. Zhao, H. Wang, B. Wu, N. Brandon, and S. Yang. "Bridging Multiscale Characterization Technologies and Digital Modeling to Evaluate Lithium Battery Full Lifecycle". In: *Advanced Energy Materials* 12.33 (June 2022), p. 2200889. ISSN: 1614-6840. DOI: [10.1002/aenm.202200889](https://doi.org/10.1002/aenm.202200889).
- [161] K. Liu, K. Li, Q. Peng, and C. Zhang. "A brief review on key technologies in the battery management system of electric vehicles". In: *Frontiers of Mechanical Engineering* 14.1 (Apr. 2018), pp. 47–64. ISSN: 2095-0241. DOI: [10.1007/s11465-018-0516-8](https://doi.org/10.1007/s11465-018-0516-8).
- [162] Y. Che, X. Hu, X. Lin, J. Guo, and R. Teodorescu. "Health prognostics for lithium-ion batteries: mechanisms, methods, and prospects". In: *Energy & Environmental Science* 16.2 (Jan. 2023), pp. 338–371. ISSN: 1754-5706. DOI: [10.1039/d2ee03019e](https://doi.org/10.1039/d2ee03019e).
- [163] P. M. Attia, A. Grover, N. Jin, K. A. Severson, T. M. Markov, Y.-H. Liao, M. H. Chen, B. Cheong, N. Perkins, Z. Yang, P. K. Herring, M. Aykol, S. J. Harris, R. D. Braatz, S. Ermon, and W. C. Chueh. "Closed-loop optimization of fast-charging protocols for batteries with machine learning". In: *Nature* 578.7795 (Feb. 2020), pp. 397–402. ISSN: 1476-4687. DOI: [10.1038/s41586-020-1994-5](https://doi.org/10.1038/s41586-020-1994-5).
- [164] H. Rauf, M. Khalid, and N. Arshad. "Machine learning in state of health and remaining useful life estimation: Theoretical and technological development in

- battery degradation modelling". In: *Renewable and Sustainable Energy Reviews* 156 (Mar. 2022), p. 111903. ISSN: 1364-0321. DOI: [10.1016/j.rser.2021.111903](https://doi.org/10.1016/j.rser.2021.111903).
- [165] H. Ruan, J. Chen, W. Ai, and B. Wu. "Generalised diagnostic framework for rapid battery degradation quantification with deep learning". In: *Energy and AI* 9 (Aug. 2022), p. 100158. ISSN: 2666-5468. DOI: [10.1016/j.egyai.2022.100158](https://doi.org/10.1016/j.egyai.2022.100158).
- [166] D. Roman, S. Saxena, V. Robu, M. Pecht, and D. Flynn. "Machine learning pipeline for battery state-of-health estimation". In: *Nature Machine Intelligence* 3.5 (Apr. 2021), pp. 447–456. ISSN: 2522-5839. DOI: [10.1038/s42256-021-00312-3](https://doi.org/10.1038/s42256-021-00312-3). arXiv: [2102.00837](https://arxiv.org/abs/2102.00837).
- [167] S. Jha, M. Yen, Y. S. Salinas, E. Palmer, J. Villafuerte, and H. Liang. "Machine learning-assisted materials development and device management in batteries and supercapacitors: performance comparison and challenges". In: *Journal of Materials Chemistry A* 11.8 (Jan. 2023), pp. 3904–3936. ISSN: 2050-7496. DOI: [10.1039/d2ta07148g](https://doi.org/10.1039/d2ta07148g).
- [168] L. H. Rieger, E. Flores, K. F. Nielsen, P. Norby, E. Ayerbe, O. Winther, T. Vegge, and A. Bhowmik. "Uncertainty-aware and explainable machine learning for early prediction of battery degradation trajectory". In: *Digital Discovery* 2.1 (Dec. 2022), pp. 112–122. ISSN: 2635-098X. DOI: [10.1039/d2dd00067a](https://doi.org/10.1039/d2dd00067a).
- [169] J. Lu, R. Xiong, J. Tian, C. Wang, and F. Sun. "Deep learning to estimate lithium-ion battery state of health without additional degradation experiments". In: *Nature Communications* 14.1 (May 2023), p. 2760. ISSN: 2041-1723. DOI: [10.1038/s41467-023-38458-w](https://doi.org/10.1038/s41467-023-38458-w).
- [170] J. Zhu, Y. Wang, Y. Huang, R. B. Gopaluni, Y. Cao, M. Heere, M. Mühlbauer, L. Mereacre, H. Dai, X. Liu, A. Senyshyn, X. Wei, M. Knapp, and H. Ehrenberg. "Data-driven capacity estimation of commercial lithium-ion batteries from voltage relaxation". In: *Nature Communications* 13.1 (Apr. 2022), p. 2261. ISSN: 2041-1723. DOI: [10.1038/s41467-022-29837-w](https://doi.org/10.1038/s41467-022-29837-w).
- [171] Y. Yang. "A machine-learning prediction method of lithium-ion battery life based on charge process for different applications". In: *Applied Energy* 292 (June 2021), p. 116897. ISSN: 0306-2619. DOI: [10.1016/j.apenergy.2021.116897](https://doi.org/10.1016/j.apenergy.2021.116897).

- [172] Y. Fan, F. Xiao, C. Li, G. Yang, and X. Tang. “A novel deep learning framework for state of health estimation of lithium-ion battery”. In: *Journal of Energy Storage* 32 (Dec. 2020), p. 101741. ISSN: 2352-152X. DOI: [10.1016/j.est.2020.101741](https://doi.org/10.1016/j.est.2020.101741).
- [173] A. Vaswani, N. M. Shazeer, N. Parmar, J. Uszkoreit, L. Jones, A. N. Gomez, L. Kaiser, and I. Polosukhin. *Attention Is All You Need*. Ed. by I. Guyon, U. V. Luxburg, S. Bengio, H. Wallach, R. Fergus, S. Vishwanathan, and R. Garnett. Aug. 2017. DOI: [10.48550/arXiv.1706.03762](https://doi.org/10.48550/arXiv.1706.03762). arXiv: [1706.03762](https://arxiv.org/abs/1706.03762).
- [174] J. Chorowski, D. Bahdanau, D. Serdyuk, K. Cho, and Y. Bengio. *Attention-Based Models for Speech Recognition*. 2015. DOI: [10.48550/ARXIV.1506.07503](https://doi.org/10.48550/ARXIV.1506.07503). arXiv: [1506.07503](https://arxiv.org/abs/1506.07503).
- [175] F. Wang, Z. E. Amogne, J.-H. Chou, and C. Tseng. “Online Remaining Useful Life Prediction of Lithium-Ion Batteries Using Bidirectional Long Short-Term Memory with Attention Mechanism”. In: *SSRN Electronic Journal* 254 (Feb. 2022), p. 124344. ISSN: 1556-5068. DOI: [10.2139/ssrn.4027426](https://doi.org/10.2139/ssrn.4027426).
- [176] B. Zhou, C. Cheng, G. Ma, and Y. Zhang. “Remaining Useful Life Prediction of Lithium-ion Battery based on Attention Mechanism with Positional Encoding”. In: *IOP Conference Series: Materials Science and Engineering* 895.1 (July 2020), p. 012006. ISSN: 1757-899X. DOI: [10.1088/1757-899x/895/1/012006](https://doi.org/10.1088/1757-899x/895/1/012006).
- [177] M.-F. Ng, J. Zhao, Q. Yan, G. J. Conduit, and Z. W. Seh. “Predicting the state of charge and health of batteries using data-driven machine learning”. In: *Nature Machine Intelligence* 2.3 (Mar. 2020), pp. 161–170. ISSN: 2522-5839. DOI: [10.1038/s42256-020-0156-7](https://doi.org/10.1038/s42256-020-0156-7).
- [178] C. Ling. “A review of the recent progress in battery informatics”. In: *npj Computational Materials* 8.1 (Feb. 2022), p. 33. ISSN: 2057-3960. DOI: [10.1038/s41524-022-00713-x](https://doi.org/10.1038/s41524-022-00713-x).
- [179] P. M. Maffettone, P. Friederich, S. G. Baird, B. Blaiszik, K. A. Brown, S. I. Campbell, O. A. Cohen, R. L. Davis, I. T. Foster, N. Haghmoradi, M. Hereld, H. Joreess, N. Jung, H.-K. Kwon, G. Pizzuto, J. Rintamaki, C. Steinmann, L. Torresi, and S. Sun. “What is missing in autonomous discovery: open challenges for the community”. In: *Digital Discovery* 2.6 (Aug. 2023), pp. 1644–1659. ISSN: 2635-098X. DOI: [10.1039/d3dd00143a](https://doi.org/10.1039/d3dd00143a). arXiv: [2304.11120](https://arxiv.org/abs/2304.11120).

- [180] M. L. Green, C. L. Choi, J. Hattrick-Simpers, A. M. Joshi, I. Takeuchi, S. Barron, E. Campo, T. Chiang, S. Empedocles, J. Gregoire, A. Kusne, J. Martin, A. Mehta, K. Persson, Z. Trautt, J. V. Duren, and A. Zakutayev. “Fulfilling the promise of the materials genome initiative with high-throughput experimental methodologies”. In: *Applied Physics Reviews* 4.1 (1 Mar. 2017). ISSN: 1931-9401. DOI: [10.1063/1.4977487](https://doi.org/10.1063/1.4977487).
- [181] M. Quigley, K. Conley, B. Gerkey, J. Faust, T. Foote, J. Leibs, R. Wheeler, A. Y. Ng, et al. “ROS: an open-source Robot Operating System”. In: *ROS: an open-source Robot Operating System*. Vol. 3: *ICRA workshop on open source software*. ICRA workshop on open source software. 3.2. Kobe, Japan, 2009, p. 5. URL: <http://robotics.stanford.edu/~ang/papers/icraoss09-ROS.pdf> (visited on 05/05/2024).
- [182] D. Guevarra, K. Kan, Y. Lai, R. J. R. Jones, L. Zhou, P. Donnelly, M. Richter, H. S. Stein, and J. M. Gregoire. “Orchestrating nimble experiments across interconnected labs”. In: *Digital Discovery* 2.6 (Oct. 2023), pp. 1806–1812. ISSN: 2635-098X. DOI: [10.1039/d3dd00166k](https://doi.org/10.1039/d3dd00166k).
- [183] J.-P. Correa-Baena, K. Hippalgaonkar, J. van Duren, S. Jaffer, V. R. Chandrasekhar, V. Stevanovic, C. Wadia, S. Guha, and T. Buonassisi. “Accelerating Materials Development via Automation, Machine Learning, and High-Performance Computing”. In: *Joule* 2.8 (Aug. 2018), pp. 1410–1420. ISSN: 2542-4351. DOI: [10.1016/j.joule.2018.05.009](https://doi.org/10.1016/j.joule.2018.05.009).
- [184] F. Dinic, K. Singh, T. Dong, M. Rezazadeh, Z. Wang, A. Khosrozadeh, T. Yuan, and O. Voznyy. “Applied Machine Learning for Developing Next-Generation Functional Materials”. In: *Advanced Functional Materials* 31.51 (Sept. 2021), p. 2104195. ISSN: 1616-3028. DOI: [10.1002/adfm.202104195](https://doi.org/10.1002/adfm.202104195).
- [185] T. Lombardo, M. Duquesnoy, H. El-Bouysidy, F. Årén, A. Gallo-Bueno, P. B. Jørgensen, A. Bhowmik, A. Demortière, E. Ayerbe, F. Alcaide, M. Reynaud, J. Carrasco, A. Grimaud, C. Zhang, T. Vegge, P. Johansson, and A. Franco. “Artificial Intelligence Applied to Battery Research: Hype or Reality?” In: *Chemical Reviews* 122.12 (Sept. 2021), pp. 10899–10969. ISSN: 1520-6890. DOI: [10.1021/acs.chemrev.1c00108](https://doi.org/10.1021/acs.chemrev.1c00108).



- [186] L. Talirz, S. Kumbhar, E. Passaro, A. V. Yakutovich, V. Granata, F. Gargiulo, M. Borelli, M. Uhrin, S. P. Huber, S. Zoupanos, C. Adorf, C. Andersen, O. Schütt, C. Pignedoli, D. Passerone, J. VandeVondele, T. Schulthess, B. Smit, G. Pizzi, and N. Marzari. “Materials Cloud, a platform for open computational science”. In: *Scientific Data* 7.1 (Sept. 2020), p. 299. ISSN: 2052-4463. DOI: [10.1038/s41597-020-00637-5](https://doi.org/10.1038/s41597-020-00637-5). arXiv: [2003.12510](https://arxiv.org/abs/2003.12510).
- [187] M. D. Wilkinson, M. Dumontier, I. J. Aalbersberg, G. Appleton, M. Axton, A. Baak, N. Blomberg, J.-W. Boiten, L. B. da Silva Santos, P. E. Bourne, J. Bouwman, A. J. Brookes, T. Clark, M. Crosas, I. Dillo, O. Dumon, S. Edmunds, C. T. Evelo, R. Finkers, A. Gonzalez-Beltran, A. J. Gray, P. Groth, C. Goble, J. S. Grethe, J. Heringa, P. A. ’t Hoen, R. Hooft, T. Kuhn, R. Kok, J. Kok, S. J. Lusher, M. E. Martone, A. Mons, A. L. Packer, B. Persson, P. Rocca-Serra, M. Roos, R. van Schaik, S.-A. Sansone, E. Schultes, T. Sengstag, T. Slater, G. Strawn, M. A. Swertz, M. Thompson, J. van der Lei, E. van Mulligen, J. Velterop, A. Waagmeester, P. Wittenburg, K. Wolstencroft, J. Zhao, and B. Mons. “The FAIR Guiding Principles for scientific data management and stewardship”. In: *Scientific Data* 3.1 (Mar. 2016), pp. 1–9. ISSN: 2052-4463. DOI: [10.1038/sdata.2016.18](https://doi.org/10.1038/sdata.2016.18).
- [188] S. Liu, Y. Su, H. Yin, D. Zhang, J. He, H. Huang, X. Jiang, X. Wang, H. Gong, Z. Li, et al. “An infrastructure with user-centered presentation data model for integrated management of materials data and services”. In: *npj Computational Materials* 7.1 (June 2021), p. 88. ISSN: 2057-3960. DOI: [10.1038/s41524-021-00557-x](https://doi.org/10.1038/s41524-021-00557-x).
- [189] J. Sourati and J. A. Evans. “Accelerating science with human-aware artificial intelligence”. In: *Nature Human Behaviour* 7.10 (July 2023), pp. 1682–1696. ISSN: 2397-3374. DOI: [10.1038/s41562-023-01648-z](https://doi.org/10.1038/s41562-023-01648-z). arXiv: [2306.01495](https://arxiv.org/abs/2306.01495).
- [190] M. Krenn, R. Pollice, S. Y. Guo, M. Aldeghi, A. Cervera-Lierta, P. Friederich, G. dos Passos Gomes, F. Häse, A. Jinich, A. Nigam, Z. Yao, and A. Aspuru-Guzik. “On scientific understanding with artificial intelligence”. In: *Nature Reviews Physics* 4.12 (Oct. 2022), pp. 761–769. ISSN: 2522-5820. DOI: [10.1038/s42254-022-00518-3](https://doi.org/10.1038/s42254-022-00518-3). eprint: [2204.01467](https://arxiv.org/abs/2204.01467).

- [191] I. E. Castelli, D. J. Arismendi-Arrieta, A. Bhowmik, I. Cekic-Laskovic, S. Clark, R. Dominko, E. Flores, J. Flowers, K. Ulvskov Frederiksen, J. Friis, A. Grimaud, K. V. Hansen, L. J. Hardwick, K. Hermansson, L. Königer, H. Lauritzen, F. Le Cras, H. Li, S. Lyonnard, H. Lorrman, N. Marzari, L. Niedzicki, G. Pizzi, F. Rahmanian, H. Stein, M. Uhrin, W. Wenzel, M. Winter, C. Wölke, and T. Vegge. “Data Management Plans: the Importance of Data Management in the BIG-MAP Project”. In: *Batteries & Supercaps* 4.12 (Sept. 2021), pp. 1803–1812. ISSN: 2566-6223. DOI: [10.1002/batt.202100117](https://doi.org/10.1002/batt.202100117). eprint: [2106.01616](https://arxiv.org/abs/2106.01616).
- [192] BATTERY 2030+ CSA3 large-scale research initiative: At the heart of a connected green society. Project. European Commission: B2030 CSA3 Grant agreement ID: 101104022, Sept. 1, 2023. DOI: [10.3030/101104022](https://doi.org/10.3030/101104022). URL: <https://battery2030.eu/> (visited on 05/05/2024).
- [193] *The Elementary Multiperspective Material Ontology (EMMO)*. EMMC-CSA, Oct. 2021. URL: <https://emmo-repo.github.io/>.
- [194] EMMC-CSA. “The European Materials Modelling Council”. In: ed. by G. agreement ID: 723867. Funded under INDUSTRIAL LEADERSHIP - Leadership in enabling and industrial technologies - Advanced materials. European Commission. June 2016. DOI: [10.3030/723867](https://doi.org/10.3030/723867). URL: <https://cordis.europa.eu/project/id/723867> (visited on 05/05/2024). Funded under INDUSTRIAL LEADERSHIP - Leadership in enabling and industrial technologies - Advanced materials.
- [195] J. Medina, A. W. Ziaullah, H. Park, I. E. Castelli, A. Shaon, H. Bensmail, and F. El-Mellouhi. “Accelerating the Adoption of Research Data Management Strategies”. In: *SSRN Electronic Journal* 5.11 (Nov. 2022), pp. 3614–3642. ISSN: 1556-5068. DOI: [10.2139/ssrn.4175588](https://doi.org/10.2139/ssrn.4175588).
- [196] EU. *BIG-MAP. The Battery Interface Genome – Materials Acceleration Platform (BIG-MAP)*. URL: <https://www.big-map.eu> (visited on 05/08/2024).
- [197] J. F. Simon Clark and T. Vegge. *BattINFO: The ontology for the Battery Interface Genome - Materials Acceleration Platform (BIG-MAP)*. 2021. URL: <https://www.big-map.eu/dissemination/battinfo> (visited on 05/05/2024).



- [198] S. Clark, F. Bleken, S. Stier, E. Flores, C. Andersen, M. Marcinek, A. Szczęśna-Chrzan, M. Gaberšček, M. Palacin, M. Uhrin, and J. Friis. "Toward a Unified Description of Battery Data". In: *Advanced Energy Materials* 12.17 (Dec. 2021), p. 2102702. ISSN: 1614-6840. DOI: [10.1002/aenm.202102702](https://doi.org/10.1002/aenm.202102702).
- [199] *BIG-MAP App Store*. May 5, 2024. URL: <https://big-map.github.io/big-map-registry/> (visited on 05/05/2024).
- [200] M. Vogler, J. Busk, H. Hajiyani, P. B. Jørgensen, N. Safaei, I. E. Castelli, F. F. Ramirez, J. Carlsson, G. Pizzi, S. Clark, F. Hanke, A. Bhowmik, and H. S. Stein. "Brokering between tenants for an international materials acceleration platform". In: *Matter* 6.9 (Sept. 2023), pp. 2647–2665. ISSN: 2590-2385. DOI: [10.1016/j.matt.2023.07.016](https://doi.org/10.1016/j.matt.2023.07.016).
- [201] S. P. Huber, S. Zoupanos, M. Uhrin, L. Talirz, L. Kahle, R. Häuselmann, D. Gresch, T. Müller, A. V. Yakutovich, C. Andersen, F. F. Ramirez, C. Adorf, F. Gargiulo, S. Kumbhar, E. Passaro, C. Johnston, A. Merkys, A. Cepellotti, N. Mounet, N. Marzari, B. Kozinsky, and G. Pizzi. "AiiDA 1.0, a scalable computational infrastructure for automated reproducible workflows and data provenance". In: *Scientific Data* 7.1 (Sept. 2020), p. 300. ISSN: 2052-4463. DOI: [10.1038/s41597-020-00638-4](https://doi.org/10.1038/s41597-020-00638-4). arXiv: [2003.12476](https://arxiv.org/abs/2003.12476).
- [202] E. Flores, N. Mozhzhukhina, X. Li, P. Norby, A. Matic, and T. Vegge. "PRISMA: A Robust and Intuitive Tool for High-Throughput Processing of Chemical Spectra". In: *Chemistry-Methods* 2.10 (Oct. 2021), e202100094. DOI: [10.26434/chemrxiv-2021-7qs3m-v2](https://doi.org/10.26434/chemrxiv-2021-7qs3m-v2).
- [203] M. Soleymanibrojeni, C. R. C. Rêgo, M. Esmailpour, and W. Wenzel. "An Active Learning Approach to Model Solid-Electrolyte Interphase Formation in Li-ion Batteries". In: *Journal of Materials Chemistry A* 12.4 (Dec. 2023), pp. 2249–2266. ISSN: 2050-7496. DOI: [10.1039/d3ta06054c](https://doi.org/10.1039/d3ta06054c).
- [204] C. R. Groom, I. J. Bruno, M. P. Lightfoot, and S. C. Ward. "The Cambridge Structural Database". In: *Acta Crystallographica Section B Structural Science, Crystal Engineering and Materials* 72.2 (Apr. 2016), pp. 171–179. ISSN: 2052-5206. DOI: [10.1107/s2052520616003954](https://doi.org/10.1107/s2052520616003954).

- [205] G. Bergerhoff, R. Hundt, R. Sievers, and I. Brown. “The inorganic crystal structure data base”. In: *Journal of Chemical Information and Computer Sciences* 23.2 (May 1983), pp. 66–69. ISSN: 1520-5142. DOI: [10.1021/ci00038a003](https://doi.org/10.1021/ci00038a003).
- [206] C. Draxl and M. Scheffler. “The NOMAD laboratory: from data sharing to artificial intelligence”. In: *Journal of Physics: Materials* 2.3 (May 2019), p. 036001. ISSN: 2515-7639. DOI: [10.1088/2515-7639/ab13bb](https://doi.org/10.1088/2515-7639/ab13bb).
- [207] L. Sbailò, à. Fekete, L. M. Ghiringhelli, and M. Scheffler. “The NOMAD Artificial-Intelligence Toolkit: turning materials-science data into knowledge and understanding”. In: *npj Computational Materials* 8.1 (Dec. 2022), p. 250. ISSN: 2057-3960. DOI: [10.1038/s41524-022-00935-z](https://doi.org/10.1038/s41524-022-00935-z). arXiv: [2205.15686](https://arxiv.org/abs/2205.15686).
- [208] R. Duke, S. Mahmoudi, A. Kaur, V. Bhat, I. Dingle, N. C. Stumme, S. K. Shaw, D. Eaton, A. Vego, and C. Risko. “ExpFlow: a graphical user interface for automated reproducible electrochemistry”. In: *Digital Discovery* 3.1 (Jan. 2024), pp. 163–172. ISSN: 2635-098X. DOI: [10.1039/d3dd00156c](https://doi.org/10.1039/d3dd00156c).
- [209] M. B. Rooney, B. P. MacLeod, R. Oldford, Z. J. Thompson, K. L. White, J. Tungjunyatham, B. J. Stankiewicz, and C. P. Berlinguette. “A self-driving laboratory designed to accelerate the discovery of adhesive materials”. In: *Digital Discovery* 1.4 (May 2022), pp. 382–389. ISSN: 2635-098X. DOI: [10.1039/d2dd00029f](https://doi.org/10.1039/d2dd00029f).
- [210] A. A. Volk, R. W. Epps, D. T. Yonemoto, B. S. Masters, F. N. Castellano, K. G. Reyes, and M. Abolhasani. “AlphaFlow: autonomous discovery and optimization of multi-step chemistry using a self-driven fluidic lab guided by reinforcement learning”. In: *Nature Communications* 14.1 (Mar. 2023), p. 1403. ISSN: 2041-1723. DOI: [10.1038/s41467-023-37139-y](https://doi.org/10.1038/s41467-023-37139-y).
- [211] N. J. Szymanski, B. Rendy, Y. Fei, R. E. Kumar, T. He, D. Milsted, M. J. McDermott, M. Gallant, E. D. Cubuk, A. Merchant, et al. “An autonomous laboratory for the accelerated synthesis of novel materials”. In: *Nature* 624.7990 (Nov. 2023), pp. 86–91. ISSN: 1476-4687. DOI: [10.1038/s41586-023-06734-w](https://doi.org/10.1038/s41586-023-06734-w).
- [212] G. Schrimpf. *Merck Collaborates with Acceleration Consortium on Open-Sourcing AI-Driven Experimentation*. Merck Collaborates with Acceleration Consortium on Open-Sourcing AI-Driven Experimentation. Merck. 2023. URL: <https://www.>

- [merckgroup.com/en/news/opensource-ai-experimentation-planner-06-12-2023.html](https://www.merckgroup.com/en/news/opensource-ai-experimentation-planner-06-12-2023.html) (visited on 05/05/2024).
- [213] F. Martin, Š. Adrian, H. Alexander, and L. Alex. *BayBE — A Bayesian Back End for Design of Experiments*. Version 0.8.2. Visited on 13.01.2024. emdgroup. May 5, 2024. URL: <https://github.com/emdgroup/baybe> (visited on 05/05/2024).
- [214] E. McCalla. “Semiautomated Experiments to Accelerate the Design of Advanced Battery Materials: Combining Speed, Low Cost, and Adaptability”. In: *ACS Engineering Au* 3.6 (Nov. 2023), pp. 391–402. ISSN: 2694-2488. DOI: [10.1021/acsengineeringau.3c00037](https://doi.org/10.1021/acsengineeringau.3c00037).
- [215] M. Manica, J. Born, J. Cadow, D. Christofidellis, A. Dave, D. Clarke, Y. G. N. Teukam, G. Giannone, S. C. Hoffman, M. Buchan, V. Chenthamarakshan, T. Donovan, H.-H. Hsu, F. Zipoli, O. Schilter, A. Kishimoto, L. Hamada, I. Padhi, K. Wehden, L. N. McHugh, A. Khrabrov, P. Das, S. Takeda, and J. Smith. “Accelerating material design with the generative toolkit for scientific discovery”. In: *npj Computational Materials* 9.1 (May 2023), p. 69. ISSN: 2057-3960. DOI: [10.1038/s41524-023-01028-1](https://doi.org/10.1038/s41524-023-01028-1). arXiv: [2207.03928](https://arxiv.org/abs/2207.03928).
- [216] Z. Zheng, O. Zhang, C. Borgs, J. T. Chayes, and O. M. Yaghi. “ChatGPT Chemistry Assistant for Text Mining and the Prediction of MOF Synthesis”. In: *Journal of the American Chemical Society* 145.32 (2023), pp. 18048–18062. DOI: [10.1021/jacs.3c05819](https://doi.org/10.1021/jacs.3c05819).
- [217] S. Stier, C. Kreisbeck, H. Ihssen, M. A. Popp, J. Hauch, K. Malek, M. Reynaud, J. Carlsson, L. Gold, F. Goumans, I. Todorov, A. Räder, S. T. Bandesha, W. Wenzel, P. Jacques, O. Arcelus, F. Garcia-Moreno, P. Friederich, M. Maglione, S. Clark, A. Laukkanen, M. C. Cabanas, J. Carrasco, I. E. Castelli, H. S. Stein, T. Vegge, S. Nakamae, M. Fabrizio, and M. Kozdras. *The Significance of Accelerated Discovery of Advanced Materials to address Societal Challenges*. en. Dec. 2023. DOI: [10.5281/zenodo.8012140](https://doi.org/10.5281/zenodo.8012140).
- [218] R. C. Martin. *Clean code: A handbook of agile software craftsmanship. A handbook of agile software craftsmanship*. 1st ed. Robert C. Martin series. Upper Saddle River, NJ: Prentice Hall, 2008. 431 pp. ISBN: 9780132350884.
- [219] G. Zaccane. *Python Parallel Programming Cookbook*. Quick answers to common problems. s.l.: Packt Publishing, 2015. 1286 pp. ISBN: 9781785286728.

- [220] T. Rauber and G. Rnger. *Parallel Programming: for Multicore and Cluster Systems. For Multicore and Cluster Systems*. Ed. by G. Rüniger. 2nd ed. 2013. Berlin, Heidelberg: Springer Publishing Company, Incorporated, 2013. 1516 pp. ISBN: 9783642378010.
- [221] Q. Nguyen. *Mastering Concurrency in Python: Create faster programs using concurrency, asynchronous, multithreading, and parallel programming. Create faster programs using concurrency, asynchronous, multithreading, and parallel programming*. 1. Birmingham: Packt Publishing, 2018. 1446 pp. ISBN: 9781789341362.
- [222] M. Fowler. *Python concurrency with asyncio*. Shelter Island: Manning, 2022. 356 pp. ISBN: 1617298662.
- [223] S. Ramírez. *FastAPI*. URL: <https://github.com/tiangolo/fastapi> (visited on 05/08/2024).
- [224] S. J. C. Tragura. *Building Python Microservices with FastAPI: Build secure, scalable, and structured Python microservices from design concepts to infrastructure. Build secure, scalable, and structured Python microservices from design concepts to infrastructure*. Includes bibliographical references and index. [Place of publication not identified]: Packt Publishing, 2022. 1419 pp. ISBN: 9781803245966.
- [225] S. Colvin, E. Jolibois, H. Ramezani, A. G. Badaracco, T. Dorsey, D. Montague, S. Matveencko, M. Trylesinski, S. Runkle, D. Hewitt, and A. Hall. *Pydantic*. Mar. 12, 2024. URL: <https://github.com/pydantic/pydantic> (visited on 05/08/2024).
- [226] B. Lubanovic. *FastAPI Modern Python web development*. First edition. Making It Work. Sebastopol: O'Reilly Media, Inc, 2024. 1280 pp. ISBN: 9781098135478.
- [227] I. Fette and A. Melnikov. *The WebSocket Protocol*. Dec. 2011. DOI: [10.17487/rfc6455](https://doi.org/10.17487/rfc6455).
- [228] V. Pimentel and B. G. Nickerson. "Communicating and Displaying Real-Time Data with WebSocket". In: *IEEE Internet Computing* 16.4 (July 2012), pp. 45–53. ISSN: 1089-7801. DOI: [10.1109/MIC.2012.64](https://doi.org/10.1109/MIC.2012.64).
- [229] P. Murley, Z. Ma, J. Mason, M. Bailey, and A. Kharraz. "WebSocket Adoption and the Landscape of the Real-Time Web". In: *Proceedings of the Web Conference 2021 (The Web Conference)*. WWW '21. ACM, Apr. 2021, pp. 1192–1203. DOI: [10.1145/3442381.3450063](https://doi.org/10.1145/3442381.3450063).

- [230] L. Banko and A. Ludwig. “Fast-Track to Research Data Management in Experimental Material Science—Setting the Ground for Research Group Level Materials Digitalization”. In: *ACS Combinatorial Science* 22.8 (June 2020), pp. 401–409. ISSN: 2156-8944. DOI: [10.1021/acscombsci.0c00057](https://doi.org/10.1021/acscombsci.0c00057).
- [231] P. Kraus, E. Bainglass, F. F. Ramirez, E. Svaluto-Ferro, L. Ercole, B. Kunz, S. P. Huber, N. Plainpan, N. Marzari, C. Battaglia, and G. Pizzi. “A bridge between trust and control: Computational workflows meet automated battery cycling”. In: *Journal of Materials Chemistry A* (Mar. 2024). ISSN: 2050-7496. DOI: [10.1039/d3ta06889g](https://doi.org/10.1039/d3ta06889g).
- [232] J. M. Cole. “A Design-to-Device Pipeline for Data-Driven Materials Discovery”. In: *Accounts of Chemical Research* 53.3 (Feb. 2020), pp. 599–610. ISSN: 1520-4898. DOI: [10.1021/acs.accounts.9b00470](https://doi.org/10.1021/acs.accounts.9b00470).
- [233] M. Naeem, T. Jamal, J. Diaz-Martinez, S. A. Butt, N. Montesano, M. I. Tariq, E. De-la-Hoz-Franco, and E. De-La-Hoz-Valdiris. “Trends and Future Perspective Challenges in Big Data”. In: *Smart Innovation, Systems and Technologies*. Springer Singapore, Nov. 2021, pp. 309–325. ISBN: 9789811650369. DOI: [10.1007/978-981-16-5036-9\\_30](https://doi.org/10.1007/978-981-16-5036-9_30).
- [234] P. T. Inc. *Collaborative data science*. 2015. URL: <https://plot.ly>.
- [235] European Organization For Nuclear Research and OpenAIRE. *Zenodo*. en. 2013. DOI: [10.25495/7GXX-RD71](https://doi.org/10.25495/7GXX-RD71). URL: <https://www.zenodo.org/>.
- [236] M. Scheffler, M. Aeschlimann, M. Albrecht, T. Bereau, H.-J. Bungartz, C. Felser, M. Greiner, A. Groß, C. T. Koch, K. Kremer, et al. “FAIR data enabling new horizons for materials research”. In: *Nature* 604.7907 (Apr. 2022), pp. 635–642. ISSN: 1476-4687. DOI: [10.1038/s41586-022-04501-x](https://doi.org/10.1038/s41586-022-04501-x). arXiv: [2204.13240](https://arxiv.org/abs/2204.13240).
- [237] F.-X. Coudert. “Materials Databases: The Need for Open, Interoperable Databases with Standardized Data and Rich Metadata”. In: *Advanced Theory and Simulations* 2.11 (Sept. 2019), p. 1900131. ISSN: 2513-0390. DOI: [10.1002/adts.201900131](https://doi.org/10.1002/adts.201900131). arXiv: [1907.02791](https://arxiv.org/abs/1907.02791).
- [238] T. Haerder and A. Reuter. “Principles of transaction-oriented database recovery”. In: *ACM Computing Surveys* 15.4 (Dec. 1983), pp. 287–317. ISSN: 1557-7341. DOI: [10.1145/289.291](https://doi.org/10.1145/289.291).

- [239] R. Fagin. “A normal form for relational databases that is based on domains and keys”. In: *ACM Transactions on Database Systems (TODS)* 6.3 (1981), pp. 387–415.
- [240] W. Kent. “A simple guide to five normal forms in relational database theory”. In: *Communications of the ACM* 26.2 (Feb. 1983), pp. 120–125. ISSN: 1557-7317. DOI: [10.1145/358024.358054](https://doi.org/10.1145/358024.358054).
- [241] C. J. Date. *Database design and relational theory: normal forms and all that jazz*. Apress, 2019.
- [242] S. B. Kotsiantis, D. Kanellopoulos, and P. E. Pintelas. “Data preprocessing for supervised leaning”. In: *International journal of computer science* 1.2 (2006), pp. 111–117. URL: [https://www.academia.edu/download/46222694/Data\\_preprocessing\\_for\\_supervised\\_leanin20160604-9354-q8adlk.pdf](https://www.academia.edu/download/46222694/Data_preprocessing_for_supervised_leanin20160604-9354-q8adlk.pdf) (visited on 05/07/2024).
- [243] H. tom Würden, F. Spreckelsen, S. Luther, U. Parlitz, and A. Schlemmer. “Mapping Hierarchical File Structures to Semantic Data Models for Efficient Data Integration into Research Data Management Systems”. In: *Data* 9.2 (Jan. 2024), p. 24. ISSN: 2306-5729. DOI: [10.3390/data9020024](https://doi.org/10.3390/data9020024).
- [244] S. Banabilah, M. Aloqaily, E. Alsayed, N. Malik, and Y. Jararweh. “Federated learning review: Fundamentals, enabling technologies, and future applications”. In: *Information processing & management* 59.6 (2022), p. 103061.
- [245] M. Grinberg. *Flask web development: developing web applications with python. Developing web applications with Python*. Second edition. O’Reilly Media, Inc., 2018. 1292 pp. ISBN: 9781491991718.
- [246] PySimpleSoft. *PySimpleGui: Python GUIs for humans*. May 7, 2024. URL: <https://www.pysimplegui.com/>.
- [247] B. L. DeCost, J. Hattrick-Simpers, Z. Trautt, A. Kusne, E. Campo, and M. Green. “Scientific AI in materials science: a path to a sustainable and scalable paradigm”. In: *Machine Learning: Science and Technology* 1.3 (July 2020), p. 033001. ISSN: 2632-2153. DOI: [10.1088/2632-2153/ab9a20](https://doi.org/10.1088/2632-2153/ab9a20). arXiv: [2003.08471](https://arxiv.org/abs/2003.08471).



- [248] L. M. Ghiringhelli, C. Baldauf, T. Bereau, S. Brockhauser, C. Carbogno, J. Chamanara, S. Cozzini, S. Curtarolo, C. Draxl, S. Dwaraknath, Á. Fekete, J. Kermode, C. T. Koch, M. Kühbach, A. N. Ladines, P. Lambrix, M.-O. Himmer, S. V. Levchenko, M. Oliveira, A. Michalchuk, R. E. Miller, B. Onat, P. Pavone, G. Pizzi, B. Regler, G.-M. Rignanese, J. Schaarschmidt, M. Scheidgen, A. Schneidewind, T. Sheveleva, C. Su, D. Usvyat, O. Valsson, C. Wöll, and M. Scheffler. “Shared metadata for data-centric materials science”. In: *Scientific Data* 10.1 (Sept. 2023), p. 626. ISSN: 2052-4463. DOI: [10.1038/s41597-023-02501-8](https://doi.org/10.1038/s41597-023-02501-8). arXiv: [2205.14774](https://arxiv.org/abs/2205.14774).
- [249] Figshare. *Figshare - Manage your research in the cloud and control who you share it with or make it publicly available and citable*. 2024. URL: <https://figshare.com> (visited on 05/07/2024).
- [250] S. Bechhofer, I. Buchan, D. D. Roure, P. Missier, J. Ainsworth, J. Bhagat, P. Couch, D. Cruickshank, M. Delderfield, I. Dunlop, M. Gamble, D. Michaelides, S. Owen, D. Newman, S. Sufi, and C. Goble. “Why linked data is not enough for scientists”. In: *Future Generation Computer Systems* 29.2 (Feb. 2013), pp. 599–611. ISSN: 0167-739X. DOI: [10.1016/j.future.2011.08.004](https://doi.org/10.1016/j.future.2011.08.004).
- [251] B. G. Pelkie and L. D. Pozzo. “The Laboratory of Babel: Highlighting community needs for integrated materials data management”. In: *Digital Discovery* 2.3 (Mar. 2023), pp. 544–556. ISSN: 2635-098X. DOI: [10.1039/d3dd00022b](https://doi.org/10.1039/d3dd00022b).
- [252] J. R. Hattrick-Simpers, J. M. Gregoire, and A. G. Kusne. “Perspective: Composition–structure–property mapping in high-throughput experiments: Turning data into knowledge”. In: *APL Materials* 4.5 (May 2016). ISSN: 2166-532X. DOI: [10.1063/1.4950995](https://doi.org/10.1063/1.4950995).
- [253] F. Ren, L. Ward, T. Williams, K. J. Laws, C. Wolverton, J. Hattrick-Simpers, and A. Mehta. “Accelerated discovery of metallic glasses through iteration of machine learning and high-throughput experiments”. In: *Science Advances* 4.4 (Apr. 2018), eaaq1566. ISSN: 2375-2548. DOI: [10.1126/sciadv.aaq1566](https://doi.org/10.1126/sciadv.aaq1566).
- [254] M. D. Shields, K. Gurley, R. Catarelli, M. Chauhan, M. Ojeda-Tuz, and F. J. Masters. “Active learning applied to automated physical systems increases the rate of discovery”. In: *Scientific Reports* 13.1 (May 2023), p. 8402. ISSN: 2045-2322. DOI: [10.1038/s41598-023-35257-7](https://doi.org/10.1038/s41598-023-35257-7).

- [255] L. Breiman. “Random forests”. In: *Machine learning* 45.1 (Oct. 2001), pp. 5–32. ISSN: 0885-6125. DOI: [10.1023/a:1010933404324](https://doi.org/10.1023/a:1010933404324).
- [256] T. Hastie, R. Tibshirani, J. H. Friedman, and J. H. Friedman. *The elements of statistical learning: data mining, inference, and prediction. Data mining, inference, and prediction*. Ed. by R. Tibshirani and J. H. Friedman. Second edition. Vol. 2. Springer Series in Statistics. Description based on publisher supplied metadata and other sources. New York, NY: Springer, 2017. 1745 pp. ISBN: 9780387848587.
- [257] M. H. Shaker and E. Hüllermeier. “Aleatoric and Epistemic Uncertainty with Random Forests”. In: *Advances in Intelligent Data Analysis XVIII*. Springer International Publishing, 2020, pp. 444–456. ISBN: 9783030445843. DOI: [10.1007/978-3-030-44584-3\\_35](https://doi.org/10.1007/978-3-030-44584-3_35). arXiv: [2001.00893](https://arxiv.org/abs/2001.00893).
- [258] V. Vovk. “Cross-conformal predictors”. In: *Annals of Mathematics and Artificial Intelligence* 74.1–2 (July 2013), pp. 9–28. ISSN: 1573-7470. DOI: [10.1007/s10472-013-9368-4](https://doi.org/10.1007/s10472-013-9368-4).
- [259] R. F. Barber, E. J. Candes, A. Ramdas, and R. J. Tibshirani. “Predictive inference with the jackknife+”. In: *The Annals of Statistics* 49.1 (Feb. 2021). ISSN: 0090-5364. DOI: [10.1214/20-aos1965](https://doi.org/10.1214/20-aos1965).
- [260] B. Kim, C. Xu, and R. Barber. “Predictive inference is free with the Jackknife+after-Bootstrap”. In: vol. 33. 2020, pp. 4138–4149. URL: <https://papers.nips.cc/paper/2020/file/2b346a0aa375a07f5a90a344a61416c4-Paper.pdf>.
- [261] V. Taquet, V. Blot, T. Morzadec, L. Lacombe, and N. Brunel. *MAPIE: an open-source library for distribution-free uncertainty quantification*. 2022. DOI: [10.48550/ARXIV.2207.12274](https://doi.org/10.48550/ARXIV.2207.12274). URL: <https://github.com/scikit-learn-contrib/MAPIE> (visited on 05/07/2024).
- [262] T. Cordier, V. Blot, L. Lacombe, T. Morzadec, A. Capitaine, and N. Brunel. “Flexible and Systematic Uncertainty Estimation with Conformal Prediction via the MAPIE library”. In: (2023), pp. 549–581. URL: <https://cml.rhul.ac.uk/copa2023/presentations/Cordier%20-%20MAPIE.pdf> (visited on 05/07/2024).



- [263] I. Goodfellow, Y. Bengio, and A. Courville. *Deep learning*. Ed. by A. Courville and Y. Bengio. Adaptive computation and machine learning. Includes bibliographical references and index. Cambridge, Massachusetts: The MIT Press, 2016. 1775 pp. ISBN: 9780262337373.
- [264] Y. LeCun, Y. Bengio, and G. Hinton. “Deep learning”. In: *nature* 521.7553 (May 2015), pp. 436–444. ISSN: 1476-4687. DOI: [10.1038/nature14539](https://doi.org/10.1038/nature14539).
- [265] S. Hochreiter and J. Schmidhuber. “Long Short-Term Memory”. In: *Neural Computation* 9.8 (Nov. 1997), pp. 1735–1780. ISSN: 1530-888X. DOI: [10.1162/neco.1997.9.8.1735](https://doi.org/10.1162/neco.1997.9.8.1735).
- [266] A. Sherstinsky. “Fundamentals of Recurrent Neural Network (RNN) and Long Short-Term Memory (LSTM) network”. In: *Physica D: Nonlinear Phenomena* 404 (Mar. 2020), p. 132306. ISSN: 0167-2789. DOI: [10.1016/j.physd.2019.132306](https://doi.org/10.1016/j.physd.2019.132306). arXiv: [1808.03314](https://arxiv.org/abs/1808.03314).
- [267] S. J. Prince. *Understanding Deep Learning*. MIT press, 2023.
- [268] N. Srivastava, G. E. Hinton, A. Krizhevsky, I. Sutskever, and R. Salakhutdinov. “Dropout: a simple way to prevent neural networks from overfitting”. In: *The journal of machine learning research* 15.1 (Jan. 2014), pp. 1929–1958. DOI: [10.5555/2627435.2670313](https://doi.org/10.5555/2627435.2670313).
- [269] D. Bahdanau, K. Cho, and Y. Bengio. “Neural Machine Translation by Jointly Learning to Align and Translate”. In: (May 2016). Preprint at. DOI: [10.48550/arXiv.1409.0473](https://doi.org/10.48550/arXiv.1409.0473). URL: <https://arxiv.org/abs/1409.0473>.
- [270] R. Caruana. “Multitask Learning”. In: *Machine Learning* 28.1 (1997), pp. 41–75. ISSN: 0885-6125. DOI: [10.1023/a:1007379606734](https://doi.org/10.1023/a:1007379606734).
- [271] L. N. Smith and N. Topin. “Super-convergence: very fast training of neural networks using large learning rates”. In: *Artificial Intelligence and Machine Learning for Multi-Domain Operations Applications (Defense + Commercial Sensing)*. Ed. by T. Pham. Vol. 11006. SPIE. SPIE, May 2019, pp. 369–386. DOI: [10.1117/12.2520589](https://doi.org/10.1117/12.2520589).
- [272] L. Prechelt. “Early Stopping - But When?” In: *Neural Networks: Tricks of the Trade*. Springer Berlin Heidelberg, 1998, pp. 55–69. ISBN: 9783540494300. DOI: [10.1007/3-540-49430-8\\_3](https://doi.org/10.1007/3-540-49430-8_3).

- [273] G. Zubi, R. Dufo-López, M. Carvalho, and G. Pasaoglu. “The lithium-ion battery: State of the art and future perspectives”. In: *Renewable and sustainable energy reviews* 89 (2018), pp. 292–308. DOI: [10.1016/J.RSER.2018.03.002](https://doi.org/10.1016/J.RSER.2018.03.002).
- [274] W. Wu, W. Luo, and Y. Huang. “Less is more: a perspective on thinning lithium metal towards high-energy-density rechargeable lithium batteries”. In: *Chemical Society Reviews* 52.8 (Mar. 2023), pp. 2553–2572. ISSN: 1460-4744. DOI: [10.1039/d2cs00606e](https://doi.org/10.1039/d2cs00606e).
- [275] K. Xu. “Nonaqueous Liquid Electrolytes for Lithium-Based Rechargeable Batteries”. In: *Chemical reviews* 104.10 (Sept. 2004), pp. 4303–4418. ISSN: 1520-6890. DOI: [10.1021/cr030203g](https://doi.org/10.1021/cr030203g).
- [276] J. Asenbauer, T. Eisenmann, M. Kuenzel, A. Kazzazi, Z. Chen, and D. Bresser. “The success story of graphite as a lithium-ion anode material—fundamentals, remaining challenges, and recent developments including silicon (oxide) composites”. In: *Sustainable Energy & Fuels* 4.11 (Apr. 2020), pp. 5387–5416. ISSN: 2398-4902. DOI: [10.1039/d0se00175a](https://doi.org/10.1039/d0se00175a).
- [277] J. B. Goodenough and K.-S. Park. “The Li-Ion Rechargeable Battery: A Perspective”. In: *Journal of the American Chemical Society* 135.4 (Jan. 2013), pp. 1167–1176. ISSN: 1520-5126. DOI: [10.1021/ja3091438](https://doi.org/10.1021/ja3091438).
- [278] W.-J. Zhang. “Structure and performance of LiFePO<sub>4</sub> cathode materials: A review”. In: *Journal of Power Sources* 196.6 (Mar. 2011), pp. 2962–2970. ISSN: 0378-7753. DOI: [10.1016/j.jpowsour.2010.11.113](https://doi.org/10.1016/j.jpowsour.2010.11.113).
- [279] X. Hu, L. Xu, X. Lin, and M. Pecht. “Battery Lifetime Prognostics”. In: *Joule* 4.2 (Feb. 2020), pp. 310–346. ISSN: 2542-4351. DOI: [10.1016/j.joule.2019.11.018](https://doi.org/10.1016/j.joule.2019.11.018).
- [280] A. Lasia. *Electrochemical Impedance Spectroscopy and its Applications*. Springer, 2014, pp. 143–248. ISBN: 9781461489337. DOI: [10.1007/978-1-4614-8933-7](https://doi.org/10.1007/978-1-4614-8933-7).
- [281] A. C. Lazanas and M. I. Prodromidis. “Electrochemical Impedance Spectroscopy—A Tutorial”. In: *ACS Measurement Science Au* 3.3 (Mar. 2023), pp. 162–193. ISSN: 2694-250X. DOI: [10.1021/acsmearsciau.2c00070](https://doi.org/10.1021/acsmearsciau.2c00070).
- [282] V. F. Lvovich. *Impedance Spectroscopy: Applications to Electrochemical and Dielectric Phenomena*. Applications to Electrochemical and Dielectric Phenomena. John Wiley & Sons, June 2012. ISBN: 9781118164075. DOI: [10.1002/9781118164075](https://doi.org/10.1002/9781118164075).

- [283] M. D. Murbach, B. Gerwe, N. Dawson-Elli, and L. Tsui. “impedance.py: A Python package for electrochemical impedance analysis”. In: *Journal of Open Source Software* 5.52 (Aug. 2020), p. 2349. ISSN: 2475-9066. DOI: [10.21105/joss.02349](https://doi.org/10.21105/joss.02349).
- [284] “SciPy 1.0: fundamental algorithms for scientific computing in Python”. In: *Nature Methods* 17.3 (Feb. 2020), pp. 352–352. ISSN: 1548-7105. DOI: [10.1038/s41592-020-0772-5](https://doi.org/10.1038/s41592-020-0772-5).
- [285] A. Bard and L. Faulkner. “Electrochemical Methods: Fundamentals and Applications”. In: *Journal of Chemical Education* 60.1 (Jan. 1983), A25. ISSN: 1938-1328. DOI: [10.1021/ed060pa25.1](https://doi.org/10.1021/ed060pa25.1).
- [286] N. Elgrishi, K. J. Rountree, B. D. McCarthy, E. S. Rountree, T. T. Eisenhart, and J. L. Dempsey. “A Practical Beginner’s Guide to Cyclic Voltammetry”. In: *Journal of Chemical Education* 95.2 (Nov. 2017), pp. 197–206. ISSN: 1938-1328. DOI: [10.1021/acs.jchemed.7b00361](https://doi.org/10.1021/acs.jchemed.7b00361).
- [287] T. Akiba, S. Sano, T. Yanase, T. Ohta, and M. Koyama. “Optuna: A Next-generation Hyperparameter Optimization Framework. A Next-generation Hyperparameter Optimization Framework”. In: *Proceedings of the 25th ACM SIGKDD International Conference on Knowledge Discovery & Data Mining*. KDD ’19. Anchorage, AK, USA: Association for Computing Machinery, July 2019, pp. 2623–2631. ISBN: 9781450362016. DOI: [10.1145/3292500.3330701](https://doi.org/10.1145/3292500.3330701).